FE-2248-18
Distribution Categories UC-90g and UC-93

DEVELOPMENT, TESTING AND EVALUATION OF MHD MATERIALS AND COMPONENT DESIGNS

Quarterly Report for the Period
October 1 - December 31, 1977

John W. Sadler
Jeff Bein
David L. Black
Raymond Calvo
Larry H. Cadoff*
James A. Dilmore*
Gary E. Driesen
Alfred G. Eggers
Edsel W. Frantti
Edward L. Kochka
John A. Kuszyk
Joseph Lempert*
Barry R. Rossing*
Stephen J. Schneider*
Abner B. Turner

* Westinghouse Research & Development Center

WESTINGHOUSE ELECTRIC CORPORATION
Advanced Energy Systems Division
P. O. Box 10864
Pittsburgh, PA 15236

MARCH 1978

PREPARED FOR THE
UNITED STATES DEPARTMENT OF ENERGY

Under Contract No. EX-76-C-01-2248

APPROVED: John W. Sadler

J. W. Sadler, Project Manager
Advanced Energy Systems Division

96

TABLE OF CONETENTS

FIGURES

FIGURES (continued)

FIGURES (continued)

FIGURES (continued)

LIST OF TABLES

TABLES (Continued)

I. ABSTRACT

Efforts during the October to December 1977 quarter were directed towards the evaluation of MHD electrodes for both clean fuel and coal fired environments.

Electrochemical screening tests in an eastern slag have continued and are summarized. The chemistry, mechanisms and kinetics of electrode/slag reactions have been evaluated. Important electrochemical reactions include: slag electrolysis, preferential transfer of aggressive ion species in the slag to the cathodes and anodes, chemical reactions of electrodes with slag and with the products of the electrolysis of the slag, and cavitation/erosion of the anodes.

Materials development and detail design activities in support of the U-02 Proof Test Series is continuing. Fabrication and assembly has been completed for each of the three test assemblies for the Proof Test Series. Proof Test 1 (WESTF Test 38) and Proof Test 2 (WESTF Test 39) were completed in October and November, respectively. Post-test evaluation of these runs is continuing; facility and thermal analyses have been completed. Post-test material characterization is continuing, including efforts at National Bureau of Standards (NBS) and Battelle Pacific Northwest Laboratories (BNW).

II. OBJECTIVE AND SCOPE OF WORK

In continuation of the program to develop MHD power generation to commercial feasibility, Westinghouse is conducting a 36-month program to test and evaluate materials and component designs in both laboratory scale apparatus and in an integrated MHD system facility. While primary emphasis has been given to "hot generator wall" concepts under slagging conditions, the program includes efforts on cold wall designs. The program provides a link between the basic and supportive materials development and testing and the applied testing in a facility that offers an adverse MHD environment for extended periods of time. The program carries forth the engineering development of selected MHD component(s), e.g., electrode and insulating wall systems, through design, materials fabrication, initial screening tests, construction and finally to an MHD system test. The entire sequence is reiterative; i.e., each stage will involve an optimization of both design and materials.

These objectives are being pursued in accordance with a statement of work which is consistent with the National Plan for MHD development formulated by DOE.

The major elements of the program are presented in a Work Breakdown Structure which is presented in Table 1. The Level I effort is the MHD generator Electrode System Development Contract and Level II consists of the following six major tasks:

WBS 1.1 ELECTRODE SYSTEM ENGINEERING
WBS 1.2 TEST ASSEMBLY FABRICATION
WBS 1.3 WESTINGHOUSE ELECTRODE SYSTEM TEST FACILITY (WESTF)
WBS 1.4 WESTINGHOUSE MHD TEST FACILITY (WMTF)
WBS 1.5 COOPERATIVE US/USSR MHD PROGRAM
WBS 1.6 PROJECT MANAGEMENT AND DOCUMENTATION

WBS 1.1 - ELECTRODE SYSTEM ENGINEERING

The objective of this task is to provide centralized engineering for the MHD electrode development effort. This comprehensive effort incorporates all aspects

TABLE 1. WORK BREAKDOWN STRUCTURE

WBS 1.0 - MHD GENERATOR ELECTRODE SYSTEM DEVELOPMENT PROGRAM

- WBS 1.1 - ELECTRODE SYSTEM ENGINEERING
  - WBS 1.1.1 - Design and Analysis
    - WBS 1.1.1.1 - Development Requirements
    - WBS 1.1.1.2 - Electrode and Experiment Design
    - WBS 1.1.1.3 - Experiment Analysis
  - WBS 1.1.2 - Materials Evaluation
    - WBS 1.1.2.1 - Electrode and Insulator Materials
    - WBS 1.1.2.2 - Electrode/Insulator Systems
    - WBS 1.1.2.3 - MHD Materials Data Log
- WBS 1.2 - TEST ASSEMBLY FABRICATION
  - WBS 1.2.1 - WESTF Test Assemblies
    - WBS 1.2.1.1 - Material Procurement
    - WBS 1.2.1.2 - Fabrication and Assembly
  - WBS 1.2.2 - WMTF Test Assemblies
    - WBS 1.2.2.1 - Material Procurement
    - WBS 1.2.2.2 - Fabrication and Assembly
- WBS 1.3 - WESTINGHOUSE ELECTRODE SYSTEMS TEST FACILITY (WESTF)
  - WBS 1.3.1 - Facility Design and Modification
    - WBS 1.3.1.1 - Diagnostic Systems
    - WBS 1.3.1.2 - Support Systems
  - WBS 1.3.2 - Test Operations
    - WBS 1.3.2.1 - Pre-test Activities
    - WBS 1.3.2.2 - Test Operations
  - WBS 1.3.3 - Facility Deactivation
- WBS 1.4 - WESTINGHOUSE MHD TEST FACILITY (WMTF)
  - WBS 1.4.1 - Facility Design
    - WBS 1.4.1.1 - Combustor/Mixer
    - WBS 1.4.1.2 - Discharge Piping and Preheater
    - WBS 1.4.1.3 - High Pressure Air System
    - WBS 1.4.1.4 - Control Room & DAS
    - WBS 1.4.1.5 - Support Systems
  - WBS 1.4.2- Facility Modification
    - WBS 1.4.2.1 - Combustor/Mixer
    - WBS 1.4.2.2 - Discharge Piping and Preheater
    - WBS 1.4.2.3 - High Pressure Air System
    - WBS 1.4.2.4 - Control Room and DAS
    - WBS 1.4.2.5 - Support Systems
  - WBS 1.4.3 - Test Operations
    - WBS 1.4.3.1 - Facility Checkout
    - WBS 1.4.3.2 - Pre-Test Activities
    - WBS 1.4.3.3 - Test Operations
  - WBS 1.4.4 - Facility Deactivation
- WBS 1.5 - COOPERATIVE US/USSR MHD PROGRAM
  - WBS 1.5.1 - US/USSR Liaison
  - WBS 1.5.2 - U-02 Phase III Module
  - WBS 1.5.3 - USSR Testing
- WBS 1.6 - PROJECT MANAGEMENT AND DOCUMENTATION

of engineering development including: materials evaluation, design studies (including detailed analytical efforts), and experiment design and analysis.

Specifically, this task will:

- Identify and evaluate electrode systems engineering requirements and designs.
- Identify development needs to support design activities, specify test conditions and requirements, and integrate the results of engineering tests into the design activities.
- Provide for the coordinated engineering of Test Assemblies.

This task relates to Task 1.5 (Cooperative US/USSR MHD Program) in a manner to assure that the results of the US/USSR program are factored into coal firing electrode system design and development, and to the maximum extent possible will influence that effort to supplement or compliment development on this project.

Electrode system engineering effort is directed towards quantitative determination of specific design and material influence on electrode system performance and durability. There exists a close inter-relationship between thermal, electrical and geometric design considerations and material requirements and capabilities. This task provides the close engineering design and test discipline necessary to effect successful electrode system development.

WBS 1.2 - TEST ASSEMBLY FABRICATION

This task provides for fabrication of Test Assemblies for WESTF and WMTF. The Test Assembly consists of the following:

- Outer Casings (including water cooled plates)
- Electrode/Insulator Systems (including current leadout)
- Insulating Walls
- Instrumentation and Miscellaneous Hardware

Material procurement, processing, fabrication and assembly, when appropriate, are included.

WBS 1.3 - WESTINGHOUSE ELECTRODE SYSTEMS TEST FACILITY (WESTF)

Dynamic testing of electrode and insulator materials and electrode systems will be accomplished in the WESTF. The facility will simulate the "reference" combustion products associated with development of MHD generators and currently provides the capability for testing under simulated MHD stress conditions in an automated mode for extended durations. Operating parameters are summarized in Table 2, which reflect those conditions necessary to support generator development activities. The facility is flexible in that it can be operated under each of the generator operating modes - cold to hot wall, clean or slagging.

This task provides for: facility design, procurement, installation and checkout of facility hardware, and WESTF test operations.

WBS 1.4 - WESTINGHOUSE MHD TEST FACILITY (WMTF)

The Westinghouse MHD Test Facility (WMTF) is located at the Westinghouse Energy Systems Operation Site, Waltz Mill, Pennsylvania. The primary objective of the WMTF is to support through test the engineering development of open cycle MHD generators, including electrode and insulating wall designs and materials, under full MHD operating conditions (see Table 2).

WMTF operations were suspended at the end of CY'76 at which time a number of facility modifications had been initiated to extend facility capability. At the request of DOE this HOLD has been maintained.

WBS 1.5 - COOPERATIVE US/USSR MHD PROGRAM

This task provides technical support to the activities of the cooperative US-USSR program.

Specifically this involves 1) USSR Testing in Westinghouse Facilities, 2) U-25 Module Testing in Westinghouse Facilities and 3) Materials Testing in U-02, Phase I and Phase II. Each of these activities are defined by DOE appointed committees.

TABLE 2

MHD FACILITY CHARACTERISTICS

CHARACTERISTIC	WESTINGHOUSE MHD TEST FACILITY (WMFT)	WESTINGHOUSE ELECTRODE SYSTEMS TEST FACILITY (WESTF)
Mass Flow	3 lb/sec design	0.5 lb/sec
Combustion Temperature	To 2850°K	To 2850°K
Combustor Pressure	2.6 - 3.0 atmospheres normal 6 atm peak	2-3 atmospheres normal 5 atm peak
Channel Velocity	Subsonic or Supersonic (Future)	Subsonic, 500 to 800 m/sec
Seeding	K_2CO_3 or K_2SO_4 dry with ash or char additions	K_2CO_3 or K_2SO_4 wet with ash or char additions
B Field	3 Tesla flat over one meter	None (Future)
Magnet Opening	13.5 x 25.4 x 111.76 cm	N.A.
Fuel	Toluene	Toluene
Oxidant Oxygen	Oxygen enriched preheated air	Oxygen enriched preheated air
Data Collection	240 channels	60 channels
Test Duration	Up to 100 hours or greater	Up to 100 hours
Test Frequency	1 per month	2 per month
Channel Configuration	16 to 48 electrode pairs	12 electrode pairs 1" x 2" flow cross section
Startup Ramp, Minimum	~10°K/min	~25°K/min
Load Bank	Lamps	N.A.

This effort includes general liaison relative to the joint US/USSR committees active in the areas of materials and generators and monitoring USSR testing programs in US facilities, non-Westinghouse. This does not include provisions for any development or hardware effort.

Complete the design, fabrication, assembly, and delivery of a U-02 Phase III test module to the U-02 facility in Moscow. Participate as directed by the DOE Program Manager in test operations and post-test analyses (to be performed by the National Bureau of Standards). Conduct a total of three tests of up to 20 hours on candidate electrode designs as approved by the DOE Project Manager as proof testing prior to final module selection. (Note: The U-02 program agreements are set forth in Meeting Record 08.0208.03, dated February 8, 1977, of the Joint US-USSR MHD Materials Working Group.)

WBS 1.6 - PROJECT MANAGEMENT AND DOCUMENTATION

This centralized management task has been established to provide the focal point for directing the activities which comprise the full project effort. The coordination of the preparation of required contact documentation will also be completed. This documentation includes:

- Periodic Status Report
- Quarterly Technical Progress Reports
- Topical Reports
- Final Report

Preparation of revisions to this Project Management Summary Baseline Report, as may be required by program accomplishments or subsequent contract redirections, will be completed.

III. SUMMARY OF PROGRESS TO DATE

Figure 1 summarizes the overall program schedule and status. During October to December 1977 quarter primary emphasis was directed towards the U-02 Phase III Module, including supporting design and proof testing activities. These activities are all reported under WBS 1.5 - Cooperative US/USSR MHD Program. Complete detailed results of the Proof Test Series will be reported in a Topical Report on the Proof Test Series.

1.0 WBS 1.1 - ELECTRODE SYSTEM ENGINEERING

Laboratory electrochemical corrision tests, completed with a liquid synthetic eastern slag, have shown that slag/electrode reactions can be summzrized as follows:

- For most electrode materials, corrosion is the result of the formation of highly aggressive components in the liquid slag at the electrode/slag interface due to the passage of current.
- Electrode corrosion loss did not obey Faraday's law.
- The kinetics of electrochemical electrode/slag corrosion can be reduced by control of a number of operating characteristics.
- Cathodic materials must be stable under highly reducing conditions and anodic materials should be stable under oxidizing conditions.
- High purity, high density and large grain size are critically significant factors for corrosion resistance of electrode materials.
- Formation of free iron at the cathode can cause interelectrode shorting while segregation of SiO_4^{-4} and AlO_y^{-x} at the anode can result in polarizations and arcing.

Among the ceramic materials tested $MgCr_2O_4$, and to a lesser extent $MoSi_2$, exhibited the best electrochemical corrision resistance in liquid eastern coal slags. Similarly, metallic iron as a cathode and Pt or Pt-Rh alloys as an anode have demonstrated high resistance to electrochemical corrision.

2.0 WBS 1.2 - TEST ASSEMBLY FABTICATION

No significant activity was undertaken this quarter.

3.0 WBS 1.3 - WESTINGHOUSE ELECTRODE SYSTEM TEST FACILITY (WESTF)

During this quarter WESTF operations were dedicated to the U-02 Phase III Proof Test Series. Proof Tests 1 and 2 were completed (WESTF Tests 37 and 38, See Section 5.2.2 of Section IV).

Mini-computer hardware has been received; installation has been deferred pending completion of the U-02 Phase III Proof Test Series.

4.0 WBS 1.4 - WESTINGHOUSE MHD FACILITY (WMTF)

No effort was undertaken this quarter since all activities have been maintained on HOLD.

5.0 WBS 1.5 - COOPERATIVE US/USSR MHD PROGRAM

In support of the design and development of the U-02 Phase III Module, Proof Tests 1 and 2 were conducted in WESTF. These tests, WESTF Tests 37 and 38 were completed on 10/12 and 11/18/77 and provided a basis for the relative evaluation of candidate U-02 Phase III materials and electrode system designs. Proof Test 3, scheduled for early January 1978, will complete the planned test series.

Proof Test 1 incorporated MAFF 31, MAFF 41 and a HfO_2 composite electrode systems. Proof Test 2 included $LaCrO_3$ materials, capped, composite (with ZrO_3) and uncapped. The proof tests were run for a duration of 20+hours each, with surface temperatures in the range of 1650 to 1875°C and with current densities of $1A/cm^2$.

Detailed thermal and structural design activities were completed for Proof Tests 2 and 3 as was fabrication and assembly of the test sections.

6.0 WBS 1.6 - PROJECT MANAGEMENT AND DOCUMENTATION

Required project documentation was issued including the following:

- Work Plan - Proof Test 1, 2 and 3
- Express Report - Proof Test 1 and 2
- Monthly Project Management Summary Report - September, October and November
- Project Management Summary Baseline Report (Revised) dated 10/1/77.

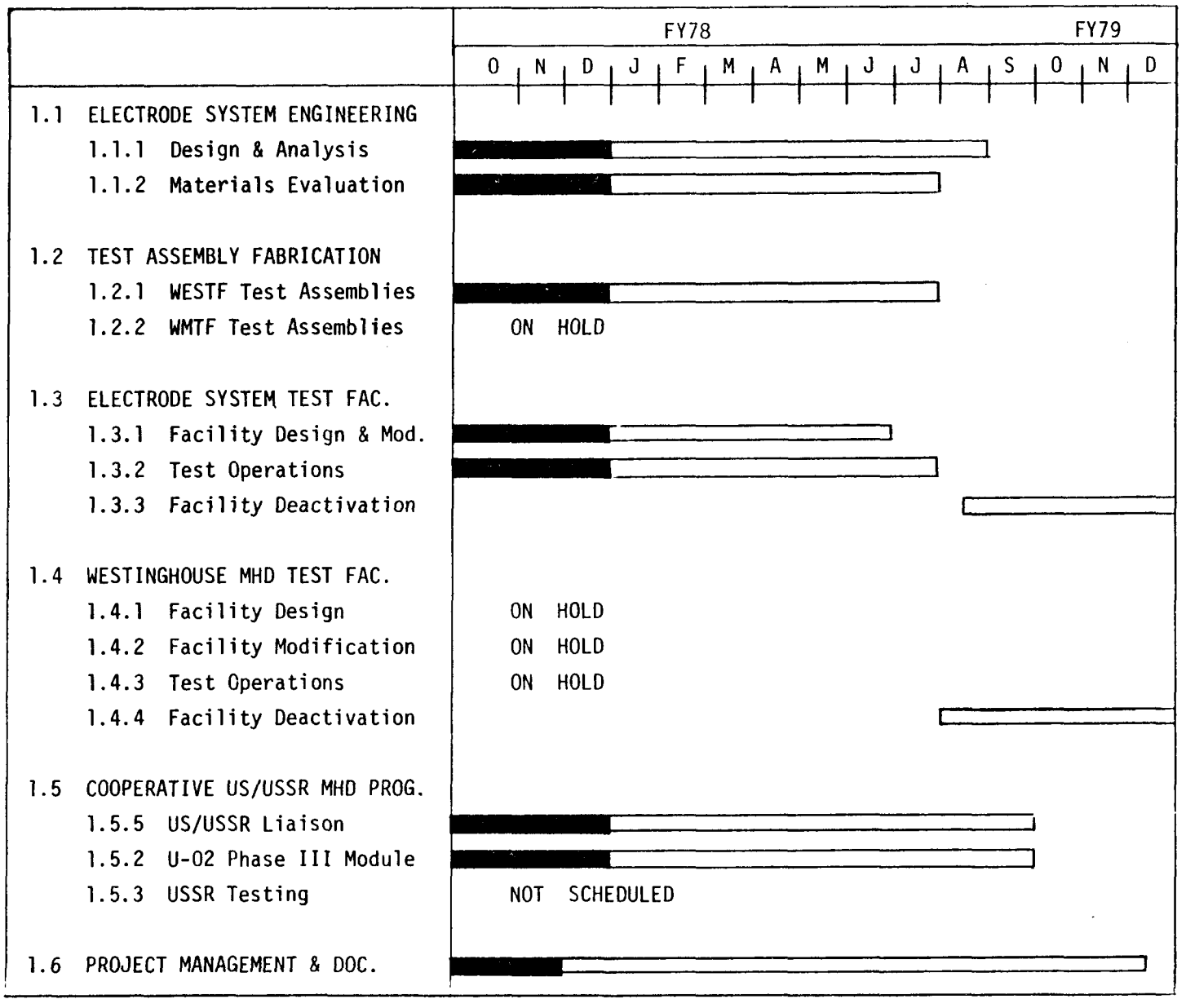

Figure 1. Program Schedule and Status

IV. DETAILED DESCRIPTION OF TECHNICAL PROGRESS

1.0 WBS 1.1 - ELECTRODE SYSTEM ENGINEERING

With the exception of laboratory testing in the area of electrochemical corrosion, primary engineering activities were associated with the U-02 Module, and in particular with the U-02 Proof Test Series, which is presented in Section 5.2.

1.1 WBS 1.1.1 - Design and Analysis

No significant activity was undertaken this quarter (see Section 5.2 for equivalent activity in support of the U-02 Phase III Module).

1.2 WBS 1.1.2 - Materials Evaluation

1.2.1 Electrochemical Corrosion

The presence of significant quantities of slag in the coal fired system requires a comprehensive evaluation of channel materials. In particular the slag layer that coats the channel walls can be both chemically corrosive and, at the same time, disruptive to current transfer (and blockage) processes in the channel. Recent generator (References 1 and 2), and laboratory experiments (Reference 3) indicate that the two major material degradation processes in slag coated channels are erosion by arcs and electrochemical corrosion, with arc erosion predominant on cold walls and electrochemical corrosion becoming more important at higher temperatures. It should be recognized that material degradation is a combination of both arc erosion and electrochemical reactions. These studies have been mainly directed at understanding electrochemical processes.

In general terms, electrochemical reactions can be described through the use of two basic equations; these are:

$$\Delta G = -nFE \qquad (1)$$

where ΔG = free energy of reaction (i.e., decomposition)

n = valency

F = Faraday constant

E = voltage across material

and

$$W = \frac{ItA}{nF} \qquad (2)$$

where W = weight of material involved in the electrochemical reaction

I = current carried by the ionic species

A = atomic weight

t = time

Equation (1) can be thought of as the thermodynamic criteria for electrochemical decomposition. Thus for most ceramic compounds, it can be readily calculated that the voltage needed to cause decomposition is less than two or three volts. Due to nonequilibrium effects such as polarization and because reaction kinetics may be slow, especially in the solid state and at low temperatures, actual decomposition voltages can, in the extreme, be several orders of magnitude greater. Witness for example the very high voltage dielectric materials can withstand before breakdown. However, under conditions inherent to the semi-hot wall operating mode for MHD generators, (where liquid slag can interface with electrodes at temperatures between 900^{o} and $1500^{o}C$ and voltage gradients in the slag layer can be in the tens of volts) it is not at all unexpected that at least one or more oxide components of the slag and, under certain conditions, the electrodes themselves, will undergo decomposition reactions (Reference 3).

Equation (2), known as Faraday's Law, describes the kinetics of electrochemical reactions. The extent of corrosion is dependent only on the number of coulombs passed, (It). Therefore, even at small ionic currents, or for materials and slags which have very low ionic transference numbers, long-term operation will incur significant electrochemical reactions. Whether these reactions will be manifested as corrosion damage is, of course, dependent on the rate at which annealing reactions take place. Thus, for example, the integrity of a ZrO_2 cathode at its interface with a metal lead out is dependent only on the relative rates of electrochemical removal of O^{-2} from this interface compared to the rate of O^{-2} replenishment from the surrounding environment (Reference 4). The higher the current, the greater the chances for decomposition.

In this report, we will combine our earlier and our most recent laboratory-scale studies directed at exploring the relevance of Equations (1) and (2) to the electrochemical corrosion of a variety of MHD electrode materials under semi-hot wall slagging conditions. Mechanisms of corrosion in a simulated eastern USA coal slag will be presented and the implications of these results to electrode survivability in real MHD channels is discussed.

Corrosion Experiments

The descriptive information on the electrode materials tested are given in Table 3. Corrosion testing was performed in a synthetic slag, E-03, designed to simulate an eastern coal ash composition. The slag composition in weight percent is: 48 SiO_2, 20 Al_2O_3, 21 Fe_2O_3, 8 CaO, 1 MgO, .8 TiO_2, 1.1 Na_2O and 1.5 K_2O. The method of slag preparation has been described earlier (Reference 3).

In Figure 2, cross-sectional views of three types of electrochemical test cells used are shown. Common to all designs is a high (90% of theoretical) density MgO crucible containing two opposing cylindrical electrodes separated by a pool of slag. Platinum lead wires are mechanically attached to the platinized electrodes to carry the current. The cell geometries are such that corrosion will occur predominately on opposing faces of the electrodes when direct current is applied, enabling accurate measurement of the extent of corrosion to be made. Little ambiguity exists as to the current path nor is there a tendency for current bunching common to other electrochemical test cells where single and/or pairs of rod samples are inserted into a slag bath (References 3 and 5).

Cell 1 (D1) in Figure 2 is a rectangular-shaped crucible having an upper reservoir section to contain excess liquid slag and a rectangular cross-sectioned lower slotted region which fixes the interelectrode gap and contains the slag between opposing electrodes. The gap dimensions can be varied to alter the voltage drop across the cell. This design offers the advantage of being a completely self-contained test system requiring no auxiliary slag bath.

TABLE 3

CHARACTERISTICS OF ELECTRODE MATERIALS

Material	Manufacturer	Density, % Theoretical	Porosity,* % Open	Purity	Comments
$La_{.95}Mg_{.05}CrO_3$	Westinghouse	92.8	1.5	99.4+	Major impurities Al, Si, Fe. Some La silicates and $MgCr_2O_4$ at grain boundaries.
$3MgAl_2O_4:1Fe_3O_4$	BNW	92.6	0.15	99.5	Major impurities Si, Cr, Ni
$MgCr_2O_4$ (60 m/o MgO:40 m/o Cr_2O_3)	Westinghouse	92	0.11	99+	MgO saturated with Cr_2O_3 at grain boundaries. Al, Si impurities in matrix.
$MoSi_2$	Kanthal Corp.	--	0.16	--	Matrix is ≈18 v/o Mo_5Si_3, 72 v/o $MoSi_2$, 10 v/o SiO_2.
80 Pt:20 Rh	Engelhard	100	0	99.5	
Mild Steel AISI C1020	--	100	0	--	

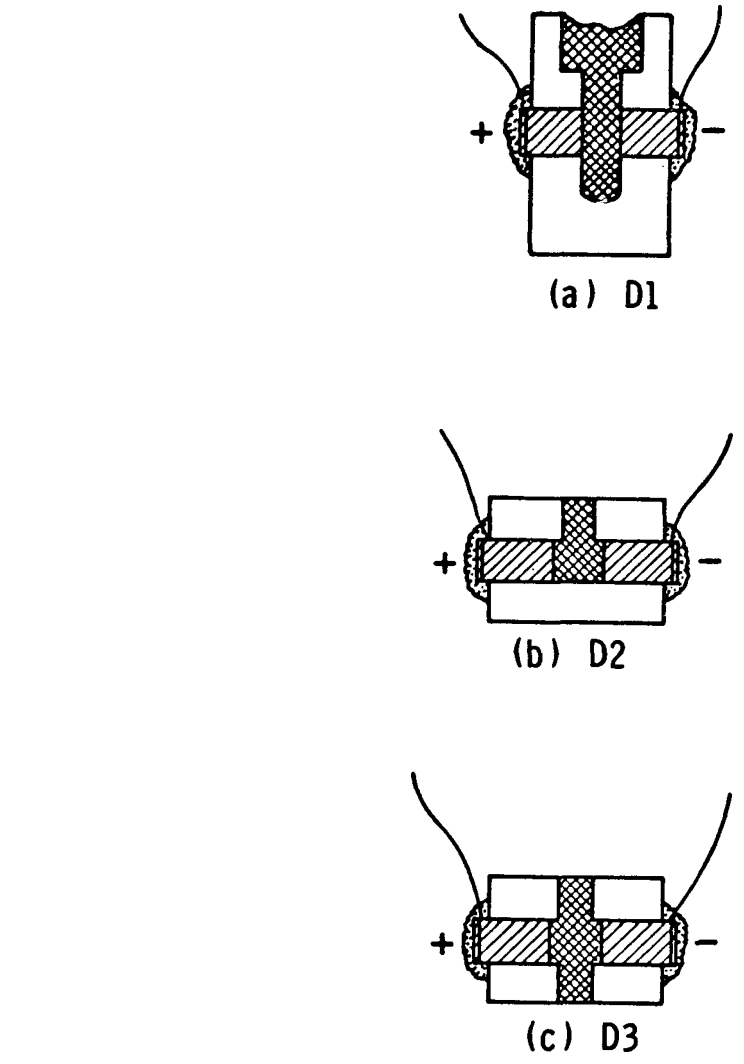

Figure 2. Schematic Cross-Sections of Three Electrochemical Test Cell Designs

Cell 2 (D2) is basically an MgO tube with cemented electrode end plugs separated by a rod of slag. A small hole or slot is machined at the top of the tube in the center to allow gases formed by the electrolysis reactions to escape and interelectrode liquid slag to be replenished. In operation, the entire cell is placed in a platinum harness and submerged into a large isothermal liquid slag bath.

Cell 3 (D3) is a variation on D2 and is run in the same manner. The only difference is that there is an additional hole or slot on the bottom, directly below the top hole. As gas bubbles out the top hole, new slag enters from the bath through the bottom hole, thereby maintaining a constant flow of liquid slag in the interelectrode region. This cell provides dynamic slag flow conditions compared to the relatively static conditions characteristic of D1 and D2.

In general, test procedures simply involve the thermal equilibration of the test cells in either the slag baths (D2, D3), or furnace (D1), a process that takes ≈15-30 minutes, followed by the passage of a constant direct current for a predetermined period of time. Voltage variations are continuously monitored. For low-temperature tests, the cells are first thermally annealed for several minutes at 1300°C. This insures that the slag wets the electrodes to provide good electrical contact. At the conclusion of a test, the cell is removed from the hot furnace or slag bath and allowed to air cool. The cell is then sectioned along a vertical or horizontal plane containing the electrodes, metallographically mounted and polished and the extent of corrosion and corrosion mechanisms investigated using procedures described earlier (Reference 3). The quantity of metallic iron deposited during some tests was determined by standard metallographic point counting techniques.

Results

The test conditions and results of a recent series of electrochemical corrosion experiments on various potential electrode materials in E-03 slag are summarized in Table 4. Analysis of these tests indicate that electrochemical corrosion is, in the main, a result of two separate but interrelated reactions--reactions that occur within the slag itself due to the passage of current and reactions between

TABLE 4

SUMMARY OF ELECTROCHEMICAL TESTS IN E-03 SLAG

Electrode Material	$3MgAl_2O_4 \cdot 1Fe_3O_4$						$MgCr_2O_4$		$LaCrO_3$	$MoSi_2$	80Pt-20Rh	Fe(-)/Pt-Rh(+)
Test ID	105,* 106	123	116	107÷	1S2	1S3	109	117	112,* 108	110	121	119
Temperature, °C	1390	1390	1390	1400	1100	1000	1390	1395	1390	1400	1395	1390
Duration, min	26	43	30	90	39	60	31	31	32	61	16	57
Electrode Separation, cm	0.45	0.64	0.64	0.64	0.32	0.32	0.64	0.64	0.32	0.64	1.2	1.3
Current Density, amp/cm^2	1.2	2.4	3.0	0.15-0.2	0.7	1.1	1.2	3.1	1.1	1.2	3.1	3.0
Voltage Drop Across Slag, Calculated												
Start	9	29	31	1.7			9	43	16	38	32	34
End	2.7	16	26	1.7			14	19	6	26	38	6
Corrosion, ΔW, µg/coulomb												
Cathode, ΔW_c	64	34‡	34‡	46	34	3.8	22	9.5‡	291	27	+5§	24
Anode, ΔW_a	10	104	194	17	7	1.9	0.95	29	127	8	0	34
$\Delta W_c/\Delta W_a$	6.4	.33	.18	2.7	4.9	2	23.2	.33	2.3	3.4	-	71
Metallic Fe in Slag, M_{exp}, gms	.033						.032		.029	.068		
Faradaic Yield	.21						.18		.16	.19		
Test Cell	D1	D2	D2	D1	D1	D1	D1	D2	D1	D1	D3	D2

*Identical test conditions. Results were within 10% of each other.

÷Test run at lowest constant voltage where no voltage fluctuations occurred. Current allowed to change. No metallic Fe found in slag.

‡Extensive cathodic grain boundary penetration by slag.

§Sample grew due to deposition of metallic iron.

the "reacted" slag and the electrode materials themselves. Each reaction is discussed in turn.

Slag Reactions

The predominant reaction occurring in the slag at voltages greater than 1.7 volts involves electrolysis. This is evidenced by the formation of metallic α-iron at the cathode as shown in Figure 3 and oxygen gas at the anode. Bubble evolution can be readily viewed during a run and is responsible for the large and frequent fluctuations in voltage during the course of a constant current test. Fluctuations usually amount to $\approx \pm$ 6-10% of the interelectrode voltage drop with a frequency of about 15-30 seconds at 1 amp/cm^2. The frequency of voltage fluctuations as well as the rate of bubble formation increases rapidly with increasing current density. The accumulation of metallic iron can be quite extensive as shown in Figure 4 for run 119. In this case, Fe has almost completely bridged the cell and is mainly responsible for the large continuous decline of interelectrode voltage from the start of the test to the end (see Figure 5, curve D2). Most test data from runs using electrochemical cells D1 and D2 exhibit the type of voltage-time dependence shown in curve D2, Figure 5. This behavior results from the build up of reaction products in the interelectrode gap. Alternately, if the reaction products are continuously swept away, as occurs in cell type D3, the voltage increases with time (see Figure 5, curve D3). The explanation for this behavior rests with the accumulation of electrically resistive ions at the slag/anode interface.

SEM-EDAX scans across the interelectrode slag indicates that with one exception, all test cells in Table 4 exhibited an enrichment in aluminum and silicon near the anode and iron, calcium and potassium (Fe^{+2}, Ca^{+2}, K^{+1}) at the cathode. These regions of segregation are usually limited to a zone within 0.5 mm of the electrodes; the slag is generally homogeneous outside of these areas.

The one possible exception to the phenomena of electrochemical ion migration in the slag occurred in the 1000^{o}C test 1S3. No evidence for voltage fluctuations, or metallic iron formation, or segregation, except for a very small increase in Fe^{+2} at the cathode, could be found.

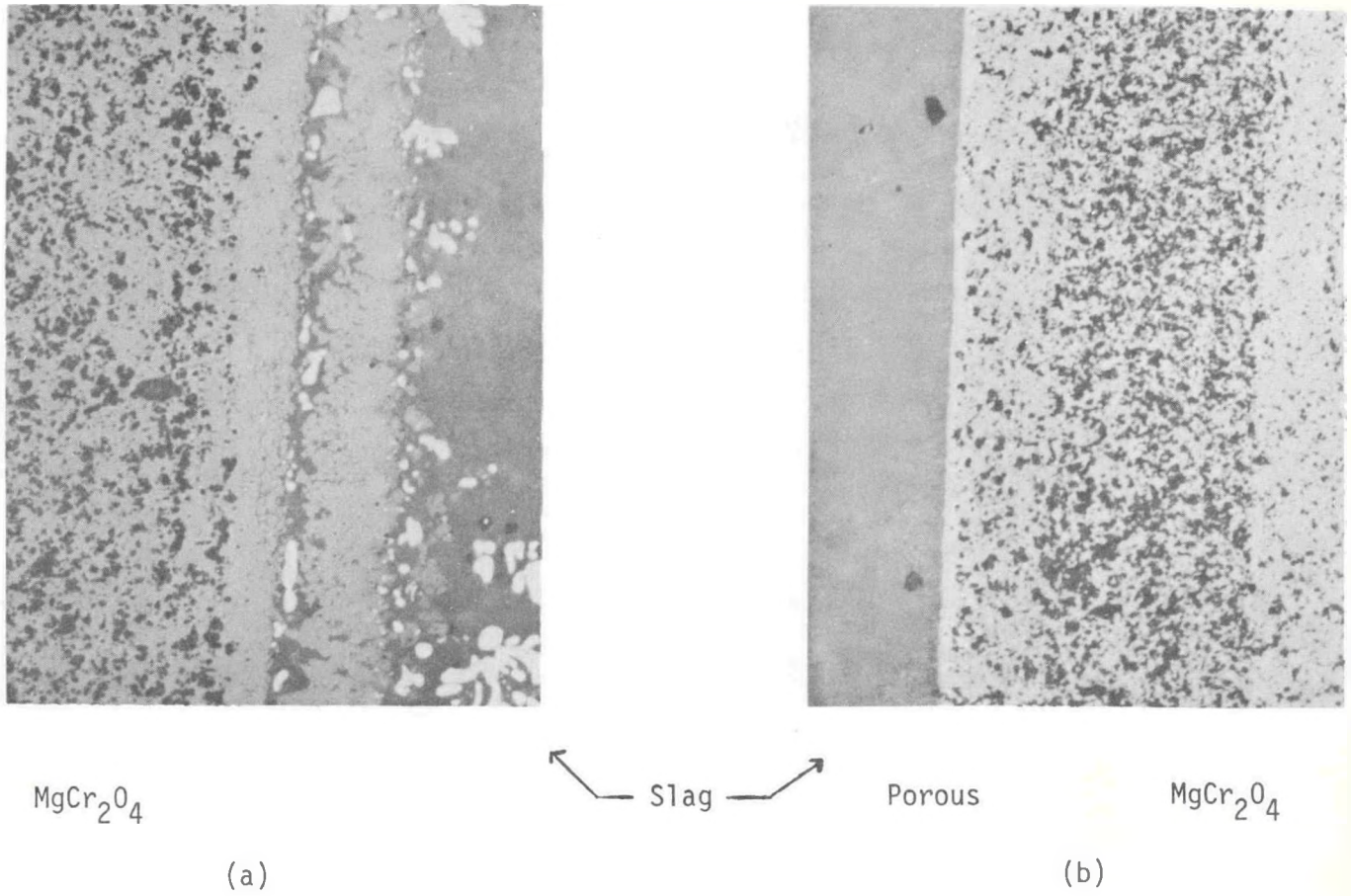

Figure 3. Photomicrographs of Slag/Electrode Interfaces for $MgCr_2O_4$, Test 109.
(a) Cathode/Slag Interface. White Particles are α-Fe. Note Splitting of Reaction Scale.
(b) Slag/Anode Interface Showing Silicate Surface Scale and Porous Reaction Zone (200X).

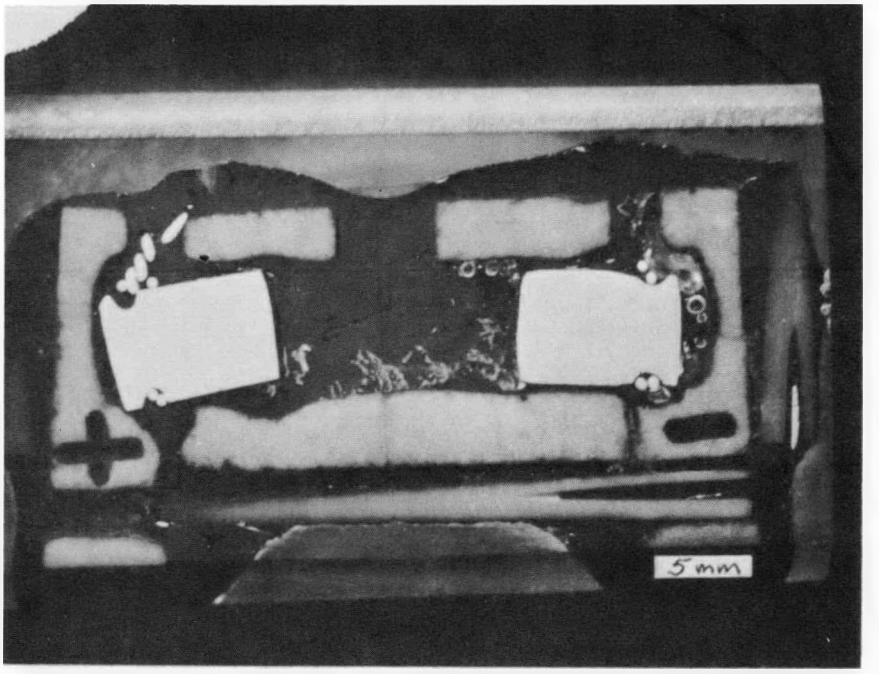

Figure 4. Cross-Section of Test Cell (Test 119) with Mild Steel Cathode and 80 Pt-20Rh Anode. Note Large Quantities of Metallic Iron at Bottom of Interelectrode Slag.

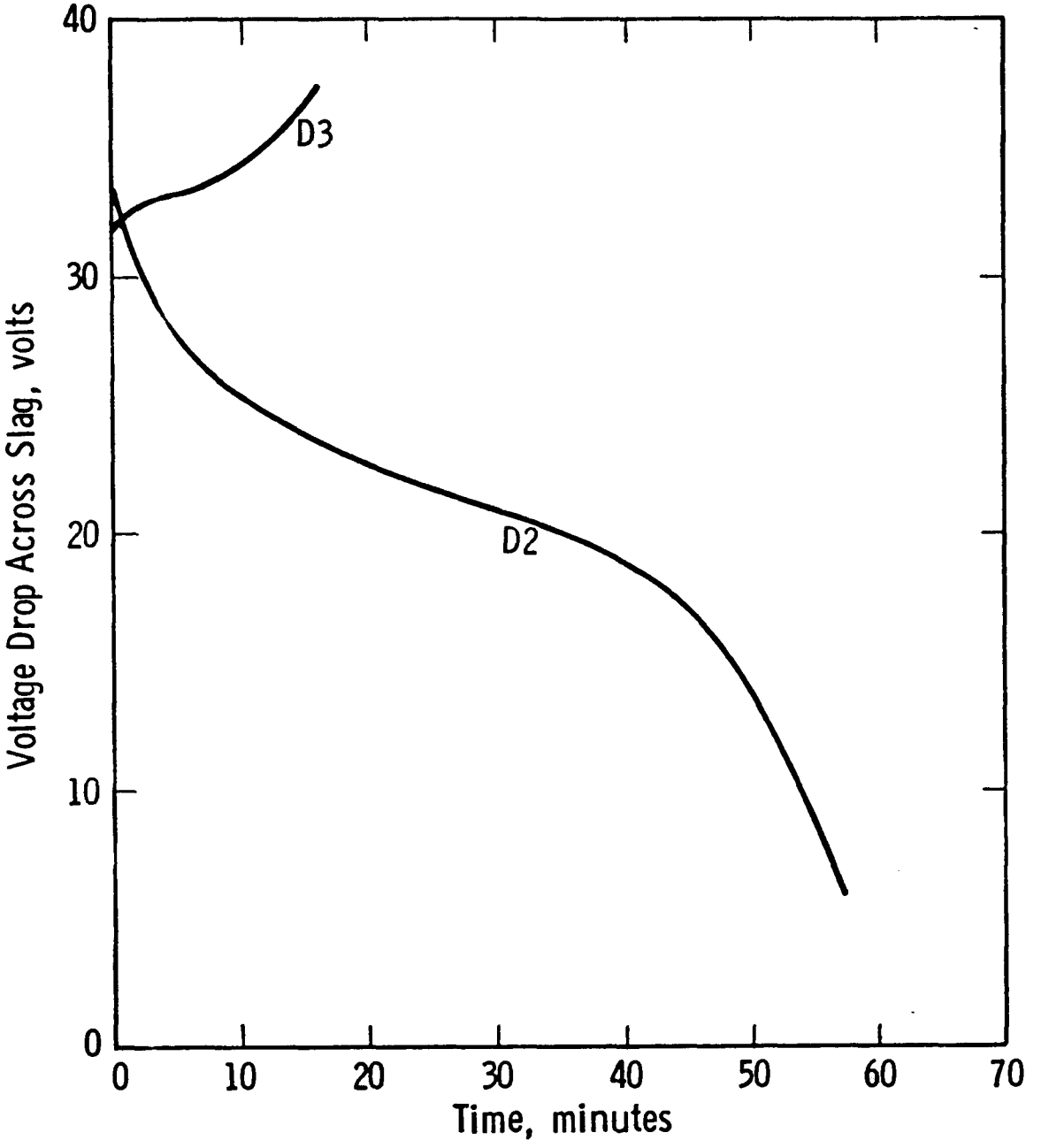

Figure 5. Typical Changes in Voltage Across Slag During Electrochemical Tests Using Cell Designs D2 (Test 119) and D3 (Test 121). Voltage Fluctuations are not shown.

Test 107 was designed to determine the minimum interelectrode voltage drop necessary to prevent electrolysis of the slag at 1400°C. The voltage was lowered to a point just below which no voltage fluctuations were observed and the test was then run at this constant voltage, 1.7 volts. Post-test examinations revealed that free Fe did not form, although there was significant ion transfer as well as reduction (decomposition) of the $3MgAl_2O_4 \cdot 1Fe_3O_4$ electrode.

The amount of metallic iron experimentally determined to be present after the electrochemical tests, M_{exp}, divided by the amount of iron, M_f, theoretically predicted by Faraday's equation for the reaction $Fe^{+2} + 2e = Fe^0$ in the test cell, is called the Faradaic yield (M_{exp}/M_f) and is a measure of the ionic nature of the slag. These values are given in Table 4 for several tests and it can be seen that the value of Faradaic yield is relatively constant. If Fe^{+2} was the only cation transferred in the slag and if it was possible to measure all the metallic iron that formed electrolytically, then the Faradaic yield would be equal to the ionic transference number of the slag, i.e., $t_i = .18$. In reality it is expected that this value may be a factor of at least 2 or 3 times too low, since much of the metallic iron that is formed reoxidizes in the slag and/or reacts with the electrode and containment materials.

Electrode Reactions

$3MgAl_2O_4 \cdot 1Fe_3O_4$

For most tests at temperatures above 1100°C, the cathode is characterized by a highly recrystallized multi-phase structure at the slag interface which consists mainly of slightly Fe depleted $3MgAl_2O_4 \cdot 1Fe_3O_4$, FeO particles and sometimes includes particles of a (Fe, Ca, Mg) silicate phase and metallic Fe globules, especially at the higher current densities. Figure 6 illustrates the nature of this microstructure. With time or increasing current density, the surface structure becomes more and more infiltrated with slag, due perhaps to the preferential dissolution of the FeO phase and the fluxing of large grains off the surface. In nearly all cases, metallic Fe globules or dendrites are found at the slag/electrode interface. A small distance into the electrode from the

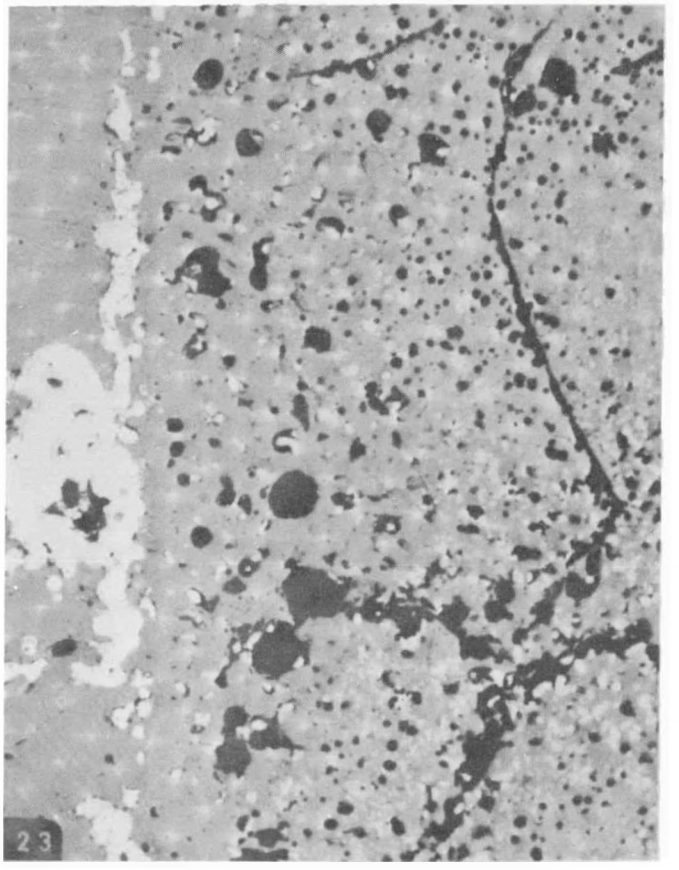

$3MgAl_2O_4 \cdot 1Fe_3O_4$ [Slag]

Figure 6. Photomicrograph showing typical cathodic corrosion of $3MgAl_2O_4 \cdot 1Fe_3O_4$ (Test 116). White particles in slag at interface are α-Fe, lighter colored particles in matrix are FeO.

slag interface is a region of partially dissociated $3MgAl_2O_4 \cdot 1Fe_3O_4$ which contains FeO particles at most grain boundaries and pores. The shape of the FeO phase, as shown in Figure 6, suggests that a liquid phase was present during its formation. No FeO is found at locations other than grain boundaries or pores. SEM-EDAX analysis shows that the $3MgAl_2O_4 \cdot 1Fe_3O_4$ is depleted in iron around the FeO particles, indicating that the iron has come from the matrix, i.e., $3MgAl_2O_4 \cdot 1Fe \rightarrow FeO + 3MgAl_2O_4 \cdot 1Fe_2O_3$. Still further into the cathode from the slag interface, a region of iron-depleted but calcium-enriched slag penetrates pores and grain boundaries of the matrix. The depth and extent of the various corrosion (reaction) regions increases with the number of coulombs passed. All indications are that cathodic corrosion is first triggered by the penetration into the matrix, via grain boundaries and pores of a highly fluid slag which is formed by the preferential transport of Fe^{+2}, Ca^{+2} and K^{+1} ions towards the cathode. The role of metallic iron in corrosion at the cathode appears to be quite passive--the metallic iron being much denser than the surrounding slag generally falls away from the interface after it is formed.

The reaction scheme at the anode differs considerably from that at the cathode. The more viscous SiO_2 and Al_2O_3 rich slag apparently does not wet nor penetrate to a significant degree into the matrix. Surface chemical reactions dominate and a nonadherent readily fluxed iron-rich spinel layer (probably hercynite, $FeAl_2O_4$) is found at the surface at low current densities. At current densities much greater than 1 amp/cm^2, the anode is rapidly machined or cavitated away by the action of oxygen bubbles. Catastrophic anodic attack is illustrated in Figure 7 for a test cell run at 3 amp/cm^2 for 30 minutes.

The severity of cavitation/corrosion of $3MgAl_2O_4 \cdot 1Fe_3O_4$ increases with current density. See for example Figure 8. Cathodic corrosion is also included in Figure 8 for comparison purposes. Corrosion at both electrodes, (W/It), does not obey equation (2), indicating non-Faradaic processes are dominating the corrosion reactions.

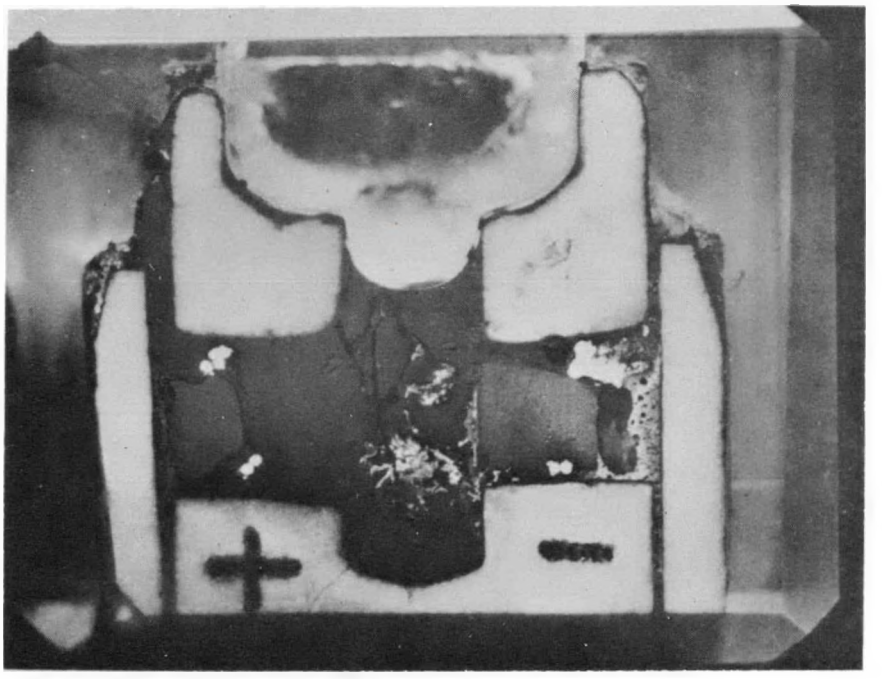

Figure 7. Cross-section of test cell (Test #116) illustrating catastrophic anodic erosion at high current density (3 Amp/cm^2).

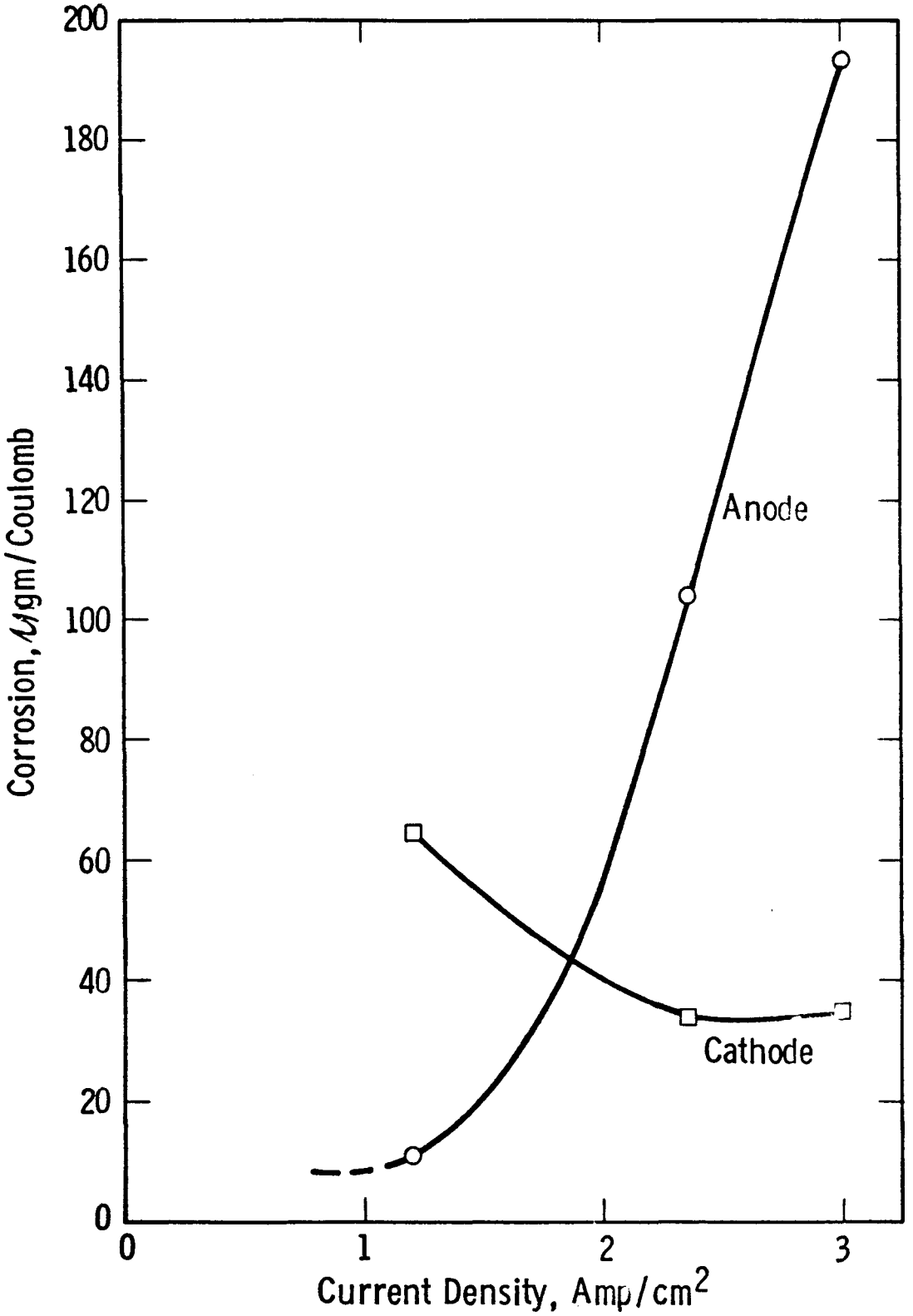

Figure 8. Dependence of anodic and cathodic corrosion losses in $3MgAl_2O_4 \cdot 1Fe_3O_4$ on current density

$MgCr_2O_4$–

The mode of cathodic corrosion is illustrated in Figure 3(a). The major features are free Fe formation at the cathode due to electrolysis of the slag, grain boundary penetration by the fluid slag and chemical transfer of Al and Fe from the slag into the reaction layer coupled with the removal of Cr from the scale into the slag.

An interesting feature shown in Figure 3(a) is the distribution of free Fe particles associated with the partially spalled off reaction scale. In all probability, Fe particles deposited first on the outer surface of the electrode but as the reaction scale grew and eventually split and spalled off, electrical conductivity was lost. This forced the slag electrolysis reaction (Fe^{+2} + $2e \rightarrow Fe$) to occur at the inner reaction scale which was still intimately bonded to the electrode. Reactions such as these, 1) illustrate the potentially complex nature of corrosion in an electric field, 2) demonstrate why Faradaic weight loss calculations are often inapplicable in predicting electrochemical corrosion of electrode materials, and 3) point to the importance of running "static" electrochemical tests as a means of monitoring the mechanism of the corrosion process.

The major phase in the cathode reaction layer appears to be a complex spinel, Mg (Al, Fe, $Cr)_2O_4$ where both Al and Fe have replaced some of the Cr. At all locations adjacent to the reaction scale, the slag is enriched in Cr but depleted in Al and Fe.

At the anode (Figure 3b), the solutioning of chromium into the slag is much less extensive than at the cathode. Other than the existence of a very thin ($\approx 5\ \mu m$) rim of a silicate (Mg, Ca, Al) at the anode/slag interface, there are no major compositional gradients across the "porous" reaction zone. The porous nature of the "reaction zone" is probably due to the transformation of the MgO at the grain boundaries to a spinel material due to the interactions with the slag. The resulting microstructure is similar to that found earlier in a slag immersion tested $MgAl_2O_4$ spinel material (S2), (Reference 6), that contained $\approx$2.8 v/o MgO as the grain boundary phase.

At high current densities (117) the reactions at the cathode are similar to those above but are more extensive. Especially noteworthy is the very large increase in penetration by slag into the grain boundaries of the matrix. The anode exhibits considerable erosion due to oxygen bubble cavitation.

$\underline{MoSi_2}$

At the cathode the slag is enriched in Fe, K and Ca and metallic Fe is discharged at the interface. A thin reaction zone $\approx$70 μm thick at the slag interface has formed and is predominately Mo_5Si_3, formed by the preferential dissolution of Si from the matrix into the slag. Some Fe, and to a lesser extent Al, has diffused into this zone, although the quantities are small. There is no evidence for Mo dissolving into the slag. The original SiO_2 matrix particles in this sample are readily attacked at the slag interface and are converted into a potassium-alumina-silicate phase. The reactions at the anode are essentially the same as at the cathode. However, since the quantities of K, Ca and Fe are reduced, the slag viscosity is higher, and there is less extensive attack of the second phase SiO_2 particles in the matrix.

$\underline{LaCrO_3}$

The lanthanum chromite cathode (112, 108) was penetrated by and chemically reacted with the eastern slag. Metallic iron is discharged at the cathode. Semi-adherent reaction zones (layers) form on the surface and consist of a complex mixture of FeCr spinel crystals, partially reacted and fluxed $LaCrO_3$ grains, (La,Cr) silicates and glassy slag. Compositional gradients exist across the thickness of the reaction zone becoming less iron and calcium-rich in the vicinity of the "unreacted" matrix. The reaction layer is not protective, allowing slag to penetrate deep into the matrix. Often, FeCr spinel is found at internal grain boundaries along with slag that is enriched in La.

Anode reactions (and corrosion product morphology) are similar to but not as severe as at the cathode. Similar to the cathode, the non-protective reaction scale appears to be held in place at temperature due to the high viscosity of La-rich slags.

Pt

80 Pt - 20 Rh anodes are quite resistant to eastern slag attack even under electrical stresses greater than 3 amp/cm^2 (119, 121). There is a very slight roughening of the surface (see Figure 9) due to localized alloying of the Pt with iron from the slag and the subsequent machining of this surface by the action of gas bubbles. Slag at the anode interface shows some enrichment of alumina and silica components.

The 80 Pt - 20 Rh cathode (121) is extensively attacked due to deposition of and reaction with α Fe dendrites (produced by slag electrolysis) onto the surface at the slag interface. There is also significant iron diffusion into the Pt, entrapment of slag components near the interface and grain boundary penetration of slag into the outer 100 μzone (Figure 9). The slag is enriched in Fe, Ca and K components at the slag/cathode interface.

The erosive effect of O_2 bubbles is readily apparent in test 119 as shown in Figure 4. The Pt anode is reasonably resistant to cavitation attack but the crucible material (which is 90% theoretically dense MgO) is not. At areas A and B significant amounts of MgO have been eroded away, loosening the anode and causing it to be displaced from its original location. Reactions of this nature would not be unexpected in a real slagging channel test at the upstream interface of the anode and the interelectrode insulator, due to current bunching.

Fe (Mild Steel)

The mild steel cathode (119) exhibits low-level reactions with the Ca and K enriched slag. There is evidence for localized surface melting but little or no deposition of electrolized -Fe onto the surface.

Mild steel is a good candidate material for the cathode wall in a slagging MHD channel. Care must be taken, however , that it be completely covered with protective slag to prevent catastrophic oxidation reactions.

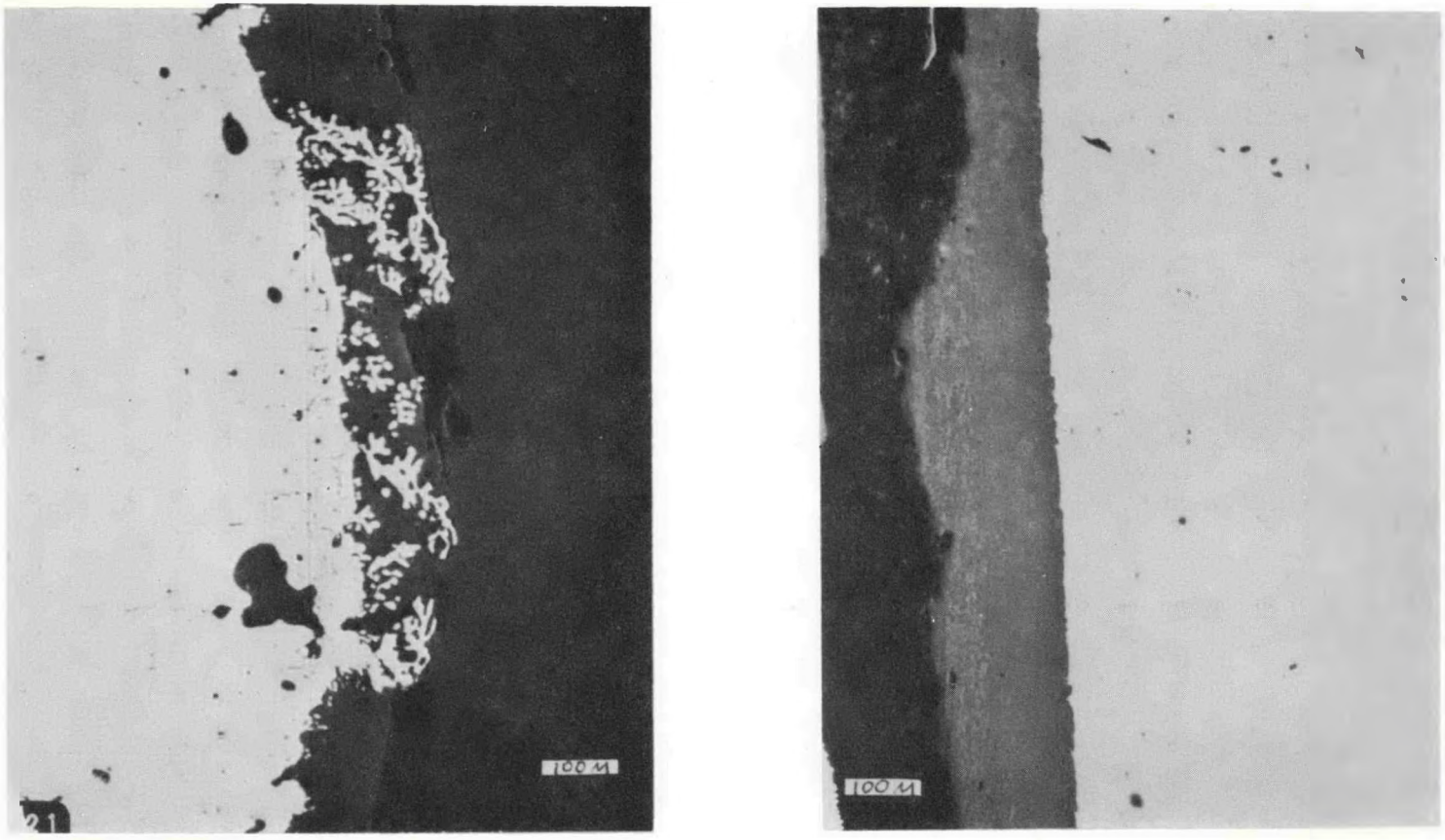

Pt (a) ↖—— Slag ——↗ (b) Pt

Figure 9. Photomicrographs of Corrosion of 80 Pt-20Rh Electrodes.
(a) Slag/Cathode Interface (Test 121) Showing Deposition of Iron Dendrites onto Cathode.
(b) Slag/Anode Interface (Test 119). (100X)

Discussion

Liquid eastern coal slag at temperatures above 1100°C seem to have a considerable ionic component of electrical conductivity. The ionic nature of the slag is manifested by the preferential transport of such mobile cations as Ca^{+2}, K^{+1}, and Fe^{+2} to the cathode and the anions O^{-2}, SiO_4^{-4}, and AlO_y^{-x} to the anode. At interelectrode voltages greater than 1.7 volts (only 0.9 volts greater than theoretically predicted for the decomposition of Fe) in slags, metallic iron and O_2 gas are discharged at the cathode and anode, respectively. Measurements of the amounts of metallic Fe produced during electrolysis indicate that the ionic transference number in E-03 slag is about 0.18 but is undoubtedly at least two or three times greater than that. Earlier electrochemical corrosion studies of SnO_2 in a low silica eastern slag, (E-01) suggest that it is approximately 60% ionic. This value is consistent with ionic transference numbers reported for various SiO_2-CaO-FeO melts in the literature, Reference 7. These studies indicate the extremely sensitive relationship existing between silica content and slag ionicity. Thus, because of preferential SiO_4^{-4} migration, one can predict that anodic polarization should be much higher than cathodic polarization (neglecting complications due to the slag-electrode interactions). Very recent experiments tend to confirm this.

At low temperatures ($\approx$1000°C) conduction in the eastern E-03 slag appears to be predominately electronic. There is very little segregation of iron at the cathode and even at 1 amp/cm^2 no evidence of voltage fluctuations characteristic of O_2 and metallic iron production exists. In addition $3MgAl_2O_4 \cdot 1Fe_3O_4$ does not undergo cathodic decomposition--a reaction characteristic of electrochemical corrosion of this material in ionic slags. Although it is possible that the high viscosity of this slag at $\approx$ 1000°C inhibits the kinetics of redox reactions, the negligible amount of segregation compared to what occurs at 1100°C supports the concept of electronic conductivity. Further support for this hypothesis is that when experimentally measured values of electrical conductivity for similar eastern-type slags are plotted according to an Arrhenius-type equation, there is in general a marked change in slope and, by implication, conduction mechanism in the approximate temperature range $\approx$1000-1200°C, References 8 and 9.

At low temperatures the activation energy for conductivity is low (0.2 - 0.9 ev), suggesting an electronic (p, n) conduction mechanism. At the higher temperatures, a large activation energy (1.5-2.5 ev) more characteristic of an ion diffusion jump process dominates. Additional evidence is that at the lower temperatures electrical conductivities are very sensitive to changes in oxygen partial pressure, whereas the conductivities at the high temperatures are independent of Po_2. Dependence of conductivity on oxygen potential is associated with changes in concentration of p or n carriers in electronic conductors while independence indicates that an ionic conduction mechanism dominates.

Figure 10 is a plot of corrosion vs temperature for $3MgAl_2O_4 \cdot 1Fe_3O_4$ at $\approx$1 amp/cm^2. It illustrates the large increase in corrosion loss between 1000 and 1100^{o}C, indicative of a change in corrosion mechanism (i.e., electronic to ionic transition). The increase in corrosion is much less at higher temperatures (>1100^{o}C) where the conduction mechanism in the slag is ionic.

The concept of a change in the current transfer mechanism in slags has interesting implications. Since electrochemical reaction products are discharged at electronically conducting materials where it interfaces with ionically conducting materials, it is possible that in a real channel where temperature gradients across the slag are steep, Fe and O_2 may form within the slag at the isotherm corresponding to the electronic/ionic transition, rather than at the electrodes themselves. The transition temperatures for a wide variety of slags can be inferred from Arrhenius conductivity curves where the change in slope, (dlnK/d[1/T]) occurs, References 8 and 9.

The major types of electrochemically induced reactions found in this work are summarized in Table 5. Under the first heading of Slag Reactions, the predominant reactions are slag electrolysis at voltages >1.7 volts (equations (3) and (4)) which give rise to extremely reducing conditions at the cathode (Po_2 <10^{-10} atm) and highly oxidizing conditions at the anode (Po_2 > 1 atm). Accompanying the electrolysis reactions are the transfer to and segregation of mobile cations at the cathode and glass netwoek forming anions at the anode, equation (5). As a

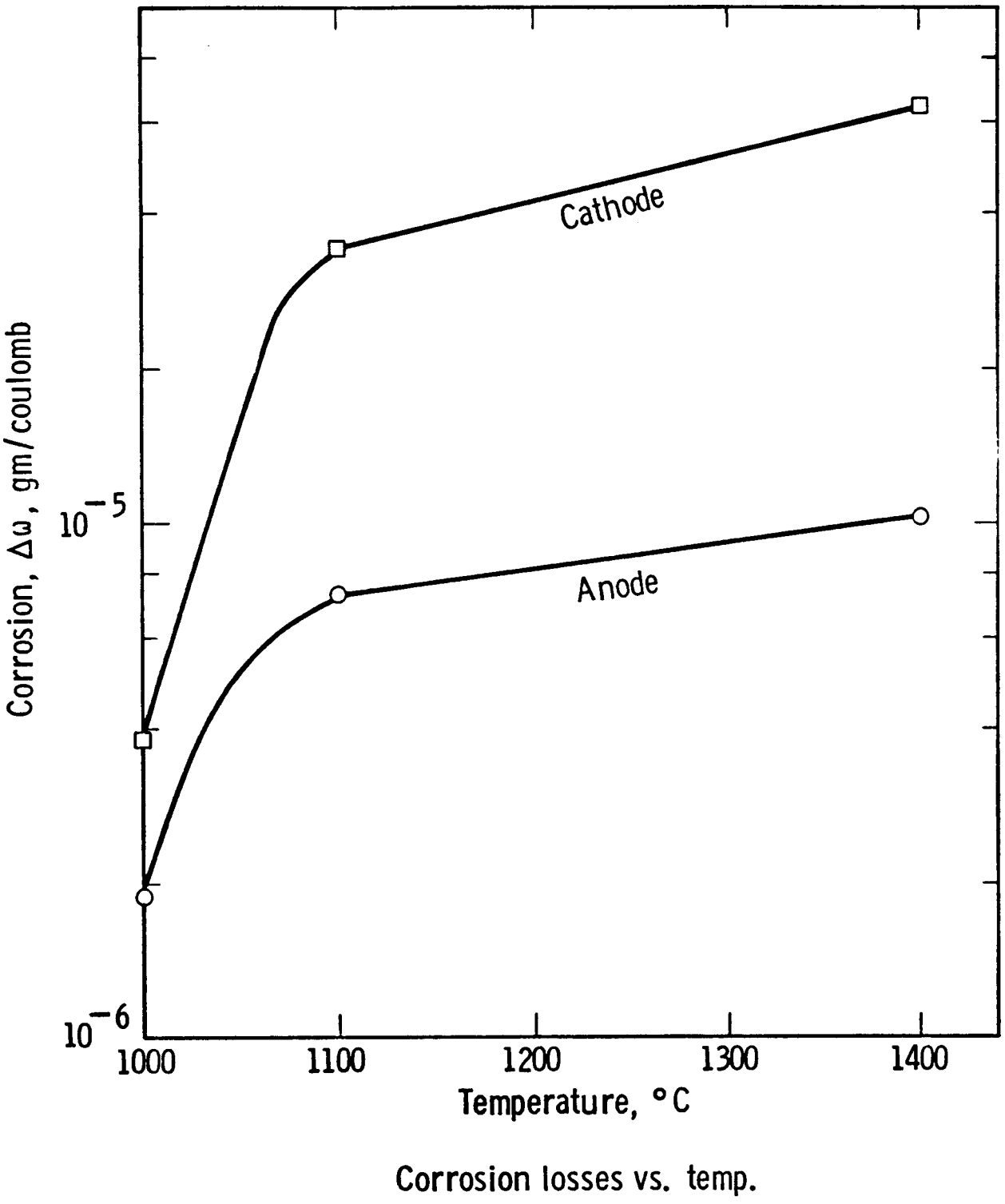

Figure 10. Anodic and Cathodic Corrosion as a Function of Temperature for $3MgAl_2O_4{\cdot}1Fe_3O_4$ Tested at $\approx$ 1 amp/cm^2

TABLE 5

SUMMARY OF SLAG-ELECTRODE REACTIONS

Slag Reactions

(-) $Fe^{+2} + 2e \rightarrow Fe$ (3)

(+) $O^{-2} \rightarrow 1/2\ O_2 + 2e$, or (4a)

(+) $SiO_4^{-4} \rightarrow SiO_2 + O_2 + 4e$ (4b)

(-) Segregation of Ca, Fe, K (5a)

(+) Segregation of Si, Al (5b)

Chemical Reactions

(-) $SiO_2 + 1/2\ Fe + LaCrO_3 \rightarrow 1/2\ FeCr_2O_4$ + La silicates (6)

(-) $Fe + Pt \rightarrow Fe(Pt)$ alloys (7)

(-) $3MgAl_2O_4 \cdot 1Fe_3O_4 \xrightarrow{slag} 3MgAl_2O_4 \cdot 1Fe_2O_3 + FeO$ (8)

(+) $SiO_2(Al_2O_3)$ slag + $MgCr_2O_4 \rightarrow$ Mg Al silicates + $Mg(Fe,Al)Cr_2O_4$ (9)

(+) $O_2 + Me \rightarrow MeO_2$ (10)

Erosion - Cavitation

(+) $O^{-2} \rightarrow 1/2\ O_2 + 2e$ (11)

(-) Fluxing due to enrichment of low viscosity components (12)

Electrolytic Dissolution

(-) $Sn^{+4} + 2e \rightarrow Sn^{+2}$ (13)

consequence of the above slag reactions, chemical interactions can occur between the segregated slag components and the electrode materials themselves. Thus, as shown in equations (6) and (7), metallic iron can react with $LaCrO_3$ to form an FeCr spinel or can alloy with Pt at the cathode, respectively. Also, since $3MgAl_2O_4 \cdot 1Fe_3O_4$ is relatively unstable under the highly reducing conditions found at the cathode, it decomposes (in the presence of liquid slag) perhaps according to equation (8). Equation (9) illustrates the greater tendency to form mixed silicate reaction products at the anode vis a vis the cathode in $MgCr_2O_4$, due to higher concentrations of silica and alumina at that interface. Equation (10) demonstrates that most metals will undergo severe oxidation reactions in slags at the anode. Experiments by Koester (Reference 10) using mild steel electrodes confirm this.

Additional slag-electrode reactions in Table 5 under the heading Erosion-Cavitation can occur under all current conditions but are especially severe when the current density much exceeds 1 amp/cm^2. At the anode, oxygen gas can be formed explosively at high current densities, equation (11), and can rapidly erode away (cavitate) the electrode surface. Figure 8 demonstrates the almost exponential dependence of cavitation corrosion on current density for $3MgAl_2O_4 \cdot 1Fe_3O_4$. Cavitation corrosion will place severe limitations on anode lifetimes under real MHD conditions, i.e., current bunching can cause very high current densities on the upstream anode edge. At the cathode, (equation (12)), surface reaction products and even the matrix grains themselves (depending on microstructure, density, etc.) can be rapidly fluxed by the low viscosity and/or more chemically aggressive slags created by rapid cation transfer to this interface at high current densities.

Finally, equation (13) is an example of electrolytic dissolution and is often referred to as a classical electrochemical or Faradaic-type electrode corrosion reaction. This involves the accelerated change in ionization state and the subsequent dissolution of electrode material into the slag due to the passage of a fixed number of coulombs, i.e., obeys Faraday's equation (2). To date, of all ceramic materials studied, only SnO_2 clearly exhibits this type of behavior (Reference 3).

When one considers the large number of reaction types given in Table 5 and realizes that in general several different slag-electrode reactions can be occurring at one time, it is obvious that classical Faradaic-type corrosion should be the exception rather than the rule for most potential electrode materials. For example, the fact that $MgCr_2O_4$ corrodes by having its reaction scale flux off, $3MgAl_2O_4 \cdot 1Fe_3O_4$ corrodes by grain fluxing, and anodes corrode by cavitation reactions, are all examples of non-Faradaic reactions. Figure 8 illustrates this finding for corrosion of $3MgAl_2O_4 \cdot 1Fe_3O_4$. Data for $MgCr_2O_4$ is given in Table 4. If a single Faradaic corrosion mechanism was acting, both anodic and cathodic corrosion rates would be constant and independent of current density, (see equation (2)). The extremely large increase in anodic corrosion with increasing current density is similar to that obtained during electrochemical machining of metallic materials and is related to improvements in material removal efficiency (erosion) due to ever more rapid and explosive release of O_2 bubbles at the slag/anode interface. The non-Faradaic behavior of cathodic corrosion, especially the decrease in corrosion with current density for both $3MgAl_2O_4 \cdot 1Fe_3O_4$ and $MgCr_2O_4$ is more complex. Perhaps as noted earlier, this is because the limiting step for corrosion in these materials is not chemical reactions at the interface with the electrochemically transferred slag components but is instead controlled by the rate and depth of slag penetration and concomitant chemical reactions at the grain boundaries. If this proceeds by a diffusion mechanism, then a decrease in corrosion rate with current density might be expected. The real problem in these cases is in how to define corrosion in materials that exhibit grain boundary attack. A consistent covention of measuring recession up to and including all reacted zones containing 20 volume percent slag component or more has been maintained (Reference 3). Clearly, this definition is not adequate to define isothermal corrosion in $3MgAl_2O_4 \cdot 1Fe_3O_4$ or $MgCr_2O_4$ where grain boundary attack and the accompanying formation of FeO and/or grain boundary phases increase dramatically with current density. Perhaps a definition such as maximum extent of grain boundary penetration is superior, although by this convention, many potential intrinsically corrosion-resistant electrode materials may be overlooked or discarded.

The principal advantages of the electrochemical cell designs used in these studies are that the electrode and current path geometries are well defined, restricting corrosion, to a single plane and thereby enabling accurate determination of corrosion mechanisms and rates. For example, in duplicate tests for runs 108, 112 and 105, 106 using cell design D1, the corrosion results obtained in each case differed by less than 10% from each other. Although these cells were primarily designed for operation with liquid slag, they will also function with solid slag, provided the slag is first melted to provide good electrical contact with the electrodes.

The main advantage of cell 1 (D1) in Figure 2 is that it is a completely self-contained system. Thus corrosion experiments can be run simply by inserting the cell into any convenient furnace and applying the desired current. The disadvantages of D1 are that it is difficult to machine and that the slag can become saturated with reaction products from both the electrode and crucible materials quite rapidly.

Cell #2 (D2) is simpler and much easier to construct than D1. For operation, however, with liquid slags, it must be submerged in an auxiliary slag bath. It also suffers from problems of corrosion product saturation of the slag, although many times, retention of the reaction products are desirable in ascertaining corrosion mechanisms.

Cell #3 (D3) operates in a liquid slag bath but is unique in that it is simple to build yet overcome the problem of corrosion product buildup. As oxygen gas is evolved at the anode and bubbles out the top-most hole, new slage rushes in at the bottom to replace the losses. Thus, this cell, in essence, functions as a liquid slag pump, ensuring that "virgin" slag is constantly maintained between the electrodes.

Figure 5 illustrates typical relationships between voltage drop across the slag and test times for constant current density electrochemical tests run

in cells of type D2 and D3 (tests 119, 121). Curves obtained for D1 cells are essentially similar to that for D2. For purposes of clarity, typical voltage fluctuations amounting to $\approx \pm$ 6-10% with a frequency of 10-30 seconds are not shown. The voltage drop across a slag is a function of two completing factors. These are the degree of polarization at the electrodes which would tend to increase voltage with test time and the amount and buildup of electrically conductive reaction products due to slag electrolysis (i.e., Fe) and/or corrosion products from the electrodes themselves which tend to cause the voltage to decrease with test time. In relatively static slag tests, characteristic of tests run in D1 and D2 cells, the latter mechanism dominates giving rise to curve D2 in Figure 5. On the other hand, in an environment where new slag is constantly flowing over the electrodes as in cell D3, the reaction products are continually removed and curve D3 in Figure 5 reflects the increase in polarization within the hydrodynamic boundary layer at the slag/electrode interface with time.

In a real MHD channel, the slag on the upstream walls will be relatively free of reaction products compared to the slag at the downstream end which will have accumulated a large amount of debris. It is clear then that cell D3 and cells D1, D2, respectively, be used in the laboratory to best simulate conditions at the entrance and exit locations of a channel.

All of the ceramic materials tested in this study exhibit a marked degree of extrinsic (erosive) type of corrosion. At both cathode and anode, at current densities $\approx$ 1 amp/cm^2, material loss was usually a result of slag penetration at grain boundaries accompanied by internal chemical reactions, often by re-crystallization reactions and finally by the fluxing off of partially reacted grains into the slag. At high current densities, at the anode, corrosion was also extrinsic in that material was rapidly eroded by the machining action of oxygen bubbles. These erosive reactions would have been greatly reduced had materials of higher quality (i.e., high purity, high density, clean grain boundaries, absence of second phases) been used. Ideally, pure single crystal ceramics are needed to truly separate intrinsic from extrinsic corrosion mechanisms and to permit unequivocal ranking of the most resistant materials.

Of the ceramic materials tested to date in eastern slags, $MgCr_2O_4$ and, to a lesser extent, $MoSi_2$ appear to have the best potential for application as anode wall electrodes in MHD channels at moderate current densities. Both these materials should exhibit adequate but unspectacular performance at the cathode walls. $3MgAl_2O_4 \cdot 1Fe_3O_4$ is unstable under highly reducing conditions and is unsuitable for use as a cathode. It is a possible candidate material for anodes. $LaCrO_3$ is an unlikely electrode material exhibiting high solubility in, and extreme reactivity with, eastern slags.

Mild steel or preferably electrolytic iron is a good cathodic material being thermodynamically in equilibrium with the iron reaction product of slag electrolysis. Mild steel undergoes extremely rapid oxidation at the anode at elevated temperatures and should not be used at this wall. An exception would be if iron was used as an expendable anode to depolarize the slag.

Platinum or Pt-Rh alloys are good corrosion resistant materials for use as anodes especially under high current density conditions. Disadvantages are its high cost and its tendency to produce high anodic polarizations. It is readily attacked by and alloys with free iron at the cathode. It high cost precludes its use as a getter for iron at the cathode wall.

If laboratory scale electrochemical test data are indeed meaningful one should be able to extrapolate these results to predict what the major problems at the anode and cathode walls will be under actual coal-fired MHD channel operating conditions. These findings and suggested ways of overcoming problems for the case of liquid slag contacting electronically conducting anodes and cathodes are summarized in Table 6.

For the special case where thermal gradients across the slag are sufficiently large such that a liquid/solid interface is formed within the slag layer itself, it is likely that metallic iron will form at this location on the cathode wall and O_2 gas at a similar isotherm on the anode wall. This is because coal slags appear to switch from an ionic to an electronic conductor

TABLE 6

IMPLICATIONS OF ELECTROCHEMICAL REACTIONS ON OPERATION OF A LIQUID SLAG COVERED MHD CHANNEL

Location	Expected Electrochemical Phenomena	Implications of Electrochemical Reactions	Methods of Minimize Adverse Reactions
Liquid Slag/ anode interface	O_2 bubble formation	Electrode and/ or insulator erosion	Maintain current density <1 amp/cm^2. Employ high purity, density, large G.S. material. Maintain <1.7 volts across slag layer.
	High Po_2	Oxidation reactions	Use oxide or noble metal anodes.
	Enrichment of Si, Al	Increased slag viscosity, high polarization-arcing	Maintain thin slag layer, increase electronic transference # of slag, use sacrificial anodes.
Liquid slag/ cathode interface	Metallic Fe formation	Interelectrode shorting	Maintain <1.7 volts across slag layer (i.e., thin layer, low resistivity, or electronically conducting slag layer). Use iron gettering electrode.
	Low Po_2	Reduction reaction	Use metal or carbide cathodes.
	Enrichment of Fe^{+2}, Ca^{+2}, K^{+1}, Ng	Decreased slag viscosity, more chemically aggressive slag, less polarization	Increase electronic conductivity of slag. Use higher quality cathode materials.

at temperatures less than $\approx 1100^{o}C$. Thus in essence, the solid slag layers act as a simple extension of the electronically conducting electrode itself. Therefore, all electrochemical reactions listed in Table 5 may occur at this new liquid/solid slag interface.

Finally, there is one other effect which can occur in real channels that complicates simple concepts that anode walls will undergo only oxidizing reactions and the cathode walls only reducing reactions. As a result of Hall voltages in real channels, anodic and cathodic regions will be found a each wall. Localized electrochemical cells may then become established creating complex and perhaps very severe regions of corrosion.

Conclusions

The major conclusions of this study of slag/electrode reactions can be summarized as follows:

1) For most electrode materials, corrosion is the result of the formation of highly aggressive components in the liquid slag at the electrode/slag interface due to the passage of current. These aggressive components include metallic iron and oxygen gas formed by slag electrolysis at the cathode and anode, respectively, and Fe^{+2}, Ca^{+2} and K^{+1} ions which segregate to the cathode and silicate and aluminate ions which segregate to the anode. Even in the absence of arcing, extensive corrosion of the electrode as well as the inter-electrode insulator can occur at high current density, due to the explosive formation of O_2 bubbles.

2) Although the eastern slag, E-03, tested has a significant component of ionic conductivity, electrode corrosion loss did not obey Faraday's law. This is because corrosion is not solely chemical in nature, but involves a large amount of physical erosion reactions such as grain fluxing and surface machining. Only 1.7 volts was needed to decompose an eastern slag E-03 to metallic iron and O_2 at $1400^{o}C$.

3) The kinetics of electrochemical electrode/slag corrosion can be reduced by increasing the electronic conductivity of the slags, reducing slag layer thickness, reducing voltage drop across slag layer to less than 1.7 volts and by reducing temperatures. Slags appear to be much more electronically conductive in the solid state than in the liquid state.

4) Cathodic materials must be stable under highly reducing conditions ($< 10^{-10}$ atm O_2) and anodic materials should be stable under oxidizing conditions. This suggests the use of metallic materials for cathodes and oxide ceramics and/or oxidation resistant metals (i.e., Pt) for anodes.

5) Among the ceramic materials tested $MgCr_2O_4$, and to a lesser extent $MoSi_2$ exhibited the best electrochemical corrosion resistance in liquid eastern USA coal slags. It is also recommended from the standpoint of corrosion resistance that metallic iron be used as cathode wall electrodes and Pt or Pt-Rh alloys be used as anode wall electrodes.

6) High purity, high density and large grain size are critically important factors for designing electrode materials for corrosion resistance.

7) The performance of an MHD channel can be adversely affected by electrochemical reactions. Free iron at the cathode can cause interelectrode shorting while segregation of SiO_4^{-4} and AlO_y^{-x} to the anode can result in large polarizations and cause arcing.

8) Several types of cells have been designed and have successfully allowed measurements of electrochemical corrosion reactions in "virgin" slag and in slag that becomes saturated with electrode/slag reaction products.

2.0 WBS 1.2 - TEST ASSEMBLY FABRICATION

No significant activity was undertaken this quarter (see Section 5.2 for equivalent activity in support of the U-02 Phase III Module).

3.0 WBS 1.3 - WESTINGHOUSE ELECTRODE SYSTEMS TEST FACILITY (WESTF)

3.1 Facility Design and Modification

Various components for the NOVA 3/12 mini-computer system have been received. However, in view of the on-going U-02 Proof Test Series, installation of this hardware has been deferred and will be accomplished upon completion of the Proof Test Series.

Test operations were completed in support of the U-02 Phase III Module as reported in Section 5.2. Table 7 provides a summary of the WESTF Test Program.

TABLE 7

SUMMARY OF WESTF TESTS (DESIGN DATA

Test No.	35-1	35-2	35-3	35-4	35-5	36	37	38
Date	6/30	7/11	9/8	9/12	9/15	9/28	10/12	11/18
Cathode Materials	←	←	Copper	→	→	$LaCrO_3$	U-02 Phase III Proof Tests	
Anode Materials	←	←	Copper	→	→	$LaCrO_3$	See Section 5.2	
Attachment Materials	←	←	None	→	→	Various	↓	
Insulator Materials	←	←	$MgAl_2O_4$	→	→	$MgAl_2O_4$ MgO	↓	
Twall - ^oC	←	←	400 - 100	→	→	1700	1700	1700
Mass Flow kg/sec	←	←	0.12	→	→	0.15	1.0	1.0
Current, Amp/cm^2	.1-.2	.1-.2	1.0	0	1.0	1.0	1.0	1.0
Heat Flux, W/cm^2	←	←	96 - 86	→	→	34 - 36	16-18	16-18
Axial Field, Kv/m	←	←	0	→	→	0	0	0
Fuel	←	←	Clean	→	→	Clean	Clean	Clean
Duration, -Hrs	2	10	5	1	4	20	20	20

4.0 WBS 1.4 - WESTINGHOUSE MHD TEST FACILITY (WMTF)

No significant activity was undertaken this quarter. As requested by DOE, facility design and modification as well as test operations have been maintained on HOLD.

5.0 WBS 1.5 - COOPERATIVE US/USSR MHD PROGRAM

5.1 WBS 1.5.1 - US/USSR Liaison

With the exception of that effort associated with the U-02 Phase III Module Test, no significant activity was completed during this quarter.

5.2 WBS 1.5.2 - U-02 Phase III Module

The objective of the U-02 Phase III Module Test, to be conducted in the U-02 Facility in May of 1978, is to evaluate the performance of refractory electrode systems during long term operation under MHD conditions with a clean fuel. For this module emphasis has been placed not only on electrode/insulator materials, but on current lead-out materials and attachments. Candidate electrode systems, summarized in Table 8, reflected a wide range of materials and fabrication techniques.

Desired operating conditions for the U-02 test are an electrode surface temperature of $\approx 1700^{o}C$ and electrode heat fluxes of 16 to 20 w/cm^2. In contrast with the prior U-02 tests, the Phase III effort includes a series of three proof tests with the purpose of providing a basis for materials and design selection. The Proof Test Series will be conducted in the Westinghouse Electrode System Test Facility (WESTF).

For this reporting period the design and development activity has been directed towards the electrode systems to be incorporated in the Proof Test Series.

TABLE 8

U-02 PHASE III MODULE CANDIDATE ELECTRODE SYSTEMS

Supplier	Attachment	Electrode	Fab.* Tech.	Insulator	Fab.* Tech.	Proof Test No.
GE	Flexbed	4 $MgAl_2O_4 \cdot 1Fe_3O_4$	S	$MgAl_2O_4$	S	1 (Oct. 77)
W/Technetics	Hoskins Mesh	3 $MgAl_2O_4 \cdot 1Fe_3O_4$	PS	$MgAl_2O_4$	S	1 (Oct. 77)
ANL	HfO_2 - Metal Composite		HP	$MgAl_2O_4$	PS	1 (Oct. 77)
W/EP	Ag Epoxy	$LaCrO_3/ZrO_2$ Cap(1)	HP	MgO	S	2 (Nov. 77)
W/APS	Cermet	$LaCrO_3/ZrO_2$ Cap(2)	PS	$MgAl_2O_4$	PS	2 (Nov. 77)
W	Ag Epoxy	$LaCrO_3$ - ZrO_2(3)	HP	$MgAl_2O_4$	S	2 (Nov. 77)
W/Technetics	Nickel Mesh	$La_{.95}Mg_{.05}CrO_3$	HP	$MgAl_2O_4$	S	2 (Nov. 77)
W	Ag Epoxy - Au	$LaCrO_3$- $LaAlO_3$(4)	HP	MgO	HP	3 (Jan. 78)
W	Ag Epoxy - Pt	.5 $LaCrO_3$·5 $SrZrO_3$	HP	$MgAl_2O_4$	S	3 (Jan. 78)
GE	Flexbed	$LaCrO_3$	S	$MgAl_2O_4$	S	3 (Jan. 78)
W/APS	$FeAl_2O_4$	3 $MgAl_2O_4 \cdot 1Fe_3O_4$	PS	$MgAl_2O_4$	PS	3 (Jan. 78)

*PS - Plasma Spray
S - Sintered
HP - Hot Pressed

(1) $La_{.95}Mg_{.05}Cr_{.9}Al_{.1}O_3/.85ZrO_2-.12CeO_2-.03Y_2O_3$ Cap

(2) $La_{.95}Mg_{.05}CrO_3/.85ZrO_2-.12CeO_2-.03Y_2O_3$ Cap

(3) $La_{.95}Mg_{.05}CrO_3/.90ZrO_2-.10Y_2O_3$ Composite

(4) $La_{.95}Mg_{.05}Cr_{.85}Al_{.15}O_3$(cold) graded to $La_{.95}Mg_{.05}Cr_{.68}Al_{.32}O_3$ (hot)

5.2.1 Material Development

5.2.1.1 Electrode Development

The overall philosophy for the Phase III tests was to include promising materials - without significant development. In other words, development would be limited to adapting materials and structures to U-02 designs. This meant the development of very thick electrode structures (due to the very low U-02 heat fluxes). Work was subcontracted to APS Materials, Inc. of Dayton, Ohio and Eagle - Picher Industries, Inc. of Miami - Okla. to develop electrode structures suitable for the U-02 Phase III proof tests. The following discussion will summarize these development efforts plus those at Westinghouse on the hot pressed $LaCrO_3/ZrO_2$ composite and $LaCrO_3$ - $LaAlO_3$ electrodes.

Hot Pressed ZrO_2 'Capped' $LaCrO_3$ Electrodes (Eagle - Picher Industries, Inc.)

The first objective was the development of a ceramic electrode structure consisting of a $La(Mg)CrO_3$ based composition with a refractory oxide cap using the semi-continuous hot pressing technique. The refractory oxide cap was to be 85 Mole % ZrO_2, 12 Mole % CeO_2 and 3 Mole % Y_2O_3. The $La(Mg)CrO_3$ composition was given by the formula $La_{.95}Mg_{.05}Cr_{1-x}Al_xO_3$ where x = 0 to 0.5, according to performance of the chosen experimental powders. The effort was directed toward producing crack free ceramic bodies of closed porosity (greater than 90% of theoretical density) with good refractory cap to electrode base adhesion. The effort was to establish powder composition, grading pattern and pressing temperatures, pressures and times.

The second objective was to produce 27 electrode blocks of the type described above with dimensions of 1.1 cm x 2.1 cm x 2.1 cm.

The scope of work was to develope the electrode configuration previously described using techniques and materials readily available in a ceramics development laboratory.

Experimental Results

The raw materials to be utilizied were evaluated by means of pressing comparison tests. These were conducted in graphite dies at 1600°C and 29.78 MPa (4300 lb/in^2). Pressure was applied until the deformation rate fell to less than 0.002 in /5 min at which time the run was ended. Table 9 shows the terminal densities and the times required to ahcieve those densities.

When actual capped electrodes were to be made, cap and body materials were paired and checked for compatability in terms of densifying at comparable rates. Other factors did, however, enter in. An example is the unsuitability of EP-D for the major constituent of an electrode body due to its lower electrical conductivity even though it pressed fairly well and was fairly compatible with EP-I cap material.

Initial electrode fabrication attempts were made in unprotected graphite dies. Pressings were made at temperatures from 1475°C to 1766°C and pressures from 29.67 MPa (4300 lb/in^2) to 32.78 MPa (4750 lb/in^2). Pressing time varied from 13 minutes to 95 minutes. The parts produced in graphite tooling always showed a "case" or dark region near the periphery of the La(Mg)CrO_3 electrode body. It varied from less than 1/16 inch to somewhat greater than 1/8 inch in thickness. The higher temperatures (beyond 1700°C) often resulted in exfoliation of the part leaving large voids. Interlayer bonding was usually poor regardless of temperature. Die liner experiments were initiated as soon as the presence of metallic Cr was discovered to exist in all the parts pressed in graphite tooling unprotected. The largest amounts of metallic Cr were found at the interfaces between layers.

The materials tested as die and punch liners were BN aerosol, nickel, tantalum, platinum, Fiberfrax paper, Al_2O_3 paper, MgO powder, Cr_2O_3 powder, and sintered Al_2O_3 sleeves. The BN and tantalum liners proved to be nearly as effective reducing agents as the graphite itself. The optimum hot pressing temperature ultimately turned out to be 1475°C. At that temperature the nickel is molten and the Fiberfrax decomposes. The fiberfrax decomposition could be helpful if O_2 is thereby released, but, it cannot stand alone as a diffusion (reduction)

TABLE 9

RAW MATERIAL CODING, VENDOR IDENTIFICATION, AND PRESSING COMPARISON

Material	Code	@1600°C & 4300 PSI	%TD Achieved
ZrO_2 w/12 st% Y_2O_3 Zircar Products	EP-A	20 Min	100.7
ZrO_2 w/12 mole% CeO_2 3 mole% Y_2O_3 CZ-CE01 Cerac	EP-B	55 Min	91
$La_{.95}Mg_{.05}CrO_3$ General Refractories	EP-C	65 Min	95
$La_{.95}Mg_{.05}Cr_{.5}Al_{.5}O_3$ A-T Research	EP-D	20 Min	83.8
$La_{.95}Mg_{.05}Cr_{.85}Al_{.15}O_3$ A-T Research	EP-E	60 Min	77.6
$La_{.8}Ca_{.2}CrO_3$ A-T Research	EP-F	19 Min	100
$La(Mg_{.05}Cr_{1.00})_{.952}O_3$ A-T Research	EP-G	25 Min	96
$La_{.95}Mg_{.05}CrO_3$ Cerac	EP-H	25 Min	95.3
ZrO_2 w/12 mole% CeO & 3 mole% Y_2O_3 A-T Research	EP-I	20 Min	106

barrier. At 1475°C the platinum (0.025 mm thick) is not reusable, a major disadvantage for a material of that cost. The ability of platinum to prevent reduction was not absolutely proven, as it was used only as punch face barriers, and never alone, but in combination with other materials.

The Al_2O_3 paper, MgO powder, Cr_2O_3 powder and sintered Al_2O_3 have the capability of remaining stable at 1475°C. The Cr_2O_3 powder imparted a purple hue to the ZrO_2 cap and was a little less effective than MgO in minimizing the "black case" of reduced $La(Mg)CrO_3$ at the edges of the part. The use of packing powder required extremely tedious die loading procedures since the procurement of a hardened steel tool and die set for performing the electrode ingots was too time consuming. There is some reason to hope that MgO packing powder could suffice under the right pressing conditions. This would have economic advantages over the use of sintered Al_2O_3 sleeves.

The sintered Al_2O_3 sleeves were extremely effective at preventing circumferential reduction. The initial problem associated with their use was the tendancy of the Al_2O_3 to bond to the part. This bonding no doubt increased die wall friction, and limited density. Cracking was initiated during cool down that was aggravated by this bonding and the CTE mismatch between Al_2O_3 and $La(MG)CrO_3$. The solution was approached first by scoring the O.D. of the sleeve longitudinally and circumferentially. The success was rather limited, but it was observed that the Al_2O_3 segments were bonded predominately in those gradients where the x value in $La_{.95}Mg_{.05}Cr_{1-x}Al_xO_3$ was largest. Therefore, the I.D. of all of the Al_2O_3 sleeves were coated with EP-C material (See Table 9 for code). Also, it was decided to reduce the average value of X to 0.10 by mixing EP-C with EP-D in the ratio of 80 vol % EP-C to 20 vol % EP-D. It was felt that retaining some EP-D would produce higher densities due to its relatively greater pressability. This 80:20 mix of EP-C and EP-D became the standard mix for the $La(Mg)CrO_3$ portion of any gradient in which the $La(Mg)CrO_3$ was mixed with cap material. With an average composition of $La_{.95}Mg_{.05}Cr_{.90}Al_{.10}O_3$ good results were achieved. The term "average composition" is used since powders were hand mixed in a mortar and pestle.

The above steps alleviated the problems associated with the Al_2O_3 sleeves. The ends of the parts also needed protection due to the oxygen mobility in the ZrO_2

cap and the tendancy to form free Cr at the interface between the cap and the first gradient layer (layer 1 & 2 interface). This was solved by the use of a layer "0" above the cap and a combination of Al_2O_3 paper discs and MgO powder between layer "0" and the graphite punch. Layer "0" was composed of the same material as the electrode body. The Al_2O_3 paper and MgO sharply limited the graphites ability to reduce the $La(Mg)CrO_3$ and the reduction that did occur was limited to the layer "0".

The final geometry, grading, and composition are shown in Figure 11. Layer "0" is not shown since it was to be ground off prior to actual testing of the electrode. The composition of the layers was as follows: Layer 1, EP-I; Layer 4, 80 vol % EP-C and 20 vol % EP-D; Layers 2 and 3 were formulated by mixing the layer 1 and Layer 4 compositions in the indicated proportions.

A sample of the electrode body product which had been oxidized at over 800°C for over one hour was found to have electrical resistance in the same order of magnitude as a sample of $La(Mg)CrO_3$ pressed under oxidizing conditions by other investigators. An unoxidized sample of the final product was found to have nearly infinite resistance.

Arc Plasma Spray Deposited $LaCrO_3$ and $3MgAl_2O_4 \cdot 1FeO_4$ Electrodes (APS Materials Inc., Dayton, Ohio)

APS Materials, Inc., had previously demonstrated unique plasma spray techniques in preparing electrodes for test in high heat flux facilities at MIT, AVCO and Reynolds for U-25 and future CDIF applications. In the U-02 program APS had the objective of producing much thicker (1 - 2 cm) electrodes while maintaining high density and proper stoichiometry. The initial phase, where spraying conditions were established to produce the desired densities and chemistries, was funded by the National Bureau of Standards. With the funding provided by Westinghouse, APS: 1) established a test to evalute various bonding (to copper) approaches, 2) examined several materials as graded bonding layers to copper, 3) investigated mechanical aids such as 'dog-ears' and slotting to reduce stresses, and 4) delivered six electrodes each of ZrO_2 copped $LaCrO_3$ and $3MgAlO_4 \cdot 1Fe_3O_4$ (MAFF 31) for proof tests.

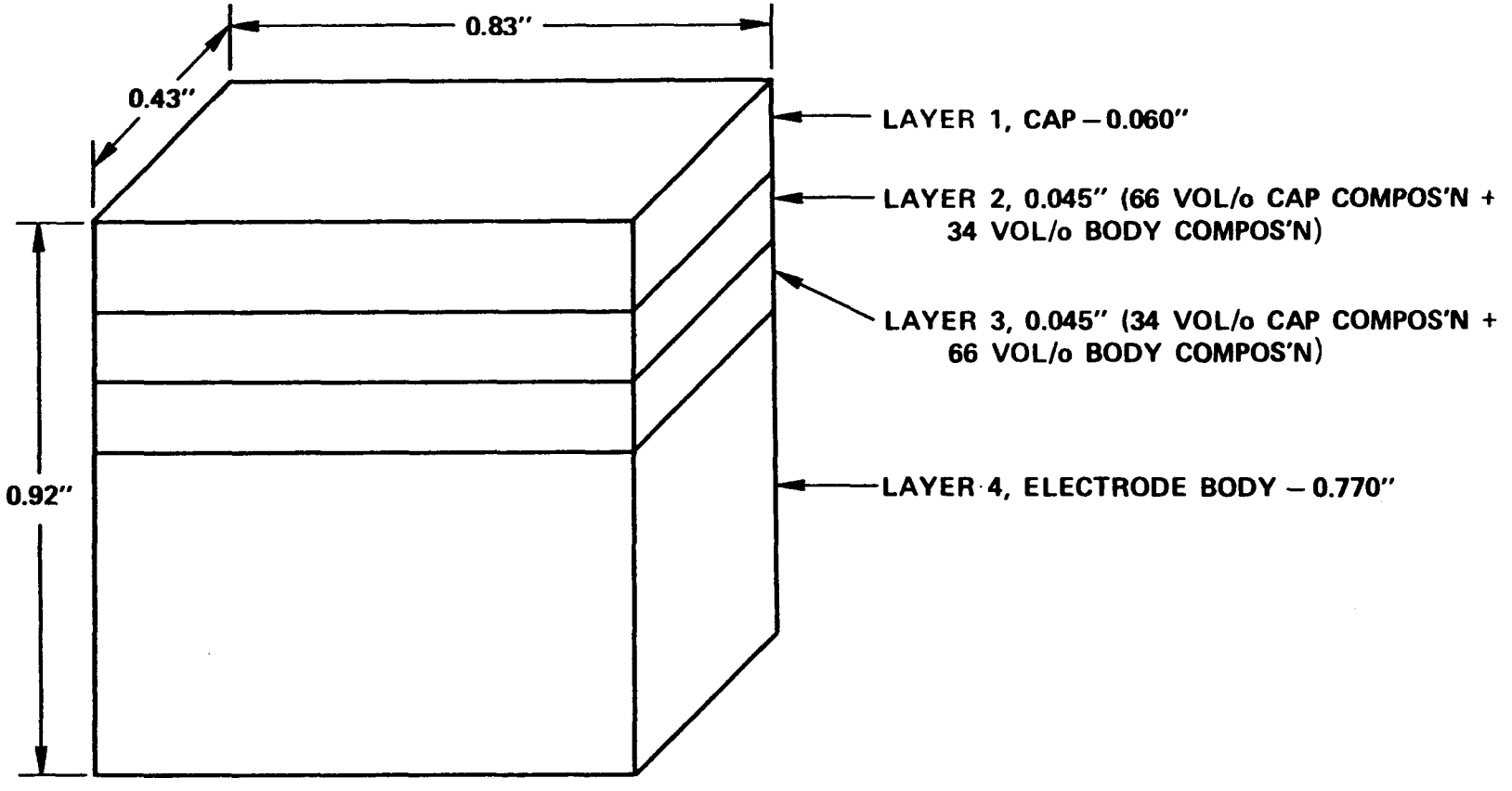

NOTE: PRESSED AS 1.5" D. DISCS, THEN SLICED & FINISH GROUND.

Figure 11. Hot Pressed ZrO_2 Capped $LaCrO_3$ Electrodes

Figure 12 illustrates the test facility. The copper substrate is in the shape of a 3/8" square tube with 1/4" diameter copper tubing soldered to the ends as water connections. Thermocouples are mounted in the inlet and outlet sides to monitor water temperatures. The sample to be tested is sprayed on one side of the square tube for a length of 2" and at a thickness of 6 mm. which is typical for MIT-type samples. This arrangement permits any type of bonding mechanism to be tested, including mechanical and graded cermet.

The plasma torch was chosen to provide the most readily controllable operating temperatures over a fairly broad length of the sample. It is traversed along the length of the sample — the total traversing distance being of the order of 3". The surface of the torched sample is measured by the use of an Ircon Series 2000 optical pyrometer which has a sensitivity in the appropriate range to measure either the surface or the plasma temperature itself in that region.

Empirical studies were conducted which showed that the torch-to-test piece distance of 3" and a water flow rate of 225 grams/min provided the best over-all test range and control.

On the basis of these torch tests, materials, material's grading, substrate preparation and electrode configuration were optimized. The specific materials and dimensions for both ZrO_2 capped $LaCrO_3$ electrodes and MAFF 31 are given in Table 10.

$LaCrO_3$ Electrodes

The first type consists of a series of graded layers having varying percentages of APS M-447 (nickel-molybdenum-aluminum alloy) and $LaCrO_3$. This was followed by a layer of $LaCrO_3$. A cap material (ZrO_2-CeO_2-Y_2O_3) was then applied over the $LaCrO_3$. This is shown schematically in Figure 13.

Prior to spraying, the top surface of the electrodes were roughened by sawing grid lines into the surfaces to form a pattern of 0.3 cm squares. The surface was then pounded with a special rotary shaft preparation tool designed to roughen surfaces prior to plasma coating. The roughened surfaces were then nickel plated.

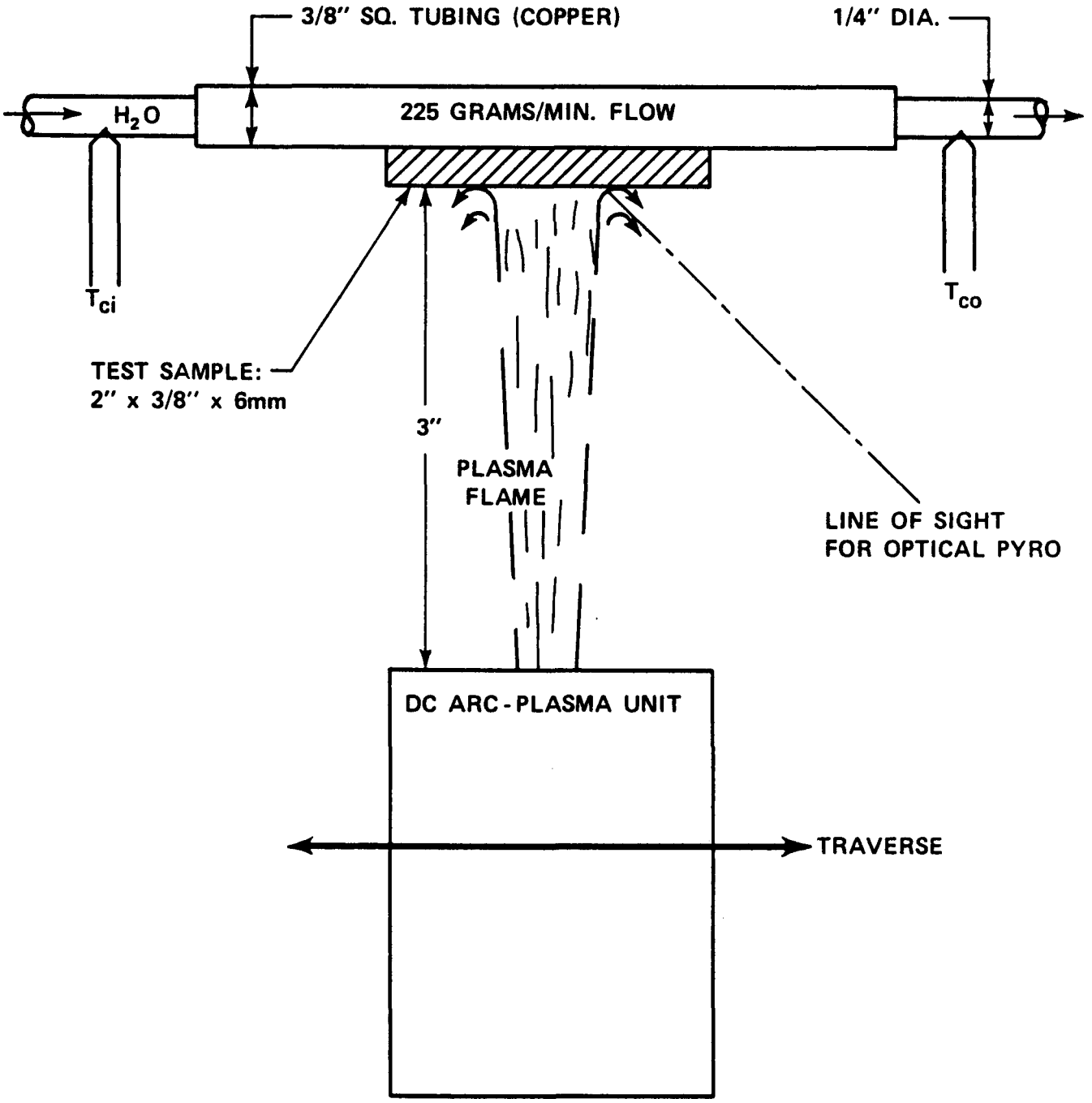

Figure 12. The Test Facility

TABLE 10

MATERIALS OF CONSTRUCTION AND PHYSICAL DIMENSIONS OF PLASMA-SPRAYED U-02 ELECTRODES

TYPE	$LaCrO_3$	MAFF 31
Substrate		
Type	water cooled copper block	water cooled copper block
Length, cm	5.9	5.9
Width, cm	1	1
Thickness, cm	4.8	4.8
Surface Preparation		
Step 1	Roughened	Roughened
Step 2	Nickel Plated	Nickel Plated
Step 3	Fine Grit Blasted	Fine Grit Blasted
Plasma-Sprayed Layers		
Bond Layer Graded Layer(s) Type	67% APS M-447 - 33% $LaCrO_3$ 50% APS M-447 - 50% $LaCrO_3$ 33% APS M-447 - 67% $LaCrO_3$	APS M-447-Hercynite Continuous Grade
Total Thickness, cm	∿0.3	∿0.2
Intermediate Layer Type	—	Hercynite
Thickness, cm	—	∿0.5
Intermediate Layer Type	$LaCrO_3$	MAFF-31
Thickness	∿1.2	∿1.2
Top Cap Layer Type	ZrO_2-CeO_2-Y_2O_3	None
Thickness, cm	∿0.1	
Total Sprayed Thickness, cm	1.6	1.9
Side Wall Insulation Type	$MgAl_2O_4$ (Spinel S-71)	$MgAl_2O_4$ (Spinel S-71)
Thickness, cm	∿0.1	∿0.1

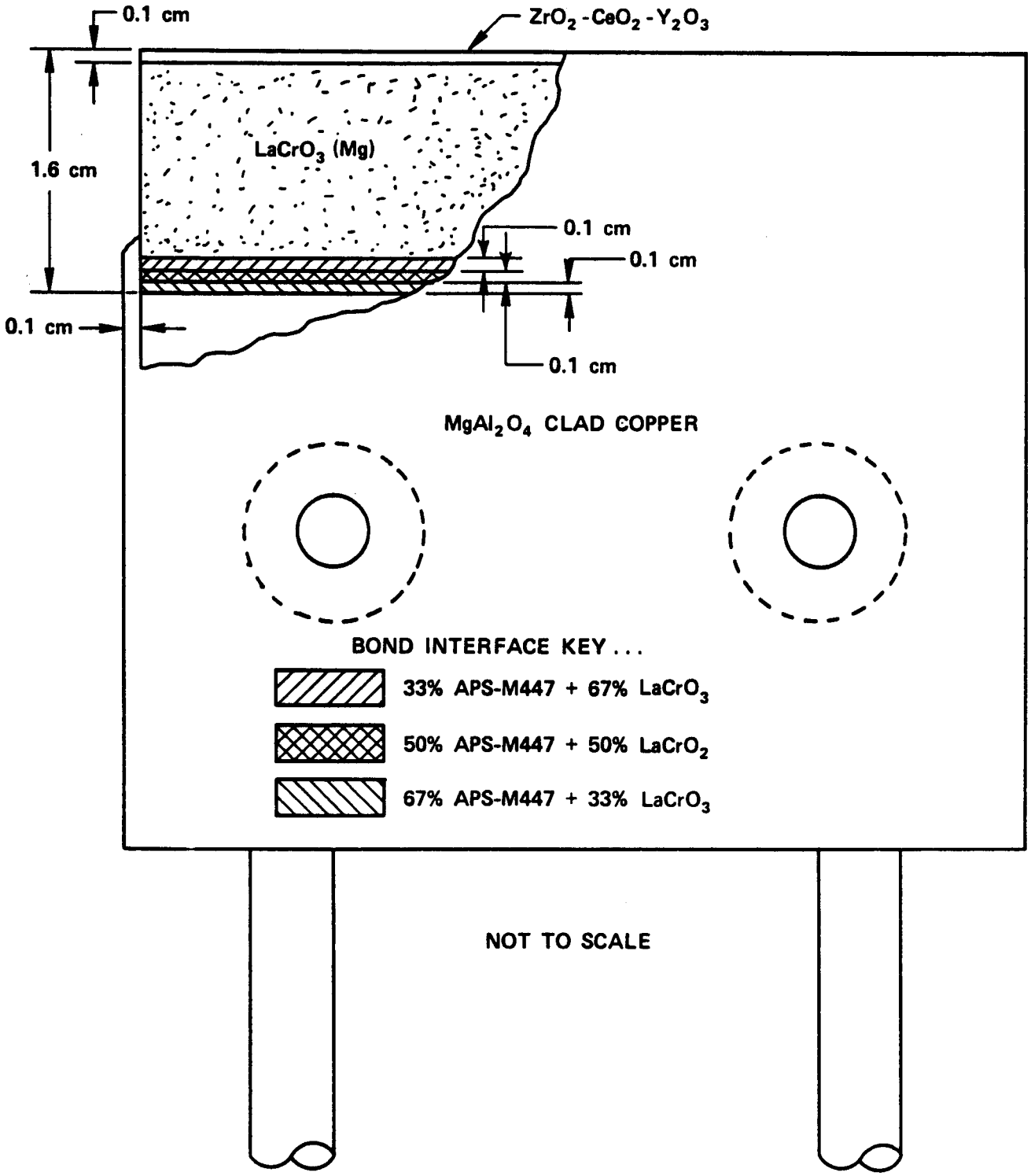

Figure 13. $LaCrO_3$ Electrodes

The shiny nickel plate was frosted using a fine grit blasting medium. A bond coating of APS M-447 was then applied over the top electrode surface. Then three different mixtures of APS M-447 and $LaCrO_3$ were successfully sprayed to make a transition from 100% APS M-447 to 100% $LaCrO_3$. A layer of $LaCrO_3$ was then plasma-sprayed to the required thickness and ground flat. Stress relieving saw slots were then placed at 1.5 cm intervals perpendicular to the length dimension. The surface was grit blasted and a cap material of ZrO_2-CeO_2-Y_2O_3 was applied over the $LaCrO_3$. The slots were then cut through to mate with those in the $LaCrO_3$ layer to a total depth of 0.5 cm. An insulating layer of $MgAl_2O_4$ was applied to the sides of the electrodes and the sides and top were subsequently ground parallel.

MAFF 31 Electrodes

The second type consists of a continuously graded layer of APS M-447 and Hercynite followed by intermediate layers of hercynite and MAFF-31, respectively. The hercynite was used in this case because of its relatively lower electrical resistivity at lower temperatures when compared to MAFF-31. No cap material was required. A schematic of the Type II Electrode is shown in Figure 14. Physical dimensions and other data are also given in Table 9 for the Type II Electrodes.

The same procedure was used for preparing the copper substrate surface as detailed in the previous section for the Type I Electrodes. However, for applying the graded layer, two powder feeders containing APS M-447 and hercynite were used to obtain an infinitely varying mixture of the two materials. The two materials were blended prior to entering the plasma stream. In actual practice, the feed settings were incrementally changed after each rastered pass over the electrode surfaces. In this manner, ten different graded layers were applied to make the transition from 100% APS M-447 to 100% Hercynite. Successive layers of hercynite and MAFF-31 were then applied. Stress relieving saw slots were placed at 1.5 cm intervals perpendicular to the length dimensions to a depth of 0.5 cm. Insulating layers of $MgAl_2O_4$ were then applied to the sides and ground parallel.

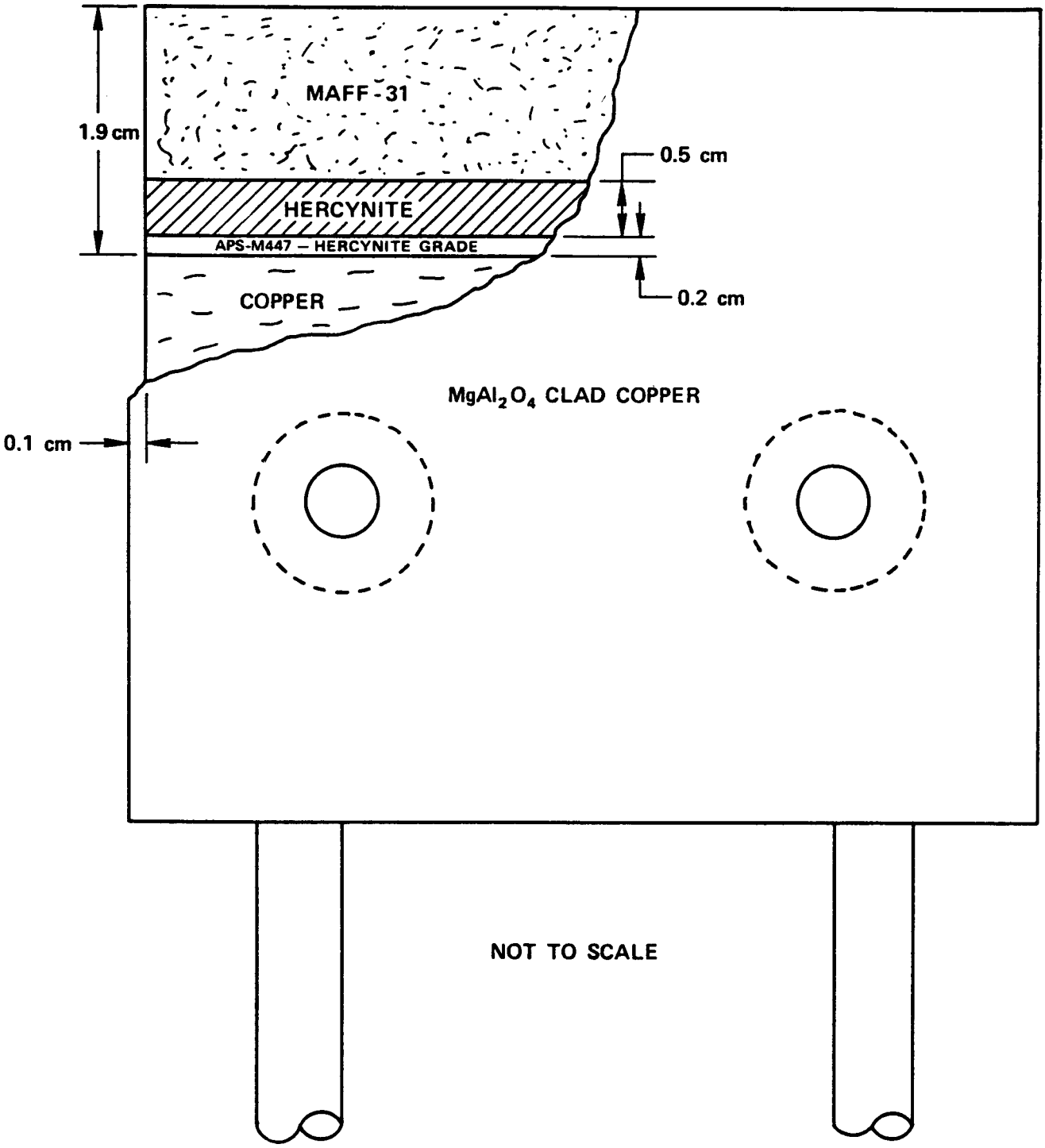

Figure 14. MAFF 31 Electrodes

Thermocouple Placement

Two electrodes of each electrode type were equipped with thermocouples in order to provide more reliable temperature characteristics. A schematic of the electrodes showing thermocouple placement is shown in Figure 15. Two thermocouples were imbedded in each specimen during spraying. A chromel-alumel thermocouple was placed about 0.3 cm above the surface of the copper substrate and a Type B, Pt-Rh was placed about 1.3 cm above it. In both cases, the thermocouples were bent at a right angle about 0.6 cm from the bead and placed over the top surface and down in a slot machined in the copper substrate as shown in Figure 15. Considerable difficulty was experienced in covering the thermocouples due to thermocouple vibration and expansion. In some cases, several attempts were required to successfully imbed them. A more desirable alternative in future work might be to drill a small hole from the side or bottom into the top surface and expose only the bead of the thermocouple to the spray.

Hot-Pressed $LaCrO_3/ZrO_2$ Composite and $LaCrO_3/LaAlO_3$ Electrodes (Westinghouse)

The objective was the development and fabrication of two hot-pressed ceramic electrode structures consisting of the following:

1) $La_{.95}Mg_{.05}CeO_3$ with Y_2O_3 stabilized ZrO_2 dispersed in the matrix.

2) A layered structure of three compositions — $La_{.95}Mg_{.05}Al_{.32}Cr_{.68}O_3$, $La_{.95}Mg_{.05}Al_{.24}Cr_{.76}O_3$, and $La_{,96}Mg_{.05}Al_{.15}Cr_{.85}O_3$

The first structure was a mechanical mixture of $La_{.95}Mg_{.05}CrO_3$ powder (A-T Research, Vichy, Missouri) and coarse (-40 + 70 mesh) fused 88 m/oZrO_2 - 12 m/oY_2O_3 grains (Norton Company, Worchester, Mass.). The addition of the refractory ZrO_2 grains to $LaCrO_3$ should increase its erosion resistance and decrease its volatilization rate. The second structure consisted of three layers of MgO doped $LaCrO_3$ (A-T Research, Vichy, Missouri) with Al substituted for Cr to lower the volatilazation rate of the material.

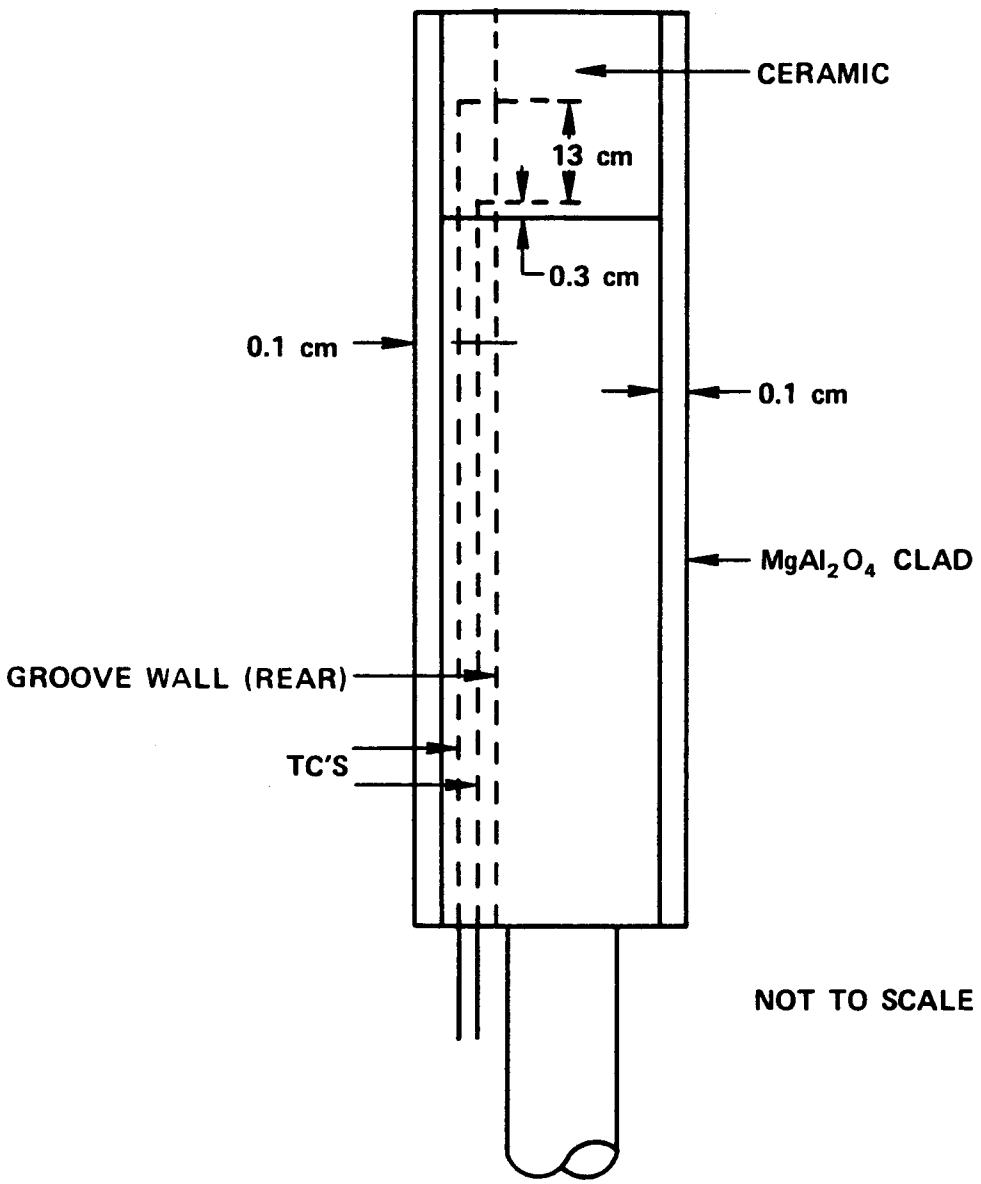

Figure 15. Thermocouple Placement

Fabrication Technique

It is the consensus that to impede the corrosive nature of potassium compounds in an MHD channel environment high density electrode materials must be fabricated. To this end a primary objective was to hot-press these two electrode structures to greater than 96% of theoretical, to reduce the amount of open porosity.

Figure 16 shows the set-up used for hot-pressing 3" x 5" billets. Thicknesses up to 1.4" were fabricated satisfactorily to high densities in this manner. A radio frequency generator was used to heat the powder in a static nitrogen atmosphere. Graphite components were used exclusively to hold the powder charge. Graphite inserts were placed inside the circular graphite die to obtain the 3" x 5" billet dimensions. A 2" diameter hydraulic press was used in applying the necessary pressure. In most cases the maximum pressure was applied at room temperature and then the temperature was raised. For the $LaCrO_3/ZrO_2$ composite electrode, the optimum pressure and temperature was 4,000 psi and 1650°C. Time at the maximum temperature was 2 - 3 hours. For the $LaCrO_3/LaAlO_3$ electrode structure, the pressure was reduced to 3,000 psi while retaining a temperature of 1650°C. Experience has shown that increasing the temperature above 1650°C causes reaction of the electrode billet with the graphite die components. Additionally, increasing the pressure above 4,000 psi causes structural problems in the electrode billet, i.e., formation of cracks and fissures, laminations, etc. Pyrolytic graphite was found beneficial in reducing heat loss through the upper and lower plungers during operation by placing it closer to the powder charge.

After hot-pressing the electrodes they were ground, sliced to proper dimensions, and then oxidized to significantly improve their electrical conductivity. Temperatures of 1500 - 1600 °C for 4 - 8 hours were necessary for oxygen diffusion through the electrodes and a resulting conductivity adequate for the proposed current passage. Lower temperatures were found unacceptable in increasing the conductivity sufficiently through the bulk of the materials.

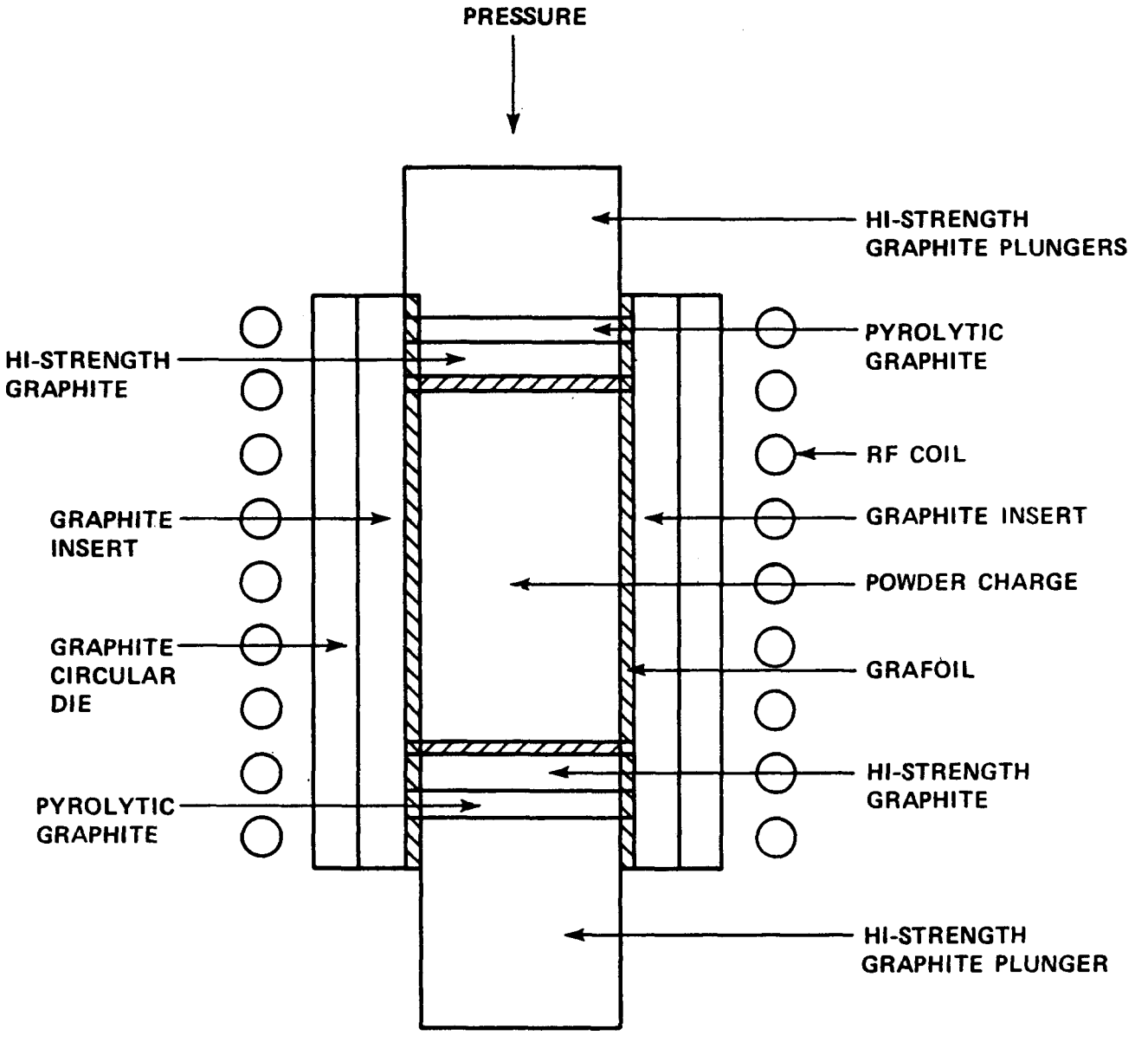

Figure 16. Hot-Pressing Technique for Fabricating MHD Electrodes (Die Dimension 3" x 5") N_2 Atmosphere

5.2.1.2 Electrode/Insulator Characterization

Pre-test characterization of the electrodes/insulators being run in the U-02 Proof Tests are necessary to fully evaluate the materials' performance. These properties include: thermal and electrical conductivity, thermal expansion, elastic modulus, fracture strength, chemical composition, phase composition, microstructure and porosity.

Densities - Porosities

Table 11 lists the materials which have been or will be tested in each of the three U-02 Proof Tests. The majority of the electrodes and insulators have a density greater than 90% of theoretical. It is the consensus that high density materials are necessary to impede the corrosion by potassium seed compounds. It is especially important to try to limit the amount of open pores in any given material.

Lab measurements have shown that electrode materials which have been fabricated to a density greater than 95% of theoretical have relatively little open pores. When the density slips below this level, the majority of the porosity becomes open. Consequently, one of the aims in the fabrication of the U-02 module is to further increase the material densities and reduce the amount of open porosity.

Powder Characteristics and Microstructure

Electrode Powder Characteristics

Three vendors have supplied $La_{.95}Mg_{.05}CrO_3$ powder for development of U-02 electrodes, General Refractories, Transtech, and A-T Research. Figure 17 shows the general size and shape of each of the three powders at 1000 x. It is quite obvious that the A-T Research powder has many larger grains (420 μm) with an angular shape, in contrast to the other two powders which have a much smaller size ($\sim$ 2 μ m) and a spherical shape.

A-T Research has supplied several additional $La_{.95}Mg_{.05}CrO_3$ powders which have substituted different percentages of Al for Cr. Figure 18 shows the size and

TABLE 11

PHASE III U-02 PROOF TEST MATERIALS

Electrodes	Total Porosity (%)	Open Porosity (%)	Interelectrode Insulator	Proof Test #
3 $MgAl_2O_4$ - 1 Fe_3O_4 (PS)	10	4	$MgAl_2O_4$(S)	1
4 $MgAl_2O_4$ - 1 Fe_3O_4 (S)	~5	<1	$MgAl_2O_4$(S)	1
3 $MgAl_2O_4$ - 1 Fe_3O_4 (PS)	10	4	$MgAl_2O_4$(PS)	3
$La_{.95}Mg_{.05}CrO_3$ (S)	4	0	$MgAl_2O_4$(S)	2
$La_{.95}Mg_{.05}CrO_3$/88 ZrO_2 - 12 Y_2O_3 composite (HP)	7	2	$MgAl_2O_4$(S)	2
$La_{.95}Mg_{.05}Cr_{.9}Al_{.1}O_3$ graded to 85 ZrO_2 - 12 CeO_2 - 3 Y_2O_3 (HP)	4	<1	MgO(S)	2
$La_{.95}Mg_{.05}CrO_3$ graded to 85 ZrO_2 - 12 CeO_2 - 3 Y_2O_3 (PS)	10 - 20	5 - 10	$MgAl_2O_4$(PS)	2
$La_{.95}Mg_{.05}Cr_{.85}Al_{.15}O_3$ graded to $La_{.95}Mg_{.05}Cr_{.68}Al_{.32}O_3$ (HP)	5	<1	MgO(HP)	3
50 $LaCrO_3$ - 50 $SrZrO_3$ (S)	11	8	$MgAl_2O_4$(S)	3
Insulators				
MgO (S)	2	0.5	--	2
MgO (HP)	16	12	--	3
$MgAl_2O_4$ (S)	2	0.5	--	1,2,3
$MgAl_2O_4$ (PS)	5 - 10	3 - 5	--	2,3

P - Arc plasma sprayed, S - Sintered, HP - Hot pressed.

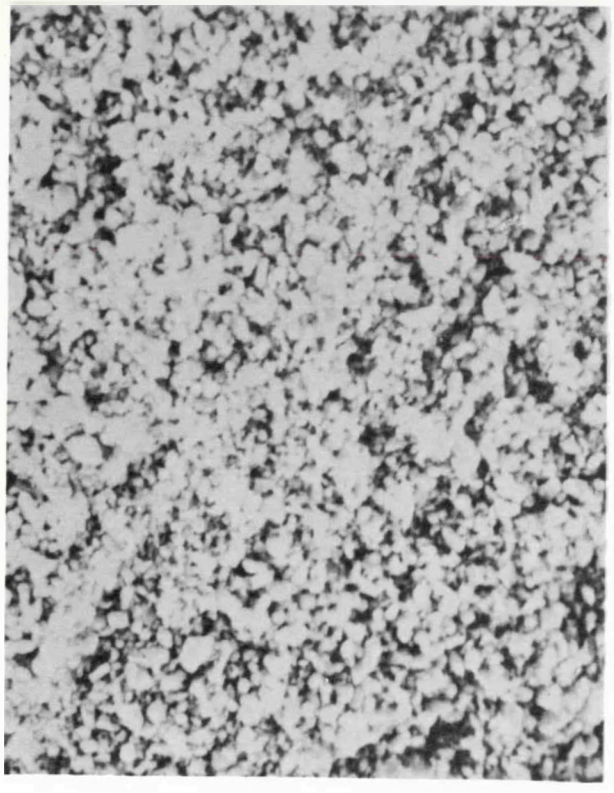

1000 x

General Refractories

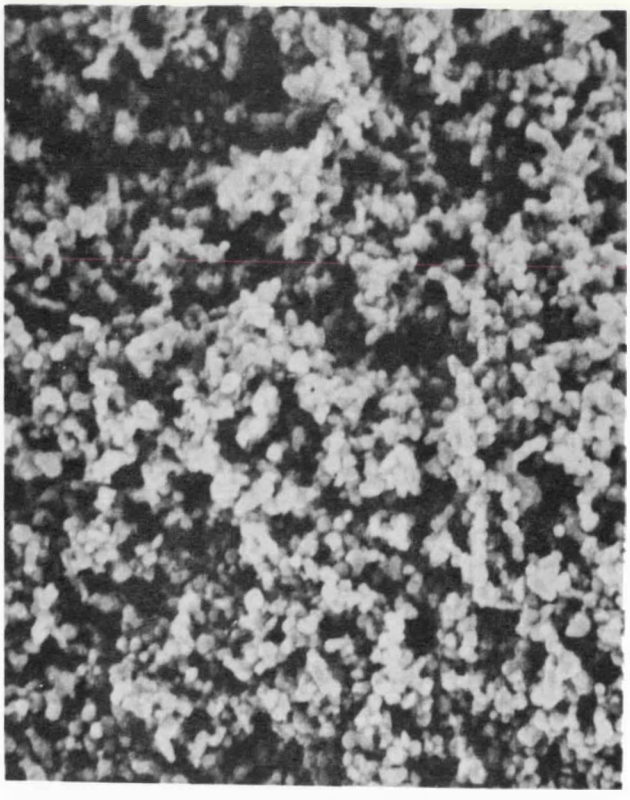

1000 x

Transtech

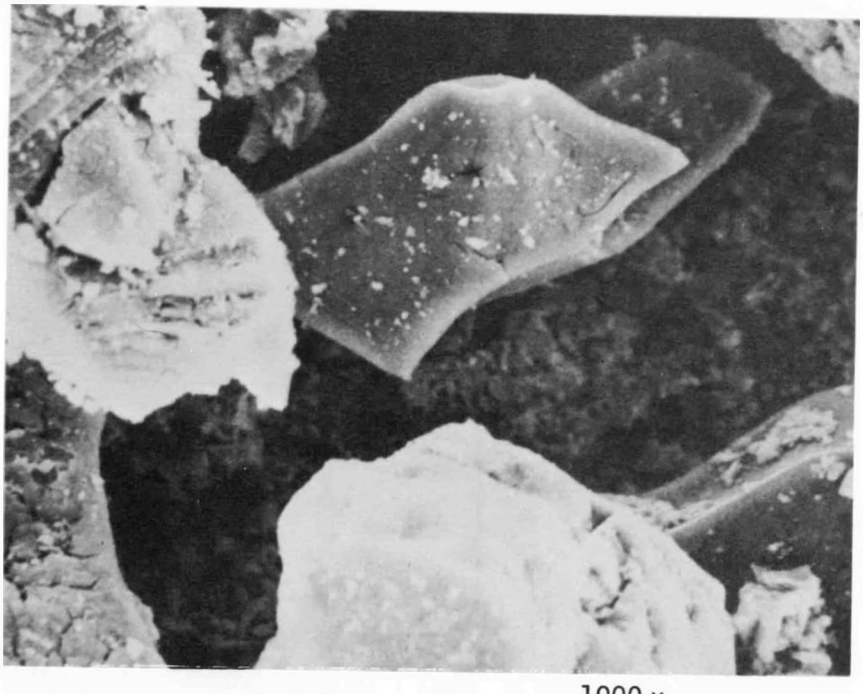

1000 x

A-T Research

Figure 17. SEM Microphotographs of $La_{.95}Mg_{.05}CrO_3$ Powder From Three Different Vendors

$La_{.95}Mg_{.05}Al_{.15}Cr_{.85}O_3$
(A-T Research)

1000 x

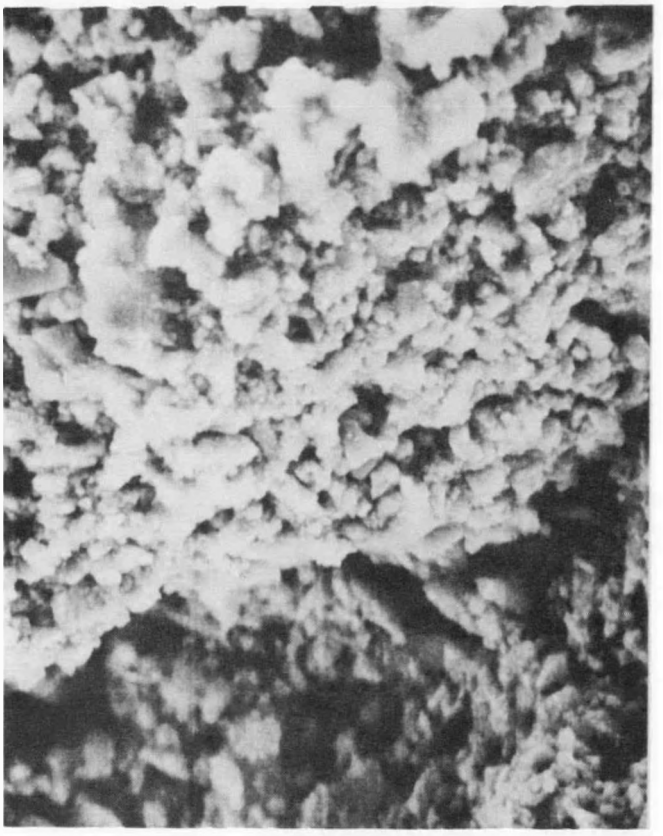

$La_{.95}Mg_{.05}Al_{.5}Cr_{.5}O_3$
(A-T Research)

1000 x

Figure 18. SEM Microphotographs of $La_{.95}Mg_{.05}CrO_3$ With Amounts of $LaAlO_3$ Substitution

shape of each of the two powders at 1000 x. The powder with the greater percentage of Al has much larger grains present and has a more angular shape. The powder with the lesser percentage of Al is spherical and smaller in overall size.

Insulator Microstructures

The microstructure of the interelectrode insulators used in the U-02 Proof Tests are shown in Figure 19. Both the spinel and MgO from Transtech are ~97% of theoretical density whereas the MgO from Norton is only 86% of theoretical. The density difference between the MgO types contributes to their contrasting microstructures. The denser MgO (Transtech) has a fused cast type structure, with the pores dispersed and isolated from each other within the grains. The mode of fracture is primarily transgranular. The other MgO type (Norton) has a large amount of intergranular porosity which is open throughout the structure. This results from the bimodel particle size distribution of the starting (fused) powders, i.e., relatively coarse grains surrounded by a matrix of smaller grains. The spinel insulator exhibits primarily intragranular fracture, with the grain size smaller than the dense MgO. It has the majority of its porosity at triple points or grain boundaries between small dense particles which are fused together.

Thermal Conductivity

Thermal conductivity measurements were made on a number of materials being tested in the U-02 Phase III Proof Tests. These measurements were conducted at Battelle-Northwest using a laser pulse technique.

Figure 20 depicts the thermal conductivity curves for electrode materials being tested in Proof Tests 2 and 3. Notice the large fluctuation of the 0.5 $SrZrO_3$ - 0.5 $La_{.95}Mg_{.05}CrO_3$ curve at the lower temperatures. This is most likely due to a phase change in the $SrZrO_3$ portion of the material. $La_{.95}Mg_{.05}CrO_3$ + 30 w/o ZrO_2 shows the least amount of conductivity change across the temperature range. Figure 21 shows the changes in thermal conductivity of the same material as the amount of ZrO_2 (Y_2O_3 stabilized) is decreased.

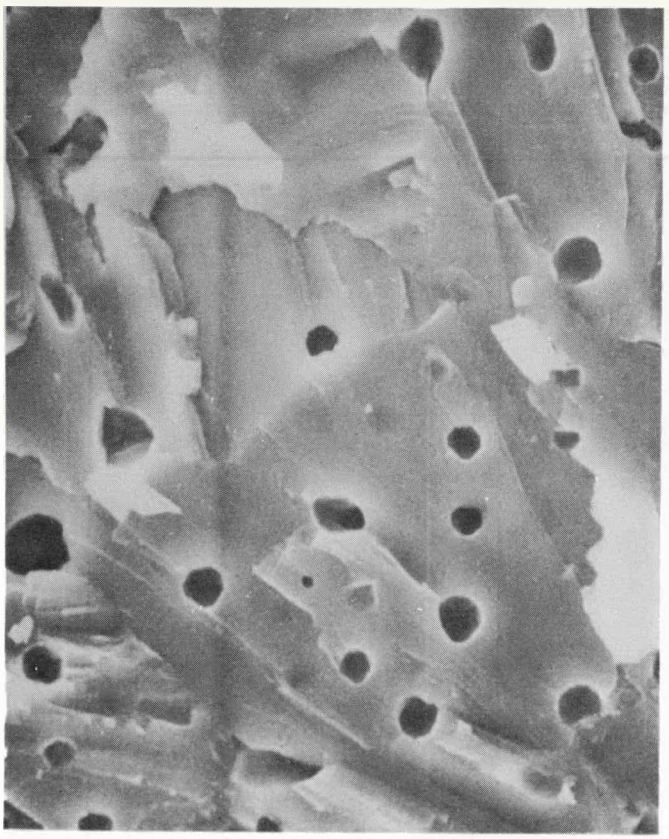

1500 x

MgO (Transtech)

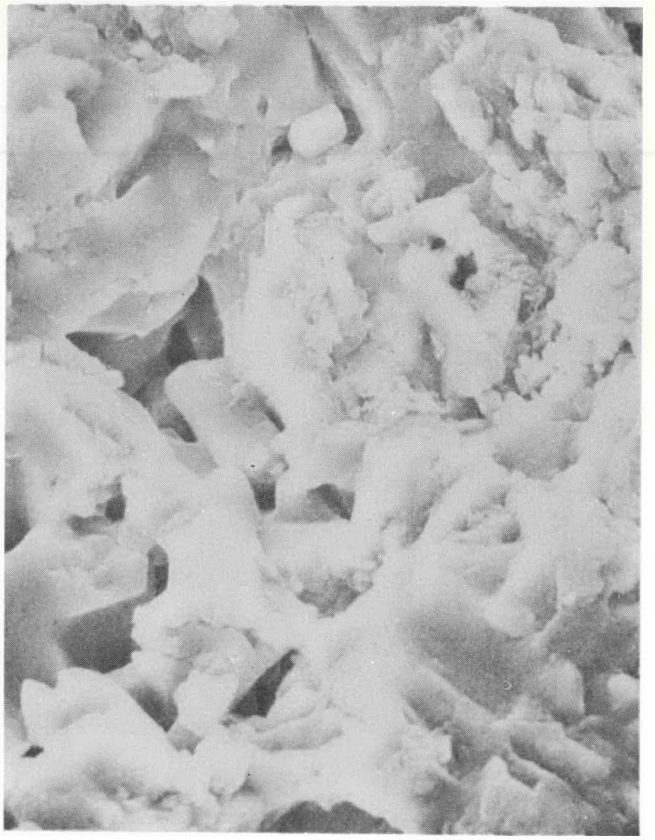

1500 x

MgO (Norton)

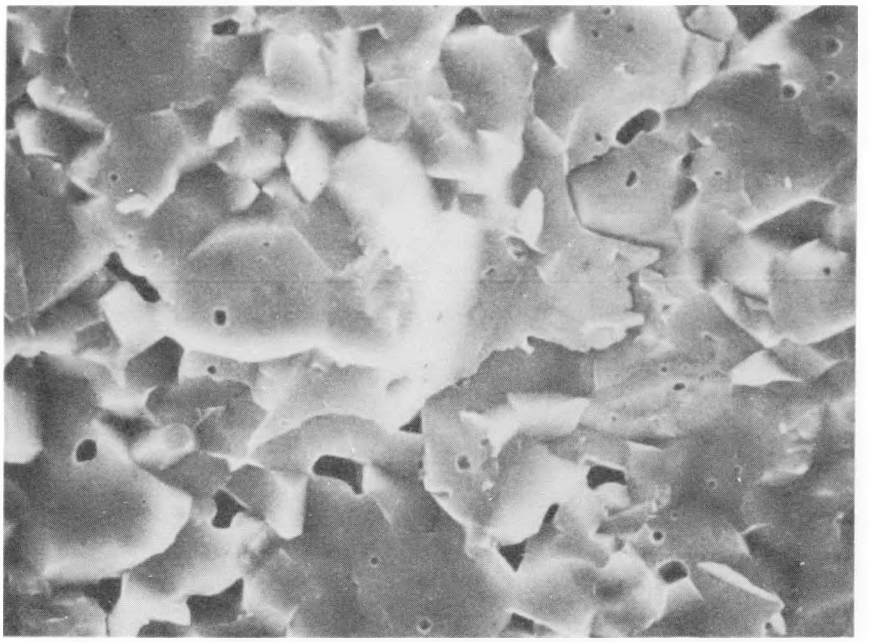

1500 x

Spinel (Transtech)

Figure 19. SEM Microphotographs of Fractured Surfaces of Interelectrode Insulators Used in U-02 Proof Tests

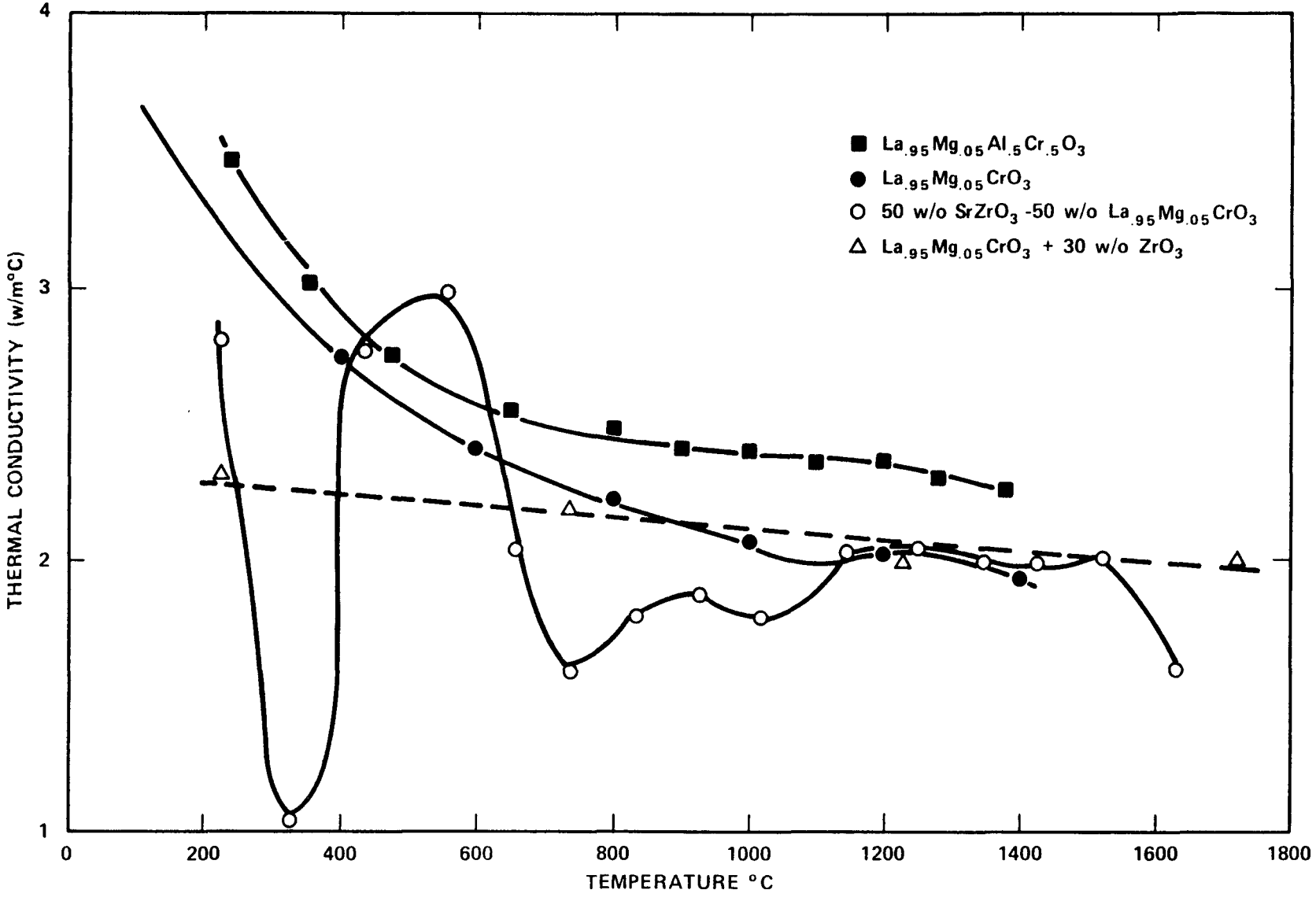

Figure 20. Thermal Conductivity of Electrode Materials Tested in U-02 Proof Tests No. 2 and 3. Data Taken by Battelle-Northwest

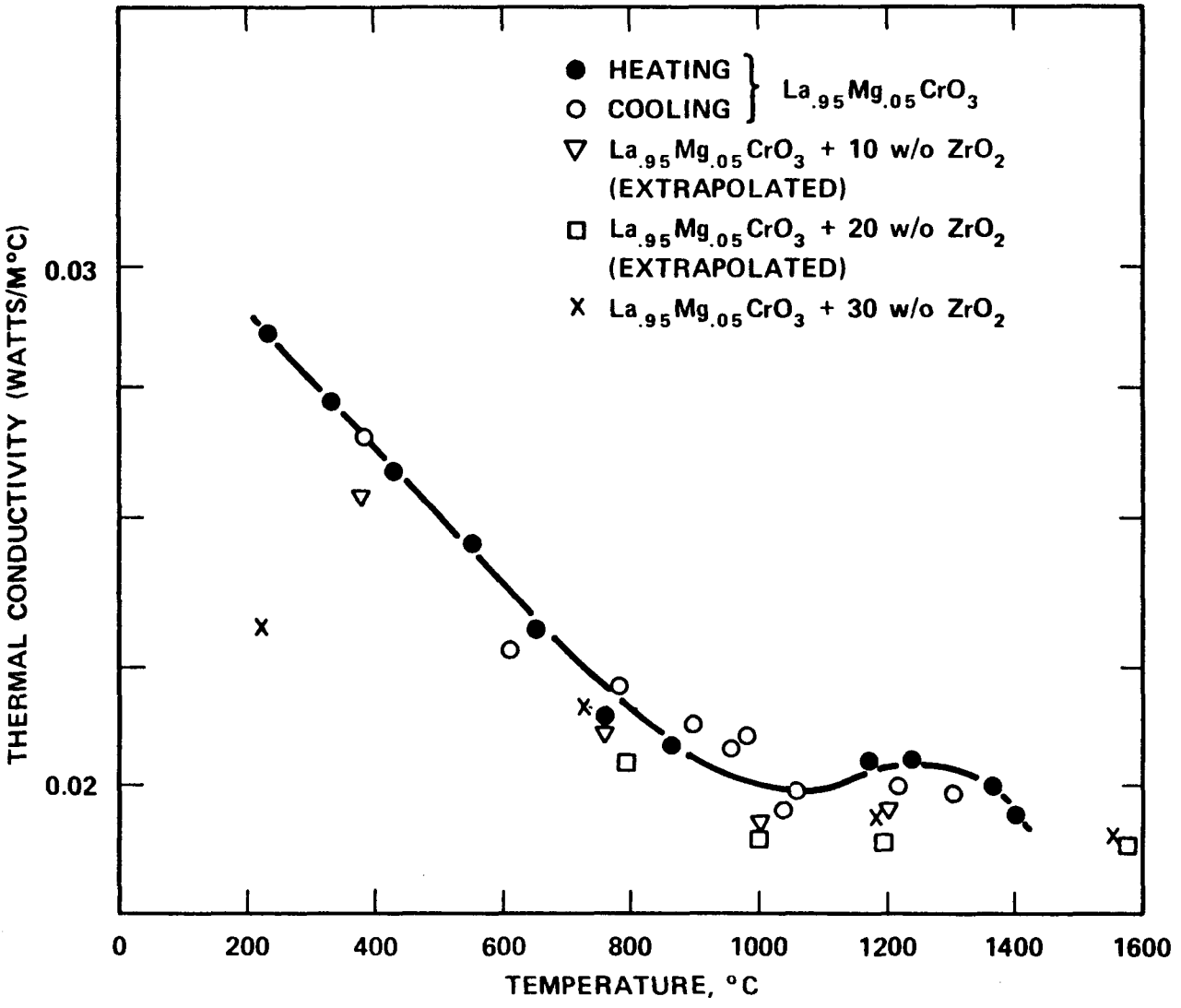

Figure 21. Thermal Conductivity of $La_{.95}Mg_{.05}CrO_3$ + Increasing Amounts of Dispersed ZrO_2. Data Taken at Battelle-Northwest

The thermal conductivity of the two primary candidate interelectrode materials are shown in Figure 22. Both materials are approximately 97% of theoretical density.

Electrical Conductivity

The electrical conductivity of electrode and insulator materials were determined by the National Bureau of Standards using a dc four probe technique. Data was measured at 10^{-3} O_2 in N_2 to simulate the partial pressure of oxygen in an actual MHD environment.

Figure 23 shows the electrical conductivity of $La_{.95}Mg_{.05}CrO_3$ with varying amounts of dispersed ZrO_2. Some of the curves have been extrapolated due to the lack of conductivity data in certain temperature ranges. For all four materials the conductivity drops off significantly at the lower temperatures. Fortunately, the design of the electrode assemblies calls for the backface of the electrodes to see a temperature greater than 250°C, which is high enough to obtain a conductivity adequate for the intended current passage.

Figure 24 gives a different perspective of the same materials. The conductivity is plotted vs. the w/o ZrO_2 dispersed in $La_{.95}Mg_{.05}CrO_3$ showing decreasing conductivity as either the temperature decreases or % ZrO_2 is increased.

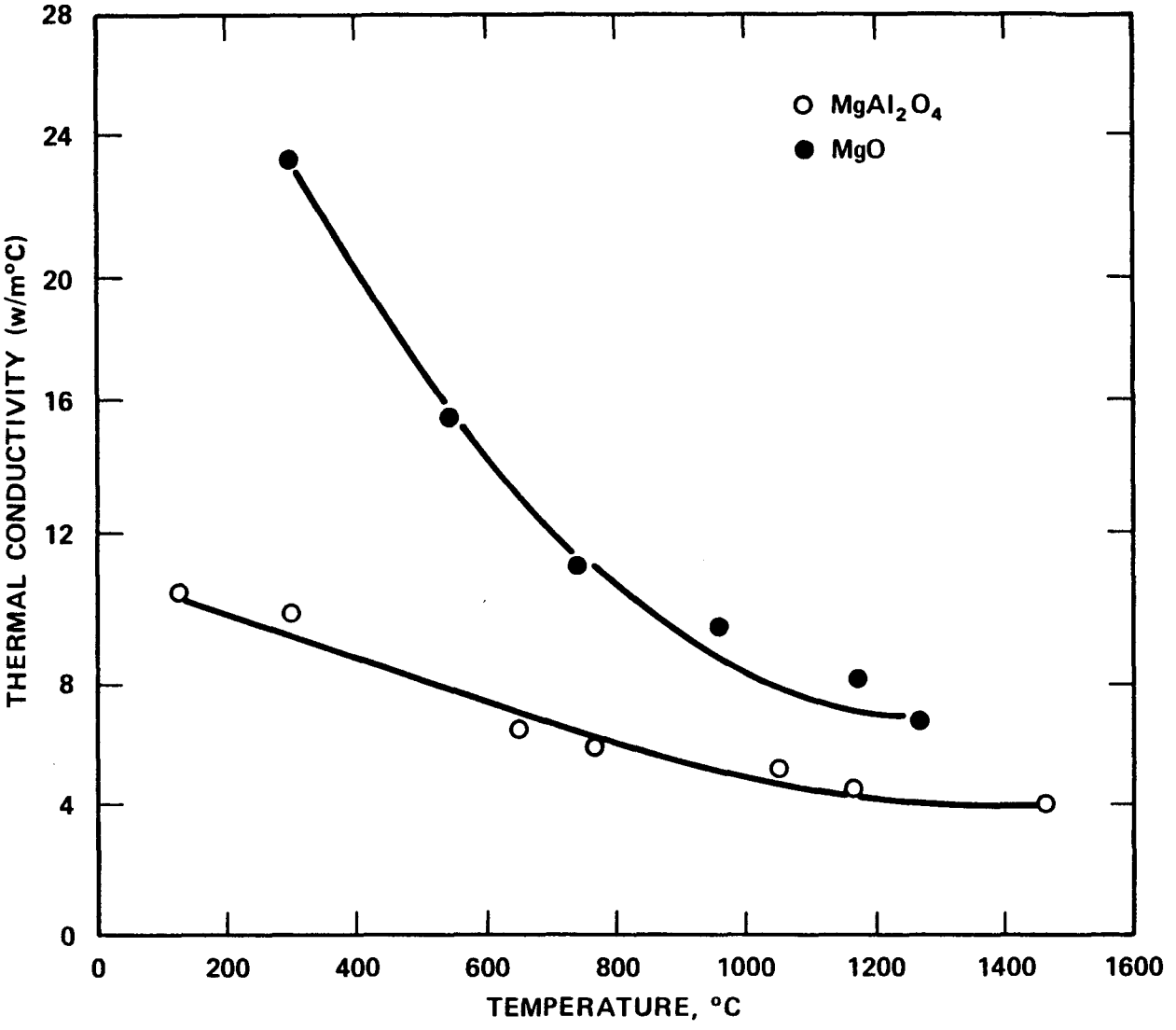

Figure 22. Thermal Conductivity of MgO and $MgAl_2O_4$ Insulators to be Used in U-02 Phase III Test. Both Materials Sintered to 97% of Theoretical Density by Transtech.

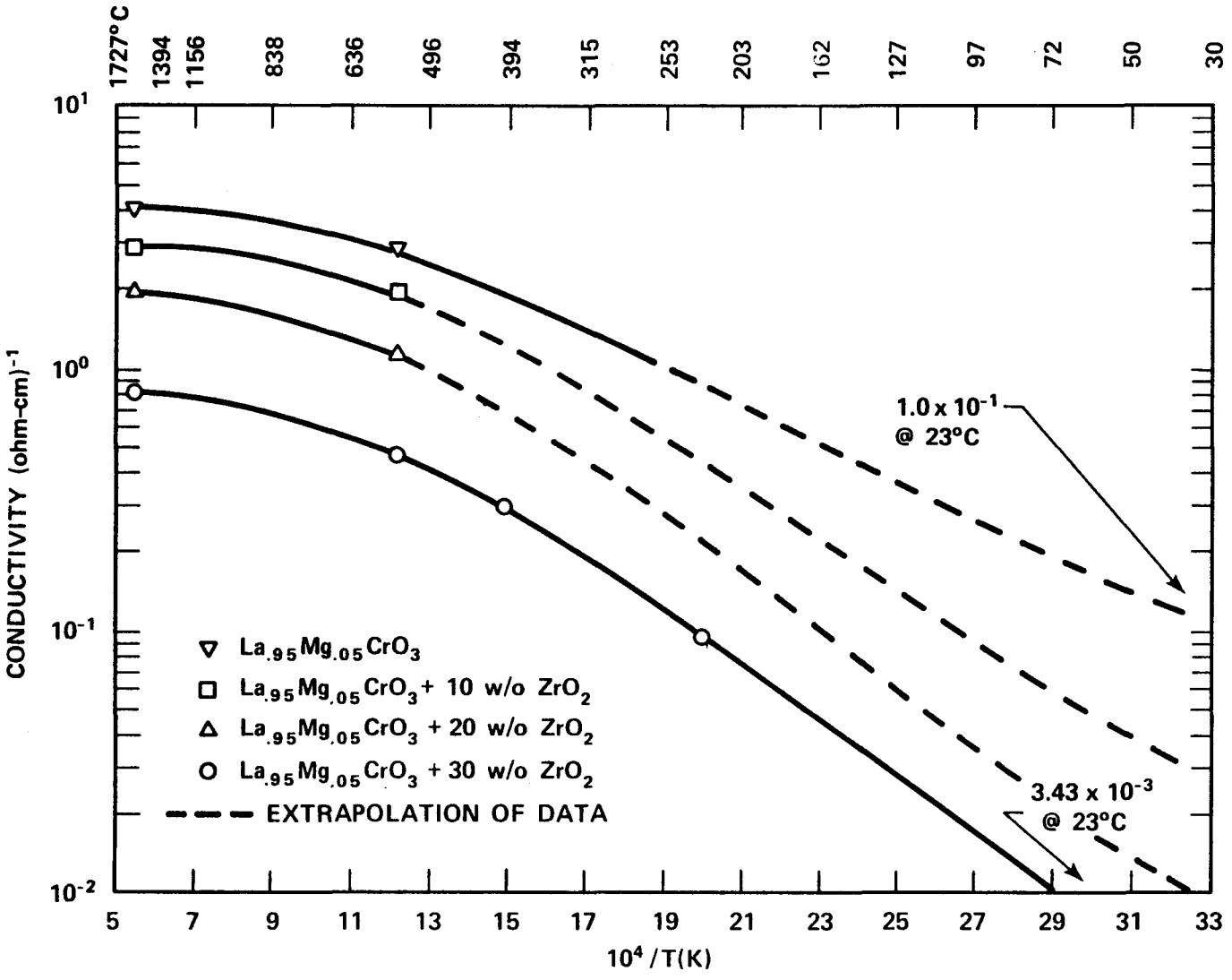

Figure 23. Electrical Conductivity of $La_{.95}Mg_{.05}CrO_3$ + Increasing Amounts of Dispersed ZrO_2. Data Taken at 10^{-3} O_2 in N_2 by NBS. Material Hot-Pressed at 1650°C and 4000 psi

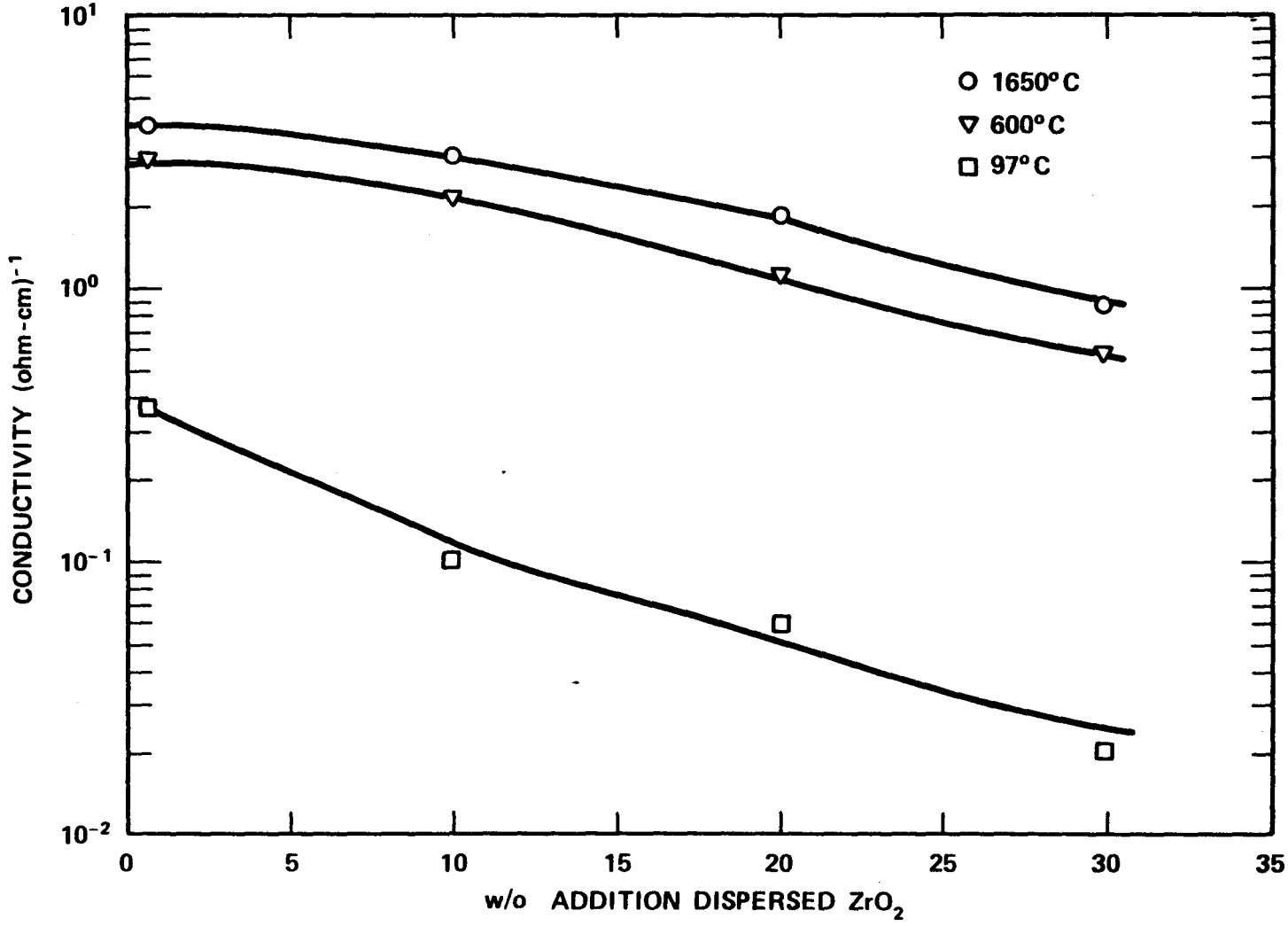

Figure 24. Electrical Conductivity of $La_{.95}Mg_{.05}CrO_3$ with Increasing Amounts of Dispersed ZrO_2 at a Number of Different Temperatures. Data Taken at 10^{-3} O_2 in N_2.

5.2.2 U-02 Proof Tests

The U-02 Proof Tests were structured to allow evaluation of:

- General resistance of electrode sytstems to high temperature and corrosive conditions,
- electrode system thermal design, interface temperatures and heat flux and
- electrical performance of electrodes and interelectrode insulators.

Table 12 presents a brief comparison of pertinent facility characteristics while Figure 25 shows the electrode/test section configuration for U-02 and WESTF.

The proof tests were conducted in accordance with a Work Plan which included the general objectives, operating conditions, test philosophy and test procedure. This Work Plan was approved by the non-Westinghouse electrode suppliers. Test Monitors, selected by DOE-MHD, participated in and monitored the conduct of the proof tests.

During this quarter the following significant activities for the U-02 Proof Test Series were completed:

- Electrode thermal/structural design
- Fabrication and assembly of test sections for Proof Tests 1, 2 and 3
- Conduct of Proof Tests 1 and 2, including preparation of the Express Reports for these tests
- Post-test evaluation of facility operation and electrode thermal and electrical performance for Proof Tests 1 and 2, and
- Post-test material characterization for Proof Test 1.

Results of these activities are presented in the following sections.

5.2.2.1 Electrode System Design

Thermal Design

Thermal design analyses were completed to size the electordes to meet the thermal gradients expected in the U-02 Proof Test Series. The electrode

TABLE 12
COMPARISON OF U-02 AND WESTF

Parameter	U-02	WESTF
Fuel	Natural Gas	Toluene
Plasma Temperature, °K	2500-2600	2500-2600
Plasma Velocity, m/sec	400-500	∿450
Mass Flow Rate, kg/sec	∿0.7	∿0.1
Static Pressure, atm	∿0.9	∿1.05
Channel Dimensions, cm (w x h)	26.0 x 6.0	2.5 x 5.0
Number Electrode Pairs	36	12
Current Density, A/cm^2	0 to 1.25	1.25
Magnetic Field, T	1.5 - 1.7	None
Test Duration, hours	∿100	∿20

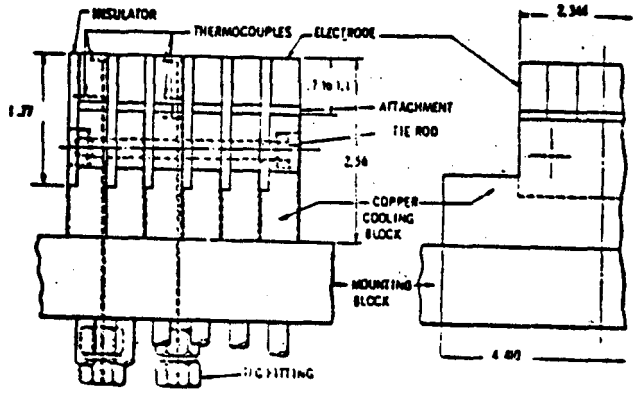

a) U-02 Electrode Assembly

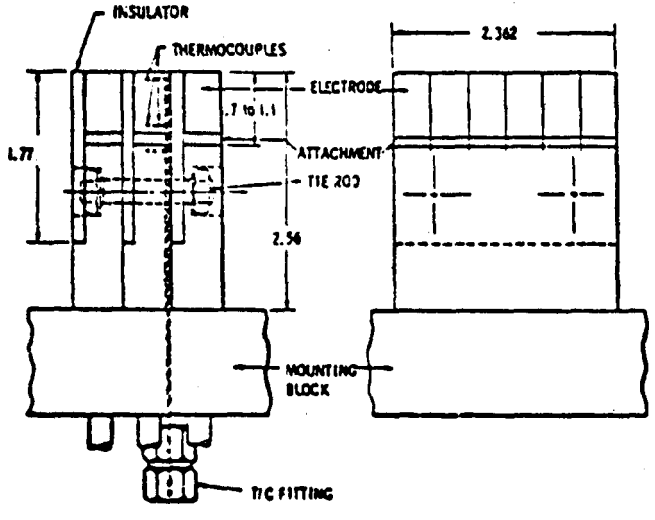

b) WESTF Electrode Assembly

Figure 25. U-02 and WESTF Electrode Assembly

analysis is a continuation of the analysis reported previously, Reference 11.

Five electrodes were analyzed as follows:

1) Graded lanthanum chromite, with alumina, (graded from $La_{.95}Mg_{.05}Cr_{.85}Al_{.15}O_3$ to $La_{.15}Mg_{.05}Cr_{.68}Al_{.32}O_3$), epoxy compliant layer, magnesium oxide (MgO) insulator.
2) MAFF-31 electrode graded to an approximately 7 mm thickness of hercynite ($FeAl_2O_4$) interface layer, spinel insulator
3) Ceramic electrode with 1 mm thick zirconia cap (.12 CeO_2 - .03 Y_2O_3 - .85 ZrO_2), 0.5 mm thick mixture of 50% zirconia and 50% lanthanum chromite intermediate layer, followed by pure lanthanum chromite, 0.25 mm thick METCO-447 (.895 Ni - .05 Mo - .055 Al) interface layer, spinel insulator
4) Ceramic electrode with 1.5 mm thick zirconia cap, 1 mm thick 66% zirconia - 34% lanthanum chromite - aluminate ($LA_{.95}Mg_{.05}Cr_{.8}Al_{.2}O_3$ for simplicity called LC) layer, 1 mm thick 34% zirconia - 66% LC layer, followed by pure LC layer, with a spinel insulator, epoxy compliant layer
5) Ceramic electrode consisting of a uniform composition of lanthanum chromite/strontium zirconate ($SrZrO_3$), epoxy compliant layer, spinel insulator.

The electrode configurations for designs 1, 4 and 5 are shown on Figure 26. Designs 2 and 3, however, have arc-plasma sprayed insulators along both sides and over the entire length of the electrode (from the plasma surface to the end of the copper heat sink).

All of the above design analyses included the effect of Joule heating. Since the Joule heating varies directly with the electrical resistivity, those electrode materials with the largest resistivity have the largest amount of Joule heating. Design 1 used a lanthanum chromite-aluminate material, which had a resistivity as high as 5 to 10 ohm-cm in the temperature range used in this analysis. As a result, the Joule heating contribution was significant, with temperature increases

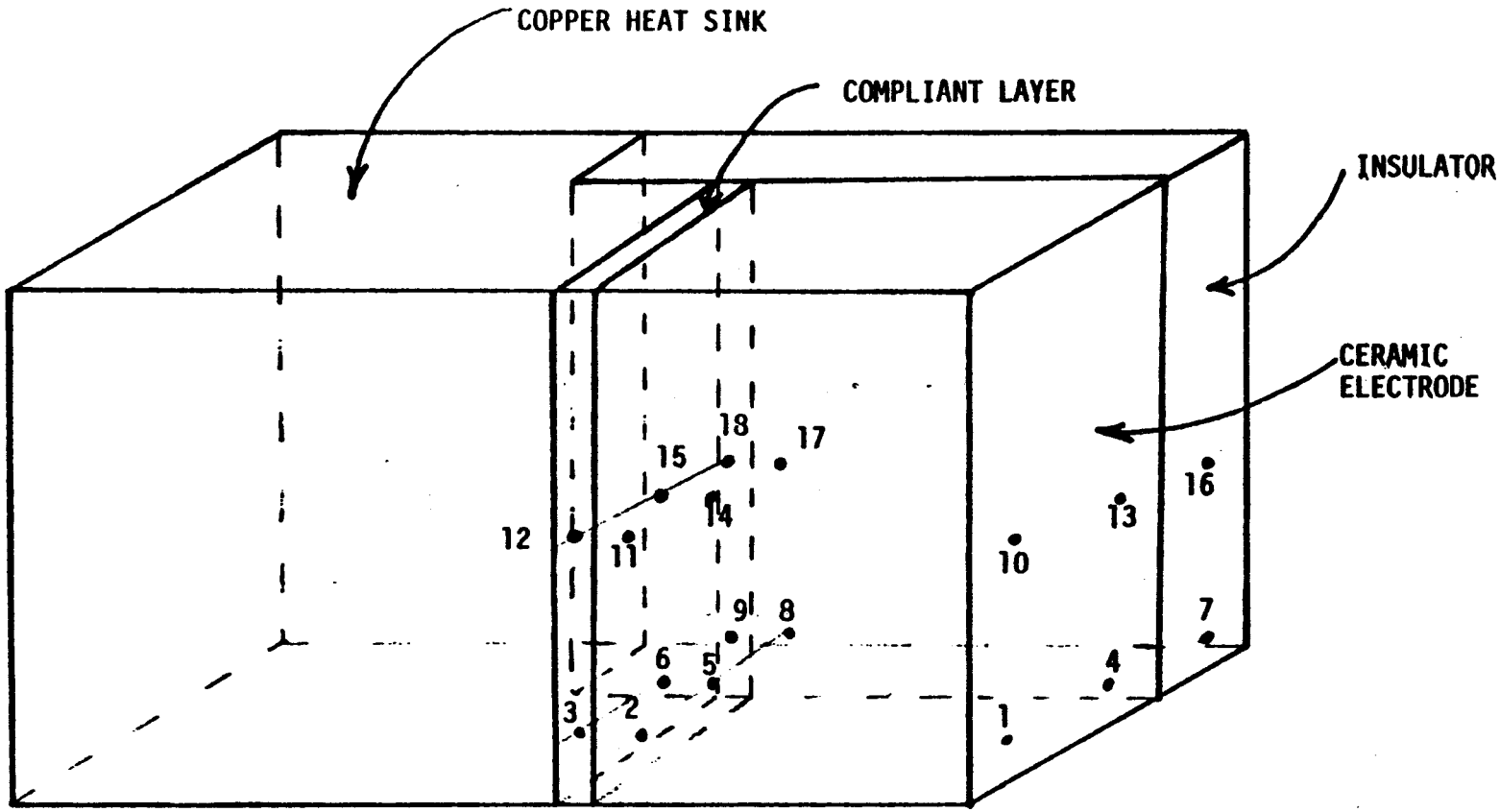

1, 4, 10, 13	-	Electrode surface facing plasma
7, 16	-	Insulator surface facing plasma
2, 5, 11, 14	-	Electrode - compliant layer interface
3, 6, 12, 15	-	Copper - compliant layer interace

Figure 26. Locations of Tabulated Temperatures

of about 100°C through the electrode. Design 4 used a more electrically conductive lanthanum chromite-aluminate mixture together with a zirconia cap, resulting in a peak resistivity of approximately 3 ohm-cm. This reduced the Joule heating temperature rise to about 80°C.

The electrode materials used in designs 2 and 3 had lower electrical resistivities than those used in designs 1 and 4, which tended to reduce the Joule heating. Design 2 used MAFF-31 which had a peak resistivity of 3 ohm-cm at 800°C but a more rapid reduction in resistivity with increasing temperature than design 4. This resulted in a Joule heating temperature rise of about 60°C. Design 3 used a low resistivity lanthanum chromite material (approximately 0.4 ohm-cm) together with a small zirconia cap. This resulted in about a 20°C temperature rise due to the Joule heating.

Design 5 used a moderately resistive $LaCrO_3/SrZrO_3$ mixture, with a resistivity of about 2 ohm-cm at 300°C, and decreasing rapidly to about 0.5 ohm-cm at 1200°C. This resulted in about a 20°C rise due to Joule heating.

In order to meet the design requirements, the resulting electrode lengths and temperatures are as follows:

ELECTRODE	COMPONENT	LENGTHS (cm)	LENGTHS (in.)	CALC. TEMP. (°C) ℓ	CALC. TEMP. (°C) Edge
1	Graded $LaCrO_3/LaAlO_3$	2.692	1.06	1732	1652
	MgO insulator	5.258	2.07	1416	1355
	Epoxy compl. layer	0.0254	0.01	180	172
2	APS MAFF-31 electrode	1.280	0.50	1755	1660
	Spinel insulator	6.502	2.56	1640	1580
	Hercynite interface layer	0.701	0.276	690	680
3	APS Capped $LaCrO_3$ electrode	1.626	0.64	1740	1652
	Spinel insulator	6.502	2.56	1620	1580
	METCO-447 interface layer	0.0254	0.01	70	66
4	Capped $LaCrO_3/LaAlO_3$	2.083	0.82	1750	1674
	Spinel insulator	4.648	1.83	1580	1520
	Epoxy compl. layer	0.0254	0.01	172	157
5	$LaCrO_3/SrZrO_3$ electrode	2.362	0.93	1745	1654
	Spinel insulator	4.928	1.94	1571	520
	Epoxy compl. layer	0.0254	0.01	172	164

The notations "℄" and "edge" refer to the temperatures at the vertical center and at the edge (interfacing with the channel insulating wall) of the electrode. For the insulator and electrode, the temperatures given are for the plasma-ceramic interface. For the compliant or interface layers, the temperatures stated are for the bond region between the electrode ceramic and the compliant or interface layer.

From these results and from those in Reference 11, it would appear that an average resistivity greater than about 1.5 ohm-cm would generate Joule heating temperature rises of greater than 50°C for the present electrode configurations and currents.

A check was also made on the temperatures generated using the TAP-A model (Reference 12) by comparing them with the finer mesh WECAN Model (Reference 13). The system analyzed was a lanthanum chromite electrode, bonded to the copper heat sink with a nickel mesh compliant layer and a spinel insulator. For this analysis, the effects of Joule heating were not considered.

Figure 26 is a schematic of the electrode, along with the numbering system used to compare the temperatures predicted by both models. The following table is a summary of the results obtained using both models.

TEMPERATURE COMPARISON (°C), WECAN VS. TAP-A

LOCATION	1	2	3	4	5	6	7	8	9
WECAN	1652	219	76	1634	228	77	1495	280	196
TAP-A	1670	232	74	1655	243	75	1478	314	236

LOCATION	10	11	12	13	14	15	16	17	18
WECAN	1734	220	76	1711	229	76	1547	281	197
TAP-A	1747	233	74	1730	243	74	1540	313	236

As can be seen, the temperature predictions from TAP-A and WECAN agree fairly closely, except for locations 8, 9, 17 and 18. These locations are in the inter-electrode insulator, near the epoxy compliant layer. The disparity can be explained by the difference in mesh sizes used in the TAP-A and WECAN models,

and also in the way material properties are entered. TAP-A uses a table to enter the material properties, and linearly interpolates between the points. The properties in WECAN must be entered using a sixth-order polynomial equation as a curve fit. This equation should be generated with care, since at regions away from the points used to generate this polynomial there could be large differences between the computed and the actual material properties. This is especially true if extrapolation is necessary outside the boundary points used to generate the polynomial. For this case, below 400°C the spinel thermal conductivity used in WECAN was about 20% larger than the value used in TAP-A, which apparently resulted in lower temperatures being predicted by the WECAN model.

These comparative analyses demonstrate that the simpler TAP-A model can be used with confidence for thermal analyses to size MHD electrodes.

Structural Design

Further structural analyses were completed to evaluate the use of $MgAl_2O_4$ and MgO as interelectrode insulators. The assumptions and methods employed were the same as those outlined in Reference 11. Material properties are shown in Figure 27. Subsequent data for plasma sprayed $MgAl_2O_4$ indicates that the data of Figure 27b is high, thus, this should produce conservatively computed thermal stress levels. Yield strength data was not available.

The thermal stress analysis was performed using the WECAN finite element computer code. The same finite element grid was used for the analysis of both insulator materials and the insulator thickness was assumed to be identical for MgO and $MgAl_2O_4$. The computer model analyzed for both cases corresponded to that of the "Eagle Picher" graded Lanthanum Chromite electrode with a ZrO_2 cap.

Prior analyses indicated the desirability of using an insulator which is traction free and contains five vertical cuts introduced at the base terminating just below the attachment bond. The computer model used for both material cases evaluated is shown in Figure 28. Symmetry of the thermal gradients has been

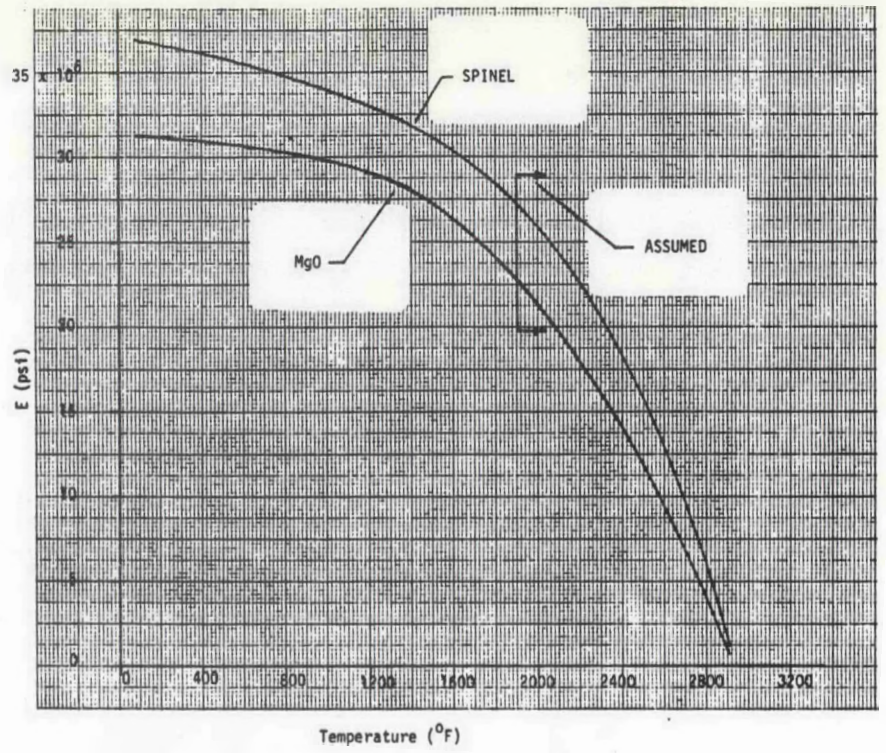

a. Young's Modulus

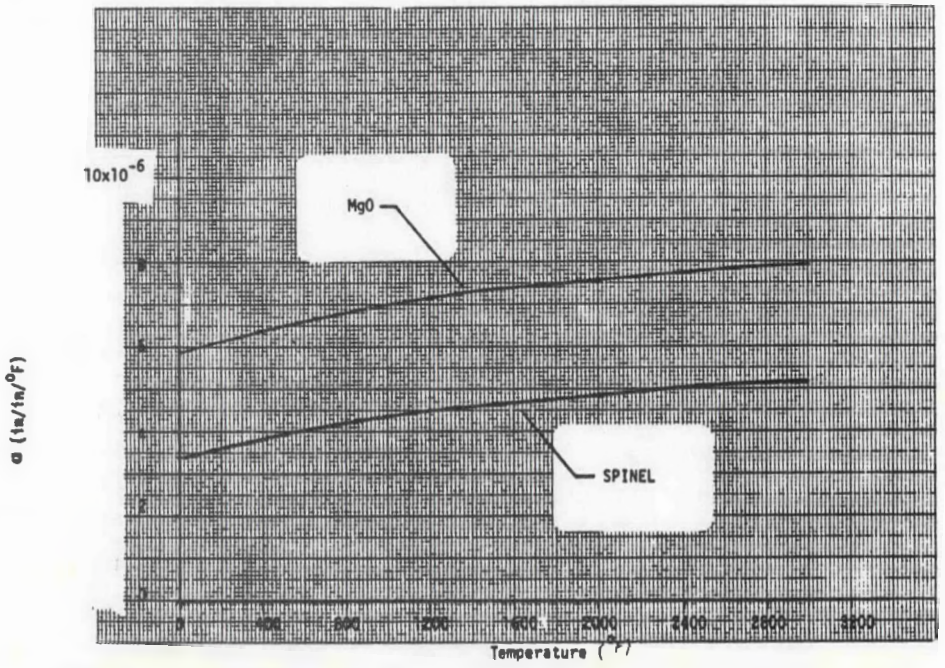

b. Coefficients of Thermal Expansion (Stress Free Temperature of 70°F)

Figure 27. Insulator Material Properties

taken advantage of in that only one-half of the insulator was modeled. The nodes along the symmetric boundary above the cut elevation of 1.674 in. were fixed in the x-direction to simulate this symmetry.

The resulting thermal gradients for both materials are shown in Figure 29. Note that the MgO insulator operates at a lower temperature level than the $MgAl_2O_4$ insulator.

The displacement plot for the insulators is shown in Figure 30 for the two material cases. Becuase of a greater expansion coefficient, the MgO insulator is shown to experience larger thermal distortion than the $MgAl_2O_4$. The thermal expansion across the insulator hot face would be 2 x 0.019 or 0.038 inches for the MgO versus 0.030 inches for the $MgAl_2O_4$. The relative displacement shown at the cuts along the insulator base indicates the degree of potential interference and therefore the required cut thickness. The required cut thickness is 0.003 in. minimum for the $MgAl_2O_4$ and 0.004 in. minimum for the MgO.

The X and Y direction stresses are shown in Figures 31 and 32 for the two material cases. The stress patterns are very similar for the two materials; however, in all cases the magnitude of the MgO stress was found to be greater than for the Spinel. Note that in the lower region of the insulators, where holes would be drilled in order to provide for the electrode bolting, the X and Y stress levels are low which is desirable.

The maximum stress intensity, shown for the two material cases in Figure 33, is defined as twice the magnitude of the maximum shearing stress. It represents a definition of stress which is frequently compared with an allowable level of normal stress in order to evaluate component structural integrity. The peak level of Spinel insulator maximum stress intensity is shown to be about 14,500 psi. The temperature at this location is shown in Figure b to be about 750°F (399°C). The peak level of MgO insulator maximum stress intensity is shown to be about 20,800 psi in Figure 29. Figure 29 indicates the temperature here to be about 600°F (316°C). Again the MgO and Spinel insulator stress patterns are similar; however, the magnitude of the MgO insulator stress levels is greater than for the Spinel.

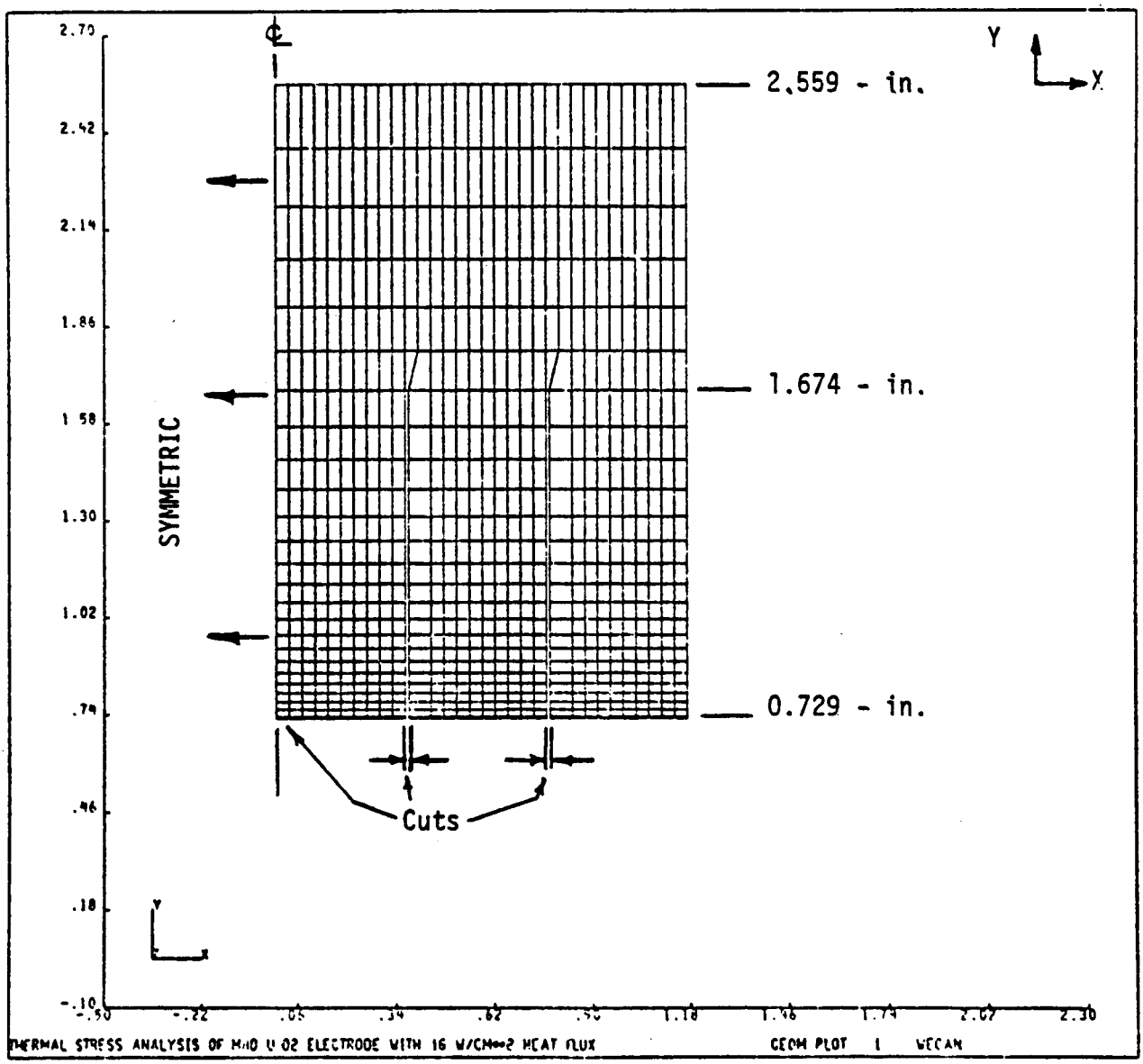

Figure 28. Finite Element Model of the Insulator for the Eagle Picher Graded Electrode

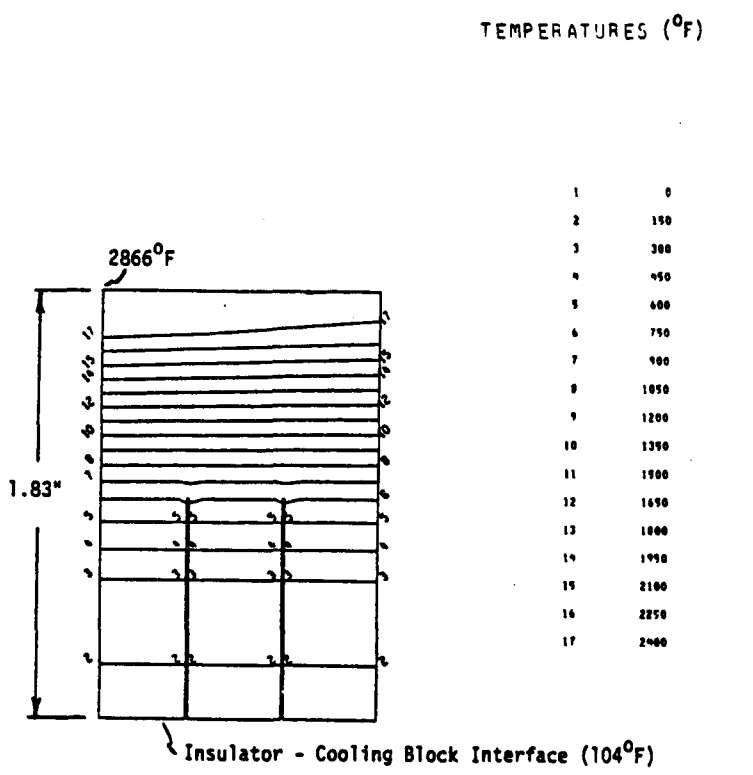

a. $MgAl_2O_4$ Insulator

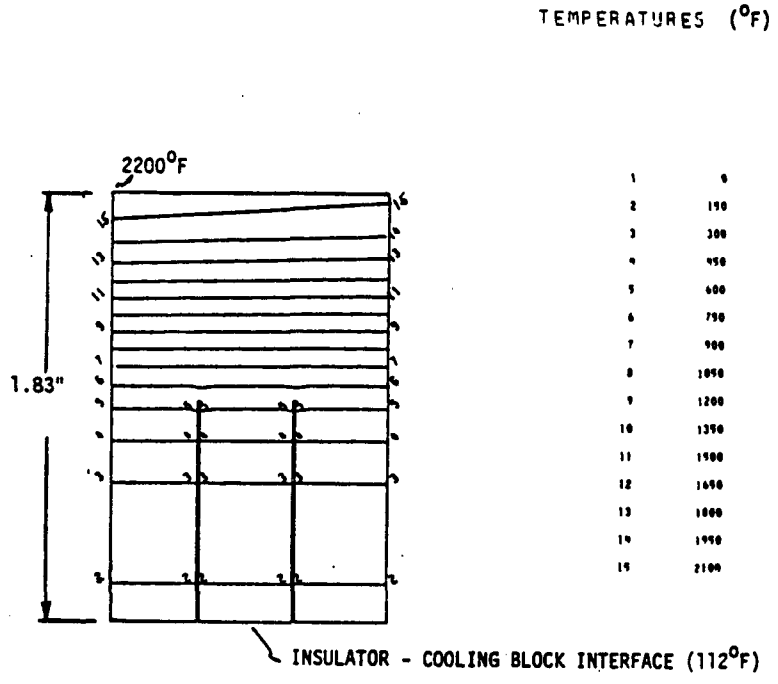

b. MgO Insulator

Figure 29. Insulator Thermal Gradients (Eagle Picher Electrode)

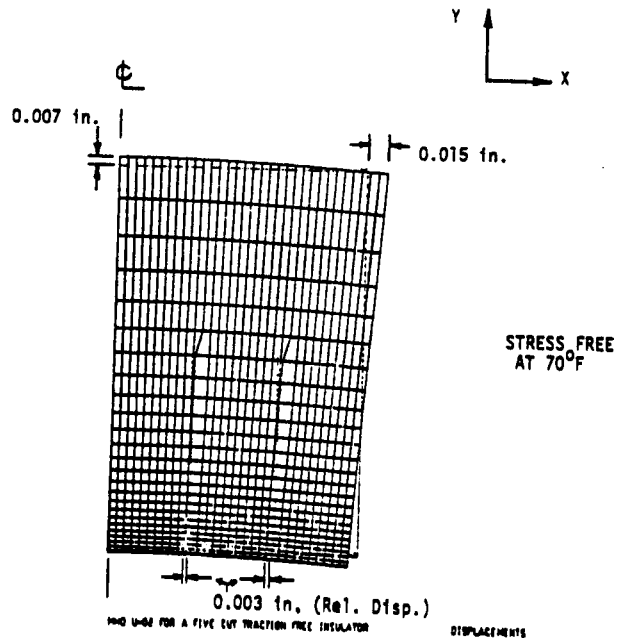

a. $MgAl_2O_4$ Insulator

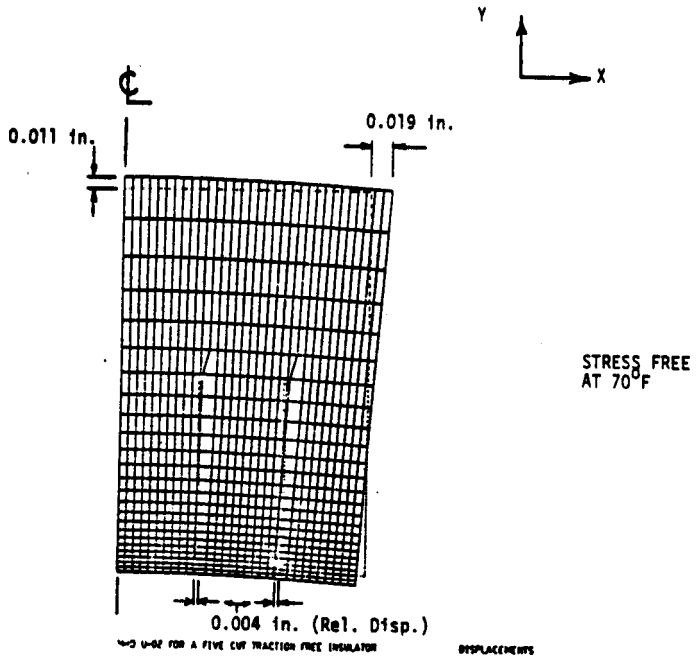

b. MgO Insulator

Figure 30. Insulator Displacement Plot

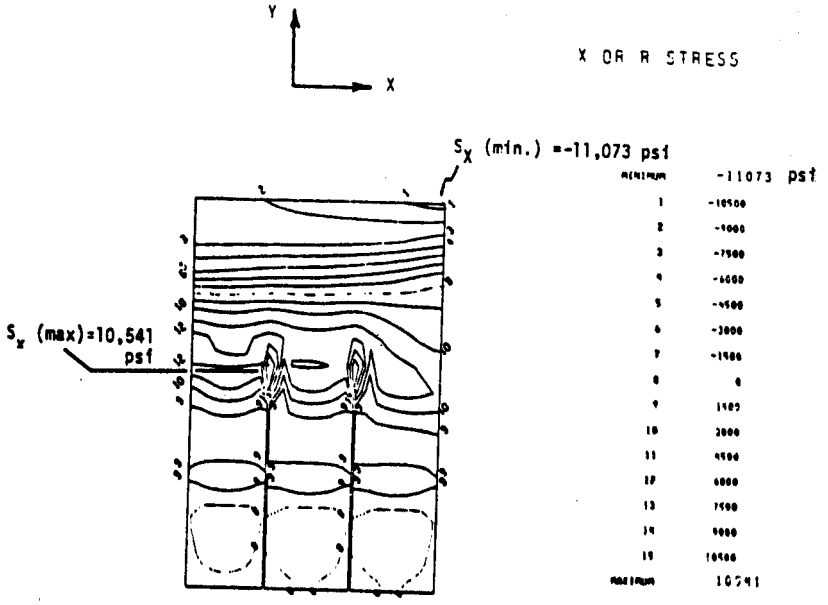

a. $MgAl_2O_4$ Insulator

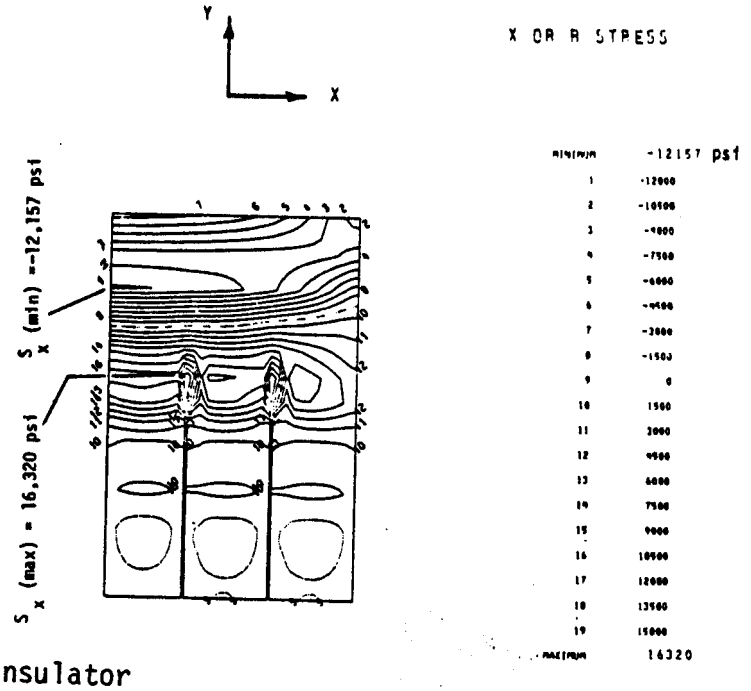

b. MgO Insulator

Figure 31. Stress in the X-Direction

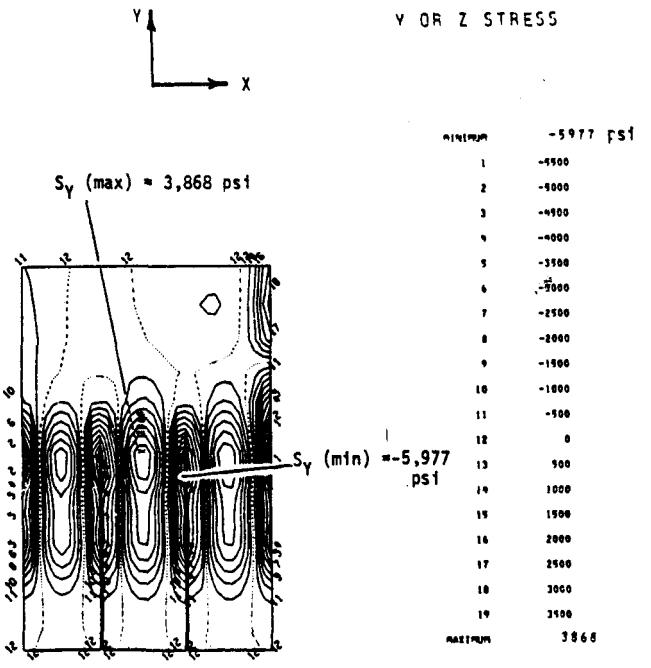

a. $MgAl_2O_4$ Insulator

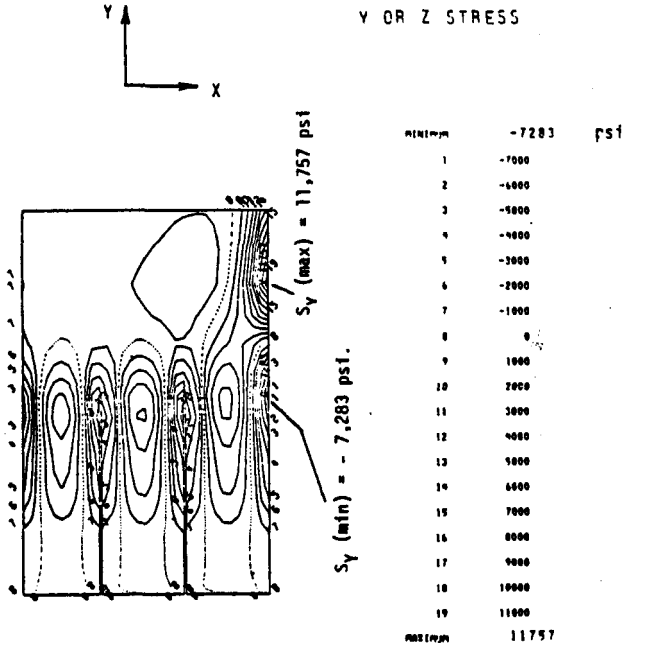

b. MgO Insulator

Figure 32. Stress in the Y-Direction

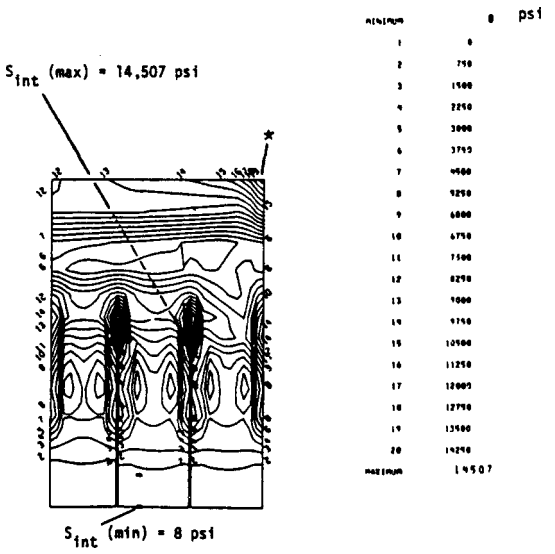

*S_{int} = 14,100 psi at 2725°F (probable location of minimum factor of safety)

a. $MgAl_2O_4$ Insulator

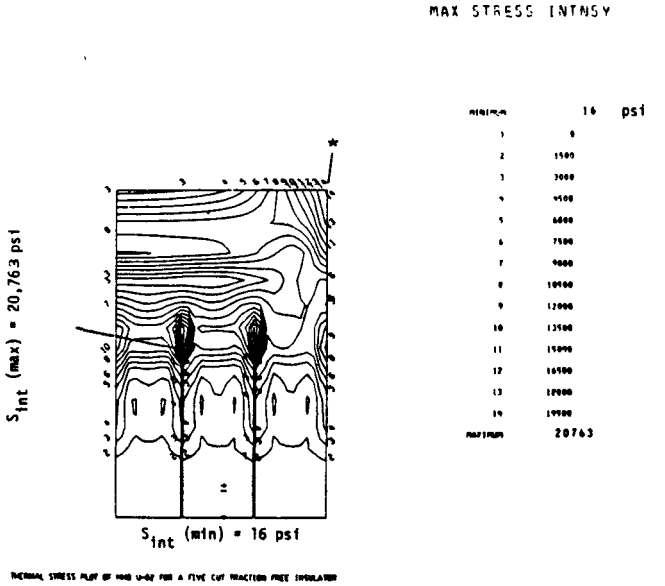

*S_{int} = 19,800 psi at 2136°F (probable location of minimum factor of safety)

b. MgO Insulator

Figure 33. Insulator Maximum Stress Intensity

The locations of probable minimum margin safety for each insulator material is also shown in Figure 29. The stress computed at these points appears to be in excess of the ultimate strength for both insulator materials. It should be noted, however, that because of the inability to account for the stress relief effects of inelastic deformation in this analysis, it is impossible to qualify or disqualify either MgO or Spinel as potential insulator materials. Only a relative comparison can be made between the two candidate materials. The ultimate strenght of MgO appears to be lower than that for Spinel (See Table 13). A comparison of the computed stress levels with the ultimate strength of these two materials indicates that Spinel is probably the structurally superior material for this application.

Since it is apparent from the material stress intensity plots that the peak stress levels occur in the region of the cut terminations, a fillet radius at the end of these cuts would eliminate any notch stress concentration effects. This could be accomplished by drilling small holes at the locations where the cuts terminate. Limitations of finite element analysis as applied to notched regions imply that the actual notch stresses could be greater than those computed. Elimination of a notch then would also serve to increase the credibility of the stresses computed at a cut termination.

The following conclusions and recommendations were drawn from these analyses:

- Use of Spinel ($MgAl_2O_4$) results in more favorable insulator stress distributions than use of Magnesium Oxide (MgO),
- The limitations of elastic analysis make it impossible to quality or disqualify either MgO or $MgAl_2O_4$ as a structurally adequate material for the present design.
- The MgO insulator has been found to operate at a considerably colder temperature level (2200°F) than the $MgAl_2O_4$ insulator (2866°F) for the same size insulator. This is of no structural advantage because the $MgAl_2O_4$ ultimate strength appears to be superior in the intended operating temperature range.
- The computed insulator stresses have been shown to be low in the colder regions of the insulator where the holes are located to accommodate the tie-bolt which holds the set of electrodes together.

TABLE 13. MATERIAL STRENGTH

Material (Reference)	Ultimate Strength (psi)
Spinel (Ref. 3)	23,100 at 70°F 27,100 at 1110°F (600°C) 15,400 at 1830°F (1000°C) 3,800 at 2550°F (1400°C)
MgO (Ref. 3)	8,380 at 70°F 10,000 at 1110°F (600°C) 6,800 at 1830°F (1000°C)

- Since the computed insulator stresses have been shown to be maximum in the region of the cut terminations, it would be advisable to eliminate any notch stress concentration effects at these locations by drilling small holes at the cut terminations in order to provide a fillet radius.
- The minimum insulator vertical cut thickness required to preclude potential interference between adjacent segments was found to be 0.003 inches for the $MgAl_2O_4$ and 0.004 inches for the MgO.
- Thermal expansion across the insulator hot face was found to be 0.030 inches for the $MgAl_2O_4$ and 0.038 inches for the MgO.

5.2.2.2 Fabrication

Proof Test 1 (WESTF Test 37)

The basic details of the construction of the test section used for the UO-2 proof test are essentially the same as for the hot wall test assembly discussed in the prior quarterly report (Reference 11). The materials used in constructing the channel, with the exception of the electrodes, are also essentially the same as for the hot wall test assembly. Therefore, a discussion of the fabrication of the proof test assemblies will be limited to the electrode wall proper.

The electrode walls for the first U-02 proof test consisted of three candidate materials (nine electrode pairs). There were also one upstream and two downstream quard electrode pairs of $La_{.95}Mg_{.5}CrO_3$ composition which were not considered a part of the test. The materials and their positions in the channel are shown in Figure 34. Top and side views of the anode wall are shown in Figure 35. The initial electrode pairs were supplied by General Electric and were composed of magnesium aluminate ferrous ferrite ($4MgAl_2O_4 \cdot 1Fe_3O_4$) as the ceramic electrode material and incorporated a proprietary "FLEXBED" construction as the electrode attachment/current lead-out.

These electrodes utilized two 0.17cm thick sintered spinel ($MgAl_2O_4$) insulators as inter-electrode insulation. The next three pairs of electrodes consisted of plasma sprayed MAFF ($3MgAl_2O_4 \cdot 1Fe_3O_4$) on a Hoskins 875 BRUNSBOND (Technetics Div., Brunswick Corp.) mesh attachment/leadout. The anodes were arc-plasma sprayed by APS Materials Inc. (Dayton, Ohio). Monolithic spinel ($MgAl_2O_4$) insulators, 0.35 thick, served as inter-electrode insulation. The final downstream

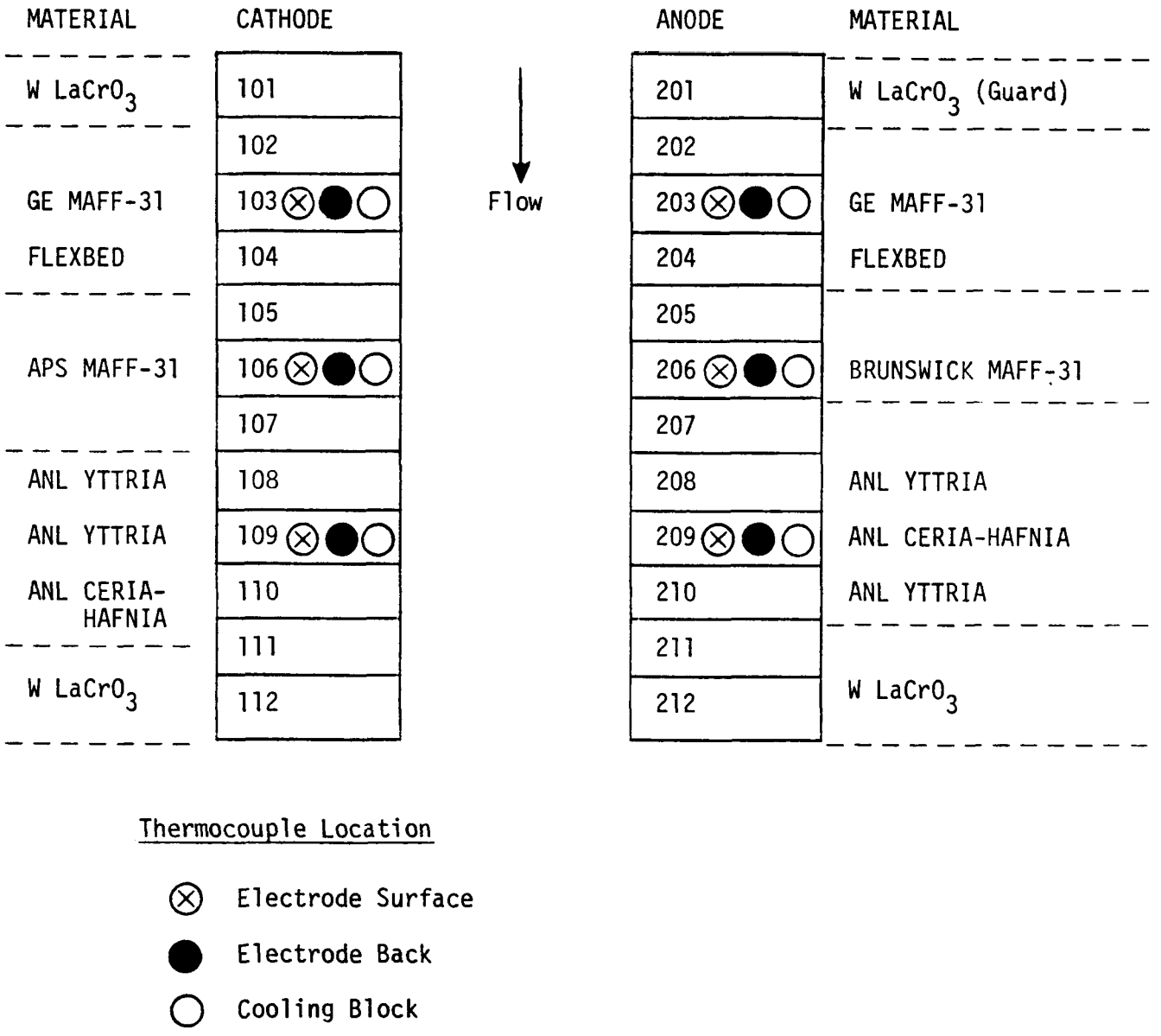

Figure 34. Material Positions in Proof Test 1 (WESTF Test 37)

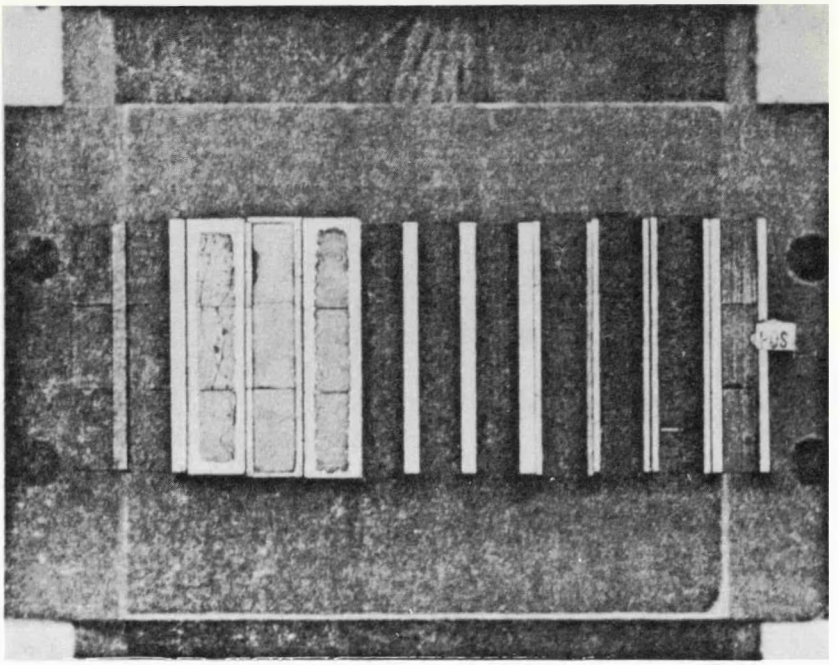

a. Top View

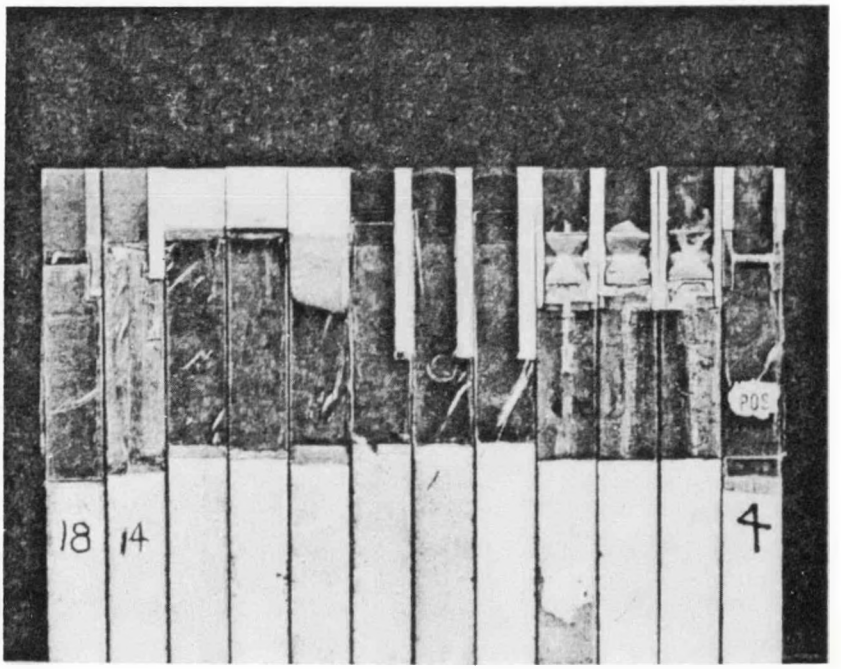

b. Side View

Figure 35. Anode Wall-Proof Test 1 (WESTF Test 37)

electrode pairs were supplied by Argonne National Laboratories (ANL) and were composed of two HfO_2 compositions and either a nichrome wire pad or a BRUNSBOND(R) metal mesh attachment. These electrodes were assembled in the following sequence:

- A composite structure is hot pressed consisting of HfO_2 - based powder throughout and a metal pad on the bottom.
- The HfO_2 metal pad composite base is subsequently brazed to BRUNSBOND(R) mesh which is brazed to the copper cooling block.
- $MgAl_2O_4$ is finally arc-plasma sprayed on all electrode side surfaces to provide interelectrode insulation.

Proof Test 2 (WESTF Test 38)

For Proof Test 2 the electrode walls included twelve active electrode pairs, reflecting four groups of electrode materials/designs. The electrodes were supplied by Westinghouse or by vendors working under the direction of Westinghouse. The materials and their position in the channel are shown in Figure 36. Top and side views of the cathode wall are shown in Figure 37.

The first or upstream three electrode pairs were zirconia-capped lanthanum chromite hot pressed by Eagle-Picher, and machined and assembled by Westinghouse to give an electrode composed of four or five segments with total dimensions of 6.0 cm (l) x 1.0 cm (w) x 2.1 cm (h). Attachment to the copper cooling block was made with 0.025 cm or less of silver-filled epoxy. The insulators, monolithic magnesia 6.0 cm (ℓ) x 0.35 cm (w) x 5.1 cm (h) and slotted at their base, are held in place by the tie rods and the polyimide tape that is used to insulate the copper blocks.

The second group of electrodes were zirconia graded to lanthanum chromite graded through a Ni-Mo-Al composition to a nickel plated copper cooling block. These electrodes were prepared by plasma spraying by APS Materials to an overall height of 1.56 cm. The inter-electrode insulation consists of 0.11 cm of plasma sprayed $MgAl_2O_4$ on all four sides completely covering both the ceramic electrode and the copper cooling block.

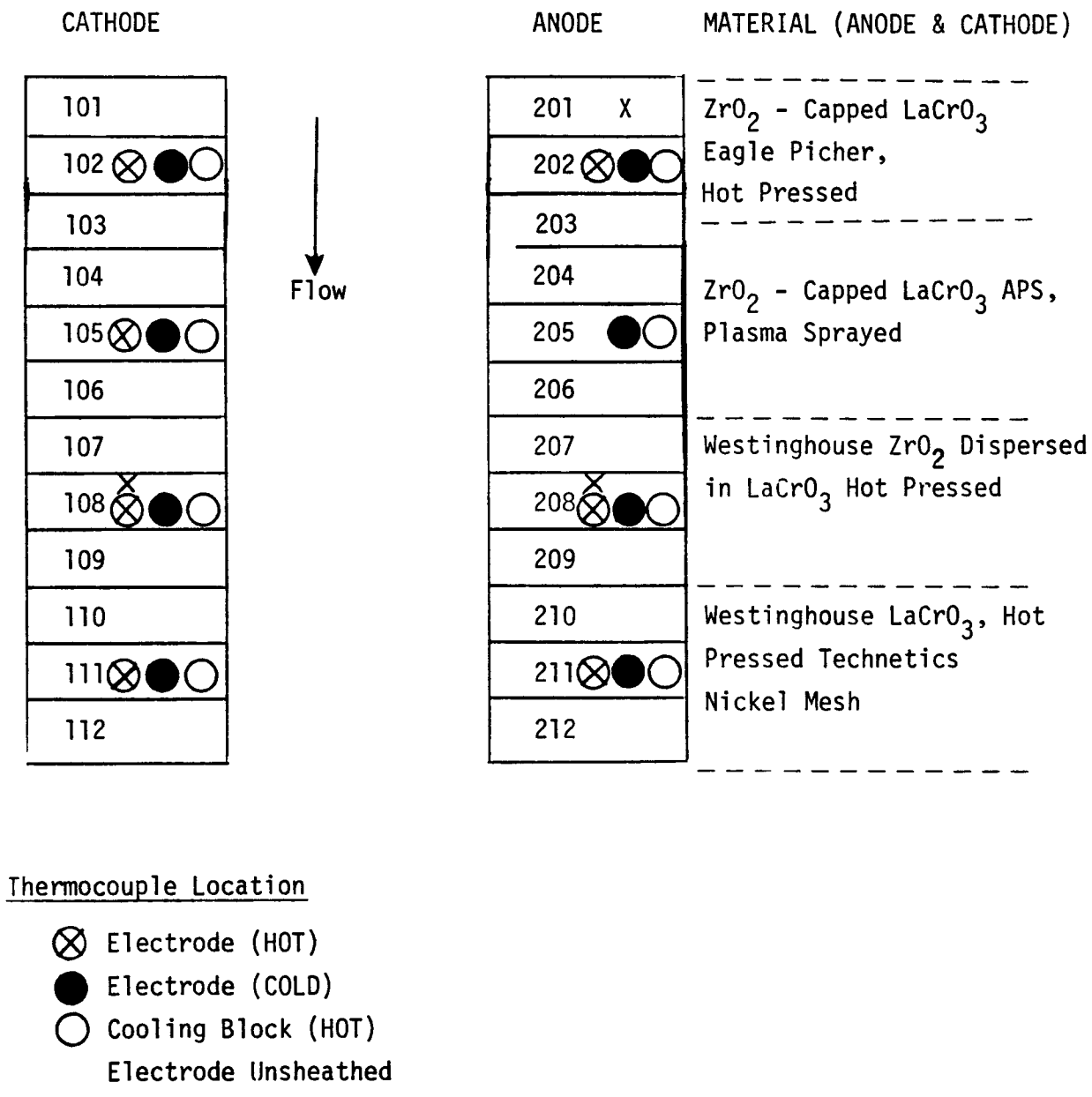

Figure 36. Material Positions in Proof Test 2 (WESTF Test 38)

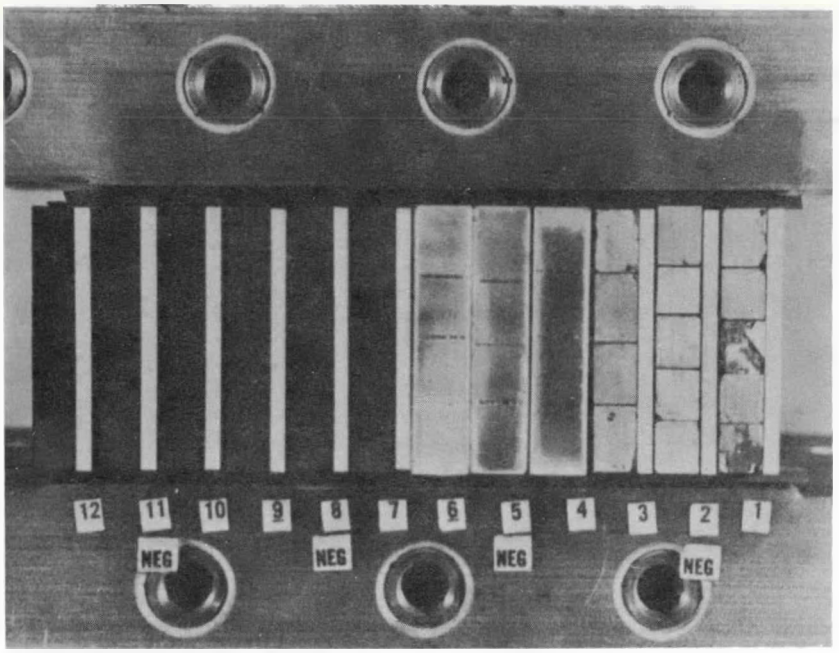

a. Top View

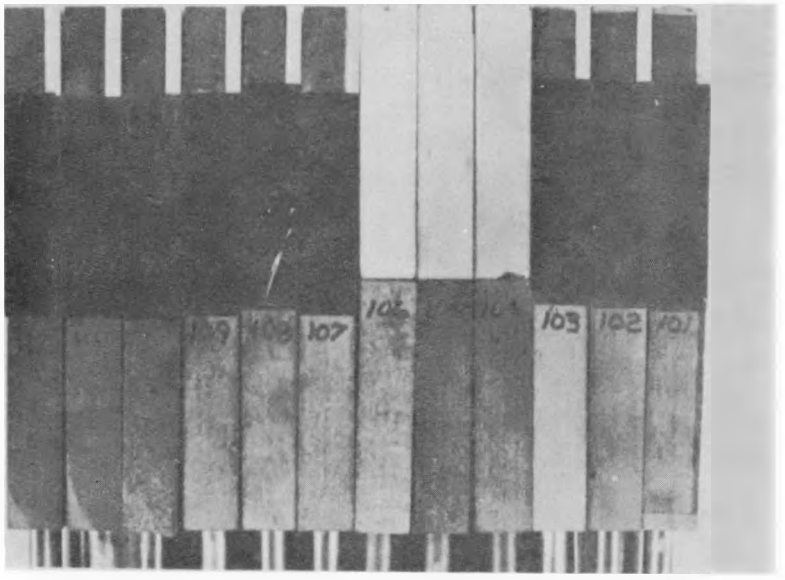

b. Side View

Figure 37. Cathode Wall - Proof Test 2 (WESTF Test 38)

The final group of electrodes consisted of a hot pressed composite of thirty weight percent zirconia dispersed in a lanthanum chromite matrix. This material was prepared by Westinghouse. The electrode consisted of 6 blocks of 1.0 cm (l) x 1.0 cm (w) x 2.1 cm (h) joined to a copper cooling block with 0.025 cm or less of silver-filled epoxy. Thin shallow cuts extended into the copper between each block to reduce interfacial stress. Ths insulators, monolithic spinel, 6.0 cm (ℓ) x 0.35 cm (w) x 4.6 cm (h), are slotted at their base and joined to the copper through heat conductive silicone grease and held in place by the tie rods and the polyimide tape that is used to insulate the copper cooling blocks.

The final three electrode pairs were lanthanum chromite hot pressed and machined by Westinghouse and brazed with TiCuSil brazing alloy to nickel mesh brazed to copper with NiCrobraz alloy by the Technetics Div. of Brunswick Corp. The electrode consists of three segments 2.0 cm (ℓ) x 1.0 cm (w) x 2.3 cm (h) and the insulators, monolithic spinel, 6.0 cm (ℓ) x 0.35 cm (w) x 5.1 cm (h). The insulators were slotted at their base and joined to the copper through a heat conductive silicone grease and held in place by the tie rods and the polyimide tape that provides electrical insulation of copper cooling blocks.

In order to reduce any heat losses due to unsealed gaps particular attention was given in sealing gaps in this test section. A phosphate-bonded zirconia cement was used in the gaps between ceramics of the electrode and insulating walls. A silicone sealant was used to fill any gaps in the cooler portions of the electrode wall.

In order to understand the variations in measured temperatures, the thermocouple bead locations in the sheathed thermocouples and the location of thermocouples in the ceramic electrodes were darefully determined through radiographs and dimensional inspection. The measured values along with materials property data were used in completing the analysis of temperature predictions and uncertainties for use in the conduct of the test.

Proof Test 3 (WESTF TEST 39)

The electrode walls were composed of a total of twelve active electrode pairs arranged in four groups of three electrode systems. A schematic of the electrode wall is shown in Figure 38. The assembled anode wall is shown in Figure 39.

The first or upstream three electrode pairs were alumina enriched lanthanum chromite hot pressed by Westinghouse. In this material aluminum replaces chromium such that the aluminum to chromium ratios are: 1 to 2.1 in the 2.5 mm top layer; 1 to 3.2 in the 2.5 mm middle layer; and 1 to 5.7 in the 21.8 mm bottom layer. The electrode segments were machined to give an electrode composed of four or five segments with overall dimensions of the 6.0 cm (ℓ) x 1 cm (w) x 2.7 cm (h). A 100 micron gold film was sputtered onto the back surface of the segments before they were joined to the copper cooling block with 0.25 mm or less of silver-filled epoxy adhesive. The insulators, monolithic magnesia, 6.0 cm (ℓ) x 0.35 cm (w) x 5.3 cm (h) and slotted at their base were held in place by the tie rods, silicone heat transfer grease (at copper-insulator interfaces) and the polymide tape that is used to insulate the copper blocks.

The second group of three electrode pairs are 0.5 $SrZrO_3$ - 0.5 $LaCrO_3$ sintered by A-T Research Company. The electrode segments were machined to give an electrode composed of four or five segments with overall dimensions of 6.0 cm (ℓ) x 1 cm (w) x 2.4 cm (h). A 100 micron platinum film was sputtered onto the back surface of the segments before they were joined to the copper cooling block with 0.25 mm or less of silver-filled epoxy. The insulators, monolithic spinel, 6.0 cm (ℓ) x 0.35 cm (w) x 4.9 cm (h) and slotted at their base, were held in place by the tie rods, silicone heat transfer grease (at copper-insulator interfaces) and the polymide tape that is used to insulate the copper blocks.

The third group of three electrode pairs consisted of sintered lanthanum chromite, approximately 0.95 cm high, attached to a "FLEXBED" leadout, approximately 1.1 cm high. This assembly had monolithic spinel insulators, approximately 0.17 cm (w) x 3.2 cm (h), on both sides of the electrode. This electrode assembly, with its proprietary attachment, "FLEXBED" lead out, was supplied by General Electric Company.

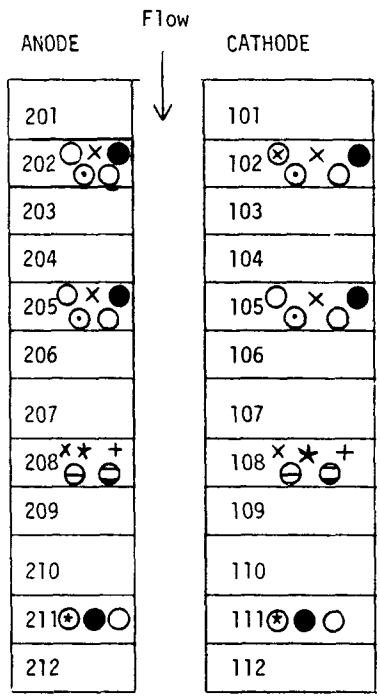

ELECTRODE MATERIAL	ATTACHMENT	INTERELECTRODE INSULATOR
Layered Al_2O_3 doped	Ag Epoxy	Monolithic
$LaCrO_3$ - Westinghouse	Au Film	MgO (Norton
Hot Pressed	(Back Face)	(one side)
$.5LaCrO_3$ - $.5SrZrO_3$	Ag Epoxy	Monolithic
A-T Research	PT Film	Spinel (Trans-
Sintered	(Back Face)	tech) (one side)
$LaCrO_3$	Flexbed	Monolithic
General Electric		Spinel
Sintered		(both sides)
MAFF-31/Hercynite	Spray Bond	S-71 Spinel (both sides)
APS Materials	To ION -	APS Materials
Plasma Sprayed	Plated Ni	Plasma sprayed

THERMOCOUPLES

Symbol	Location	Designation	Type	Sheathed	Bare Wire
⊗	Electrode (Hot) Center	T_1	B	X	
X	" " "	T_1'	B		X
✶	Electrode (Hot) End	T_1''	B		X
⊛	Electrode (Hot) Center	T_1'''	S	X	
●	Electrode Cold Center	T_2	K	X	
+	Electrode Cold Center	T_2'	B		X
⊙	Insulator (Cold) Center	T_3	K	X	
○	Copper (Block) Center	T_4	K	X	
⊖	Copper (Block) Center	T_4'	K		X
◒	Copper (Block) End	T_5	K		X

Figure 38. Electrode Wall Schematic-Proof Test 3 (WESTF Test 39)

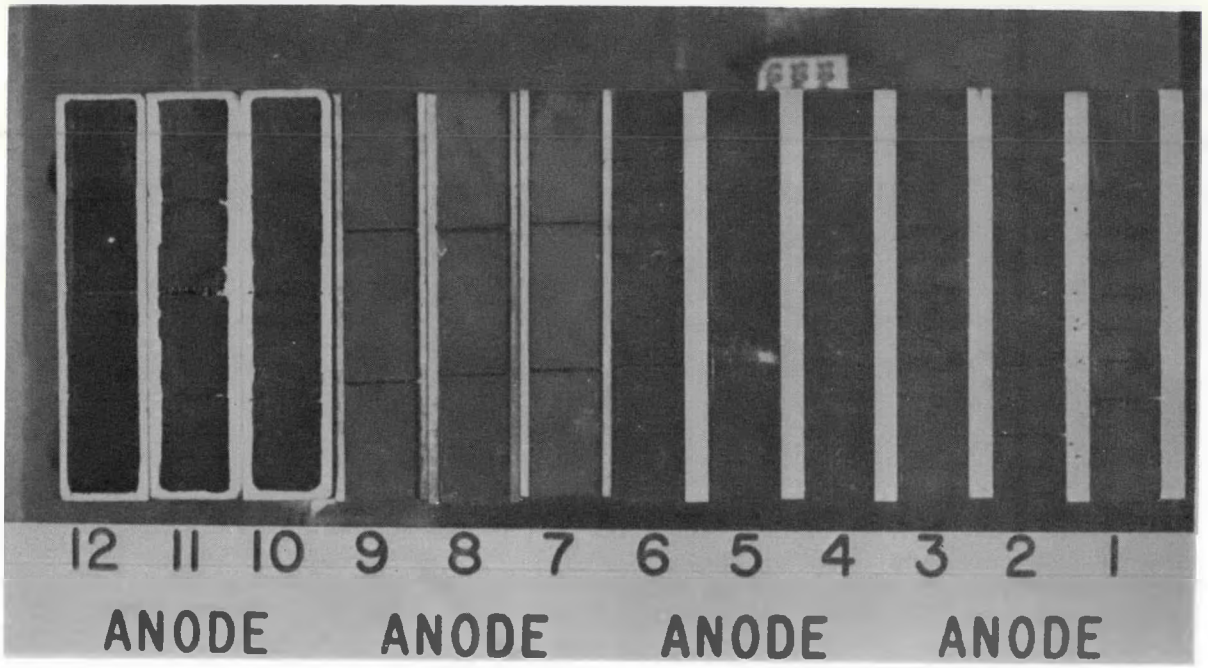

a. Top View

b. Side View

Figure 39. Anode Wall-Proof Test 3 (WESTF Test 39)

The last or downstream three electrode pairs were plasma sprayed MAFF-31 electrodes supplied to Westinghouse by APS Materials, Incorporated. These electrodes were prepared by spray bonding to a nickel surface ion-plated onto the copper cooling block, and consisted of an outer 13 mm layer of MAFF-31, a middle layer of 7 mm of hercynite, and a base layer of 3 mm of a hercynite/METCO 447 composite. The 1.5 mm thick side insulation was plasma sprayed spinel and it covered the entire length of the copper on both sides of the electrode.

5.2.2.3 Test Operations

Proof Test 1 Operational Summary

The first U-02 Phase III proof test was carried out at the Westinghouse Electrode Systems Test Facility (WESTF) on October 10-11, 1977. Three sets of three electrodes were tested; the first electrode pair and the last two electrode pair were guard electrodes.

The design test conditions were:

Gas temperature	2600°K
Electrode Surface Temp.	1700-1750°F
Static pressure	1 atmosphere
Plasma velocity	~450 m/sec
Current density (imposed)	1.25 amp/cm^2
Electrode wall heat flux	15-24 w/cm^2
Seed	1% K_2CO_3

The test was broken down into four phases. The first phase increased the temperature of the channel at the rate of not more than 10°C/minute with no seed addition. During the second phase the electrophysical characteristics of the channel was determined. The third phase constituted the life test of the electrode materials under electrical load in the presence of seed. The fourth phase constituted the ramping down of the temperature.

The mass flow rates of the air, oxygen and fuel were recorded during the test and can be seen plotted in Figure 40. Preheated air (650°C) was passed through the channel before ignition to minimize thermal shock. Immediately before ignition the air preheater was shut-off, and the air flow was reduced to approximately 50 percent of design. Upon ignition of the burner, the air flow was increased to the design point resulting in approximately a 200°C rise in plasma temperature during ignition. The fuel flow and air preheat were then increased to obtain the desired temperature ramp. Oxygen was introduced to fine tune the plasma to obtain the desired operating conditions.

The operating temperatures of the ceramic electrode, copper cooling block, and cooling water can be seen for electrodes No. 103, 203, 106, 206, 110 and 210 in Figures 41 through 43. The thermocouples that were located in the electrode wall are tabulated in Table 14. The distance that the thermocouple is located from the surface was known with the exception of the GE electrodes 103 and 203. Examination of these curves show some trends in the operation of the channel while at the same time show the individual performance of the electrodes. Heat flux data was obtained for each electrode pair and typical plots are shown in Figures 44 through 46.

Proof Test 1 Post-Test Visual Examination

After completion of the cool-down phase, the test section was removed from WESTF and moved into the laboratory for disassembly. The test team, in particular, the test monitors from NBS and Battelle, conducted a visual examination of the electrode walls. Extensive photographs were also taken to record the condition of the walls. Upon removal of the top insulating wall it was obvious (see Figures 47 and 48) that both walls showed extensive damage. Comparison of anode and cathode walls (Figure 49) showed that the anode suffered the most damage. A summary of visual observations is as follows:

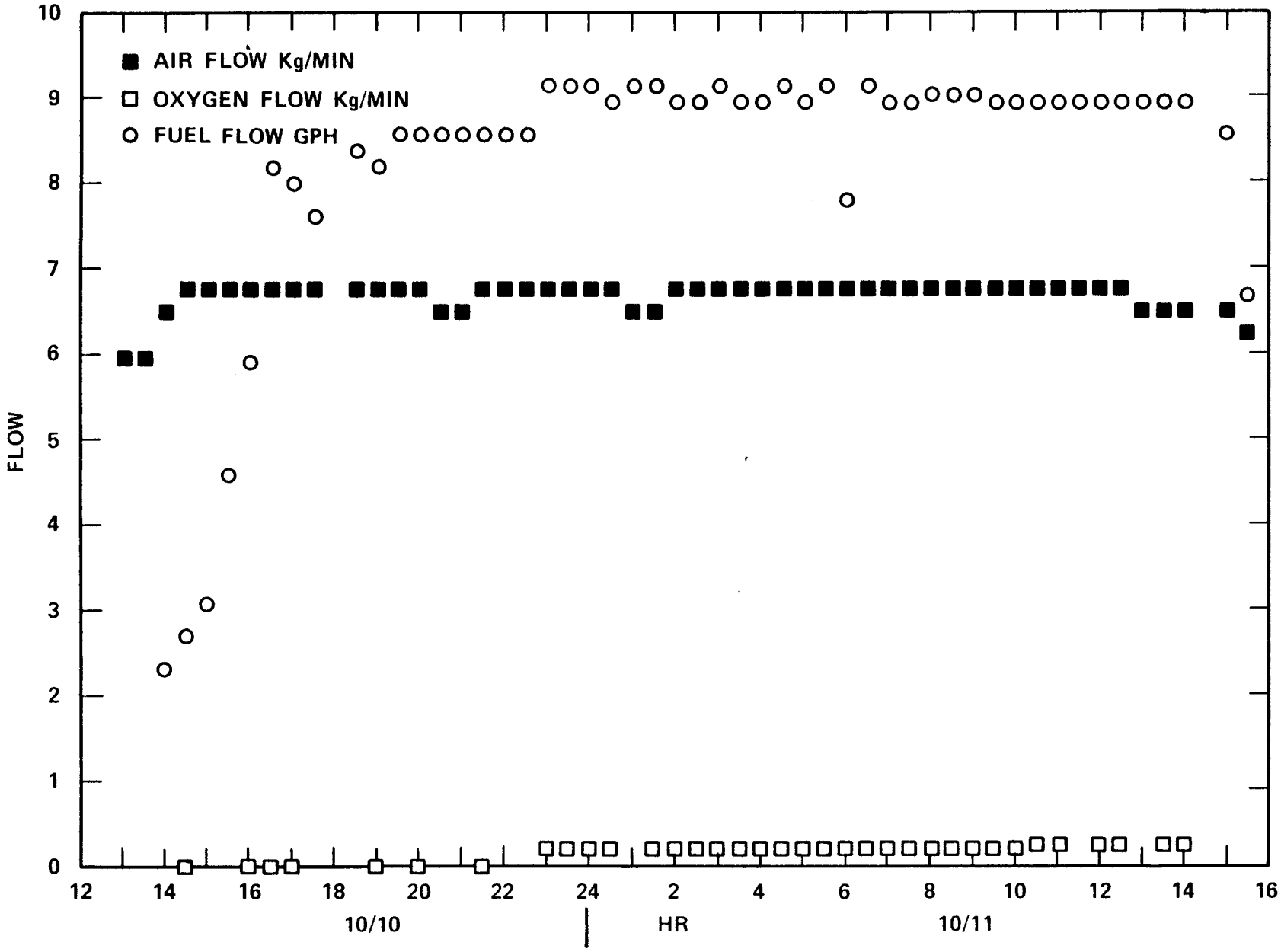

Figure 40. Proof Test No. 1 Mass Flow Rates (WESTF Test 37)

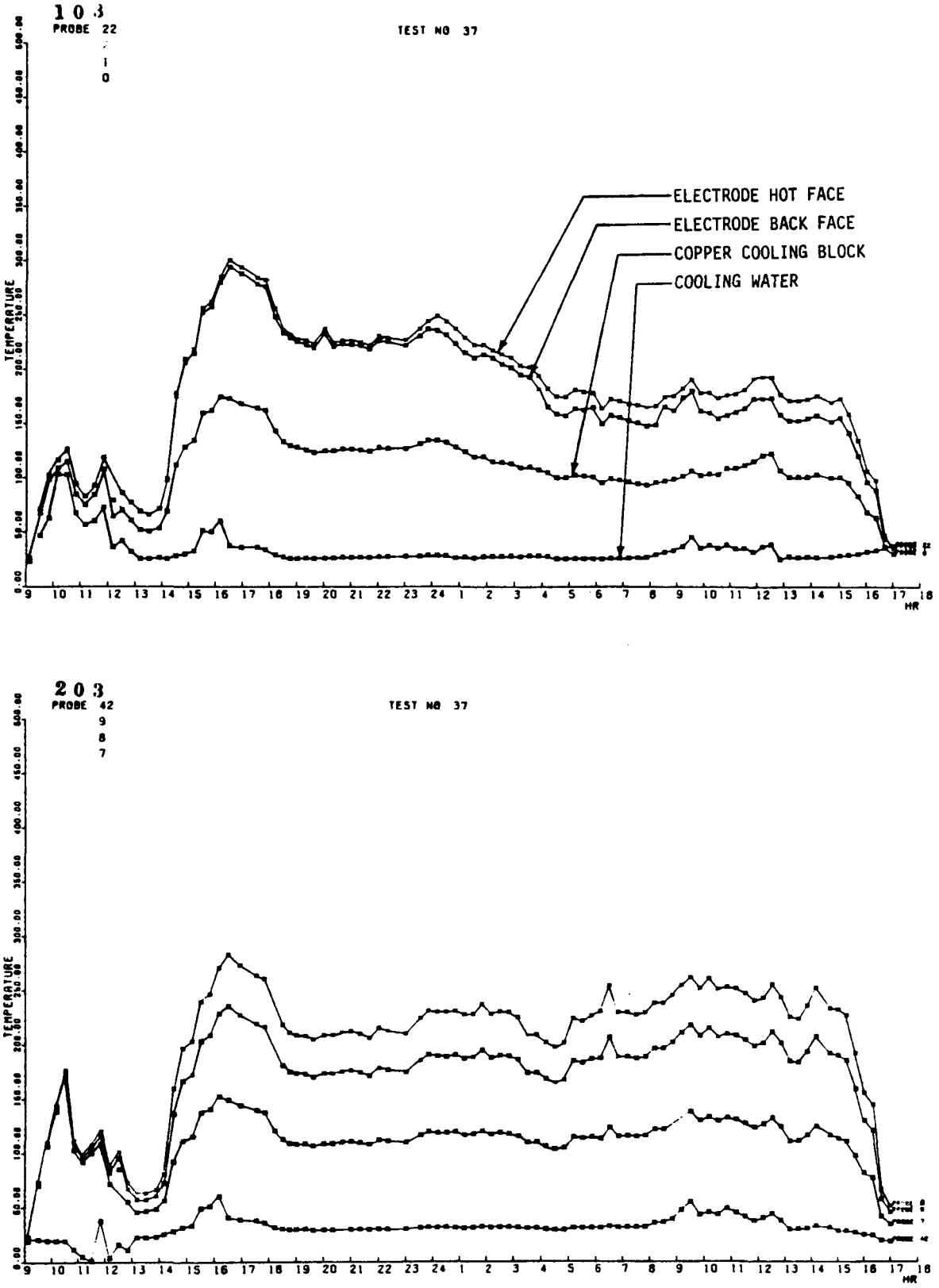

Figure 41. Proof Test 1-Electrode Pair 103-203 Temperatures

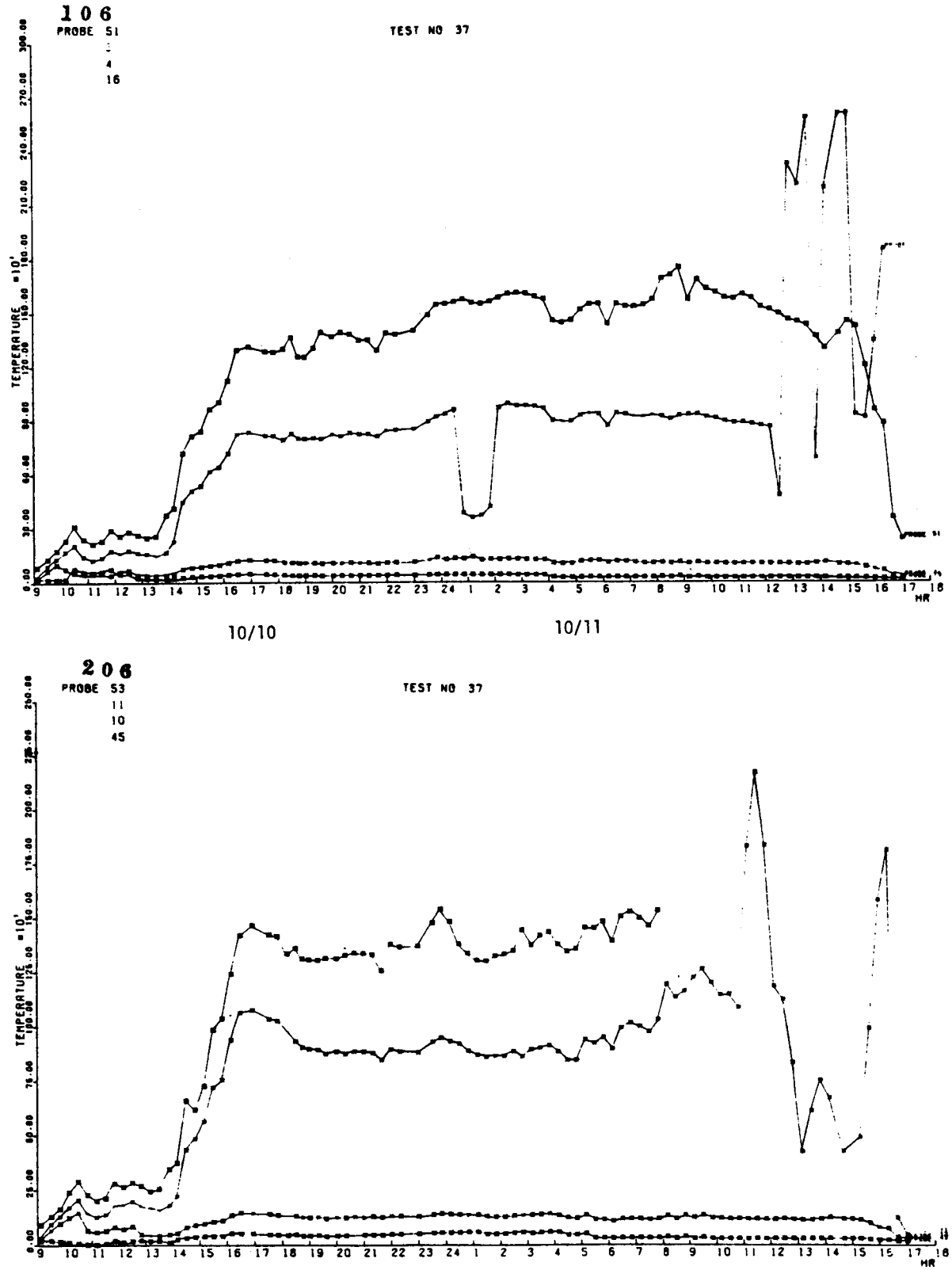

Figure 42. Proof Test 1-Electrode Pair 106-206 Temperatures

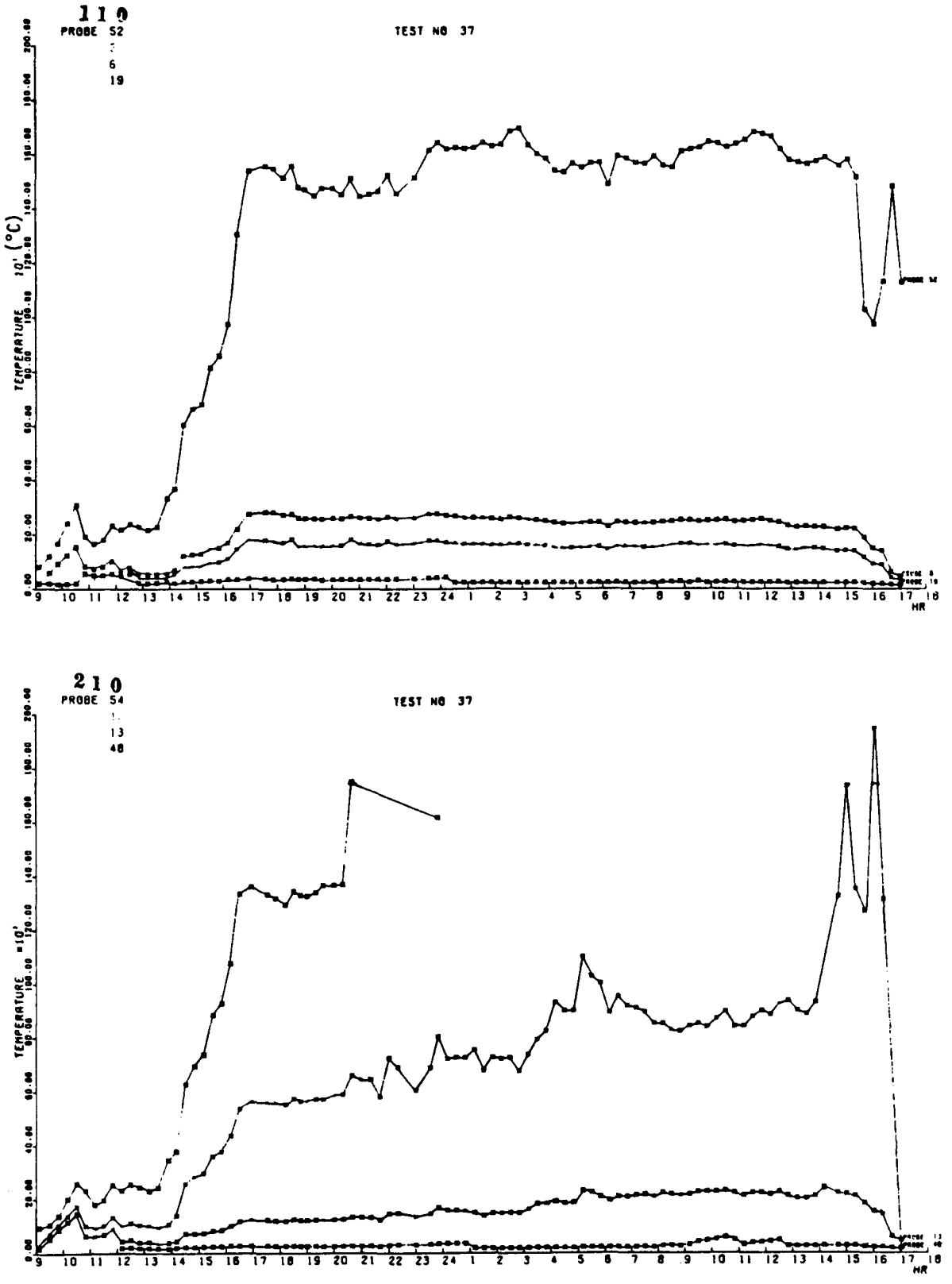

Figure 43. Proof Test 1-Electrode Pair 110-210 Temperatures

TABLE 14-ELECTRODE WALL THERMOCOUPLE IDENTIFICATION

Electrode Position Number	Temperature Measured	Distance from Surface-mm	Thermocouple Type
103	Electrode	NA	K
106	Electrode	3	B
109	Electrode	3	B
203	Electrode	NA	K
206	Electrode	3	B
209	Electrode	3	B
103	Electrode	NA	K
106	Electrode	14	K
109	Electrode	11	K
203	Electrode	NA	K
206	Electrode	14	K
209	Electrode	11	K
103	Copper	NA	K
106	Copper	22	K
209	Copper	22	K
203	Copper		K
206	Copper	22	K
209	Copper	22	K

INSULATING WALL THERMOCOUPLE IDENTIFICATION

Insulator Position Number	Temperature Measured	Distance from Surface-mm	Thermocouple Type
TE 2	MgO	13	B
TO 1	MgO	13	B
TO 4	MgO	13	B
TX 2	MgO	13	B
TE 2	MgO	1.5	B
TO 1	MgO	1.5	B
TO 4	MgO	1.5	B
TX 2	MgO	1.5	B

NA-Dimensions not available (General Electric)

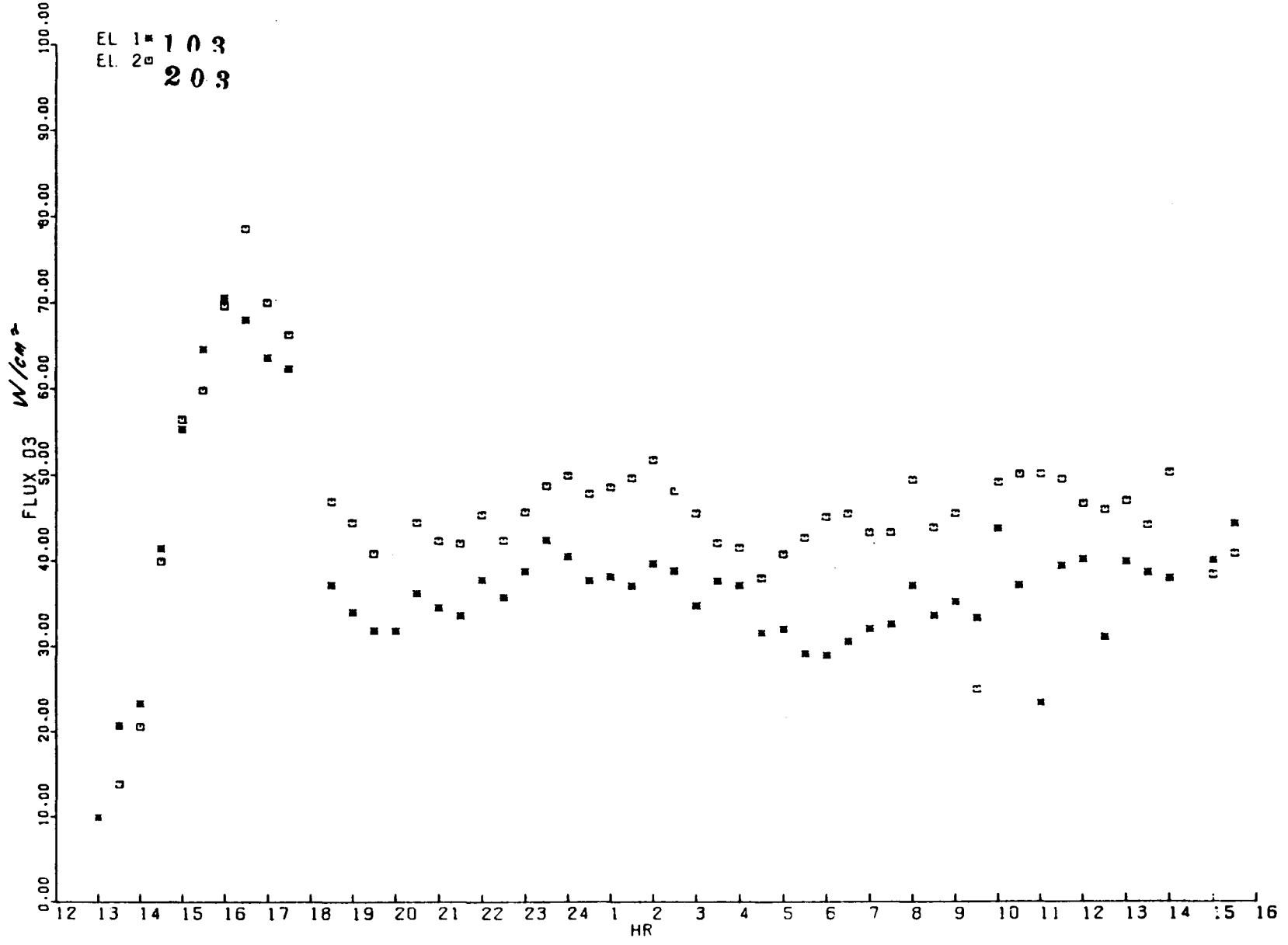

Figure 44. Proof Test 1 Heat Flux Data-Electrode Pair 103-203

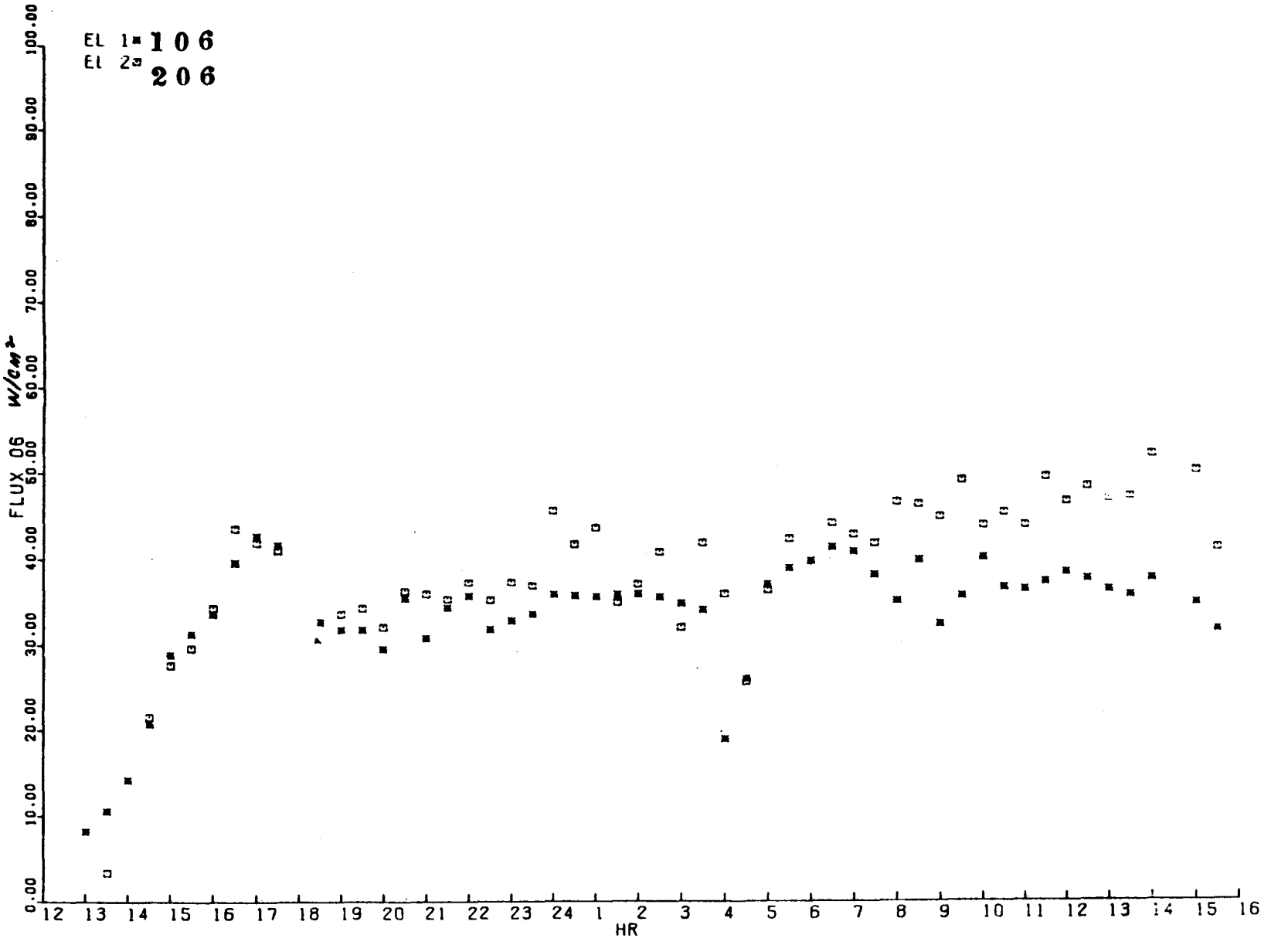

Figure 45. Proof Test 1 Heat Flux Data-Electrode Pair 106-206

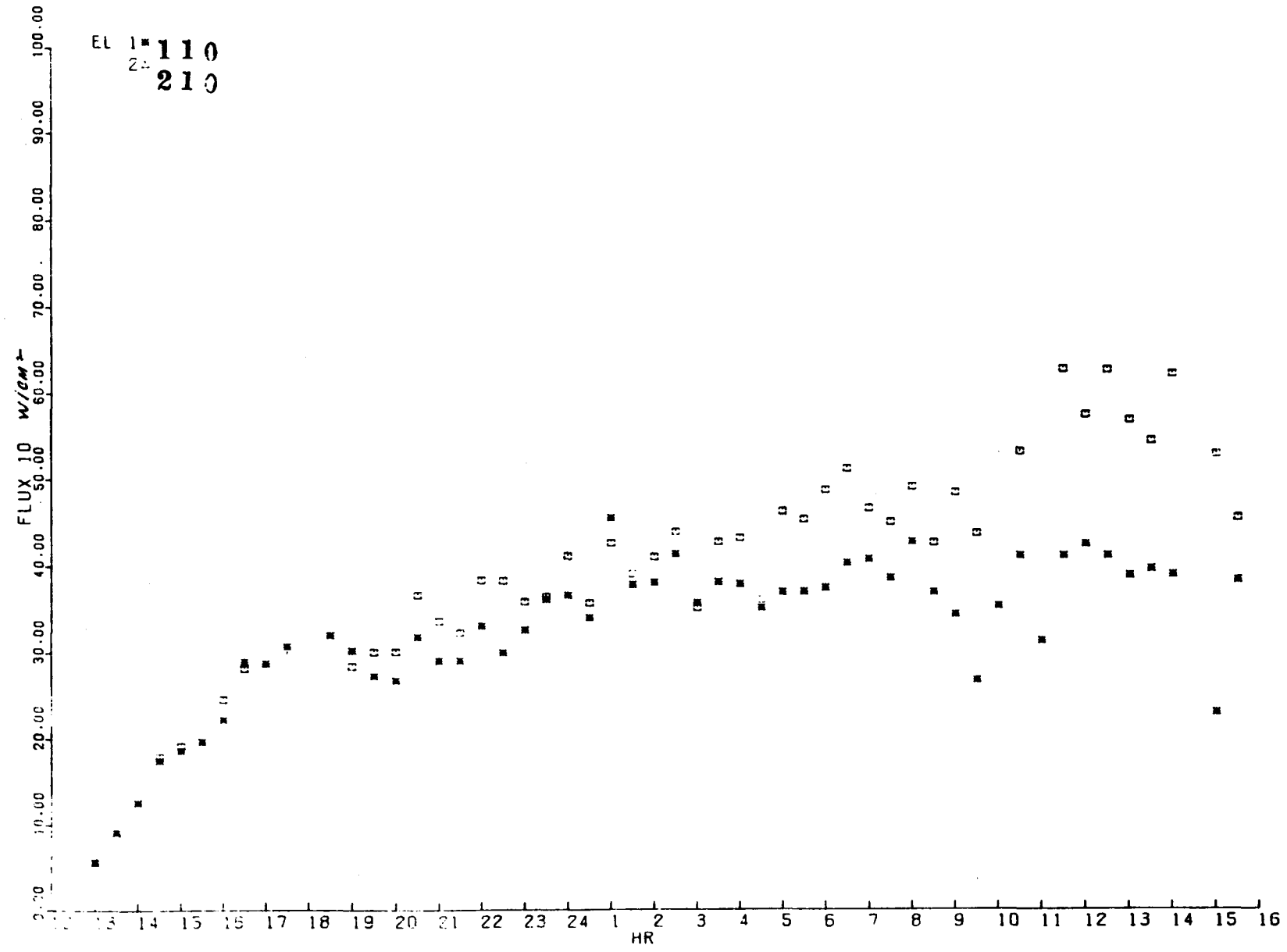

Figure 46. Proof Test 1 Heat Flux Data-Electrode Pair 110-210

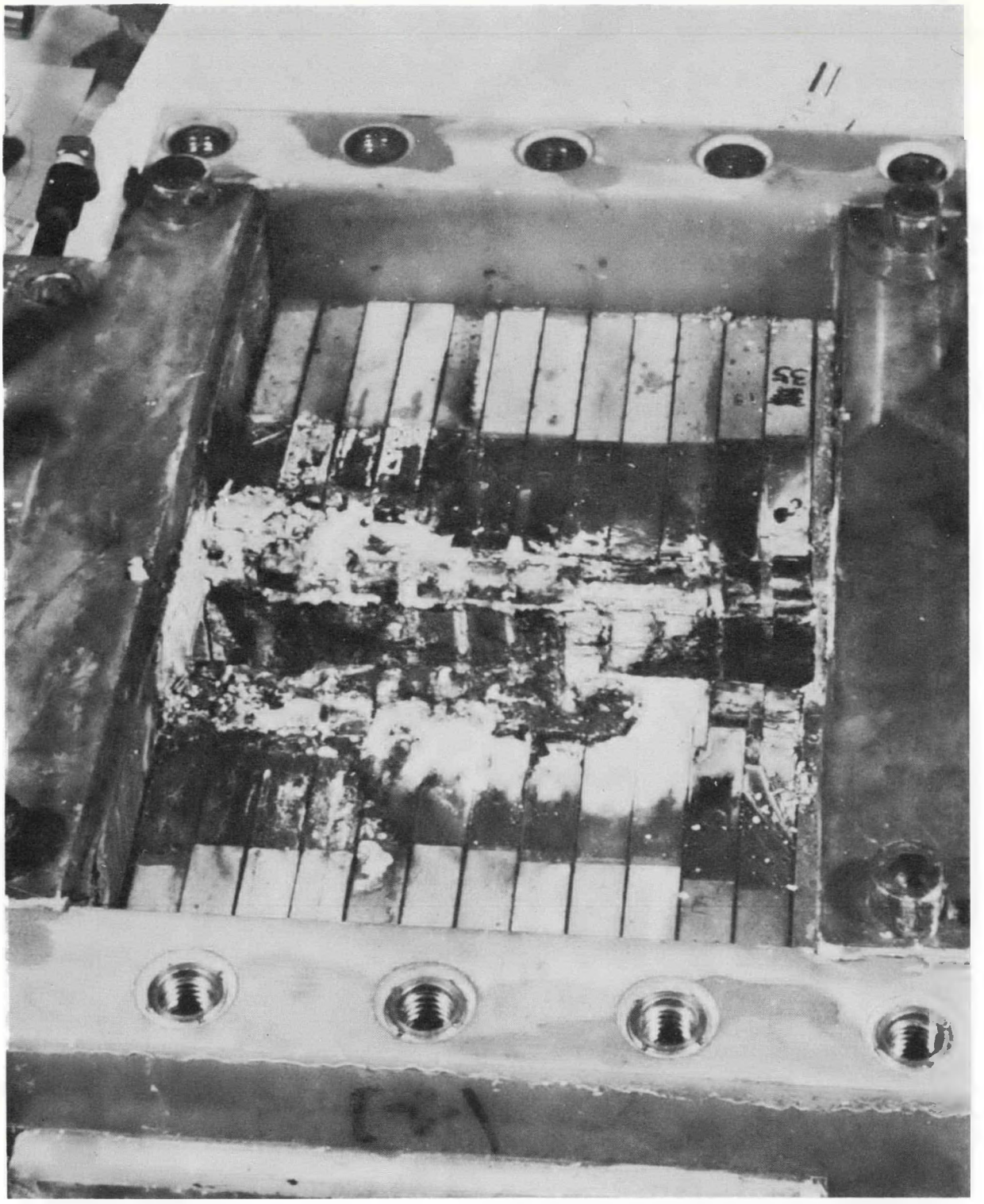

Figure 47. Proof Test 1 Test Section After Removal of Top Insulating Wall (Looking at Cathode Wall-Plasma Entered from Left)

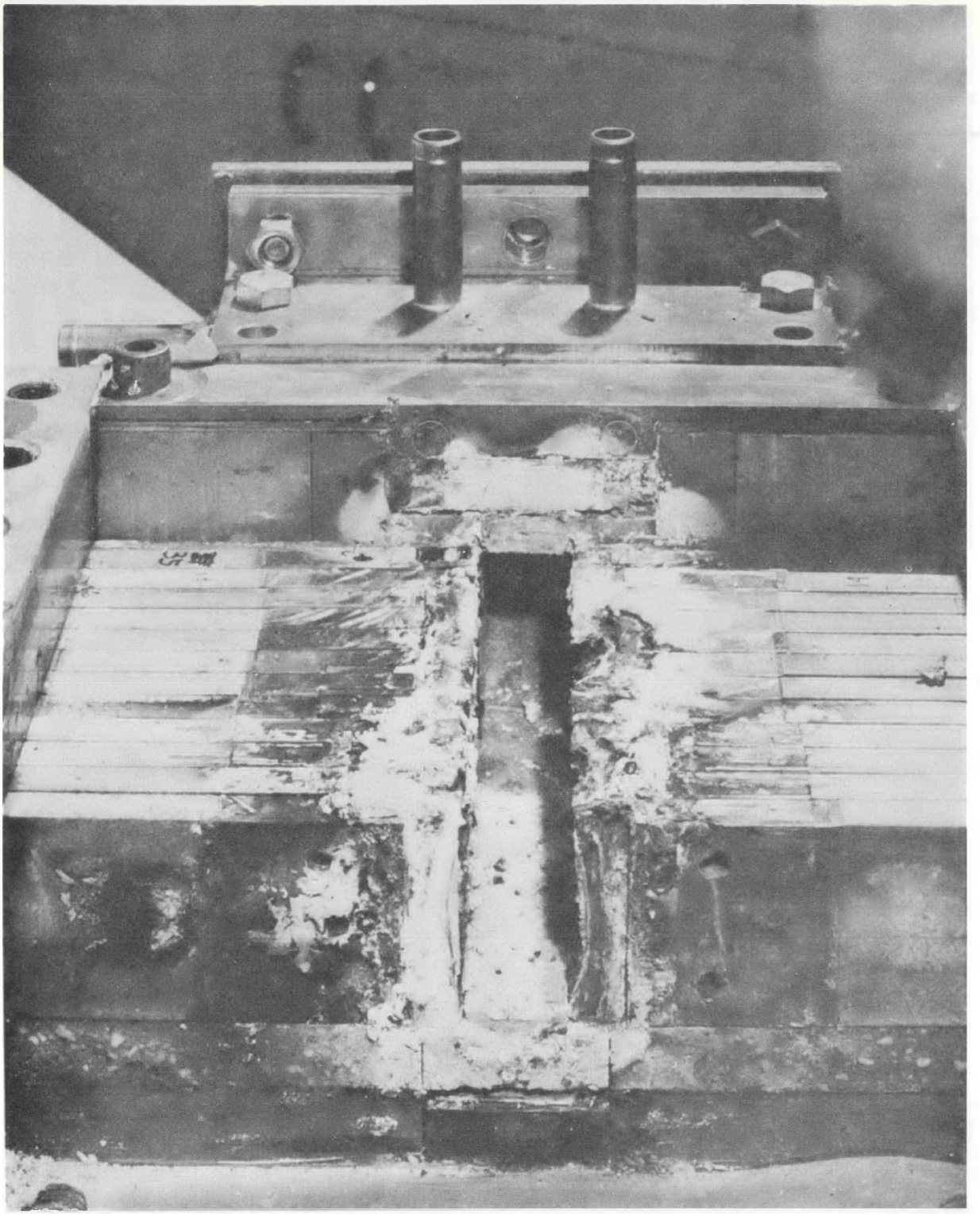

Figure 48. Proof Test 1 Test Section Viewed from Plasma Entrance (Anode Wall on Right)

Figure 40. Proof Test 1 Cathode Wall (Left) and Anode Wall (Right)

	Cathode	Anode	
101	Guard Small amount erosion/ corrosion at upper center, deposit (light color on upstream side.	Guard Slight surface erosion corrosion, large crack near one edge through electrode and downstream insulator.	201
102	Moderately eroded, maximum removal of material at mid-length position, edges of electrodes not rounded locally, insulator surfaces generally flush with electrode.	Similar to cathode but less extensive	202
103	Same as #102	Similar to cathode but less extensive	203
104	Same as #102, 103 significantly more eroded, carried maximum corrent (6 amp)	Similar to cathode but less extensive	204
105	Slight erosion (mostly in center), light brown surface, blue surface scale.	Extensive corrision, material "streaming" over downstream insulator.	205
106	Same as #105 but corrosion maximum in lower area.	Slightly less corrosion than #205, "streaming" over insulator.	206
107	Small erosion/corrosion over entire surface; sustained the design current density.	Very extensive corrosion	206
108	Good condition, no apparent swelling	Missing to compliant layer	208
109	Good condition, brownish discoloration for mesh of #110, thermocouple intact until after shutdown	Mesh exposed, vesicular or "spongy" surface areas	209

	Cathode	Anode	
110	Same as 108, 109; high current during test, "hole" at downstream side to mesh and "blobs" of brown material on surface.	Concave erosion exposing some mesh at mesh/ceramic interface, blue material within insulator regions of this electrode series.	210
111	Guard Some erosion of upstream edge, material "streaming" downstream over insulator and electrode.	Guard Uniformly concave erosion, surface pink, insulators have blue line.	211
112	Guard Same as #111 but less upstream erosion.	Guard Less erosion than #211, some "Streaming" at downstream	212

After visual and photographic inspection the cathode and anode walls each were cast in an epoxy resin. Each module (anode and cathode) was cut through the center in a plane parallel to the plasma flow and perpendicular to the plasma-electrode surface. Half of each module was given to Battelle and half to NBS for analysis.

Subsequent sectioning was done as shown in Figure 50. Disposition of the sectioned electrodes is also shown in the figure. All cutting was done using a diamond saw of appropriate diamond concentration with water as a coolant.

Proof Test 2 Operational Summary

The second U-02 Phase III proof test was carried out at the Westinghouse Electrode Systems Test Facility on November 17-19, 1977. Twelve pairs of electrodes supplied by Westinghouse ran for 21.3 hours with electrode surface temperatures between 1500°C and 1750°C. External power supplied produced a flow of current through all electrodes at a current density of 1.0 A/cm^2, with the exception of the first two electrode pairs which ran at 0.6 A/cm^2 and 0.2 A/cm^2, respectively. In general, test parameters (currents, voltages, heat fluxes, temperatures) indicated very stable operation during life test of electrodes.

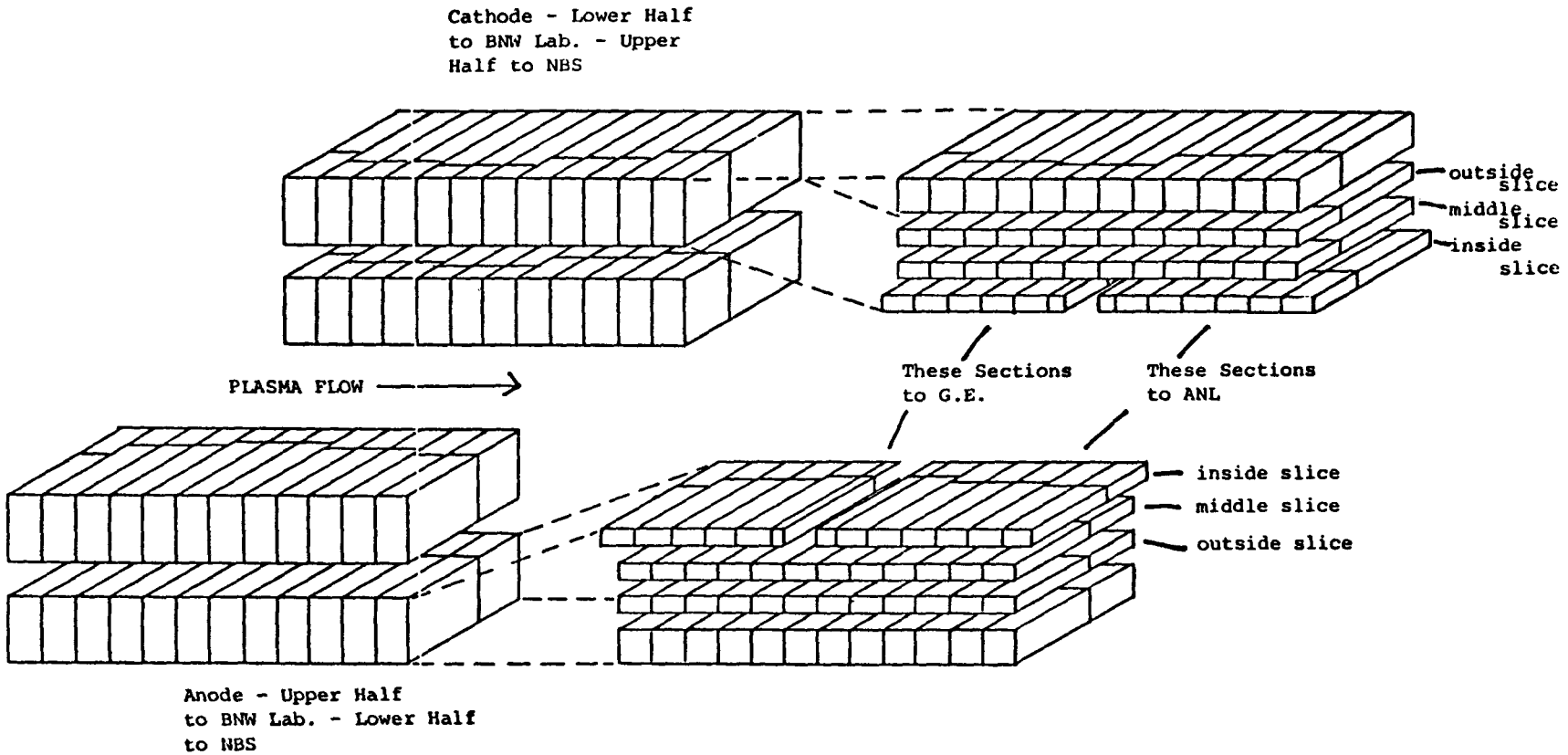

Figure 50. Schematic Diagram Showing NBS Sectioning of Electrodes From Phase III-U-02 Proof Test 1

Elapsed time from ignition until the combustor was shut off totaled 35 hours 26 minutes: Of this time, 13 hours 11 minutes, 21 hours 19 minutes and 56 minutes were heating the test section to establish conditions, life test, and cooldowns respectively. A brief chronology of this test is tabulated below. The flow rates of fuel, air and oxygen during test are shown in Figure 51.

Chronology of Proof Test 2

		Time	Date	Lapse Time
1.	Startup	0615	11-17-77	0 hours
2.	Preheater Ignition	0643	11-17-77	0.5
3.	Combustor Ignition	0939	11-17-77	3.4
4.	1850°C Plasma Calibration Hold	1230	11-17-77	6.25
5.	1600°C Electrode Surface Hold	1700	11-17-77	10.75
6.	1700°C Electrode Surface Hold Without Seed or Current	2000	11-17-77	13.75
7.	Start of Life Test with Seed and Current	2250	11-17-77	16.58
8.	Electrical Tests	1150	11-18-77	26.92
9.	Electrical Tests	1932	11-18-77	37.28
10.	Seed Off	2009	11-18-77	37.9
11.	Start of Cooldown	2032	11-18-77	38.25
12.	Fuel Off	2107	11-18-77	38.83
13.	Preheater Cooldown	2120	11-18-77	39.05

Average values for the various parameters during the life tests were:

Mass flow	79 g/s
Pressure in mixing chamger	1.22 atm
Air preheat temperature	412°C

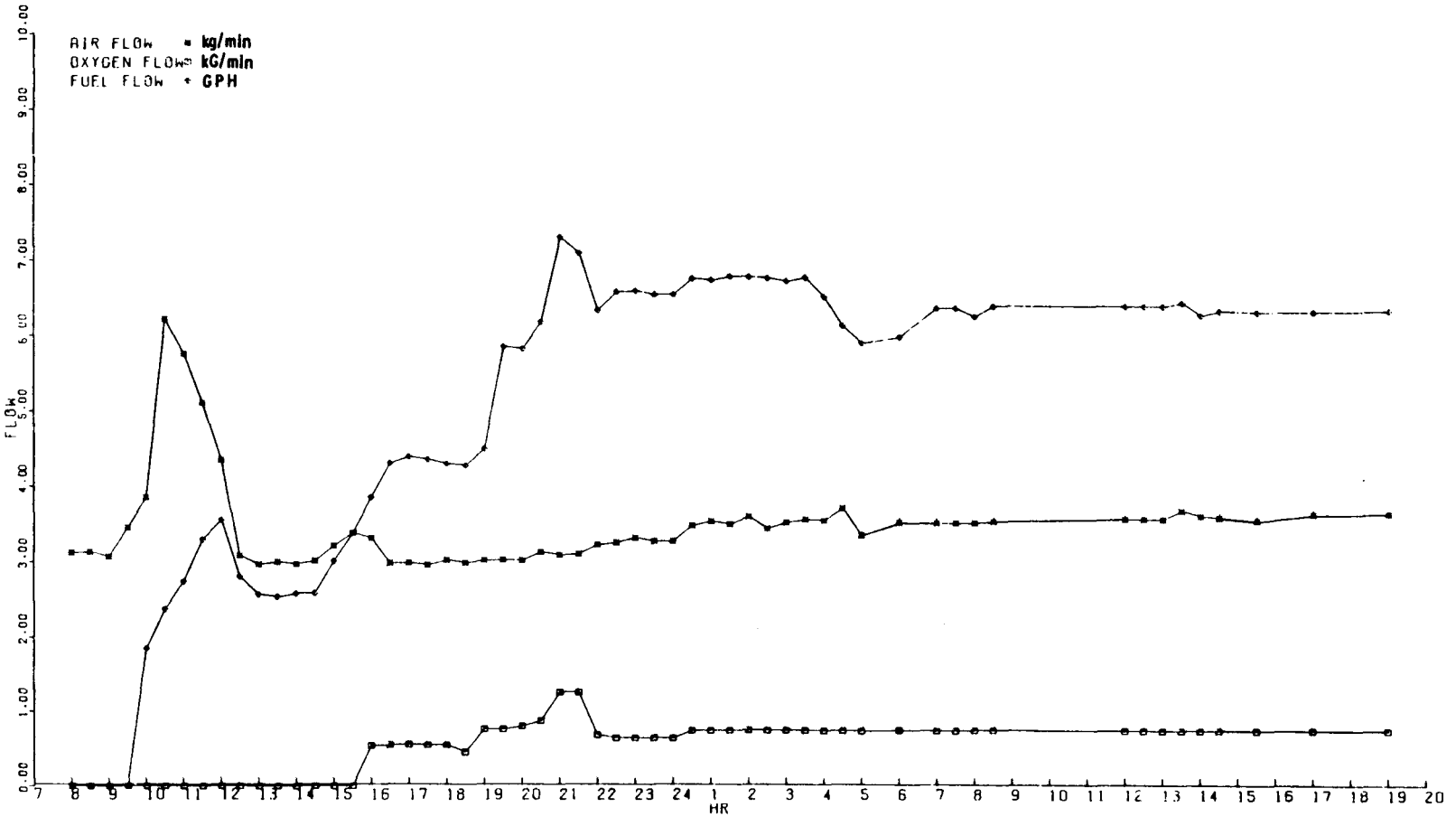

Figure 51. Proof Test 2 Mass Flow Rates (WESTF Test 39)

Oxygen temperature	23°C
Oxygen in oxidant	36.6% wt
Seed Solution	50% wt K_2CO_3/50% wt H_2O
Potassium concentration	0.83% wt
Fuel	Toluene
Stoichiometry	1.25 S.O.
Plasma temperature	2450°K
Plasma conductivity	5 mhos/m
Plasma velocity	350 m/sec

Representative thermocouple data is shown in Figures 52 through 54.

As discussed in Section 5.2.2.4 this test differed from Proof Test 1 in a number of significant ways. These are summarized as follows:

- Calibration holds were incorporated at: plasma temperature of 1850°C, electrode surface temperatures of ~1600°C and at electrode surface temperatures of ~1700°C (design point prior to seed addition or electrical loading).
- Extensive pre-test thermal predictions were prepared including error analyses and reflecting as-built thermocouple bead locations and as-built electrode dimensions.
- Sacrificial gas stream thermocouples were incorporated in the mixer and inlet transition sections to provide better data on plasma temperatures.
- Unsheathed thermocouples were included to provide a check on electrode hot face sheathed thermocouples.

Proof Test 2 Post-Test Visual Examination

After completion of the cool-down phase of the proof test, the test section was removed from WESTF and moved into the laboratory for disassembly of the test section. The top insulating wall was removed from the test section showing both walls to be in good to excellent condition (see Figures 55 and 56). However, during removal of the insulating wall some water from the cooling passages of the insulating wall spilled into the test section. Subsequently, hydration and swelling was noted on several electrodes (mostly cathodes) in

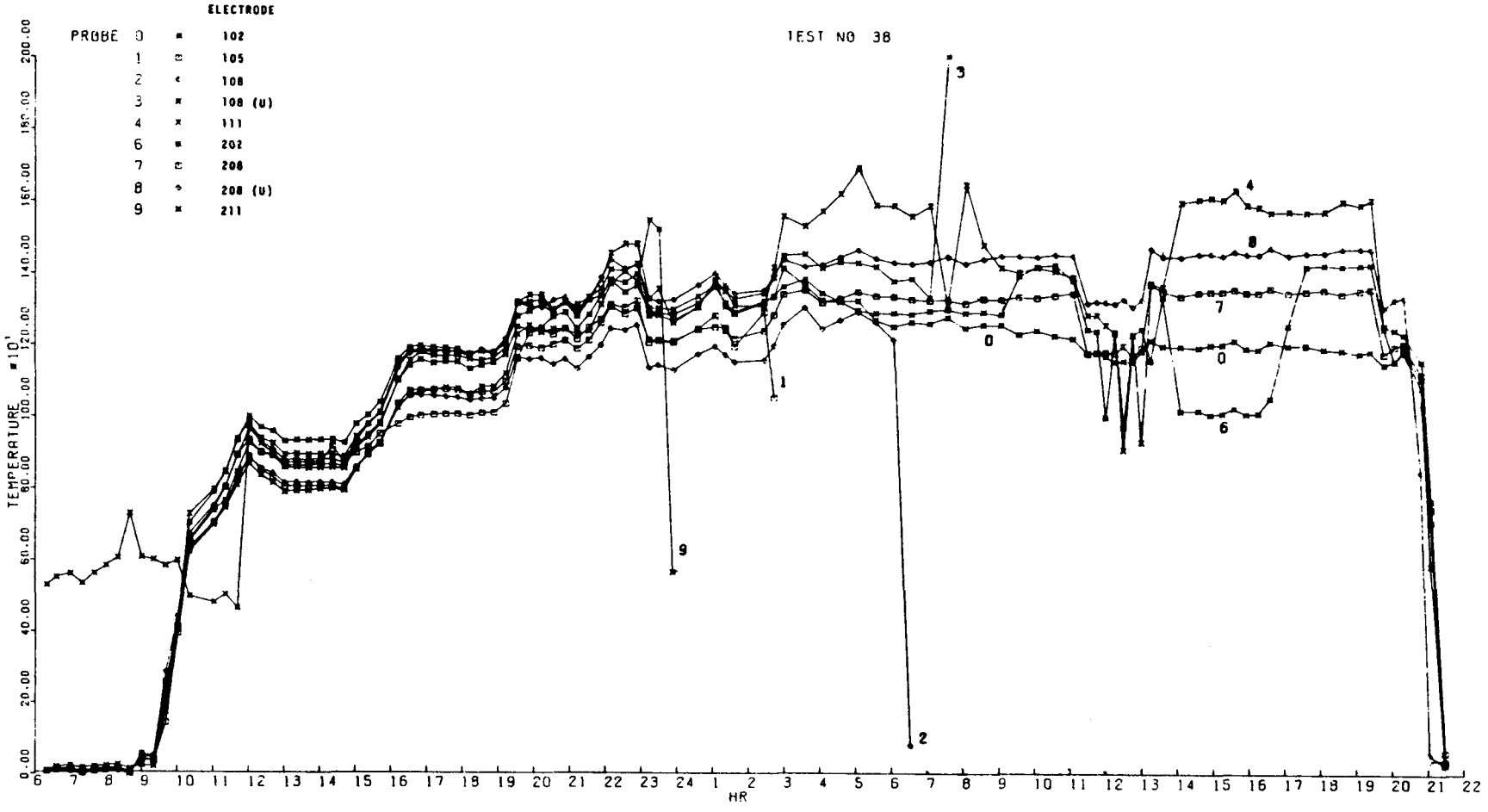

Figure 52. Proof Test 2-Electrode Temperatures (T/C mm from Plasma)

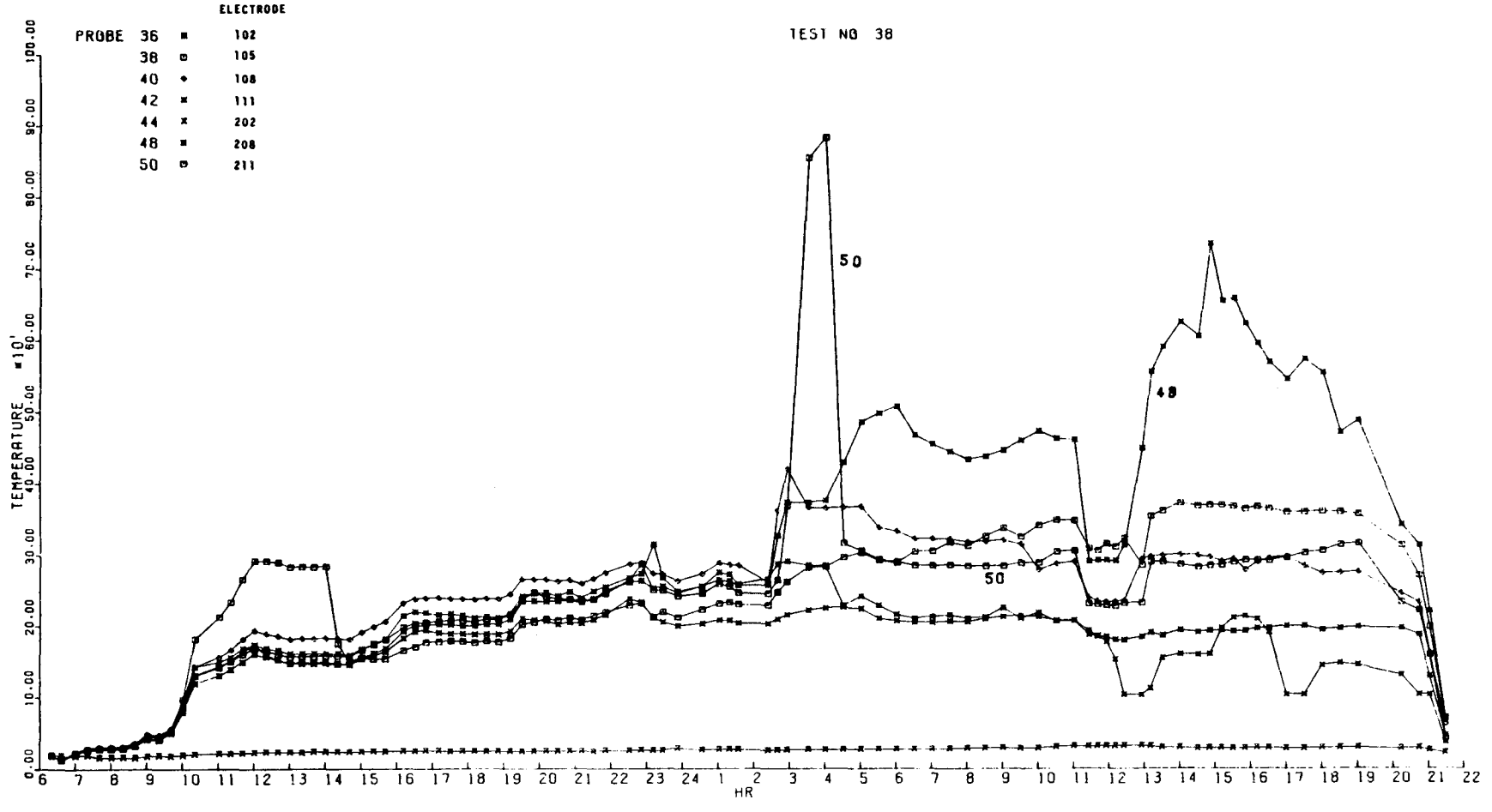

Figure 53. Proof Test 2-Electrode Temperatures (T/C 3 mm from Copper)

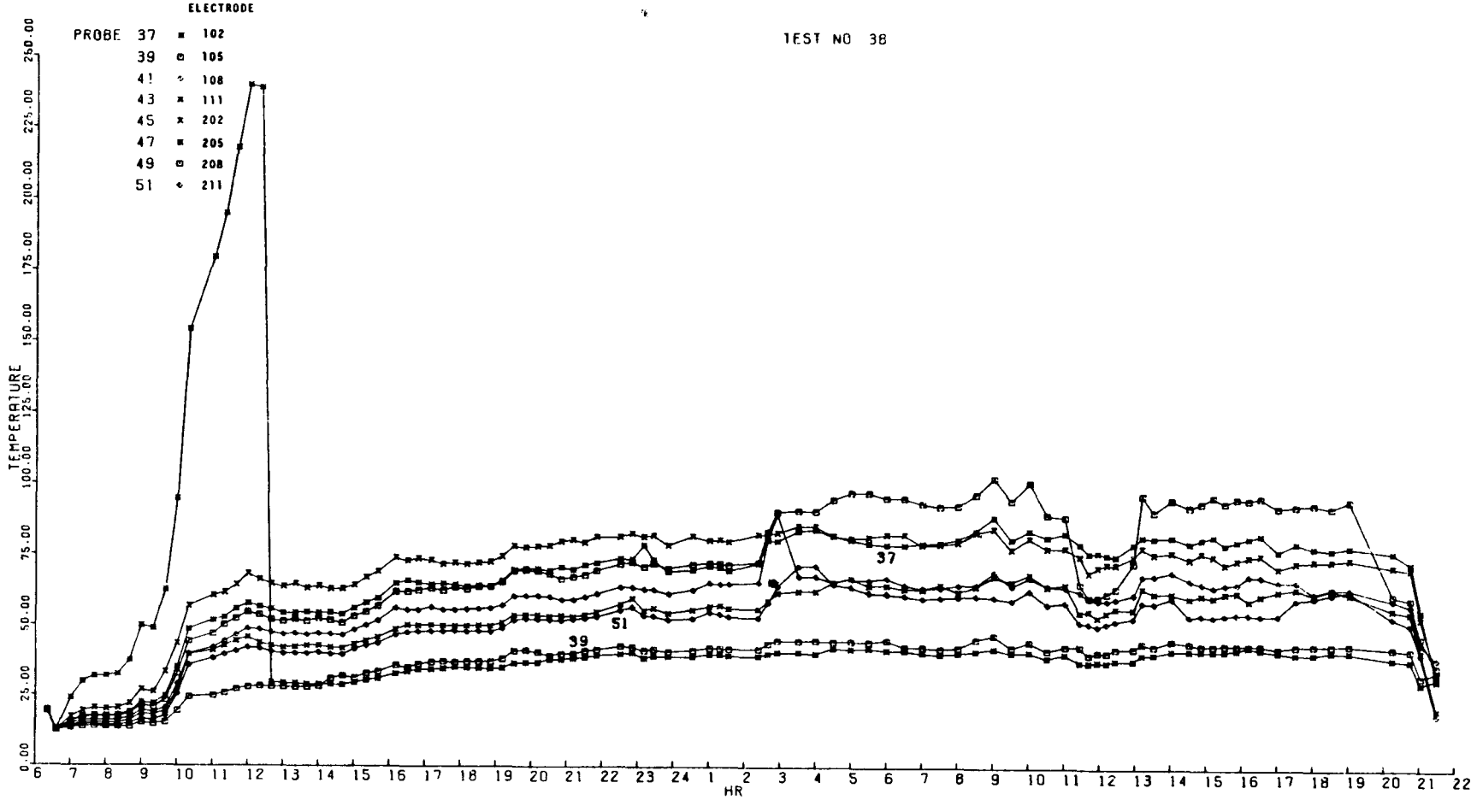

Figure 54. Proof Test 2-Copper Temperatures (T/C 3 mm from Electrode)

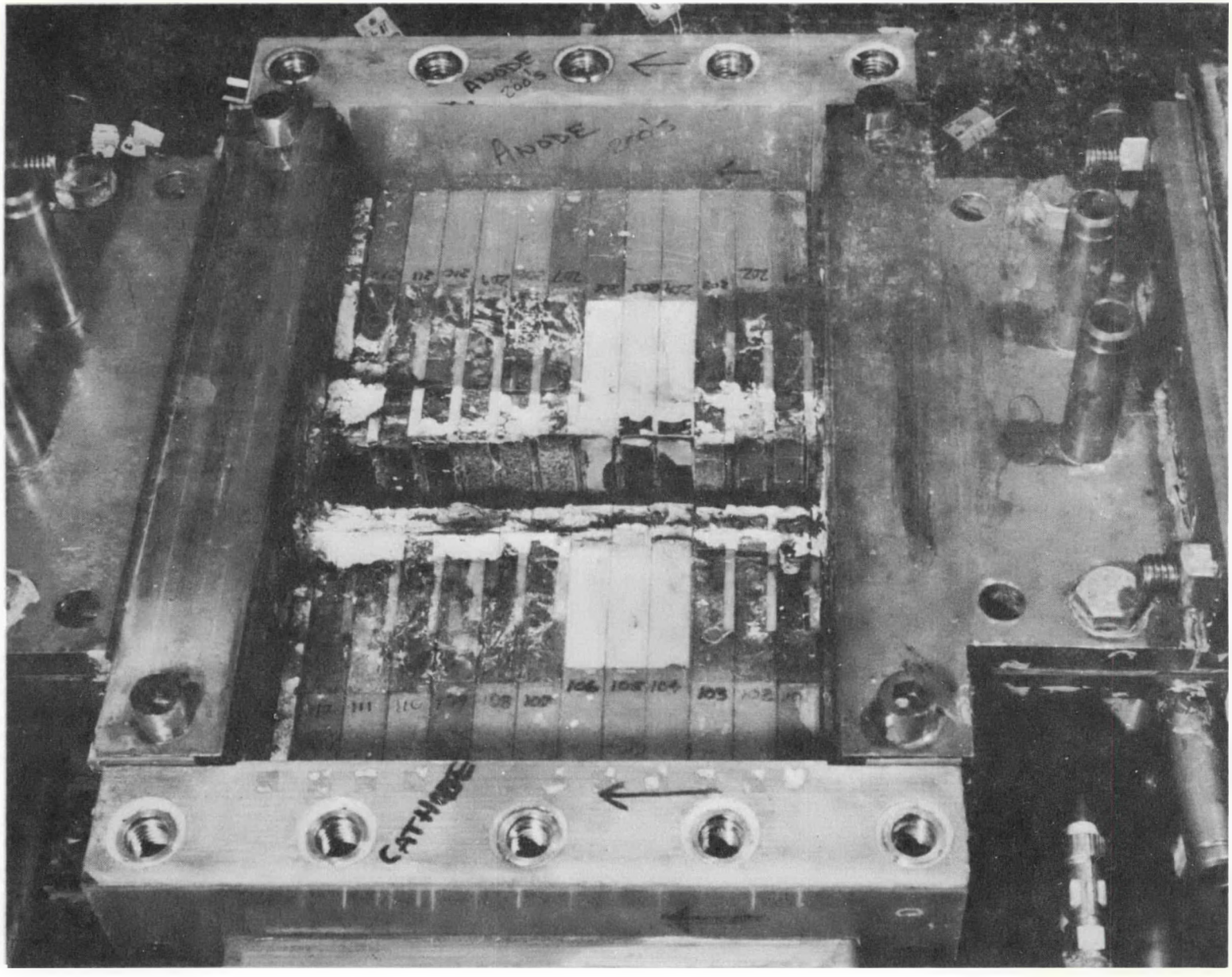

Figure 55. Proof Test 2 Test Section (Looking at Anode Wall) After Removal of Top Insulating Wall

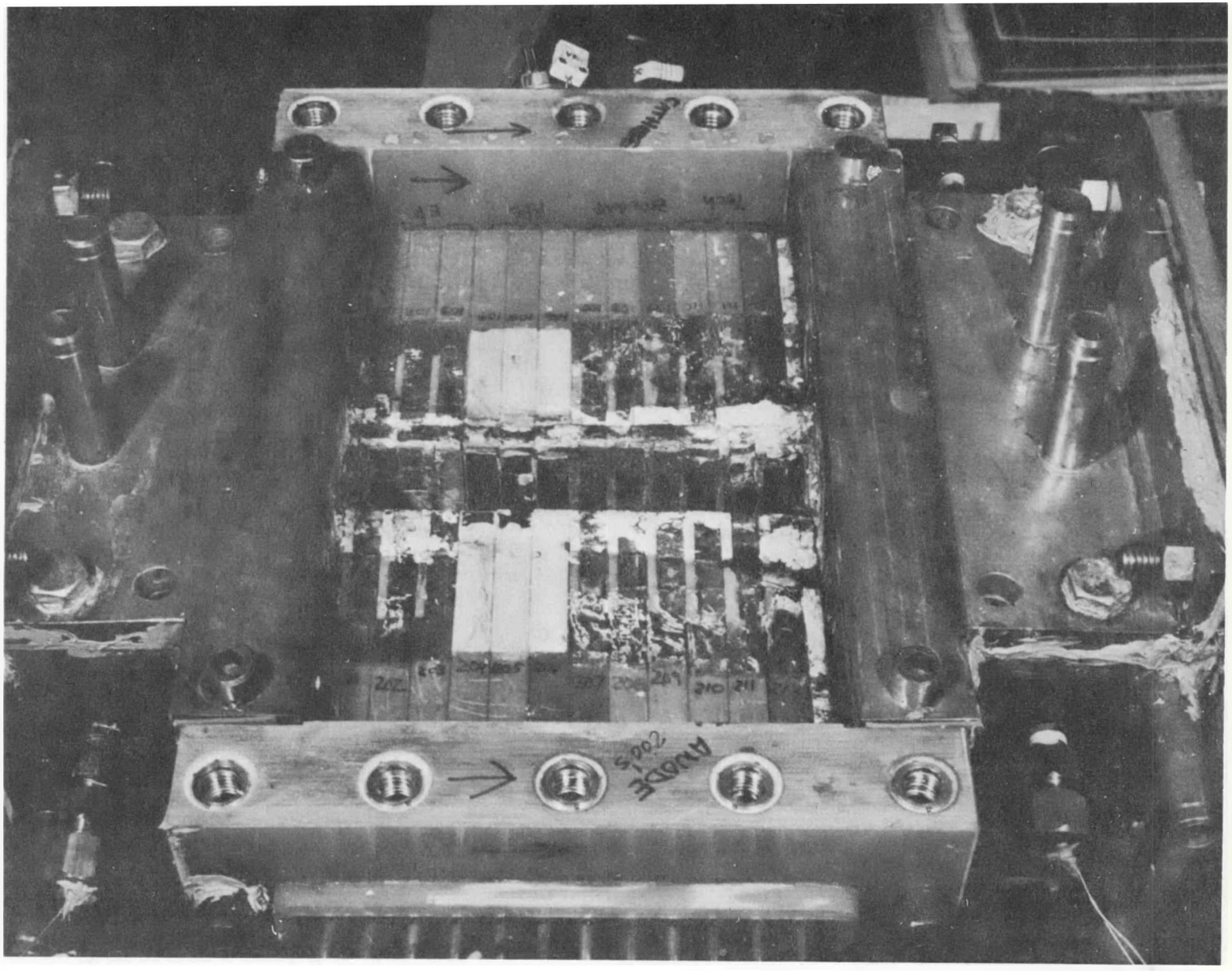

Figure 56. Proof Test 2 Test Section (Looking at Cathode Wall) After Removal of Top Insulating Wall

the next hour. Comparisons of cathodes and anodes (Figure 57) showed that the cathodes suffered the most damage. Much of this damage appeared to be associated with seed penetration, hydration and swelling. A summary of visual observations of individual electrodes is as follows.

All electrodes appeared in excellent condition; very little damage and no general differences between anode and cathode appearance. No cavities, no arcing or erosion paths were noticeable. Insulators looked good. Major insulator cracks were evident only on insulators upstream of electrodes 101 and 201. Electrode 101 had material flow over the insulator to 102. No other gross material flow was observed.

Hydration of seed started in 10 minutes with cathode 112, followed by 110 and 111. After 20 minutes, 105 and 106 began to show signs of hydration. After 30 minutes hydration effects were noted on electrodes 211 and 210 of the anode. Hydration caused swelling and general degradation with time and should not be construed as damage during test. Observations of individual electrodes are as follows:

Cathode		Anode	
101	Center tile cap appears missing, melting flow appearance, rest of surface appears undamaged.	201	All three in this group have the same general appearance, surface slightly recessed.
102	Very good condition, all caps in place, no evidence of melting.	202	Possible top cap gone or slight wear.
103	All tiles in place, some swelling on downstream edge, some evidence of melting on upstream edge in one spot migrating on MgO.	203	Possible raised cap or swelling compared to 201 or 202
104, 105, 106	All caps gone, surface under caps appears undamaged, hydration has started after opening.	204	Most of cap gone (~85%) little wear on $LaCrO_3$.
		205	Cap gone but no wear on $LaCrO_3$.
		206	Most of cap remaining but slightly curled, hydration has started on opening channel.

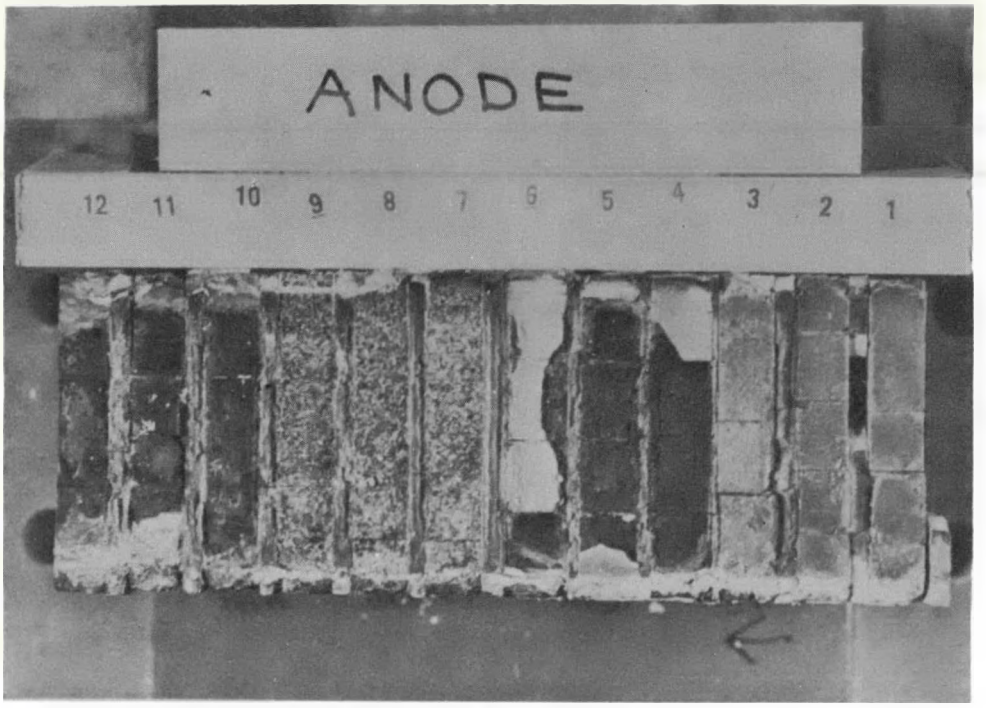

a) Anode Wall

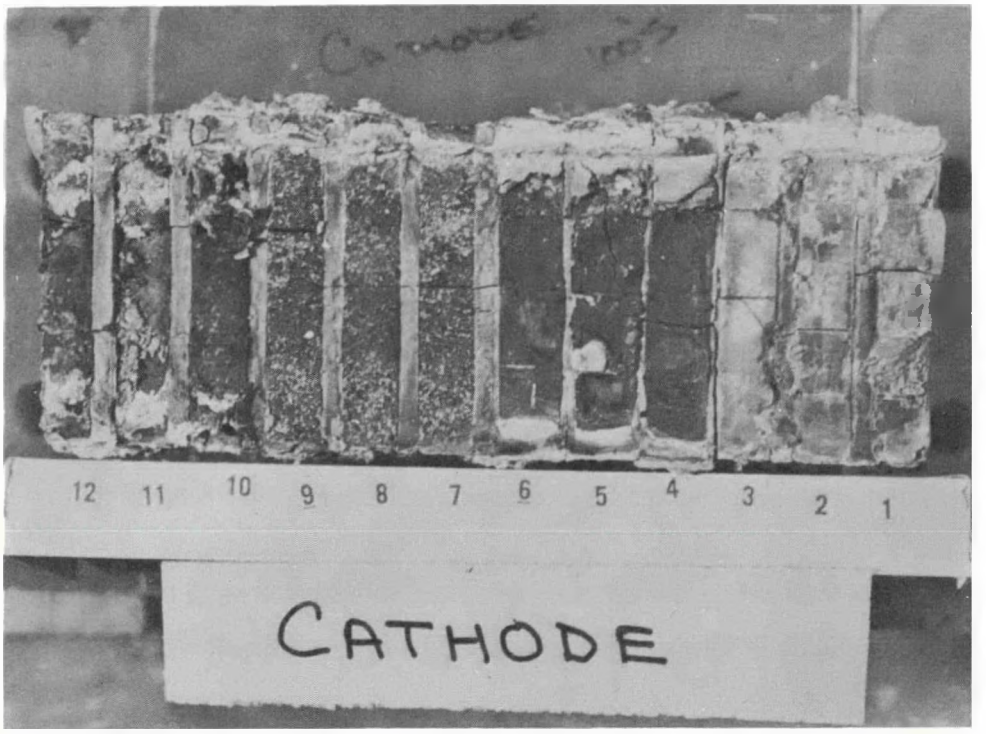

b) Cathode Wall

Figure 57. Proof Test 2-Top View of Walls

Cathode		Anode	
107, 108, 109	Very good condition, granular appearance on surface probably due to exposed ZrO_2, no evidence of wear, not much hydration.	207, 208, 209	All appear identical, very little or no wear, some granular (ZrO_2) showing, not much hydration, brown grains (ZrO_2), black $LaCrO_3$.
110, 111, 112	Very good condition, no damage on opening module, severest hydration on exposure to moisture	210, 211, 212	Good condition on all electrodes electrodes on opening, shows hydration effects and surface falling apart due to hydration.

Subsequently both anode and cathode walls were each cast in epoxy resin. Each module (anode and cathode) was cut through the center in a plane parallel to the plasma flow and perpendicular to the plasma-electrode surface. Sections were distributed to the National Bureau of Standards and to Battelle's Pacific Northwest Laboratories for post-test analysis. This analysis should be completed in early January and will be reported in the next quarterly report.

5.2.2.4 Experiment Analysis

Results of the post-test experiment analysis are presented in the following sections for Proof Tests 1 and 2. Subsections are provided for each test to cover thermal performance, electrical performance and materials performance. However, prior to presenting the detailed results some discussion is in order relative to the impact of Proof Test 1 on the subsequent test.

Detailed thermal analyses were completed for each electrode system under Westinghouse design cognizance to size the electrodes for the proof tests (see Section 5.2.2.1 and the prior quarterly report, Reference 11).

Definition of facility operating conditions is accomplished through predictions using a one-dimensional duct analysis code. For a given electrode thermal design, i.e. with surface temperature and heat flux specified, this code can be used to identify mass flow and plasma temperautre.

Thermal Performance-(Proof Test 1-WESTF Test 37)

During Proof Test 1 primary reliance was placed on extrapolating electrode hot face thermocouple data to the surface and on data provided by the two-color pyrometer which was viewing a section of the electrode wall. Plasma temperature must be known to insure establishing the correct thermal conditions; there is a minimal problem in defining mass flow rate. No direct measure of plasma temperature is available in the facility and the two-color pyrometer was indicating neither the wall temperature nor the plasma temperature, but something in between.

At the same time wide variations in electrode cooling block water calorimetry were observed and inferred heat fluxes from the hot and cold face electrode thermocouples were similarly subject to wide variations. As a result thermal conditions for Proof Test 1 were excessive and overtemperaturing of the electrodes resulted. This was evident in the physical condition of the electrode walls noted during disassembly and further supported by the post-test materials characterization.

Studies were initiated to investigate methods of refining testing techniques and to better understand the interactions encountered in the test assembly. These studies were directed towards a better understanding of:

- plasma temperature,
- thermocouple influences on local material temperatures, particularly with regard to the hot face electrode thermocouple,
- cooling block water calorimetry
- the impact of variations in material properties on temperature projections, and
- the effect of other "errors" inherent in the use of thermocouples.

To obtain a better estimate of plasma temperature, sacrificial iridium-rhodium thermocouples were located in the mixer and inlet transition section. A heat balance model of the iridium rhodium thermocouple was used to predict the error in the thermocouple reading; the error is the difference between apparent and real plasma temperature. The heat convected to the thermocouple is equated to

the heat irradiated from the couple plus the heat conducted from the couple to the wall. The thermocouple error (T_g - Tc) i.e., plasma temperature minus indicated temperature, is then a function of velocity of the plasma, couple bead diameter, distance of the couple bead from the wall, couple bead radiant emmisivity, wall temperature, and couple wire diameter.

A map of mixer thermocouple error is shown in Figure 58 for a 1/4 inch (6.3 mm) imersion of a bare thermocouple in a 55 ft/sec (16.8 m/sec) velocity plasma, typical of Proof Test 2. The error is given as a function of indicated temperature (TC) and a measured wall temperature TW, which is most accurately determined by a vanishing filament pyrometer. A calibration hold point was established for Proof Test 2 in order to compare this plasma temperature prediction with heat fluxes and material temperatures in the electrodes.

A design point match between plasma temperature, mass flow, heat transfer coefficient, heat flux and wall temperature is shown as a function of axial position in Figure 59. The calibration point was chosen such that the plasma was 2123°K at the entrance of the channel and this calculation, being subject to a geometry constraint gave a wall temperature of 1347°C. The theoretical match between the various quantities affecting heat transfer at the calibration point is shown is shown in Figure 60. Note that the mass flow is held constant and the more dense plasma has a lower velocity.

Returning now to Figure 58, the calibration point and design point mixer temperatures are drawn on the map of mixer thermocouple error. Two triangles locate the estimated operating points of the mixer at the cal point and the design point. Note that the thermocouple error did not vary appreciably in this operating range, the error being 130°C at the cal point and 160°C at the design point. Also note that the mixer wall temperature (TW) is estimated to operate at 1810°K at the cal point and 2300°K at the design point. This method of measuring the plasma temperature is subject to inaccuracies resulting from deviations in assumed plasma velocity and assumed radiation emmisivity of the thermocouple as well as errors in the estimation of wall temperature, but still establishes the temperature of the plasma within $\pm$ 50°C and is as accurate as most radiation detection methods.

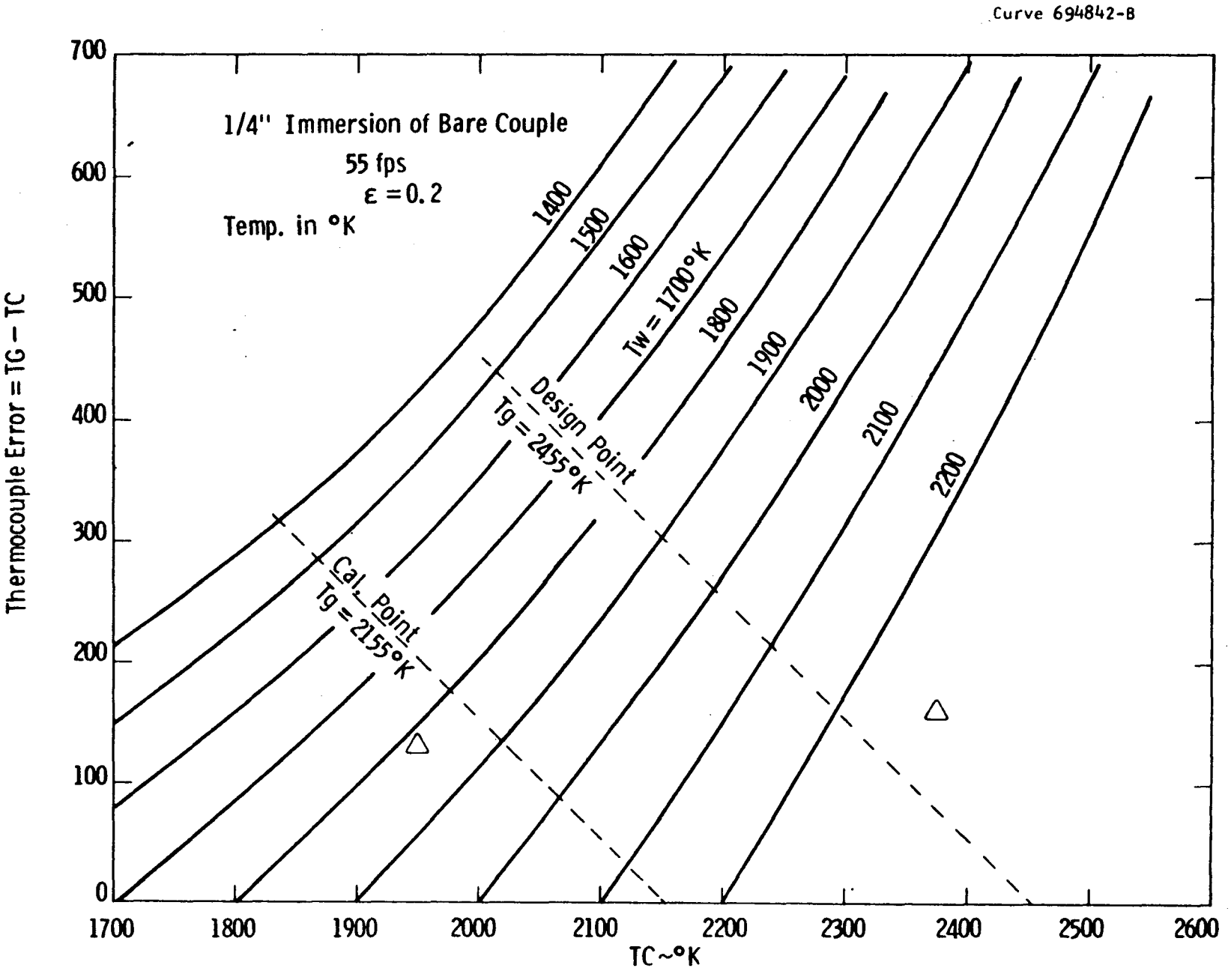

Figure 58. Map of Thermocouple Error in Measuring Plasma Temperature in Mixing Section

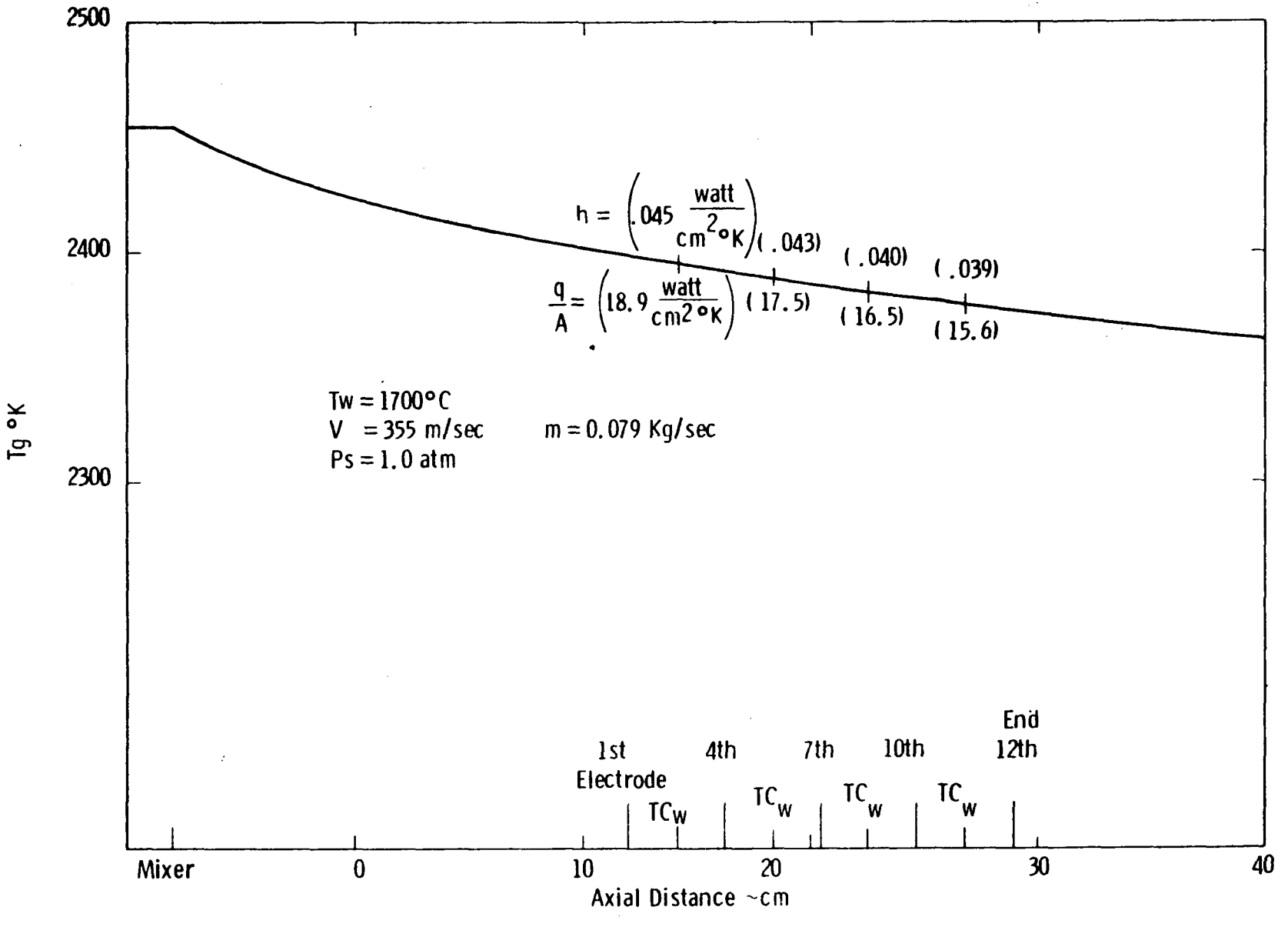

Figure 59. Design Point Theoretical Match Between Various Quantities Affecting Heat Transfer in Proof Test 2

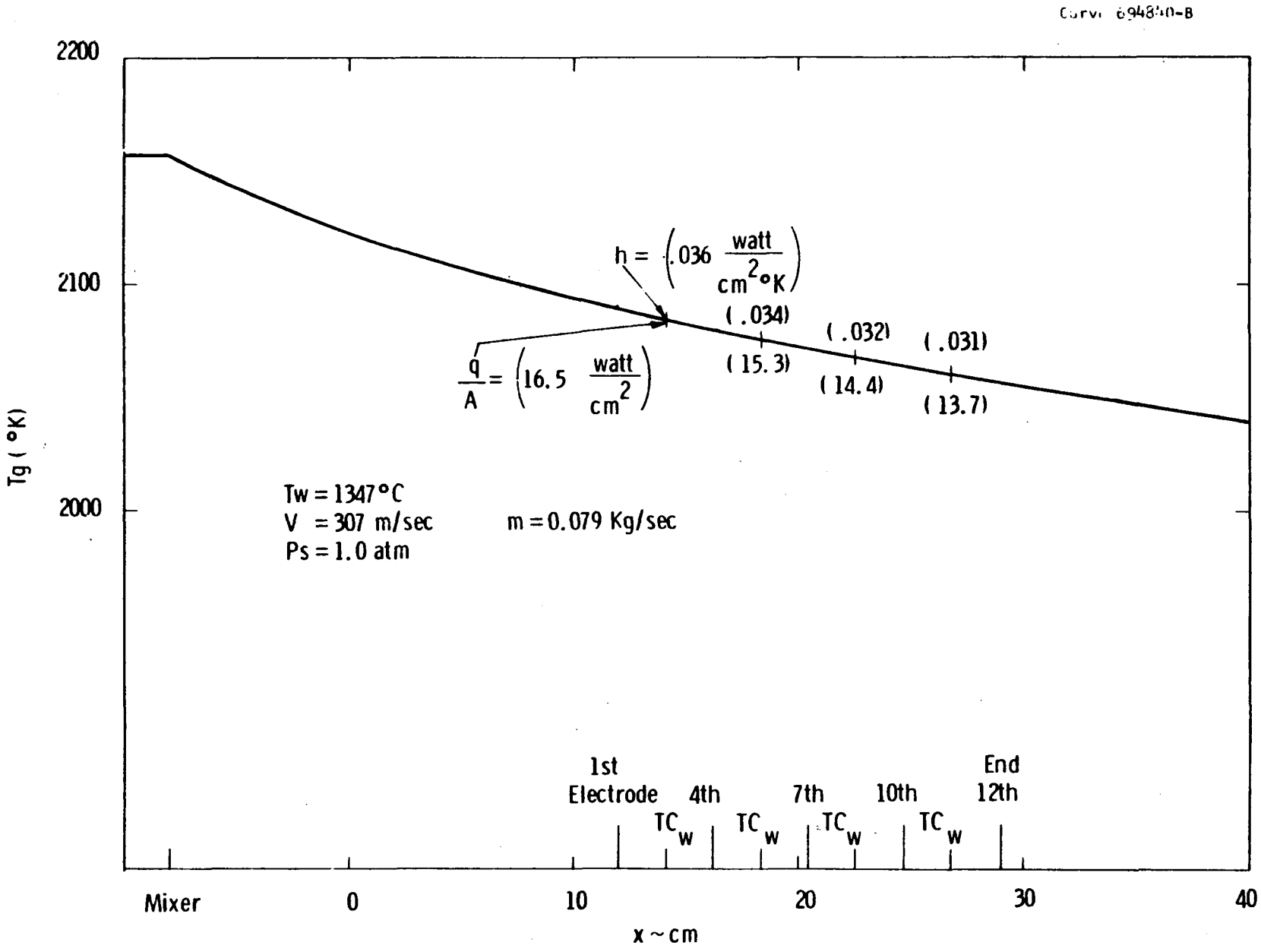

Figure 60. Calibration Point Theoretical Match Between Various Quantities Affecting Heat Transfer in Proof Test 2

Analytical investigations have shown that the thermocouple located close to the hot face of the electrode does result in a lower indication of material temperatures even though the thermocouple tip is positioned along isothermal lines. These analyses have not yet been completed but empirical data from Proof Test 2 gives an indication that this effect could be as much as 100 to 150°C when reflected to the surface. This empirical data is a comparison of sheathed as unsheathed thermocouples included in Proof Test 2 at equivalent thermal positions.

Cooling block water calorimetry did not provide an accurate measure of electrode system heat flux normal to the electrode surface. Significant heat inputs came from the insulating sidewalls and from heat transferred into the electrode and its high thermal conductivity attachment by gas flowing in the interstitial spaces between the electrode wall elements. In Proof Test 1 this was particularly true in the case of the "FLEXBED" attachment. The addition of seed resulted in a significant reduction in heat input measured by calorimetry. Sealing of selected surfaces in Proof Test 2 materially improved the usefullness of the calorimetry data.

The detailed thermocouple investigations resulted in completing an error analysis which included uncertainty in plasma temperature and material property uncertainty. A parametric study was made of the electrode temperature variation with $\pm 2\sigma$ variations of the heat transfer coefficient and material conductivity. It was found that the electrode hot surface temperature would vary as much as $\pm$ 80°C with heat transfer coefficient and $\pm$ 85°C with material conductivity. The SRS of the surface temperature variation proved to be 94 to 100°C. A parametric analysis also indicated that the variation in temperature at the nominal sensor location is similar to the variation at the surface. In addition the physical size of the thermocouple introduces these effects: there is a large temperature variation in the ceramic across the diameter of the sensor and the thermocouple alters the local temperature profile, (sheath conductivity versus ceramic conductivity). Finally the actual location of the thermocouple bead within the thermocouple tip is quite important since the ceramic temperature varies hundreds of degrees in one thermocouple diameter. The thermocouple bead locations were very carefully

determined through dimensional inspection and radiographs. Combining all of the above uncertainties at the thermocouple locations resulted in a net uncertainty of ± 60 to 90°C at the hot side thermocouples, ± 25 to 50°C at the cold side couples and ± 70 to 95°C on the difference between the hot and cold thermocouples. Finally the uncertainty between surface temperature and hot thermocouple was ± 45 to 80°C. Typical magnitudes of these numbers are: for a surface temperature of 1700°C, the hot thermocouple would read about 400°C less ± 80°C and the hot-cold thermocouple reading would be about 1000°C ± 90°C.

Following Proof Test 1 complete temperature predictions were made for each electrode using the fine grid three dimensional model at each of two calibration holds incorporated in the test sequence at the approach to design conditions and at the nominal design point. Using pre-test inspection data to precisely define thermocouple bead location, predictions were made for each sensor located in the electrode. Results of the error analyses were applied to these predictions to define the expected temperature band.

These predictions were compared graphically with actual test data during the test as was predicted and measured plasma conditions, In this manner it was possible to relate the performance of each instrumented electrode to the predicted envelope and effectively interpret test conditions.

Electrical Performance (Proof Test 1 - WESTF Test 37)

A summary of voltages impressed on the electrodes system and the load currents drawn through each electrode-pair is given in Table 15. The original work plan had been to operate each individual electrode-pair at a 1.25 A/cm^2 load density, corresponding to a current of about 6.2 amperes. However, a number of the electrode-pairs were not brought up to full loading in order to minimize operational instabilities and to decrease the joule heating of electrodes.

The channel was operated continuously except when voltage was interrupted for special electrical tests at the beginning, in the middle and at the end of the run. The special tests consisted of the conductivity measurements discussed in Reference 11 and interelectrode leakage measurements (See Figure 61).

TABLE 15. IMPRESSED VOLTAGE VS. AMPERES AT DIFFERENT INTERVALS DURING TEST 37, ELECTRODES FLOATING, 10/10 to 10/11/77

Date	Time		ELECTRODE - PAIRS												
		VL IL	1	2	3	4	5	6	7	8	9	10	11	12	
10/10	18:00						(SEED ON)								
	18:13	VL	45	46	46	45	47	47	46	50	50	52	56	56	Volts
		IL	1.0	1.0	1.0	1.0	0.7	0.85	0.8	0.2	0.25	0.5	1.6	1.3	Amps
	19:45	VL	33	33	31	26	28	25	26	31	40	39	34	40	Volts
		IL	14	1.3	1.1	1.0	0.6	1.0	0.9	0.2	0.2	1.0	.15	2.0	Amps
	20:25	VL	67	68	69	69	71	62	69	75	89	86	81	85	Volts
		IL	2.7	2.4	2.1	2.5	1.7	2.8	2.3	1.1	2.5	4.1	0.1	4.4	Amps
	22:40	VL	68	80	68	69	90	53	84	73	94	58	112	63	Volts
		IL	2.5	4.2	2.2	2.4	2.3	3.3	3.6	1.6	1.2	2.6	0	3.2	Amps
	23:52	VL	80	121	127	120	123	120	114	116	122	94	120	73	Volts
		IL	2.4	6.3	6.0	6.3	4.6	6.2	5.8	5.8	1.5	4.0	6.0	3.0	Amps
10/11	1:00	VL	78	120	132	130	136	130	124	116	124	97	104	76	Volts
		IL	2.5	6.4	5.7	6.3	4.5	4.8	6.0	5.8	1.2	4.9	6.4	2.4	Amps
	2:30	VL	88	94	129	128	138	135	126	128	123	112	104	78	Volts
		IL	0.6	7.0	6.2	6.2	3.8	6.0	6.2	66	1.2	6.0	6.5	2.1	Amps
	4:07	VL	36	34	65	110	126	106	110	116	127	103	106	78	Volts
		IL	4.1	0.0	2.0	6.0	4.0	4.0	5.4	2.9	2.4	5.5	6.5	2.0	Amps
	5:00	VL	28	28	64	86	106	85	98	120	89	94	90	56	Volts
		IL	2.8	0.0	2.6	6.0	39	2.7	6.2	2.0	0.6	6.0	6.2	0.1	Amps
	9:00	VL	10.0	13	43	67.0	72	42	66	35	61	69	73	40	Volts
		IL	1.6	0.3	2.5	6.0	4.0	0.3	6.0	0.5	1.3	5.8	63	0.8	Amps
	12:27	VL	14	9	46	96	83	44	94	102	63	84	66	60	Volts
		IL	0.7	0.9	1.8	6.0	1.9	0.7	6.0	2.9	0.4	5.6	6.2	0.6	Amps

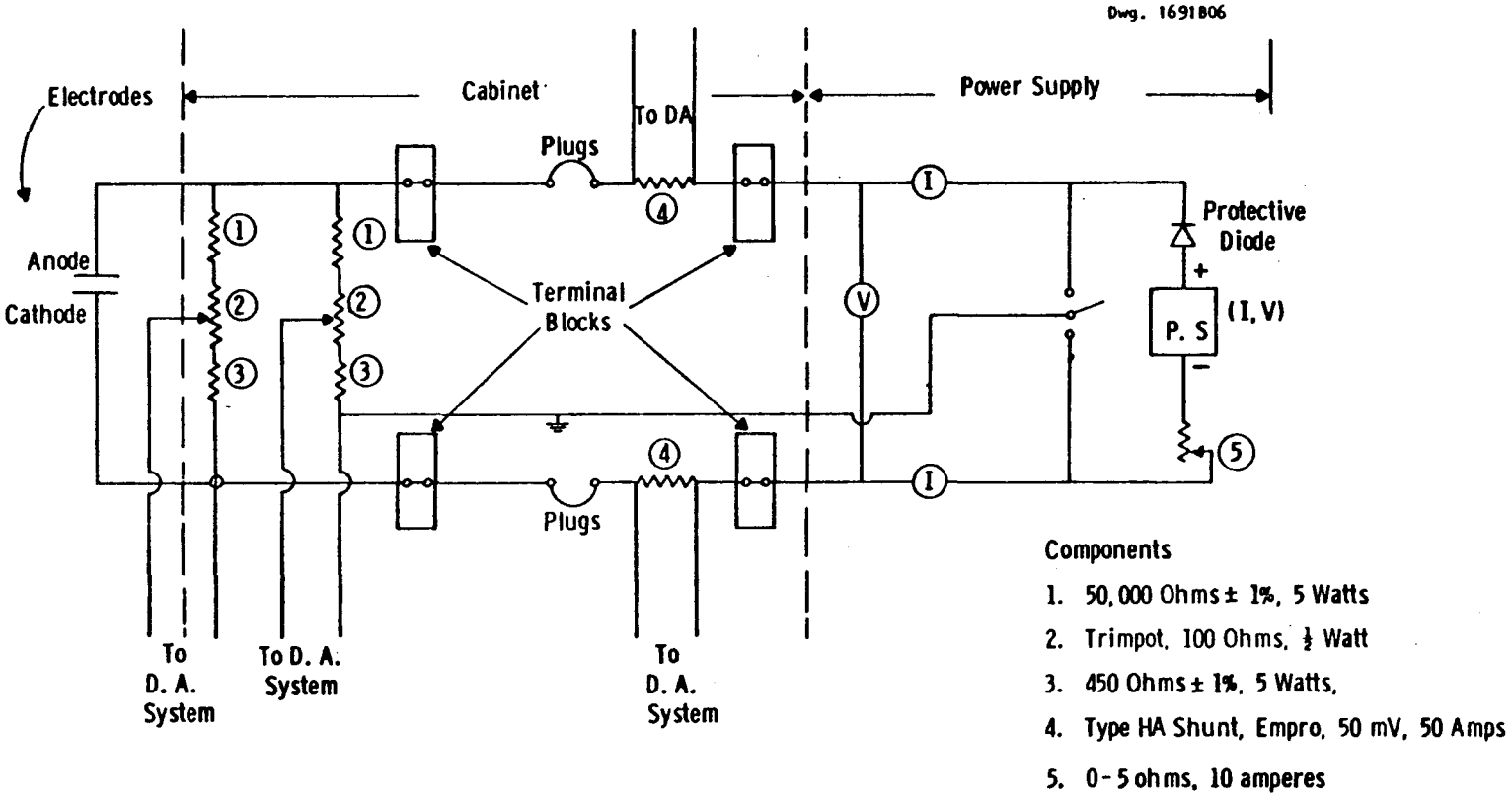

Figure 61. Circuit Diagram for Electrical Measurements on Electrodes Showing Access by the Data Acquisition System (D.A.S.)

At the beginning of the test the average value of plasma conductivity calculated from the measurements was about 3.1 mhos/meter. The average value of the conductivity determined in the middle of the test was 4.5 mhos/meter, and at the end of the test was 4.4 mhos/meter.

The plasma voltage drop, V_p i.e. the voltage necessary to impress the required electrode current through the plasma, neglecting anode and cathode falls and the voltage drop across the electrodes, is given by the equation:

$V_p = IR = I \rho L/A = I37.8/\sigma$, where σ is the conductivity in mhos/m.

The assumption is made that the effective electrode length is 5 cm and its pitch is 1.349 cms. For a current of 6 amperes, and σ = 3.1 mhos/m, the voltage drop expected is 73 volts. The expected voltage drop across the plasma for σ = 4.5 mhos/m for a current of 6.0 amperes is about 50 volts.

It is evident that the voltage difference ΔV between the voltage, V_L, applied to an electrode-pair to produce a given current through it, and the voltage drop across the plasma, V_p represents the sum of the anode and cathode falls and the potential drop across the anode and cathode electrodes.

$$\Delta V = V_L - V_p.$$

For a good MHD electrode design it is of course desirable to have ΔV, which can be considered to be an electrical figure of merit, as small as possible. At the same time the electrode configuration must demonstrate the capability of standing up in the MHD environment with minimum evidence of mechanical or electrical degradation.

Referring to MHD type operation, the voltage V_L applied to the electrodes to pass a given current, represents the total voltage losses which would be incurred in an MHD system having the same electrodes design for a given value of plasma conductivity depend on the anode-cathode spacing, ΔV which is the

sum of the potentials loss across the electrodes, plus the anode and cathode falls, is an appropriate value to use as an electrode figure of merit. It should be pointed out that much of the power, $I_L V_L$, which is lost in an MHD generator, may be used either downstream in the same generator or in the bottoming plant.

Table 16 lists calculated values of ΔV for the different electrode pairs of run 37 for the early and final parts of run 37. The 2352 time listed is the time when the electrode-pairs which were to run at 6 amperes were first brought to their maximum operating loadings. The last readings of the run were taken at time 1354, 10/12/77, just before operation of the life test was terminated to permit making the final electrical tests. The electrode materials used in run 37 are also listed in Table 16 for reference purposes.

Comparisons of ΔV values can only be made between electrode-pairs operating at the same currents since the voltage drops which occur in a given electrode-pair vary with current. At the beginning of the tests the ΔV values for 6 ampere loading varied between 44 and 54 volts. The electrode-pairs operating at 6 amperes were 2, 3 and 4, MAFF 41 material, electrode pairs 6 and 7 plasma sprayed MAFF 31, electrode pair 8 with yttria electrodes, and electrode pair 11 with $LaCrO_3$. Electrode-pair 11 served as a guard electrode. From Table 15 electrode-pair 10 (cathode-ceria-hafnia, anode-yttria) which was brought up to 6 amperes loading some 2-1/2 hours later than the others. Its ΔV value at this time was 39 volts.

From Table 16 only four of the electrode-pairs listed were still being operated at 6 amperes at the end of test 37. The electrode-pairs still operational at 6 amperes were:

- Electrode-pair 4 (MAFF 41), ΔV, = 52 volts
- Electrode-pair 7 (MAFF 31), ΔV = 47 volts
- Electrode-pair 10 (ceria-hafnia cathode, yttria anode) ΔV = 39 volts
- Electrode pair 11 ($LaCrO_3$), ΔV = 15 volts.

TABLE 16. VALUES OF ΔC FOR DIFFERENT ELECTRODE PAIRS AT BEGINNING AND END OF RUN 37, ELECTRODES FLOATING WITHOUT SLAG

Electrode Pair	10/11/77, T=3.1 mhos/m TIME: 2352 VL volts	IL amps	V_p volts	ΔV volts	ELECTRODE MATERIALS	10/12/77, T=4.5 mhos/m TIME: 1354 VL volts	IL amps	V_p volts	ΔV volts	Electrical Performance
1	80	2.4	29	51	Sintered $LaCrO_3$ Guard Electrode	19	1.1	9.2	7	
2	121	6.3	77	44	Sintered $4MgAl_2O_4.1Fe_3O_4$ (MAFF41) Fe_3O_4	25	0.4	3.4	22	
3	127	6.0	73	54		49	1.8	15	34	
4	120	6.3	77	43	Sintered $4MgAl_2O_3.1Fe_3O_4$ (MAFF41) Fe_3O_4	102	6.0	50	52	good
5	123	4.6	56	67	Plasma Sprayed $3MgAl_2O_4.1Fe_3O_4$ (MAFF31)	91	3.9	33	58	
6	120	6.2	76	44	Plasma Sprayed $3MgAl_2O_4.1Fe_3O_4$ (MAFF31)	52	.05	--	52	
7	114	5.8	68	46	Plasma Sprayed $3MgAl_2O_4.1Fe_3O_4$ (MAFF31)	97	6.0	50	47	good
8	116	5.8	68	48	Hot Pressed HfO_2 - Metal Composite	102	3.0	25	77	
9	122	1.5	18	104	Hot Pressed HfO_2 - Metal Composite	64	1.1	9.2	55	
10	94	4.0	49	45	Hot Pressed HfO_2 - Metal Composite	86	5.6	47	3.9	good
11	120	6.0	73	47	Sintered $LaCrO_3$ Guard Electrode	67	6.2	52	15	excellent
12	73	3.0	37	36	Sintered $LaCrO_3$ Guard Electrode	42	1.5	13	29	

The ΔV value for electrode-pair 4 increased from 43 to 52 volts during the run. The value of ΔV did not change for electrode-pair 7. The ΔV value for electrode-pair 10 dropped 10 volts during the run. However, electrode-pair 11 ($LaCrO_3$) dropped some 32 volts from 47 to 15 volts during the run.

On the basis of the electrical data it would appear that electrode-pair 11 ($LaCrO_3$) demonstrated the best electrical performance during the test. Yet there was some difficulty at the beginning of the run, See Table 15, in passing significant current through this electrode-pair. When seed was first introduced, electrode-pair 11 operated satisfactorily at low currents for about 20 minutes. For the next 3 hours negligible current was drawn despite an increase in V_L to 100 volts. Electrode-pair 11 then operated satisfactorily for the remainder of the test.

From life tests that were conducted at a later date with $LaCrO_3$ samples under electrical loading as a function temperature it is possible to surmise why the ΔV value for electrode-pair 11 ($LaCrO_3$) dropped during the run. From the special $LaCrO_3$ tests it was clear that many of the $LaCrO_3$ samples initially had relatively high electrical resistances. The resistance of such $LaCrO_3$ samples tend to drop by an order of magnitude after the samples are heated for fairly long periods of time while passing electrical current. It is surmised that the 30 volt drop in ΔV for electrode-pair 8 was due to a similar decrease in the resistance of the $LaCrO_3$ and possibly to improvement in the electrical contact to the $LaCrO_3$ during the early hours of Test 37.

The obstruction to the passing of current experienced for a few hours after EP-11 successfully passed current for some 20 minutes may be due to an initial overheating of the Ag-epoxy seal used with the electrodes to EP-11. Our tests have indicated that the Ag epoxy seal will fail if heated to the order of 250°C to 300°C. Just how electrical contact was re-established is not clear.

It seems likely that the final ΔV value of 15 volts observed for EP-11 is the sum of the anode and cathode falls. It is possible to gain some insight into

the anode and cathode potential falls experienced with hot electrodes from data obtained during the course of measurements on plasma conductivity.

Our test data, which will be discussed later in this report shows that the cathode and anode falls are relatively small for electrodes running at surface temperatures of the order of 1600°C or higher. The low anode and cathode fall associated with hot electrodes is confirmed in the data on electrode-pair 11 just cited.

Two of the six MAFF 31 electrode pairs were operable at 6 amperes for the duration of the test. Of the HfO_2 metal composites, electrode-pairs 8 to 10, only EP-10, could be operated at approximately 6 amperes for the duration of the test. At the end of the test the ΔV values for the electrode-pairs operated at 6 amperes were between 39 and 52 volts for the non $LaCrO_3$ electrodes, which leads to the conclusion that the electrode-pairs having MAFF 31, MAFF 41 and the hot pressed HfO_2 metal composites all experience relatively high IR drops across the electrodes during operation at 6 amperes.

In order to obtain a better picture of the speed of decay of conductivity when the seed was turned off, the seed was interrupted at the end of the test with the electrode voltages on. Data taken just before and after seed was interrupted are given in Table 17. From Table 17 it is evident that within 4 minutes after seed interruption occurred, the load current dropped by the order of 30 to 40%. However as much as 40 minutes later a number of electrodes were still carrying of the order of 20 to 30% of the original load current.

As noted in earlier quarterly reports when the circuit shown in Figure 61 is operated cathode grounded, the anmeter in the anode circuit in addition to reading plasma current also reads leakage currents from the anode electrodes to ground. The difference between the two currents generally constitute the anode leakage to ground. Operation in the anode grounded mode permits determining cathode leakage currents to ground. Table 18 summarizes various measurements involving anode and cathode grounded operation taken at various intervals of time during test 37.

TABLE 17. IMPRESSED VOLTAGE VS. AMPERES AT DIFFERENT TIMES IN TEST 37
BEFORE AND AFTER SEED WAS TURNED OFF, 10/11/77 ELECTRODES FLOATING

TIME	E.P.	1	2	3	4	5	6	7	8	9	10	11	12
1354	VL	19	25	49	102	91	52	97	102	64	86	67	42
	IL	1.1	0.4	1.8	6.0	3.9	0.0	6.0	3.0	1.1	5.6	6.2	1.5
1412	VL	21	25	52	116	98	64	108	93	64	93	69	44
	IL	0.9	0.2	1.1	6.0	2.4	0.7	6.0	3.0	0.9	4.9	4.1	1.0
1417						S E E D O F F							
1421	VL	20	25	53	120	102	78	116	98	66	93	69	48
	IL	0.65	0.4	0.9	3.6	1.7	0	3.8	0.6	0.0	1.9	1.1	0.3
1445	VL	22	32	56	120	107	84	123	93	78	93	69	47
	IL	0.35	0.0	0.3	2.0	0.8	0.0	2.6	0.3	0.1	1.6	0.7	0.5
1500	VL	22	34	56	128	107	84	124	99	76	93	69	51
	IL	0.4	0.0	0.2	0.8	.75	0.0	2.5	0.4	0.0	1.2	0.5	0.1

TABLE 18. IMPRESSED VOLTAGE VS. AMPERES LOADING FOR CATHODE AND ANODE OPERATION, Test 37, 10/11 and 10/12/77

TIME		1	2	3	4	5	6	7	8	9	10	11	12	
	VL	44	44	45	44	47	45	44	50	60	55	56	55	
10/11 1820	I2	1.2	1.3	1.1	1.1	0.8	1.2	1.2	0.2	0.2	1.0	2.9	2.0	CATHODE
	I1	1.3	1.2	1.0	1.0	0.9	0.9	0.9	0.3	1.5	0.4	2.2	2.0	GROUNDED
	VL	34	30	64	106	112	102	107	136	127	103	105	78	
10/12 401	I2	44	0	2.1	6.6	6.4	4.6	6.0	2.8	2.1	4.4	7.0	2.3	CATHODE
	I1	2.0	1.9	2.1	2.9	2.6	2.5	3.4	3.7	4.1	4.6	4.0	3.2	GROUNDED
	VL	15	23	42	97	82	46	89	93	63	84	61	38	
10/12 1234	I2	0.6	1.9	2.6	6.0	2.2	0.3	6.0	2.9	0.6	5.6	6.3	1.1	CATHODE
	I1	1.4	1.4	2.0	2.6	0.9	2.5	2.7	2.5	3.0	3.6	4.0	2.8	GROUNDED
	VL	22	25	53	123	94	81	120	98	66	93	69	49	
1430	I2	0.5	0.8	0.8	2.9	1.2	0.1	3.3	0.5	--	1.6	1.0	0.2	CATHODE GROUNDED
	I1	0.7	0.6	0.8	1.2	0.6	0.7	1.3	0.7	--	1.4	0.6	0.7	
	VL	43	43	43	43	45	45	45	50	53	55	56	55	
10/11 1813	I2	1.4	1.6	1.3	1.6	.8	1.8	2.0	0.2	0.3	1.2	3.0	2.2	ANODE
	I1	1.5	1.6	1.4	1.5	1.2	1.2	0.9	0.2	2.5	0.5	2.6	2.0	GROUNDED
	VL	40	28	60	101	92	94	95	102	110	105	106	94	
10/12 0404	I2	1.0	0.5	2.6	7.3	0.2	3.7	6.0	1.0	1.2	5.5	2.0	6.0	ANODE
	I1	9.6	0.0	2.6	7.3	10.0	6.2	8.2	7.2	10.0	0.2	4.0	0.1	GROUNDED
	VL	26	32	36	51	63	56	98.0	62	63.0	62.0	60.0	60	
10/12 1240	I2	2.2	1.5	2.0	1.2	0.6	3.7	6.0	0.5	0.6	2.0	3.6	5.4	ANODE
	I1	0.1	0.1	2.4	6.0	5.6	6.0	6.0	3.0	1.5	5.6	6.2	0.1	GROUNDED

At the beginning of test 37 the anode current, I_2, was generally only slightly larger than I_1, the cathode current, when the cathode was grounded. As the test progressed, the differences between the two currents increased, indicating that the leakage currents were increasing. It is evident from Table 18 that cathode leakage to ground which is the difference between I_1 and I_2 when the anode is grounded, tends to be substantially higher than the corresponding anode leakage currents. Thus it would appear that deposition of seed on the cathode by the applied electric field is responsible for a significant increase in leakage current to ground at the cathode electrodes.

One of the problems with operation of the test channel with one set of electrodes grounded is that the presence of a common electrode ground on a particular power supply permits its current to traverse the plasma by way of electrodes which offer a lower impedance contact to the plasma. Such a division of current can occur if there is a significantly lower potential drop across a given electrode configuration, as when the electrode surface is running significantly hotter than its neighbors and as a result the anode or cathode fall is appreciably lower. (The life tests are now conducted with the electrodes floating to insure equal loading of the different electrode-pairs.)

Performance of Insulation

Evaluation of the quality of the insulation is extremely difficult because of the many parallel paths which the leakage currents can take. In addition spurious galvanic potentials occur between different electrodes when seed is present. These potentials are high enough to make it difficult, if not impossible, to make reliable resistance readings during the course of the test using conventional ohmeters, once seed has been introduced.

Table 19 summarizes leakage resistance data taken during run 37 between opposing electrodes, and between the electrodes and ground. The last column in the table indicates the average values of leakage resistance for the measurements taken at a given time. The electrodes, which at the beginning of the tests had leakage resistances substantially higher than 50,000 Ω demonstrate their usual marked characteristic decline before introduction of seed as the temperature

TABLE 19

ANODE TO CATHODE, ANODE TO GROUND, AND CATHODE TO GROUND LEAKAGE RESISTANCE IN OHMS TAKEN AT DIFFERENT TIMES DURING TEST 37

Date	Time	Mode	Remarks	Electrode - Pairs (ohms) 1	2	3	4	5	6	7	8	9	10	11	12	Average
10/10/77	1602	A to C	Prior to Seed	5000	3200	2300	2200	3000	4000	4400	6800	6000	9500	9000	8000	5280
	1738	A to C	Prior to Seed	380	610	460	410	440	550	550	580	660	320	310	135	450
	1804	A to C	Seed On													
	1833	A to C	Seed On	17	18	23	20	46	33	30	310	500	200	16	4	100
10/11/77	410	A to C	Mid-Point	10	12	41	34	145	31	34	260	160	250	28.5	2.5	84
	1252	A to C	End-Point	230	59	52	93	140	23	50	102	84	135	57	112	95
	1504	A to C	End-Point	290	78	89	170	130	35	130	230	112	340	94	11	142
10/10/77	1607	A to G	Prior to Seed	6400	3800	3300	3000	3200	3500	3800	6500	4500	6800	10,500	3800	4295
	1738	A to G	Prior to Seed	1350	900	900	910	990	1020	1010	1600	1700	1080	2000	860	1193
	1804	A to G	Seed-On													
	1833	A to G	Seed-On	95	60	65	63	80	78	75	260	450	180	170	80	138
10/11/77	410	A to G	Mid-Point	9.5	12	40	36	105	44	54	110	109	150	230	60	80
	1253	A to G	Mid-Point	15.0	52	46	49	100	41	48	78	76	120	180	43	82
	1506	A to G	Mid-Point	40	22	17.5	27	26	10	18	35	19	32	36	17	25
10/10/77	1609	C to G	Prior to Seed	6200	2800	3800	2850	2700	2600	2700	6800	7000	4200	10,000	9000	5050
	1738	C to G	Prior to Seed	1380	890	910	950	940	950	960	1350	1220	1150	2200	2200	1260
	1804	C to G	Seed-On													
	1833	C to G	Seed-On	100	60	65	70	82	84	86	140	105	120	195	170	105
10/11/77	410	C to G	Mid-Point	4.5	19	17	19	15.5	19	19	2.5	8.0	7.0	130	170	36
	1255	C to G	Mid-Point	3.0	8.5	11	4.5	9	28	1.0	Short	1.0	1.0	56	54	16
	1507	C to G		84	10	1	4	2	11	7	*	*	*	26	25	19
	1507	C to G	**Reverse Polarity	--	2	35	20	70	80	Short	*	*	*	62	190	

*No reading, galvanic generation of 1 volt D.C.
Symbols: A per anode, C per cathode, G for ground potential
**Reverse polarity refers to reversing polarity on ohmeter.

of the system was increased. About 20 minutes prior to the introduction of seed, the average leakage resistance between anode and cathode for the 12 electrodes averaged about 450 ohms.

After seed was introduced, the average value of leakage resistance across the channel dropped to about 100 ohms. However, the higher values of resistance were across electrode pairs 8, 9 and 10. The average resistance across the remaining electrodes was only 23 ohms. The electrode material for electrode-pairs 8, 9 and 10 consisted of the hot-pressed HfO_2 metal composites shown in Table 16. From Table 19 it is safe to conclude that the low temperature resistance of these electrode materials is high. The reason that the ΔV values of electrode-pairs 8, 9 and 10 did not appear to be significantly higher than the ΔV values for the MAFF 31 in test 37 is apparently due to substantial decrease in the electrical resistance of electrode-pairs 8, 9 and 10 as their temperature was increased by I^2R losses.

Table 20 summarizes the lateral leakage resistances between adjacent electrodes measured during run 37 for the anode and cathode electrodes. Average values for all of the electrodes taken at a given time are shown in the last column of the table. The average values of leakage resistance listed in Tables 19 and 20 are summarized in Table 21. It is evident in all instances that the lateral leakage resistance between adjacent electrodes is less than the leakage resistances observed across the channel, and between the electrodes and ground. It is clear that the lower leakage resistance in the axial direction is a direct consequence of the shorter path lengths for the insulation used between adjacent electrodes.

It is also apparent that the lateral leakage between adjacent cathode electrodes and the resistance between the cathodes and ground is significantly lower for the cathode than for the anode electrodes due to migration of seed ions to the cathode during electrical loading. From Tables 19 and 20 it is clear that the leakage resistance tends to be higher upstream. However, this effect was significantly more pronounced in tests in the copper electrode channel. (See Tables 8 to 14 of the last quarterly report, Reference 11).

TABLE 20. LATERAL LEAKAGE RESISTANCE BETWEEN ADJACENT ELECTRODES IN OHMS TAKEN AT DIFFERENT TIMES DURING TEST 37

TIME	DATE	REMARKS	1-2	2-3	3-4	4-5	5-6	6-7	7-8	8-9	9-10	10-11	11-12	AVG.
		Anode Side												
1611	10/10/77	prior to seed	3500	2800	900	2000	1600	3000	2600	5500	3000	4800	13,500	2600
1741		prior to seed	850	540	340	600	470	690	640	1060	680	45	910	569
1804		seed on												
1839		seed on	40	19.5	17.5	28	25	22	80	350	300	34	135	88
0418	10/11/77	mid point	1.6	14	21	43	45	13.5	29	49	33	200	35	40
1257		end point	42	18.5	22	33	38	17	14	17	12.8	8	48	23
1512		end point	62	34	50	67	38	39	54	68	28	28	75	45
		Cathode Side												
1612		prior to seed	2850	400	410	1000	1200	1150	750	2700	5200	1250	3800	1726
1743		prior to seed	850	355	305	345	415	430	230	140	115	60	185	286
1804		seed on												
1840		seed on	39	18	16	28	34	35	80	75	90	25	20	38
0420		mid point	7	12	12	26	11	1	18.5	8	1.5	9.5	15	10
1258		end point	1.8	short	10	13.5	short	25	13	2.8	1.5	short	4.8	9
1258		*reverse polarity	--	10	--	--	41	--	--	--	0.5	.2	--	16
1514		end point	16	7	27	13	6	28	50	9	25	18	31	19

*reverse polarity refers to reversing polarity on ohmeter

TABLE 21. AVERAGE VALUES OF LEAKAGE RESISTANCE IN OHMS TAKEN AT DIFFERENT TIMES DURING RUN 37, 10/10 and 10/11/77

Date	Approximate Time	Anode & Cathode	Anode to Ground	Cathode to Ground	Lateral Leakage Anode	Lateral Leakage Cathode
10/10	1602	5280	4925	5050	2600	1726
	1738	450	1190	1260	569	286
	1804	SEED INTRODUCED				
	1833	100	140	105	88	38
10/11	0410	84	80	36	40	10
	1252	95	82	16	23	9
	1504	142	25	19	45	19

The effect of the galvanic action referred to previously is shown in Tables 19 and 20 at the close of run 37. Note the substantial differences on Table 18 depending on the polarity of the ohmeter. Similar effects were noted in the cathode leakage resistances between adjacent electrodes at time 1258 hours. See Table 20.

From measurements made to date in the effort to evaluate insulation quality, it is clear that measurements of leakage resistance, while they shed light on processes which occur during channel life test, do not go far enough. In future tests we propose to superimpose axial fields across the channel while at the same time utilizing the present external supplies to simulate normal MHD generator current loading.

It is believed that changes is axial currents observed when axial fields are applied will be directly indicative of changes in insulation quality with life. Perhaps the best test of insulation quality levels will occur when the axial fields are increased to simulate the magnitude of the Hall fields anticipated during operation of MHD generators. Ability of the insulation to survive under MHD Hall field conditions appears to be the best way of ensuring that the insulation will be satisfactory in the MHD environment.

Materials Performance-Proof Test 1 (WESTF Test 37)

Anode and cathode wall sections were cut and polished for examination. Figure 62 shows the as-cut cross-sections of the cathode and anode walls. It is obvious that there is greater loss of material on the anode wall. In particular anodes 208 and 209 show loss of material to the mesh (almost to the copper cooling block). Progressing away from these two anodes there is decreasing recession of electrode material. The $LaCrO_3$ quard electrodes appear more resistant to the plasma and show less material loss than the electrodes under test. Subsequent examination was conducted by use of the scanning electron microscope (SEM) with EDX attachment for semi-quantitative micro-chemical analysis and by X-ray diffraction analysis. Optical microscopy was used for orientation purposes and detecting gross features. Almost all this post-test materials characterization work has been conducted at either the National

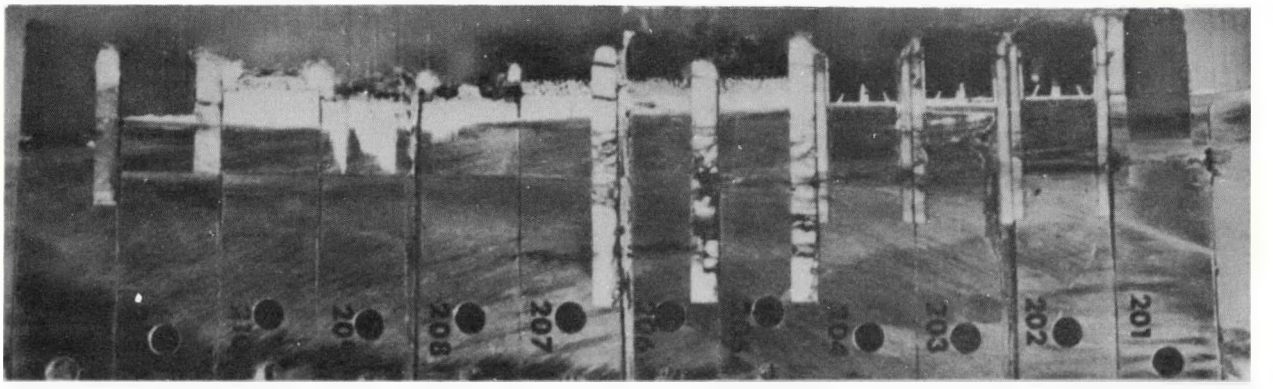

1.15X

a. Anode Wall

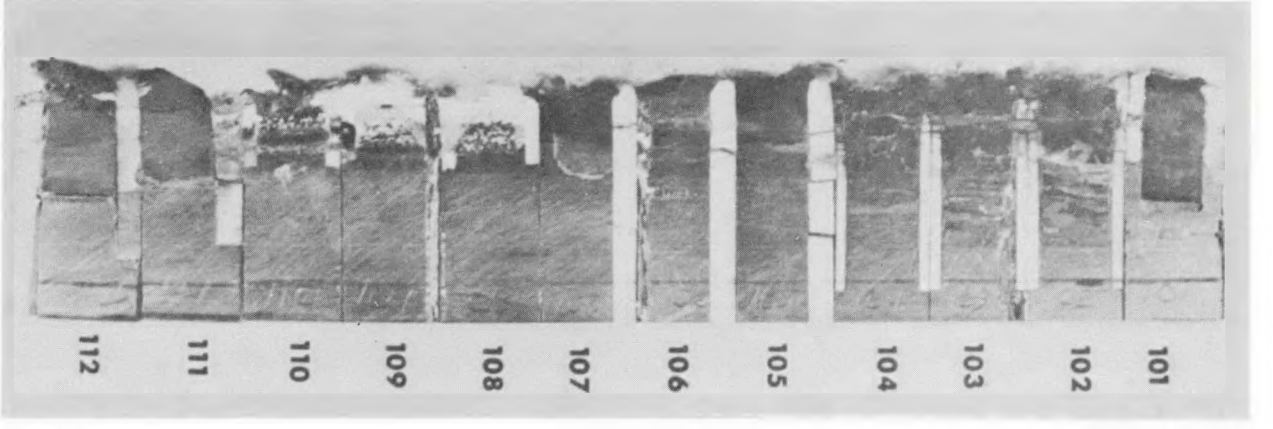

b. Cathode Wall

Figure 62. Proof Test 1, Wall Cross Section (As Received

Bureau of Standards or Battelle's Pacific Northwest Laboratories. Analysis is complete and preliminary reports have been submitted. Detailed reports of these analyses will be included in a topical report summarizing the three proof tests. In this report only a summary of these results will be given.

During the test temperatures exceeded the 1700°C design temperature. This was due, in large part, to uncertainties in heat fluxes and thermocouple measurements. Heat fluxes, during the test ran higher for anodes. While the resultant morphologies and microchemistries were consistant with melting/recrystallization for both walls, 'melting' phenomena is more evident at the anode wall. Furthermore, significant amounts of ZrO_2(CaO) contaminant were found on both walls (with higher contents on the anode wall). This contamination most likely came from the upstream CaO-stabilized ZrO_2 'nozzle'. Available evidence suggest that anodes 208-209 and 210 ran very hot and were subjected to extensive surface melting, perhaps accelerated by interaction of HfO_2-based materials with Fe-containing upstream electrodes. Conceivably, zirconia from upstream more easily could be entrapped digested and retained within anode areas containing an extensive, pre-existing fluid phase. Hence, the apparent partitioning between electrode walls.

Also, analysis showed considerable cross-contamination between $MgAl_2O_4.Fe_3O_4$ electrodes and $LaCrO_3$ quard electrodes. In all, it is quite clear that in future tests a multitude of differing materials must be avoided to decrease the probability of degradation due to interactions among adjacent (but unlike) materials.

A summary of the individual groups of electrodes follows.

Sintered MAFF Electrodes (General Electric)

The overall integrity of both the anode assemblies appears to have been fairly well preserved in spite of extensive corrosion (see Figure 63). An estimated 35-50% corrosion has occurred at the anode and 20-35% at the cathode, using $LaCrO_3$ electrodes 101, 201 for comparison and assuming all electrodes were at the same level at start-up. Penetration of seed has caused severe weakening of the

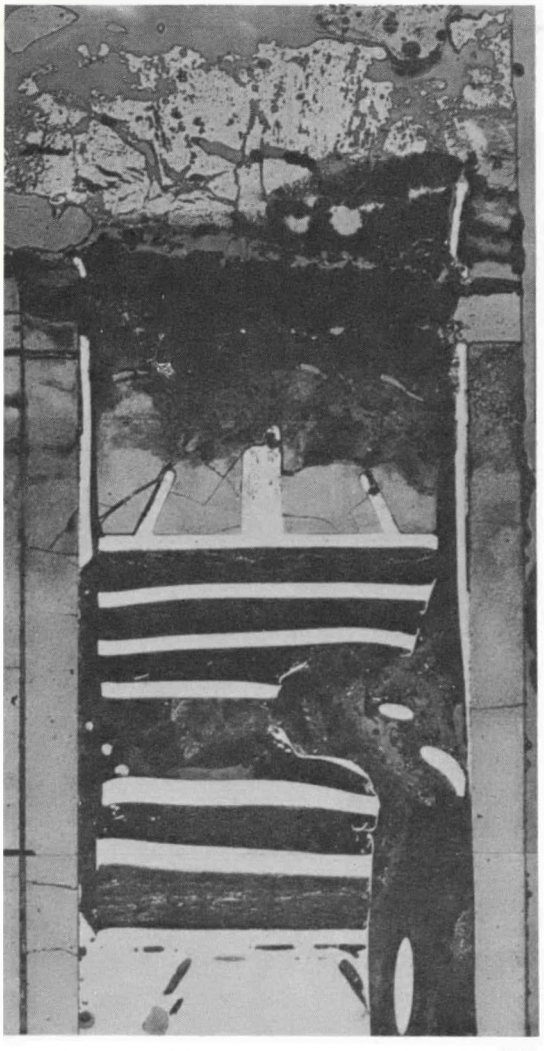

8X

#103

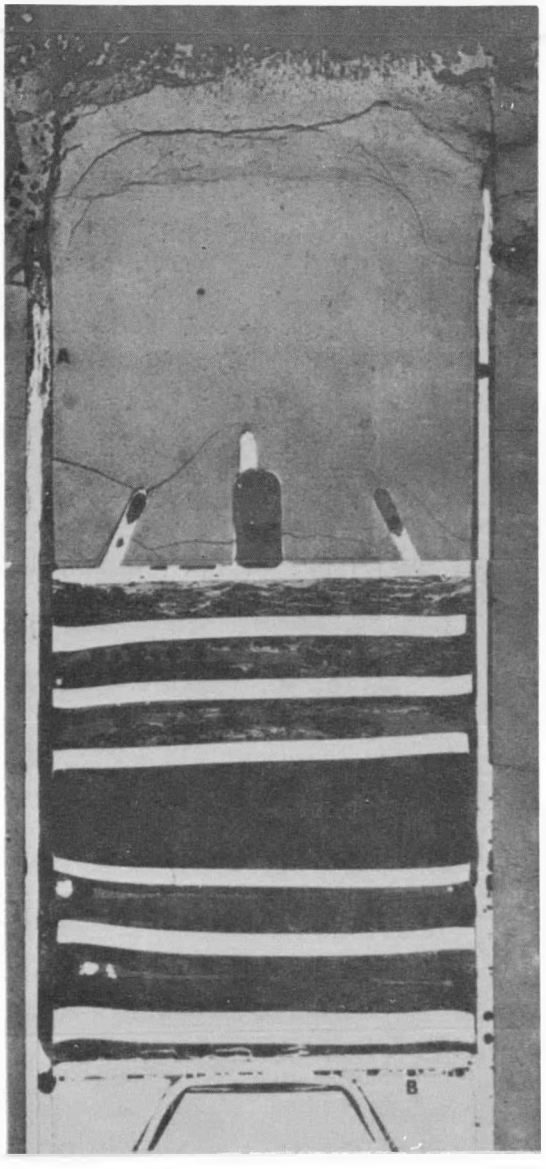

8X

Figure 63. Cross Section of Sintered $4MgAl_2O_4.1Fe_3O_4$ (#103-203) Proof Test 1 (8X)

interior of the ceramic at the cathode (see Figure 63); seed has penetrated the interior of the anode only along cracks, some of which appear to have healed themselves. Cracking has occurred in all electrodes near the base along the tips of the (Ni,Cu) lead-outs.

Recrystallization of a zone of spinel a few mm in from the surface occurs to a certain extent in all electrodes and appears to be associated with a significant K content -- possibly this represents the K_2CO_3 condensation isotherm. Such recrystallization is locally much more intense in the anode, where evidences of a K, Fe-rich intergranular phase were noted.

Melting is difficult to estimate and interpret because of the complexity of the interaction with upstream components; Zr has obviously reacted with the spinel, possible to produce a melt. The fact that shut-down was gradual further complicates the interpretation of microstructure. It is estimated that melting has occurred at one time or another in a surface zone of variable thickness ~1-5 mm. Melting appears to have been much more extensive at the anode. As would be expected, spinel immediately adjacent to the plasma shows significant Fe-depletion.

The insulators were also subject to alteration by (K, Fe) but primarily along the deeper parts were cracking has occurred. The anode insulators underwent corrosion by melting th the upper parts and were bridged by a (Fe Ni)-containing phase (a spinel?).

Untested specimens were not available for comparison, and certain features seem best related to the initial fabrication process: narrow zones of Ca and Mg-rich oxides at the junction between electrode and insulator; interspersed (La, Zr) oxides within the electrode spinel in a regular zone several mm from the surface; Si in the electrode spinel.

Plasma Sprayed MAFF Electrodes (Brunswick Anodes and APS Materials Cathodes)

This spinel is sensitive to contamination (internal or external in origin). At elevated temperature, certainly above 1600°C, this Fe-containing material may be subjected to plastic flow and, combined with interactions with the insulation will bridge adjacent electrodes. The material is sensitive to oxidation, alteration by seed and electro-chemical activity particularly at the cathodic side (see Figure 64). The G.E. spinel is similar in many respects. However, of electrodes fashioned from plasma sprayed spinel, this particular set out-performed all others tested in other facilities utilizing clean fuel. Microstructure and microchemistry at the anodic side reveal considerable evidence for melting/recrystallization (see Figure 64).

Metal-ceramic bonds basically retained their integrity.

HfO_2-Metal Electrodes (Argonne National Laboratories)

The microstructure, microchemistry and macro-scale phase distribution particularly for the HfO_2-Y_2O_3-CeO_2 materials varies considerably. This was done either intentionally or unintentionally during fabrication. Alumina is a significant contaminant for all of these materials. It, generally, resides within a groundmass containing other elements of the ceramic bulk composition. Within this matrix is coarser-grained ceramic. This contaminant may compromise the very refractory nature of HfO_2-based materials, contribute to a lowering of the electrical conductivity and provide reaction paths for seed. "Bloating" of these materials during electrical measurements above 1600°C (see above) could, in part, reflect formation of a fluid phase initiated by the presence of Al_2O_3. Original ceramic powders may include this contaminant or it might have been introduced during a "ball-milling" procedure prior to final fabrication.

HfO_2-based materials retain substantial anionic conductivity. Electrochemical reduction of the cathodic ceramic near and above the mesh was demonstrated. This does not appear to cause severe mechanical degradation in the short duration test. The melting temperature of the metal leadout and pertinent oxidation products, are particularly important for anode metal meshes combined with anion

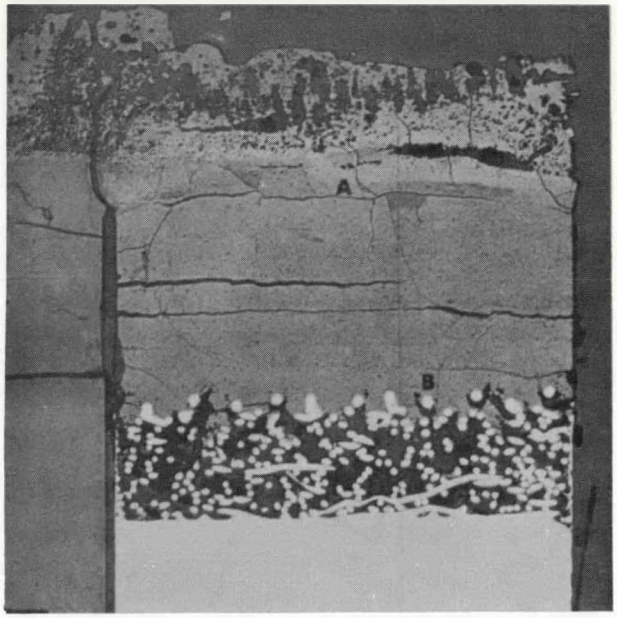

8X

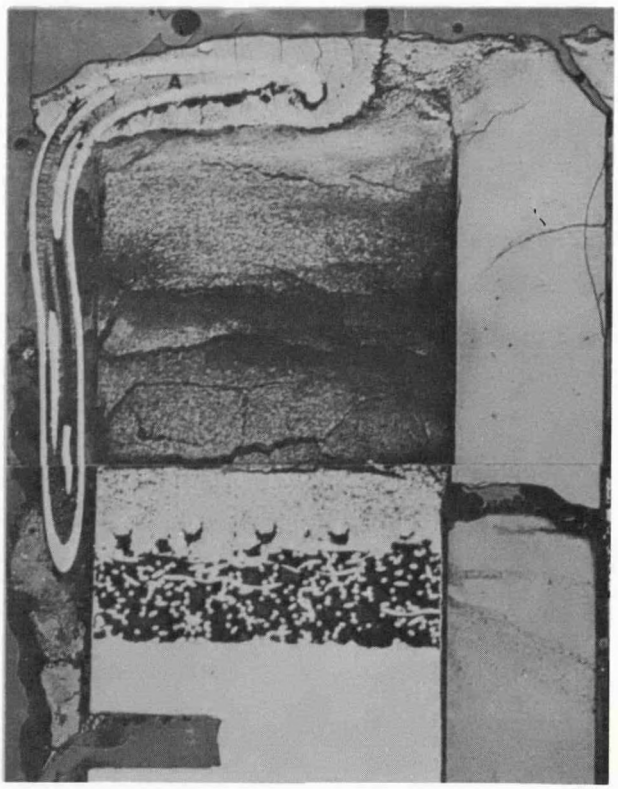

8X

Figure 64. Cross Section of Plasma Sprayed $3MgAl_2O_4 \cdot 1Fe_2O_4$ (#106-206) Proof Test 1 (8X)

conductors. Oxidation of the metal is accelerated due to directed oxygen-electron transfer. Anodic oxidation/dissolution of metal could lead to formation of a resistive phase assemblage around the wires and loss of thermal/electrical contact. These ultimately would result in destruction of the anode. Evidence for these events, including melting, is suggested. Figure 65 shows typical anode and cathode cross-sections after testing.

Thermal Performance (Proof Test 2 - WESTF Test 38)

In order to simulate U-02 conditions the objective in this test was to operate all electrodes as close to 1700°C as possible with heat fluxes in the range anticipated in the U-02 test and with the plasma having a conductivity greater than 3 mhos/m. In establishing final conditions surface temperatures were calculated based on a thermal model for each electrode system. Using these models, temperatures were calculated using temperature readings from nine type B thermocouples located 3 mm from the electrode surface. These predictions also included an error analysis reflecting possible errors due to thermocouple calibration error, thermocouple bead location, uncertainty in electrode thermal conductivity data and uncertainty in the surface heat transfer coefficient. Calculated surface temperatures for several electrodes are shown in Table 22 at three different times; at 2230 on November 17 prior to the introduction of seed, at 0530 November 18 just after final thermal and electrical conditions had been established and at 1800 November shortly before the end of the life tests. Also, prior to reaching the final test conditions thermal conditions were maintained at two points for approximately 2 hours each to make cross checks between several diagnostic sensors, i.e., the electrode thermocouples, Ir-Rh thermocouples extending into the gas stream in the mixer and inlet transition section and optical pyrometers sighting onto the mixer wall and electrode 108 in the test section. At these calibration points, one at approximately 1850°C plasma temperature and a second at approximately 1600°C electrode surface temperature, comparisons were also made between thermocouple, pyrometer and heat flux data and test predictions calculated prior to testing. These comparisons, between pre-test thermal predictions and thermocouple test data,

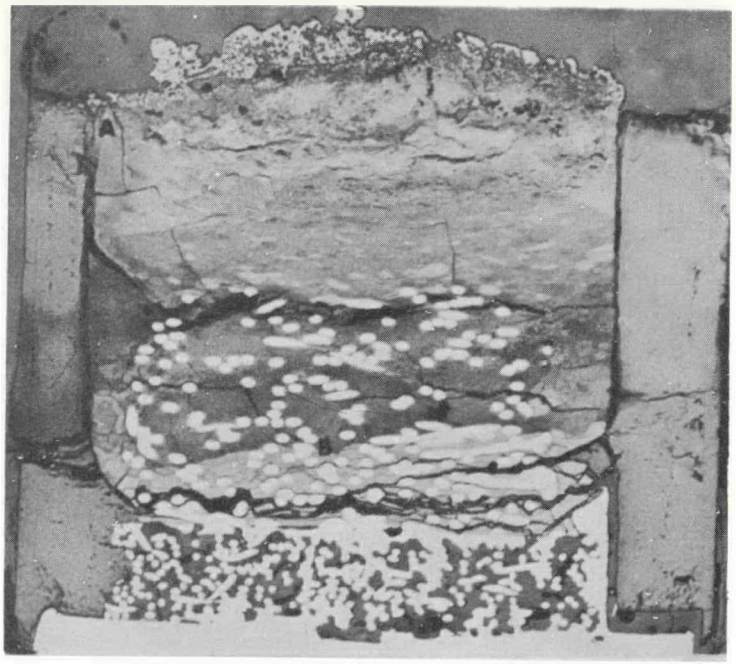

8X

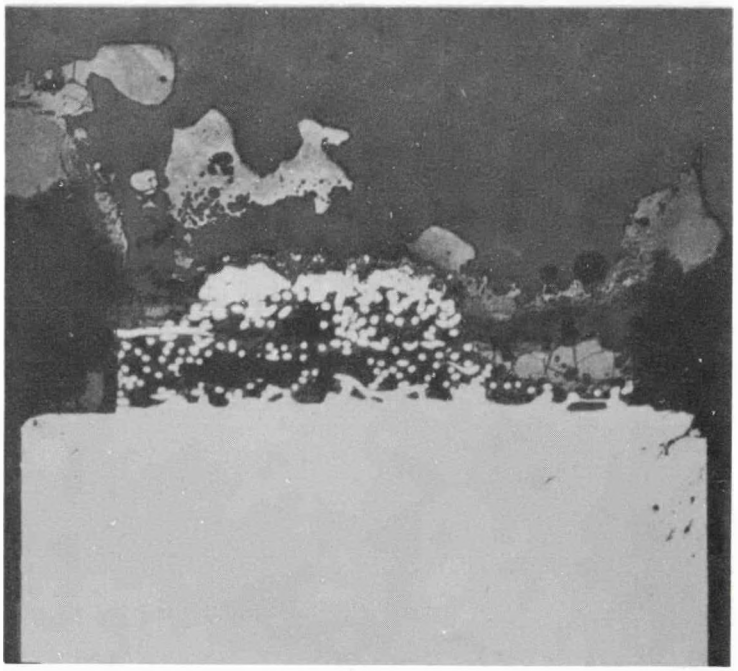

8X

208

Figure 65. Cross Section of ANL HfO_2 (#108-208) Proof Test 1 (8X)

TABLE 22

CALCULATED ELECTRODE SURFACE TEMPERATURES (^{o}C)
PROOF TEST 2

Electrode No.	Thermocouple # (Type)	Time 2230 11/17/77	Time 0500 11/18/77	Time 1800 11/18/77
102	0 (Sheath)	1875 ± 75	1745 ± 65**	1640 ± 65**
105	1 (Sheath)	1640 ± 75	*	*
108	2 (Sheath)	1475 ± 40	1525 + 45	*
108	3 (Sheath)	1675 + 40	1705 ± 50	*
111	4 (Sheath)	1780 ± 40	*	*
201	5 (No Sheath)	*	*	*
202	6 (Sheath)	1835 ± 70	1760 ± 60**	*
208	7 (Sheath)	1535 ± 70	1605 ± 45	1620 ± 45
208	8 (No Sheath)	1680 ± 40	1760 ± 60	1770 + 60
211	9 (Sheath)	1680 ± 40	*	*

*Either inoperable or unreliable thermocouple.
**No current passed through electrode pair 102-202.

and cross checks were used in the decisions to set final conditions. As can be seen from Table 22 there was a progressive loss of thermocouples during the life test. Also, the unsheathed thermocouples read 100-150°C higher than sheathed thermocouples in the same electrode to give calculated surface temperatures 150-200°C higher. Temperature rise due to Joule heating was measured at the mid-point of the test and found to be ~70°C (as expected) in the Eagle-Picher $ZrO_2/LaCrO_3$ composite electrodes. See Section 5.2.2.3 for typical thermocouple data.

Cooling water flow rates to eighteen electrodes were individually controlled and ranged between 3 and 5 cc/sec. The first and last two electrodes of each wall were run in a series water circuit at a flow rate of 10.5 cc/sec. Heat fluxes, as determined calorimetrically, ranged from 25 to 35 w/cm^2 and averaged close to 30 w/cm^2 for both anode and cathode walls. In general, there was little change in heat fluxes during the life tests. In contrast to proof test #1, there was no change in heat fluxes when seed was introduced. It is estimated that the contribution to heat fluxes by Joule heating varied from 1 to 9 $watts/cm^2$.

Electrical Performance-Proof Test 2 (WESTF Test 38)

The wiring work necessary for accomplishing the automatic reading of the test channel voltages and currents using the D.A. (data acquisition) system was completed prior to Test 38. The circuit of Figure 61 was utilized for the interface between the D.A. system, the experimental channel and its associated power supplies. Use of the D.A. system in Test 38 greatly increased the volume of data which could be obtained during a run, the speed with which it could be recorded, and substantially improved the accuracy. Use of a Facit paper punch allowed communication of the data to the computer after the test was completed, thus permitting tabulation of the data, making calculations on it, and automatically plotting the results.

Based on the results obtained in the testing of earlier experimental channels, during the life test the electrodes were operated in the electrically floating position. Operation in this mode assured uniform loading of each electrode pair. The constant current of features of the power supplies were utilized during the test. Thus the voltage, V_L, required to impress a given current across an electrode-pair varied depending on the extent that the plasma conductivity, the anode and cathode potential falls and the IR drop across the electrodes varied with life.

Figures 66, 67 and 68 show how V_1, the voltage impressed across the electrodes, V_H, the voltage of the positive, and V_K, the voltage of the negative electrodes relative to ground, varied during run 38. The gaps in the curves in the middle of the run resulted from an interruption at the mid-point in the test to measure plasma conductivity and to make other electrical measurements. I_2 is the current in the positive leg of Figure 61 and I, is the current in the negative leg.

From the graphs of electrode-pair 1 and 2, see (a) and (b) of Figure 66, it is evident that the impressed voltage V_2 decreased somewhat with time during the run. Both of these electrode-pairs utilized hot pressed ZrO_2 capped electrodes. From later measurements on $LaCrO_3$ samples, it is believed that the $LaCrO_3$ material employed in the test had a fairly high initial resistivity.

The later tests on initially resistive $LaCrO_3$ samples demonstrated that the resistivity of the material decreased substantially when the material was heated to several hundred °C while subject to load currents of the order of one ampere/cm^2. It is surmised that this effect was responsible for the reduction in value of V_L observed with the passage of time in electrode-pairs 1, 2 9, 10, 11 and 12 of run 38. Apparently electrode-pair 2 was fabricated from an unusually resistive $LaCrO_3$ material, since it did not prove to be possible to increase its load current over the order of about 2 amperes during the test for values of V_L which were comparable to the other electrode pairs.

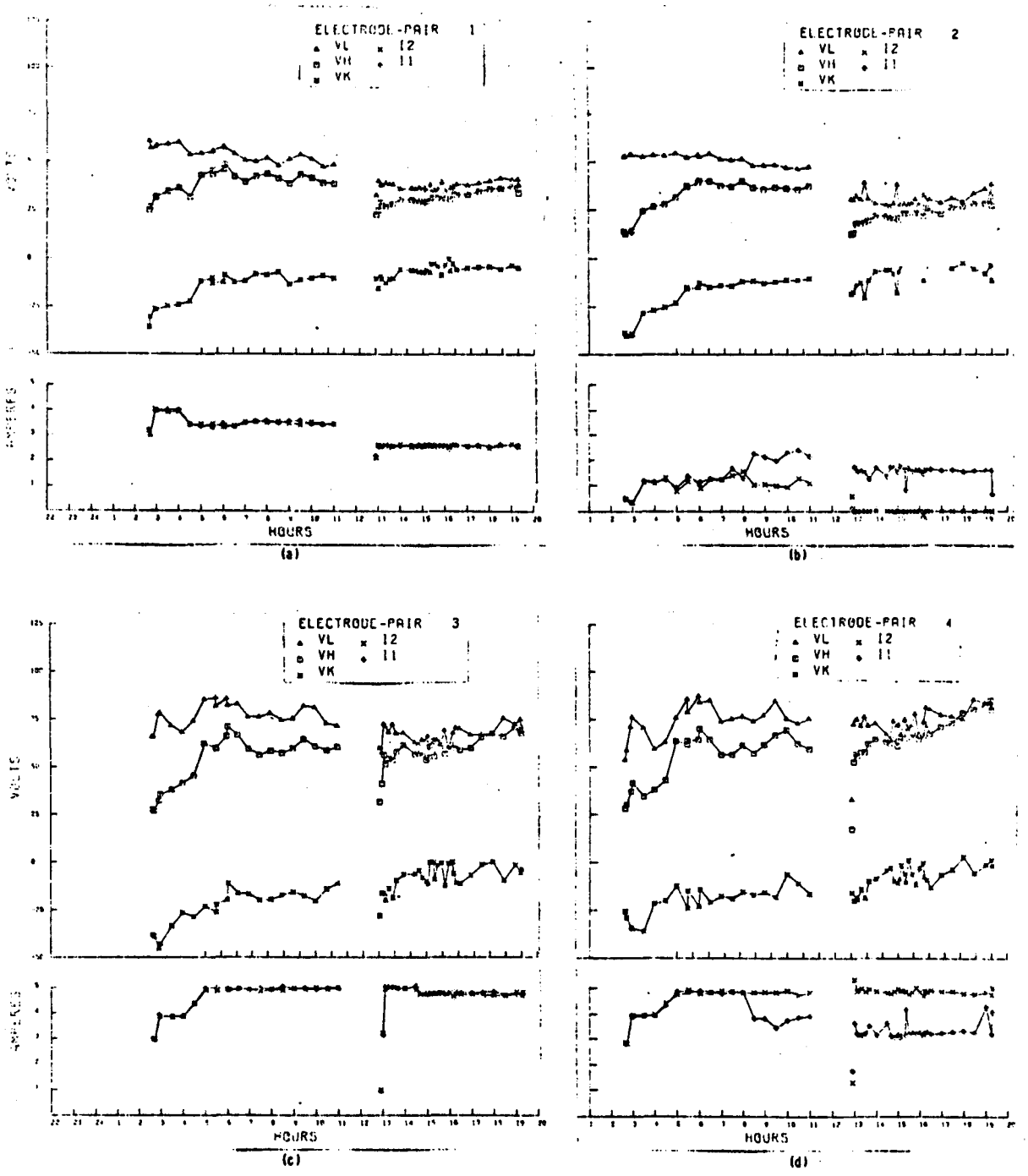

Figure 66. Applied Voltages and Currents for Different Electrode Pairs as Function of Time, Test 38

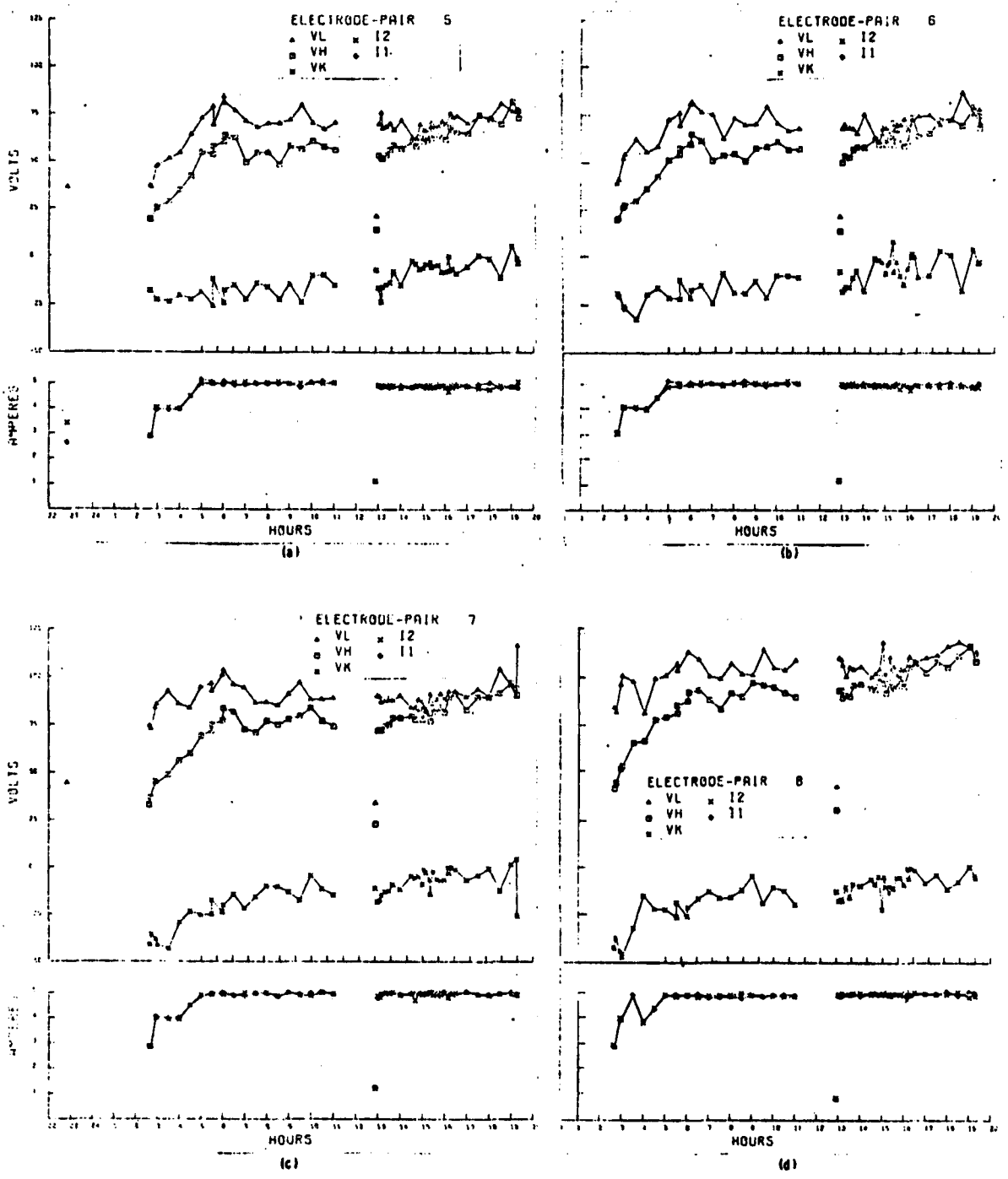

Figure 67. Applied Voltages and Currents for Different Electrode Pairs as Function of Time, Test 38

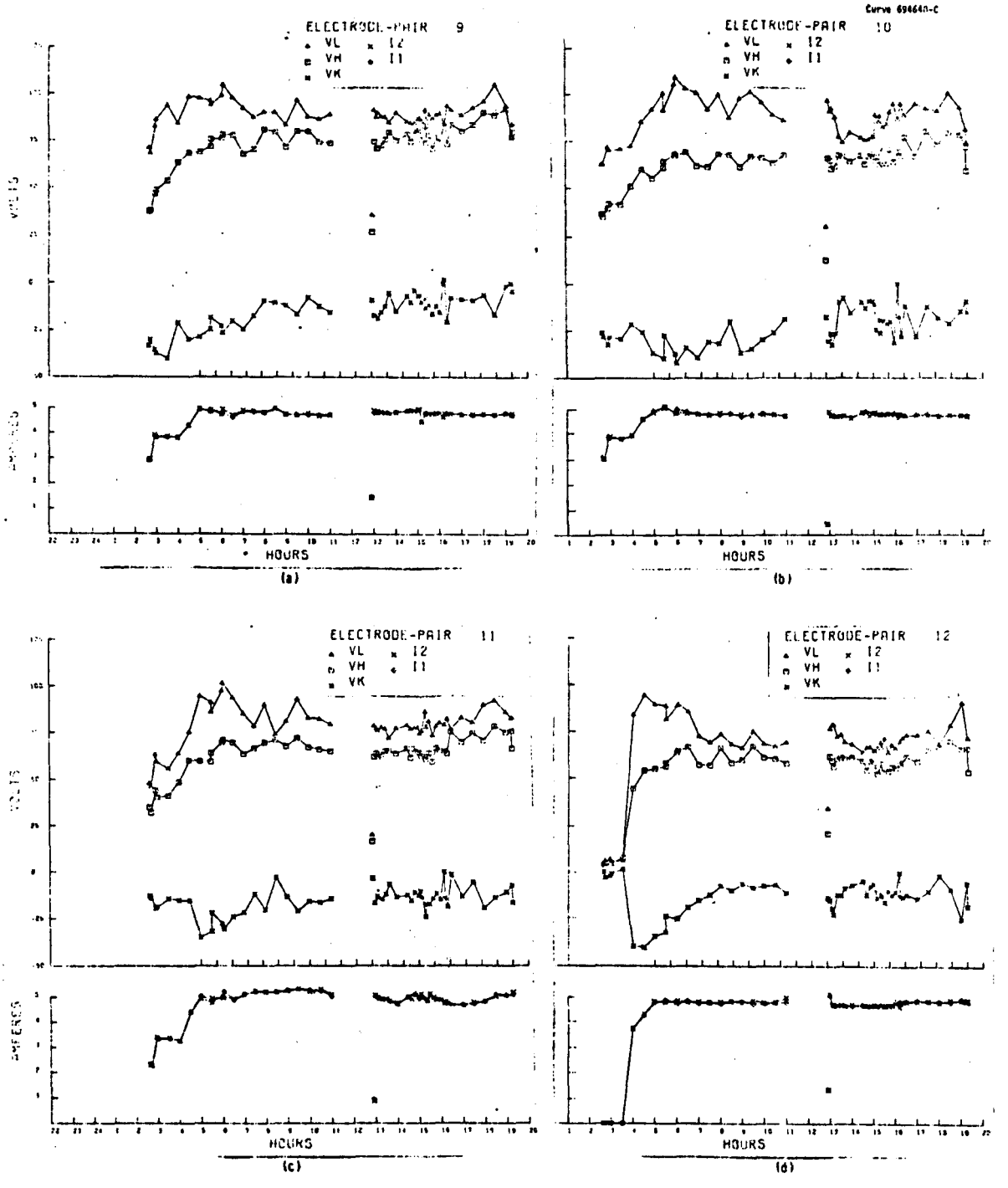

Figure 68. Applied Voltages and Currents for Different Electrode Pairs as Function of Time, Test 38

The voltage drops across the different electrode-pairs of run 38 can more easily be compared with each other when the voltage and current parameters are plotted as a function of electrode-pair number for different times, See Figures 69, 70, 71, and 72. The leakage current characteristics of the channel when no seed was present, are plotted on Figure 69 and 70. Seed was introduced in the channel at 2249 on 11/17/77. The electrical circuits for the different parts of Figures 69 through Figure 72 correspond to the floating cathode grounded and anode grounded conditions as labeled on the figures. From Figure 70 part (c) it is evident that the leakage resistance across the channel some 15 minutes before seed was introduced varied from 170 to 600. From part (b) of the same figure it is evident that the leakage resistance to ground of the electrode pair 11, which had the highest leakage was about 130 ohms at 1943 hours.

The increase in channel current once seed was introduced is apparent in Figure 71 part (b) at 2250 one minute after seed was introduced. It is further evident that electrode-pairs 4, 5, and 6 which utilized plasma sprayed, ZrO_2 capped $LaCrO_3$ electrodes had substantially lower ohmic voltage losses than the hot-pressed $LaCrO_3$ electrodes. For approximately the same increased voltage these electrode-pairs had almost a factor of two more current.

When the external voltage supplies were adjusted to impress approximately 1 ampere of current through the different electrode-pairs, see part (c) of Figure 71, it is evident that the plasma sprayed electrodes initially have more than a factor of two lower ohmic voltage losses than the electrodes fabricated from hot pressed $LaCrO_3$ materials.

As the currents through the different electrode-pairs of the channel was increased from one to three or four amperes, see parts c and d of Figures 71 and 72 it became increasingly clear that electrode-pairs 7, 8 and 9 requires higher impressed voltages than any other electrode-pairs of the channel. The material for electrode pairs 7, 8, and 9 was a hot pressed $LaCrO_3/ZrO_2$ composite.

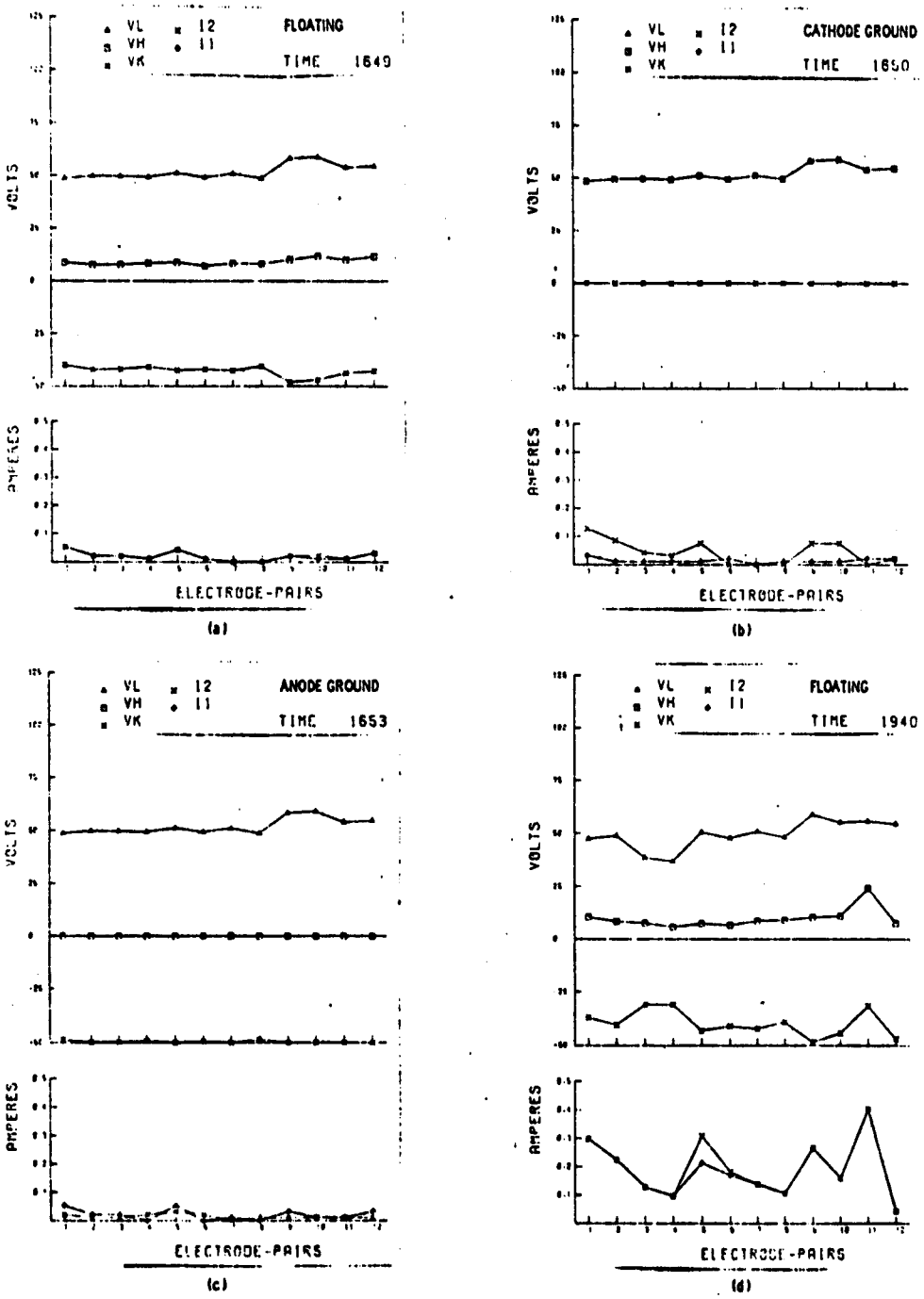

Figure 69. Applied Voltage, Voltage to Ground of Positive and Negative Electrode, Currents as Function of Electrode-Pairs at Different Time During Run 38

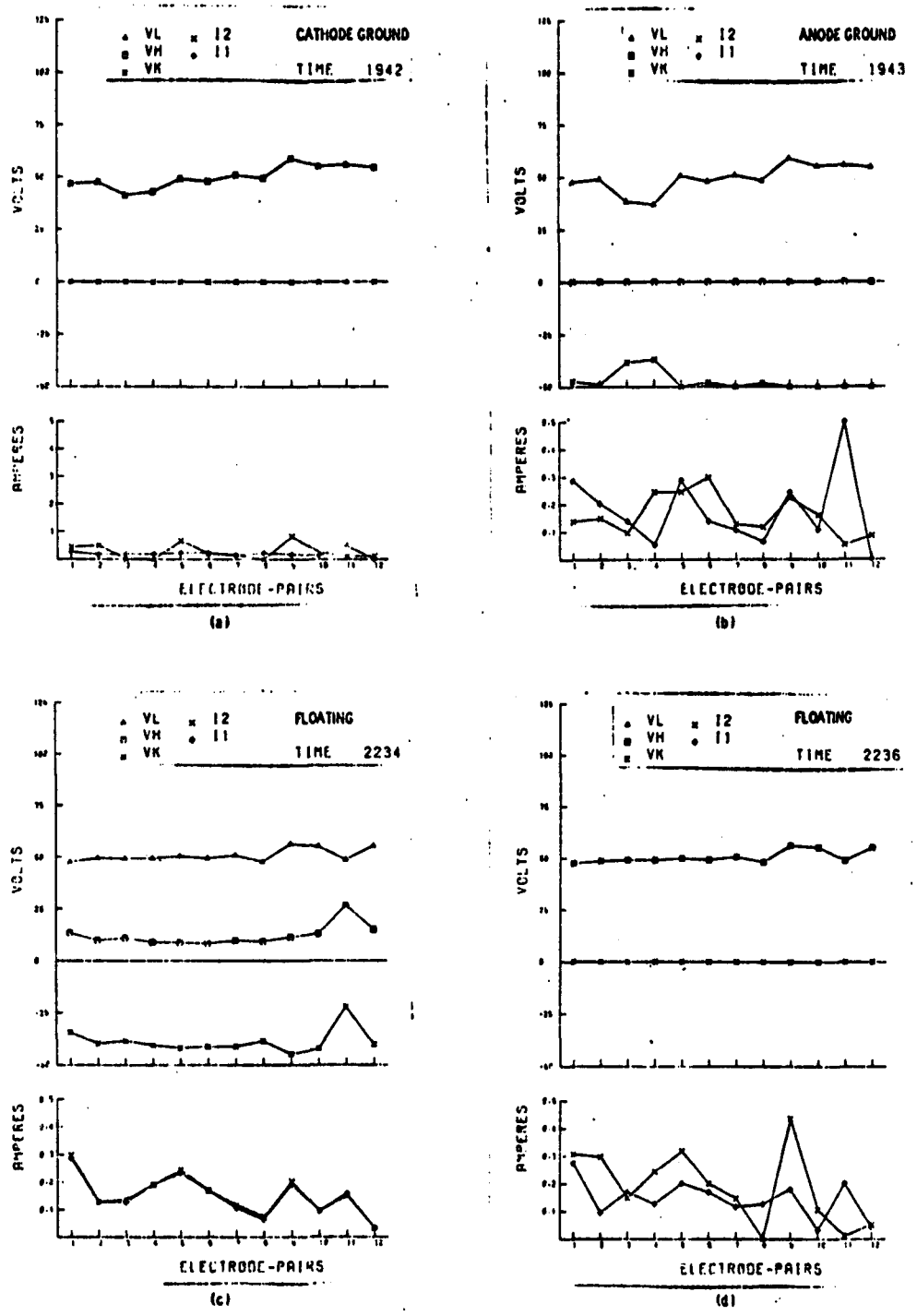

Figure 70. Applied Voltage, Voltage to Ground of Positive and Negative Electrode, and Electrode Currents as Function of Electrode-Pairs at Different Time During Run 38

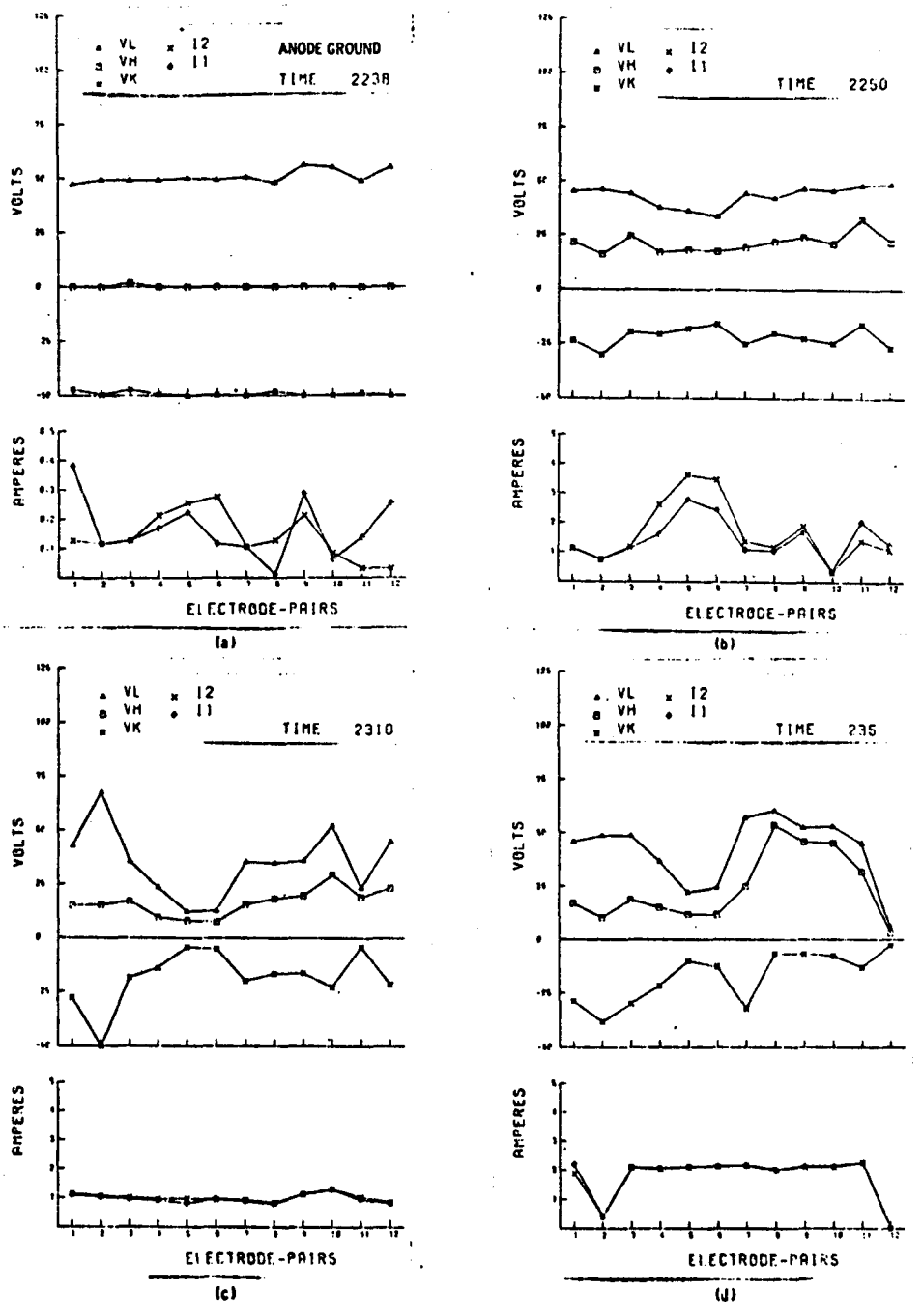

Figure 71. Applied Voltage, Voltage to Ground of Positive and Negative Electrode, and Electrode Currents as Function of Electrode-Pairs as Different Times during run 38. Seed was introduced at 22:49.

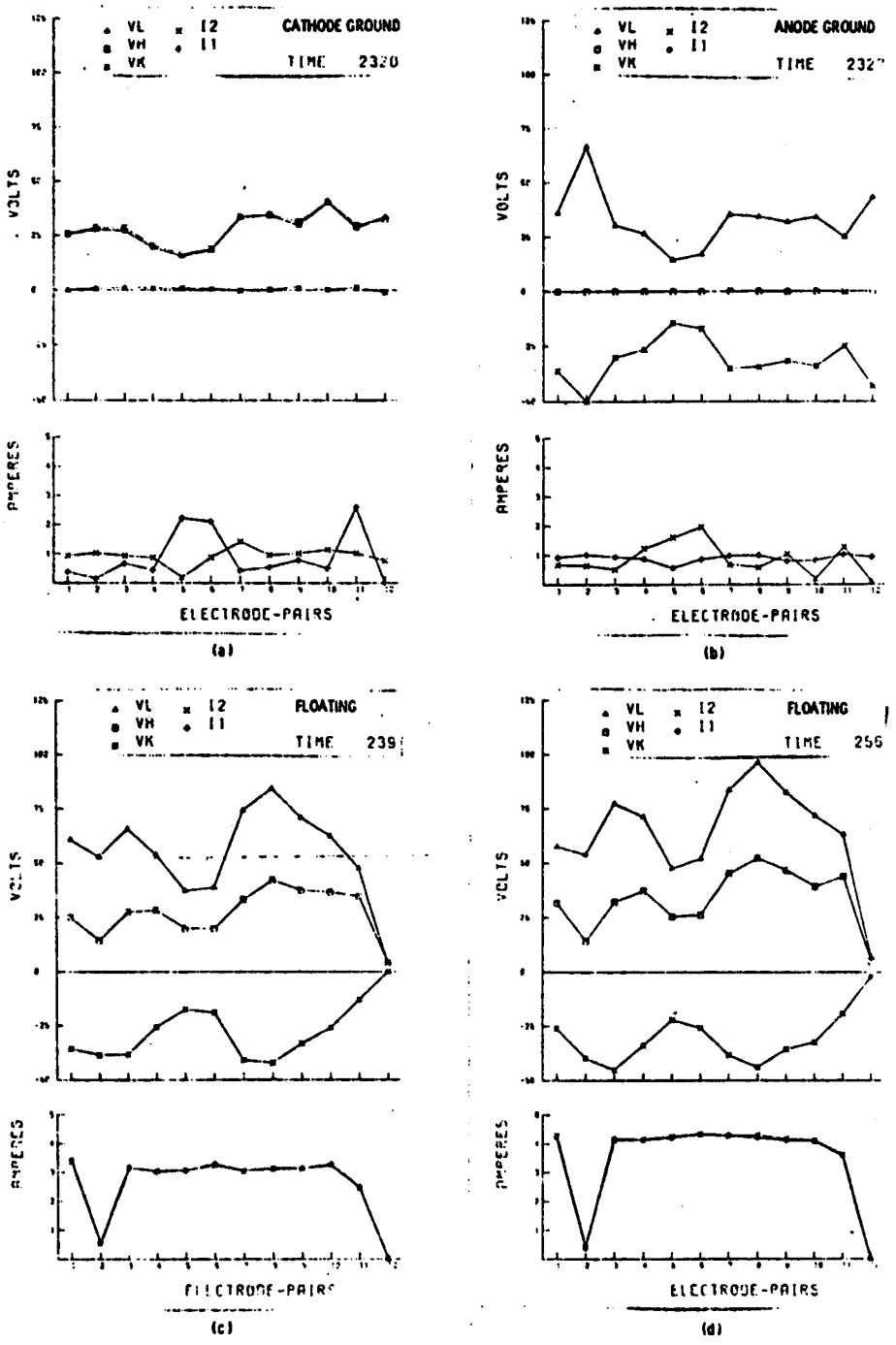

Figure 72. Applied Voltage, Voltage to Ground of Positive and Negative Electrode, and Electrode Currents as Function of Electrode-Pairs at Different Time During Run 38

The remainder of the life test was conducted in the floating mode with all electrodes-pairs capable of being operated at higher currents held at 5 amperes, see Figures 73 and 74. From these figures it is apparent that electrode-pairs 7, 8 and 9, the hot pressed $LaCrO_3/ZrO_2$ composites, continued to require higher impressed voltages than the other electrode materials.

Final electrical data taken at the end of the test are shown in Figure 75. Comparing the cathode grounded versus the anode grounded operation, it is evident that I1, the current in the cathode leg, is substantially greater than I2 the current in the positive leg for anode grounded operation. Thus, as explained previously the leakage current to ground at the completion of the duration test was significantly higher at the cathode electrodes. It is believed that the migration of seed ions to the cathode electrodes by the electric field was responsible for the increase cathode leakage.

By comparing anode and cathode grounded curves taken at the beginning and end of the duration run, for example see Figure 72 part a and b and Figure 75, it is clear that the cathode leakage to ground increased substantially during the tests. The exact mechanism for the increased leakage to ground is not clear since the only grounded regions on the channel were the entrance and exit flanges. It is believed that the leakage path A ground resulted from the deposit of seed along the surfaces responsible for channel axial insulation.

When the electrodes are operated in the floating mode, the potentials that the cathode and anode electrodes assume relative to ground also provides important clues on the relative leakage to ground. Before seed is injected into the system, a definite asymmetry could be perceived. For example in Figure 69 part a and Figure 70 part c, the average value of V_H, the potential that the positive electrodes assume relative to ground, was about 10 watts positive relative to ground, whereas the average potential of the cathode electrodes was about 40 volts negative to ground.

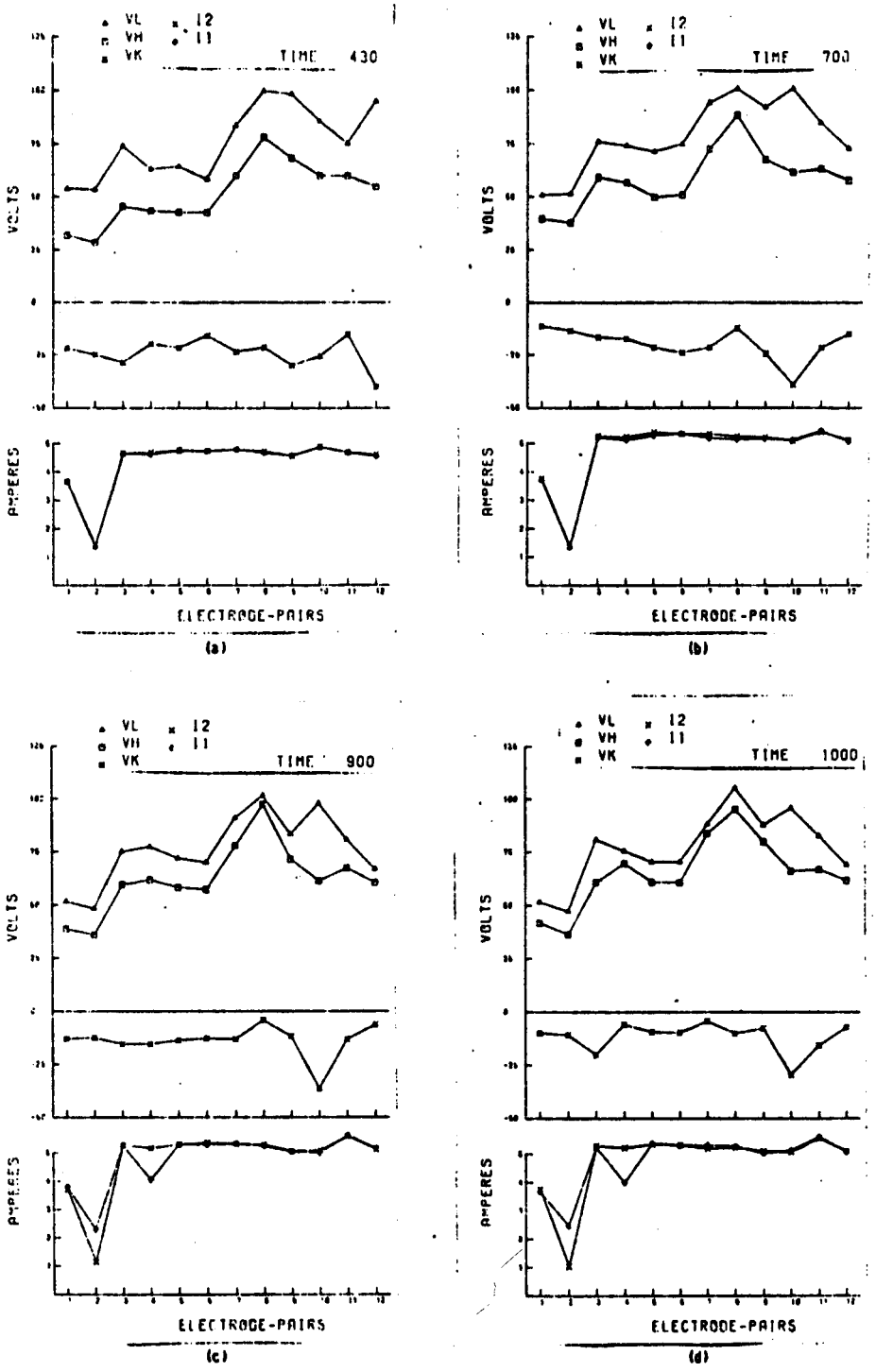

Figure 73. Applied Voltages and Currents as Function of Electrode-Pairs at Different Times During Test 38

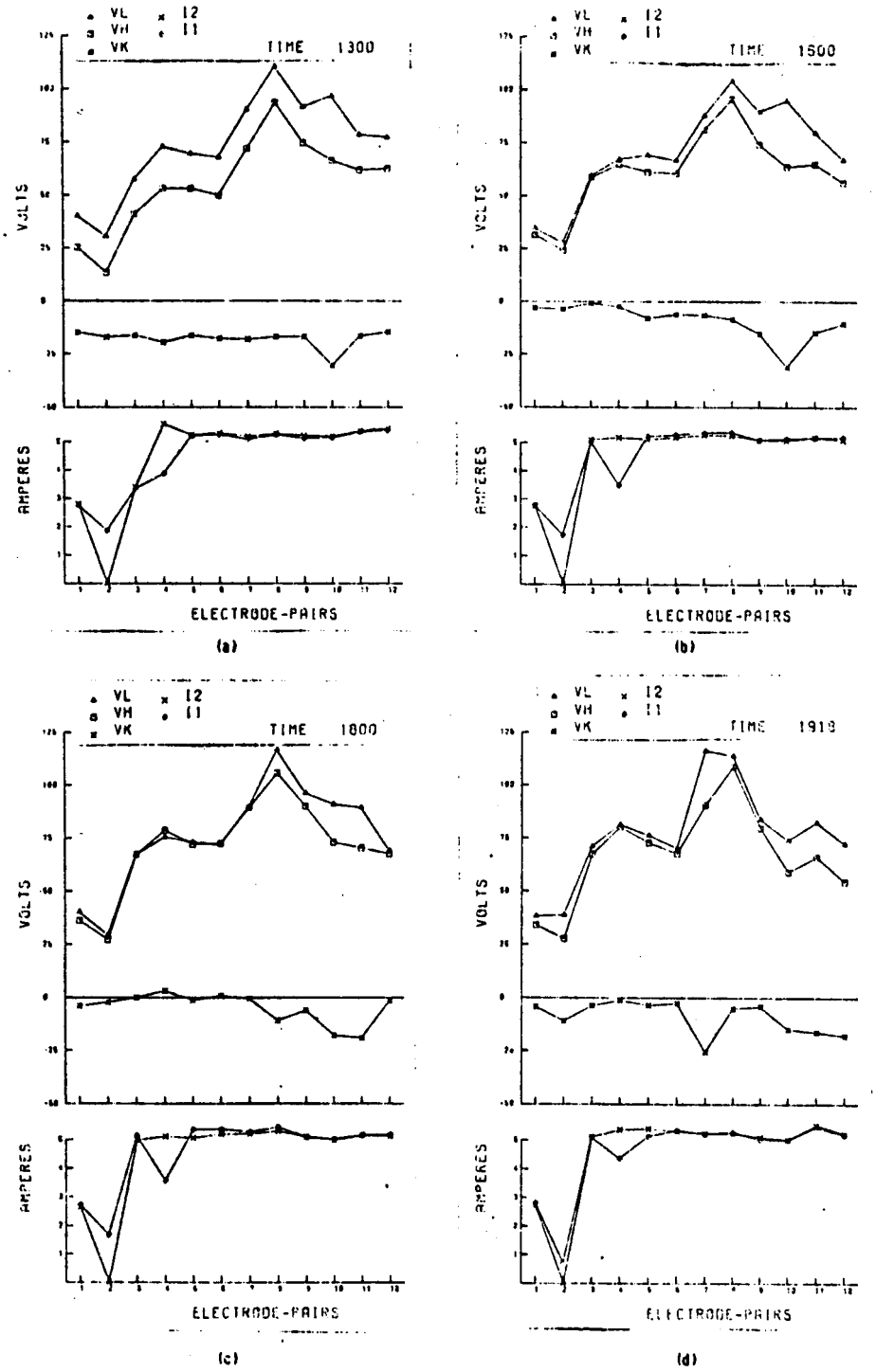

Figure 74. Applied Voltages and Currents as Function of Electrode-Pairs at Different Times During Test 38

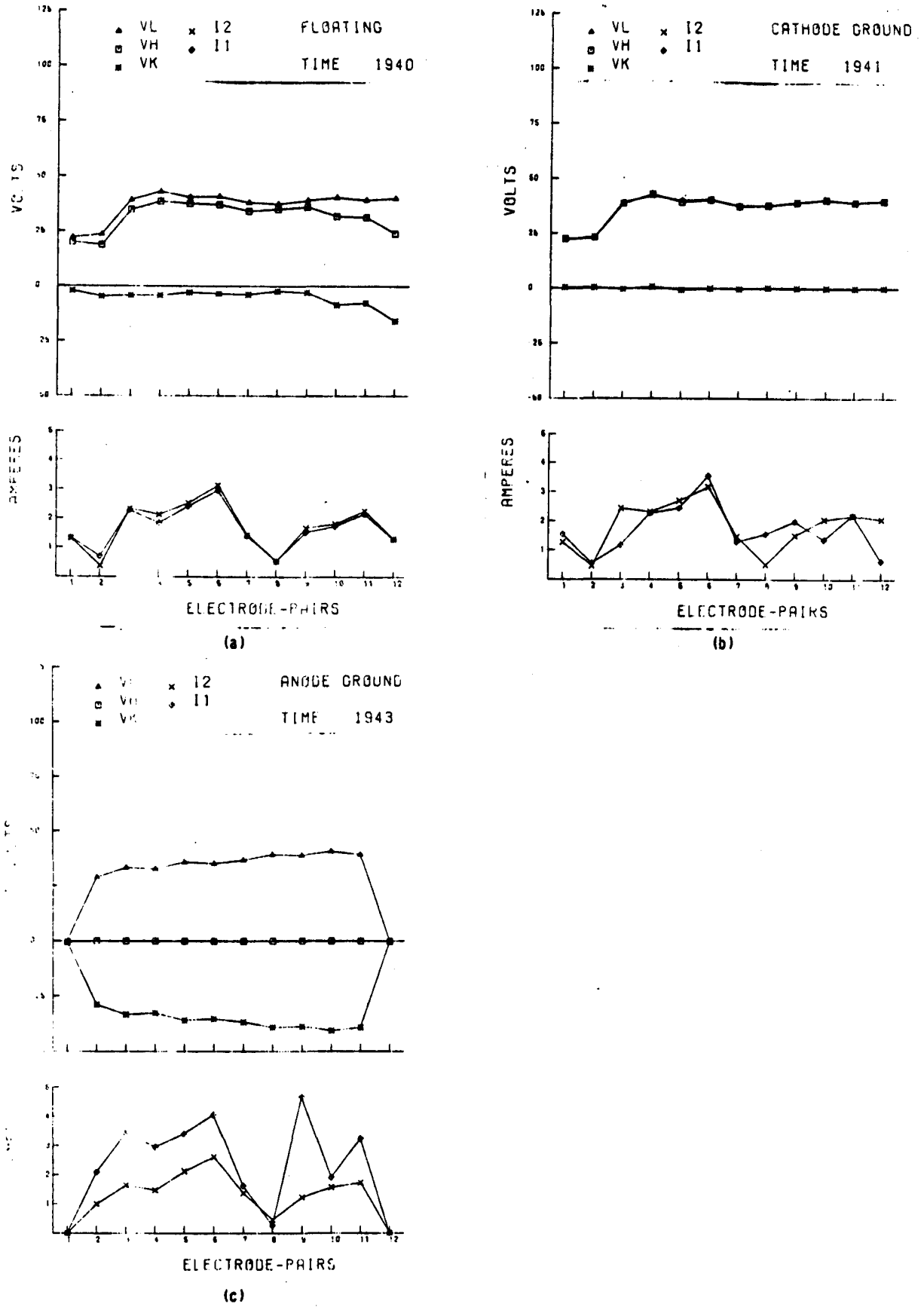

Figure 75. Applied Voltage, Voltage to Ground of Positive and Negative Electrodes and Electrode Current as Function of Electrode-Pairs at end of Run 38 for Electrodes Floating, for Anode Grounded for Cathode Grounded Operation

This particular asymmetrical distribution of potentials is entirely due to the electrical circuits employed. The anode electrodes are tied to ground through the 50, 500 ohm potential dividers used to measure V_H, see Figure 61.

However, within a minute after seed is introduced, see Figure 71 part b, potentials V_H and V_K are roughly equal. Thus the positive and negative electride at this time are symmetrical relative to ground (as noted earlier, seed was introduced at 2249 hours).

By 0430 about 5-3/4 hours after seed was introduced, it is evident that an asymmetry in the electrode potentials has been reestablished which is opposite to the one which was originally produced by the electrical circuit considerations. The cathode potentials have moved closer to ground potential and the anode potential have shifted in the more positive direction.

By the end of the test, see Figure 75, the cathode potentials were within a few volts of ground potential, and almost all of the impressed voltages were between the positive electrodes and ground. The variation of cathode and anode potentials with life can also be observed in Figures 66 through 68. Measurements of leakage currents, as performed in the anode and cathode grounded tests, and measurements of the electrode potentials during the course of the life test both verify that the migration of seed during operation greatly decreases the magnitude of the leakage resistance on the cathode electrode side of the channel.

In the present tests in which no axial fields are introduced to simulate the Hall fields, and the electrode potentials are permited to float, the decreased leakage resistance at the cathode terminals has the effect of increasing the power dissipated on the anode side of circuit. If I_1 is the leakage current circulating via the ground circuit in a given electrode pair, and R_c and R_a are the cathode and anode leakage resistances to ground respectively then $I_1^2 R_c$ and $I_1^2 R_a$ are the magnitudes of the voltage dissipated in the anode and cathode configurations. Since $\frac{V_H}{V_K} = \frac{R_a}{R_c}$, and V_H is about 6 times greater than V_K in Figure 75 part a, it is clear at the end of the test that the power

dissipated in anode circuit at the end of run 38 is about 6 times greater than the power in the cathode circuit.

However when axial fields are applied to simulate the Hall fields, the leakage currents in the cathode region will be substantially increased. In future tests the effect of leakage resistance on the power dissipated in the cathode and anode circuit will be investigated as a function of applied axial fields. Such an investigation will also provide important information on the ability of insulation to stand up under Hall type fields in MHD generators.

As noted in the last quarterly report, average plasma conductivities have been determined by applying axial potentials along the channel between upstream and downstream electrodes which are started together. The plasma conductivity is then determined from measurements of the potential of the intervening electrodes, and by measurement of the resulting currents.

Figures 76 and 77 are computer plots of the potentials established during such conductivity measurements. When the axial fields are applied, the potentials of the "positive" electrodes, V_H, turn out to be essentially equal in magnitude to the potential of the negative" electrodes, V_K. In this instance $V_L = V_H - V_K$ represents the difference in potential between the two electrodes of a given electrode-pair, and is essentially zero.

In the computer plots the lines between the different experimental points are connected by straight lines. The linear representation areas do not do justice to the contour of the anode cathode fall regions of the curves, which would be expected to be steeper than shown, since the change in potential at the electrodes occurs over a relative small distance region in front of the electrode surfaces, see Figure 13 of the last quarterly report, Reference 11.

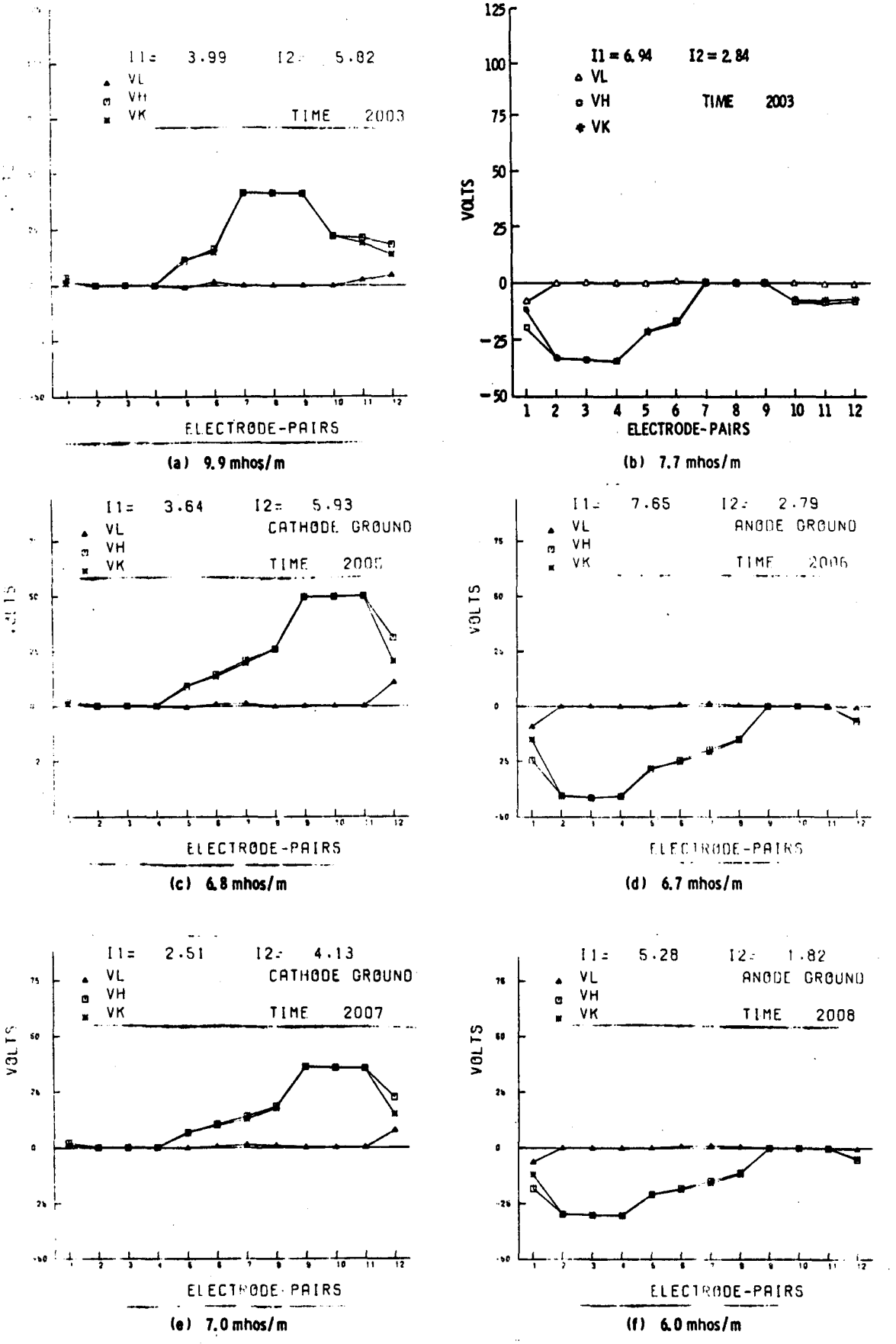

Figure 76. Voltage Profiles taken during Conductivity Measurements at End of Run 38 Just Prior to Seed Cut Off at Time 2008

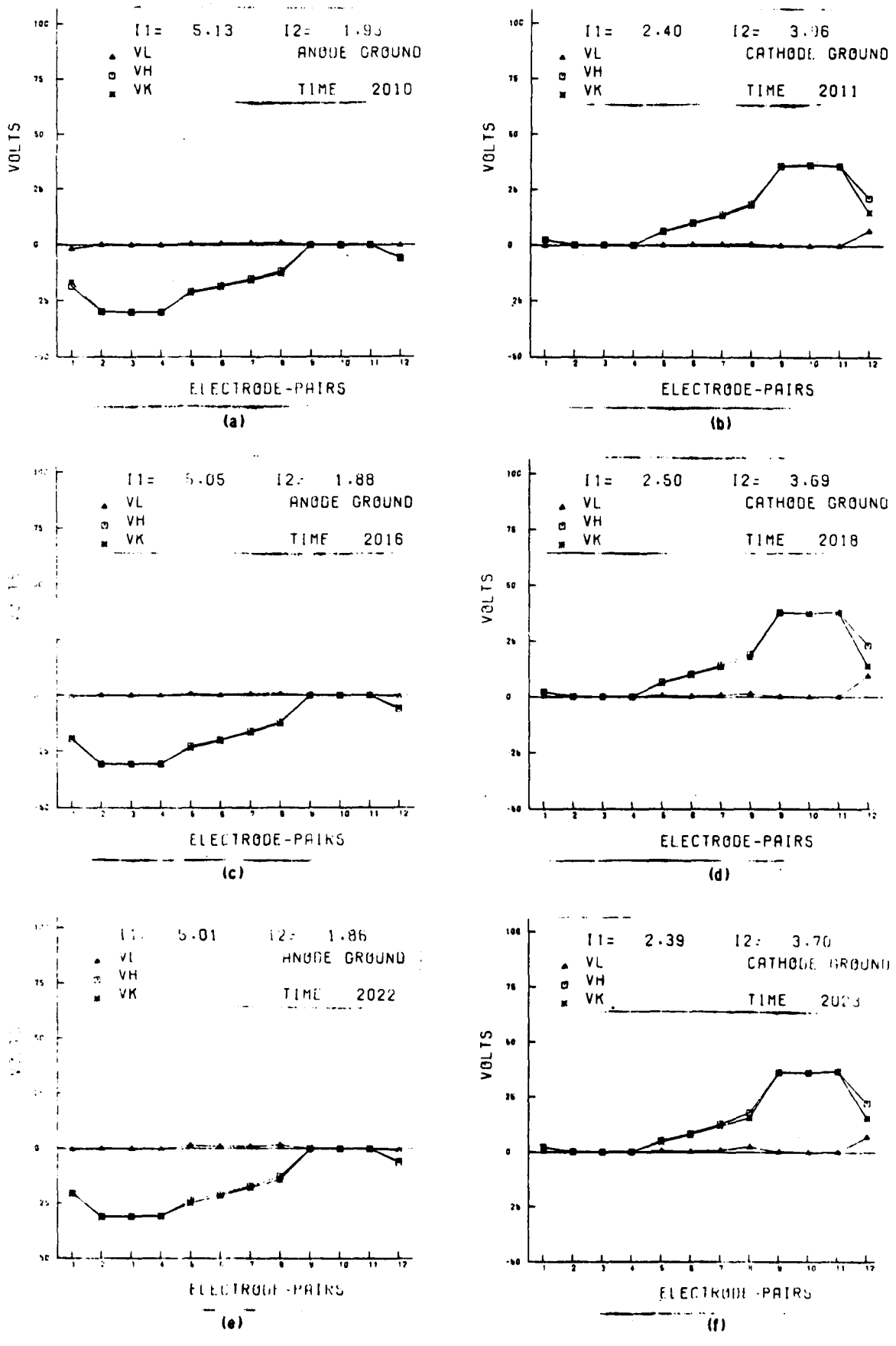

Figure 77. Voltage Profiles Taken During Conductivity Measurements at End of Run 38 Just Prior to Seed Cut Off at Time 2008

The electrical fields in the intervening electrodes are clearly uniform. The increase in the shape of the potentials at the cathodes and the anodes is somewhat deceptive. The potentials given in Figures 76 and 77 basically are equipotential lines which occur in the plasma along the length of the channel. These lines are perpendicular to the axis of the channel. However, the electrodes which are shorted together at the upstream and downstream ends of the channel in fact are equipotential lines which are perpendicular to the equipotential plasma lines to which we have just referred.

The point is that the equipotential lines curve as they enter the cathode and anode regions of the channel. Once corrections are made for the curvature of the electric fields, it appears safe to conclude that the cathode fall is negligible for the electrode temperatures which occur in the test (between 1500°C and 1750°C).

In general the anode fall proved to be higher than the cathode fall. However, the magnitude of the anode fall depends on whether the anode or cathode of the measuring circuit was grounded when the measurements were made. The higher anode falls observed when the cathodes of the circuit were grounded were probably due to that fact that electron leakage current through the plasma can travel to the positive anode from any grounded surface in the system, thus increasing the current density at the anode, and hence the anode fall. When the anode is grounded, electron currents cannot reach the anode from neighboring grounded regions, but only from negative electrodes.

Once plasma conductivities are known it is possible to calculate the theoretical expected plasma drop V_p across each electrode pair for the current being drawn, as indicated in the discussion of Run 37. Table 23 summarizes typical values of impressed voltages used at the beginning and end of the run, as well as the values of current observed. Table 24 lists the ΔV values, i.e. the sum of the ohmic potential drop in the electrodes plus the anode and cathode falls for each electrode pair. From Table 24 it is clear that the $LaCrO_3/ZrO_2$ component had significantly higher values of ohmic potential drop than the other electrode pairs.

TABLE 23. IMPRESSED VOLTAGE VS. AMPERES OBSERVED AT DIFFERENT TIMES DURING TEST 38, ELECTRODES FLOATING 11/17 and 11/18/77

TIME	VL / IL	ELECTRODE-PAIRS 1	2	3	4	5	6	7	8	9	10	11	12
11/17 2234	VL	47.8	49.6	49.4	49.5	50.5	49.6	50.9	47.8	56.3	55.3	48.9	55.3
	IL	0.28	0.12	0.13	0.18	0.23	0.16	0.11	0.07	0.19	0.09	0.14	0.03
2249						SEED INTRODUCED							
2250	VL	45.2	46.1	44.1	37.6	36.2	33.5	44.4	42.2	46.7	49.8	48.3	48.6
	IL	1.1	0.70	1.1	2.5	3.4	3.3	1.3	1.1	1.8	0.32	1.3	1.0
11/18 0230	VL	46.2	42.6	50.0	36.8	19.9	23.0	58.7	62.8	49.4	51.7	41.6	36.6
	IL	2.1	2.1	2.0	1.9	1.3	2.0	2.0	1.9	2.0	2.0	2.1	0.0
0400	VL	60.3	53.9	68.0	59.6	54.9	55.5	85.7	81.6	84.1	72.5	63.6	84.4
	IL	4.0	1.1	3.9	4.0	4.0	4.0	4.0	3.9	3.8	4.0	3.3	3.8
0500	VL	54.6	54.7	85.4	75.9	73.1	72.4	94.4	101.2	97.3	92.1	94.4	89.9
	IL	3.5	0.81	4.9	4.8	5.0	4.9	4.9	5.0	5.0	4.9	4.9	4.8
0900	VL	51.7	48.4	75.1	77.4	72.0	70.0	91.0	101.6	83.3	97.8	80.6	66.8
	IL	3.5	1.1	5.0	4.9	5.0	5.0	5.0	5.0	4.8	4.8	5.3	4.8
1100	VL	48.7	47.6	71.2	75.7	70.6	67.8	88.9	109.3	88.9	86.1	79.0	69.8
	IL	3.5	1.1	5.0	4.9	5.0	5.0	5.0	4.9	4.7	4.7	5.1	5.0
1306	VL	38.1	32.7	72.3	75.0	75.4	69.9	89.7	109.8	87.6	91.0	76.5	79.3
	IL	2.6	0.0	3.2	5.4	4.9	5.0	4.9	5.0	4.9	4.9	5.1	5.2
1630	VL	38.6	30.7	69.8	80.5	73.9	74.1	92.3	108.7	91.5	88.9	76.5	74.0
	IL	2.6	0.0	4.7	4.9	4.9	4.9	5.0	5.1	4.8	4.7	4.7	4.9
1918	VL	38.3	38.7	71.2	81.4	76.4	70.2	116.3	113.8	83.9	74.0	82.4	72.4
	IL	2.6	0.0	4.8	5.0	5.1	5.0	4.9	4.9	4.8	4.7	5.2	4.9

TABLE 24. VALUES OF ΔV FOR DIFFERENT ELECTRODE-PAIRS AT BEGINNING AND END OF RUN 38, ELECTRODES FLOATING

	Time 0900 11/18/77 T=6.5 mhos/m					Time 1918 11/18/77 T=6.8 mhos/m			
Electrode-Pair	VL	IL	V_p	ΔV	ELECTRODE MATERIALS	VL	IL	V_p	ΔV
	volts	amps	volts	volts		volts	amps	volts	volts
1	51	3.5	2.0	32	Hot Pressed ZrO_2 capped $LaCrO_3$	38	2.6	15	23
2	48	--	--	--	Hot Pressed ZrO_2 capped $LaCrO_3$	38.7	---	---	
3	75	5.0	29	46	Hot Pressed ZrO_2 capped $LaCrO_3$	71	41.8	28	43
4	77	4.9	28	49	Plasma Sprayed ZrO_2 capped $LaCrO_3$	81	5.0	29	52
5	72	5.0	29	43	Plasma Sprayed ZrO_2 capped $LaCrO_3$	76	5.1	30	46
6	71	5.0	29	41	Plasma Sprayed ZrO_2 capped $LaCrO_3$	70	5.0	29	41
7	91	5.0	29	62	Hot Pressed $LaCrO_3/ZrO_2$ Composite	116	4.9	28	88
8	101	5.0	29	72	Hot Pressed $LaCrO_3/ZrO_2$ Composite	114	4.9	28	86
9	83	4.8	28	7.0	Hot Pressed $LaCrO_3/ZrO_2$ Composite	4	4.8	28	56
10	98	4.8	28	70.0	Sintered $LaCrO_3$	74	4.7	27	47
11	81	5.3	31	50	Sintered $LaCrO_3$	82	5.2	30	52
12	67	4.8	28	39	Sintered $LaCrO_3$	72	4.9	28	44

Figures 78 and 79 show values electrode-pair current with the electrodes floating as taken during the time interval when the current was increased from one ampere to the order of 5 amperes during a 6-1/2 hour interval in Run 38. Data taken during a shorter time interval had less scatter than is evident on these curves. The data in general falls into the pattern of straight lines. The scatter in the experimental points may be partly due to changes in plasma temperature which may have occurred during this time period, as well as changes in the ohmic drop across the electrodes, and variations in the anode and cathode falls.

Materials Performance (Proof Test 2 - WESTF Test 38)

A number of different center wall MgO insulating blocks were used in the U-02 Proof Tests. The objective was to test and evaluate MgO insulators of different microstructures and densities under MHD channel conditions. Four different MgO refractories from Harbison-Walker, one from Norton, and one from Kaiser were evaluated. The purity, density, and porosity of each are shown in Table 25. The microstructure of each prior to testing are shown in Figures 80 and 81.

Two of the MgO refractories (HW-0401 and HW0601) from Harbison-Walker held up exceedingly well during the test. There was very little erosion or plasma corrosion of either type. The microstructure of each are quite similar - a large number of dense MgO grog grains surrounded by a relatively pore free matrix. These two MgO types also had the greatest density of the six tested. HW-0701, also from Harbison-Walker, held up only fair during the 20 hour test. Some potassium corrosion into the matrix was apparent. This structure had somewhat larger MgO grog grains than the previous two and was surrounded by a more porous matrix. The refractory from Norton (NT-0102), a fused grain MgO, showed no signs of potassium corrosion or erosion, but suffered greatly from extensive cracking due to the thermal gradient through the material. The final two MgO structures, (KA-0101 and HW-0801) were both found to be very poor refractories in combating potassium seed corrosion. The matrix portion of each of the structures was attacked extensively by the seed disolving away the constituents and creating conductivity paths through the insulating block.

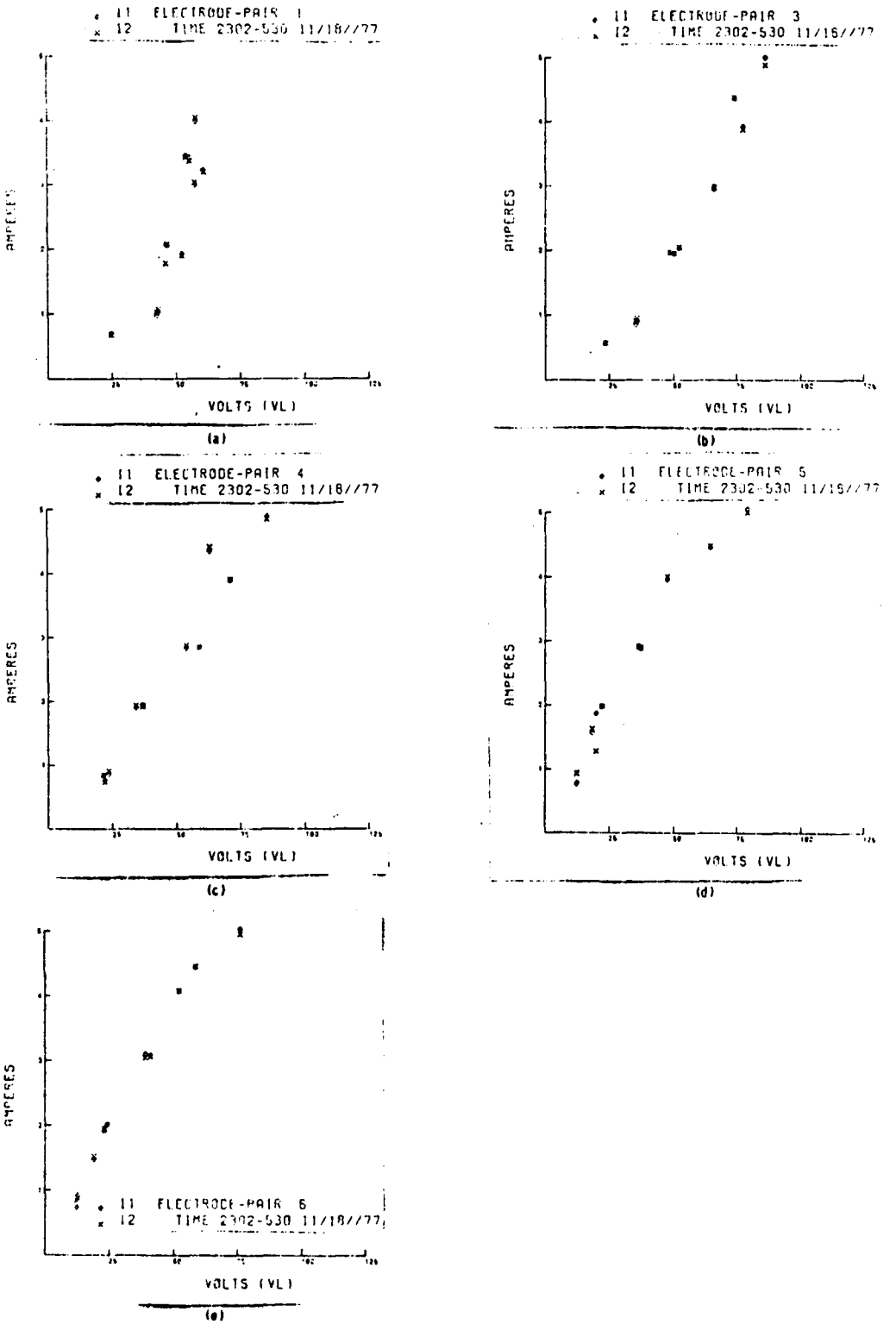

Figure 78. Load Current versus Applied Voltage V_L Taken During Test 38

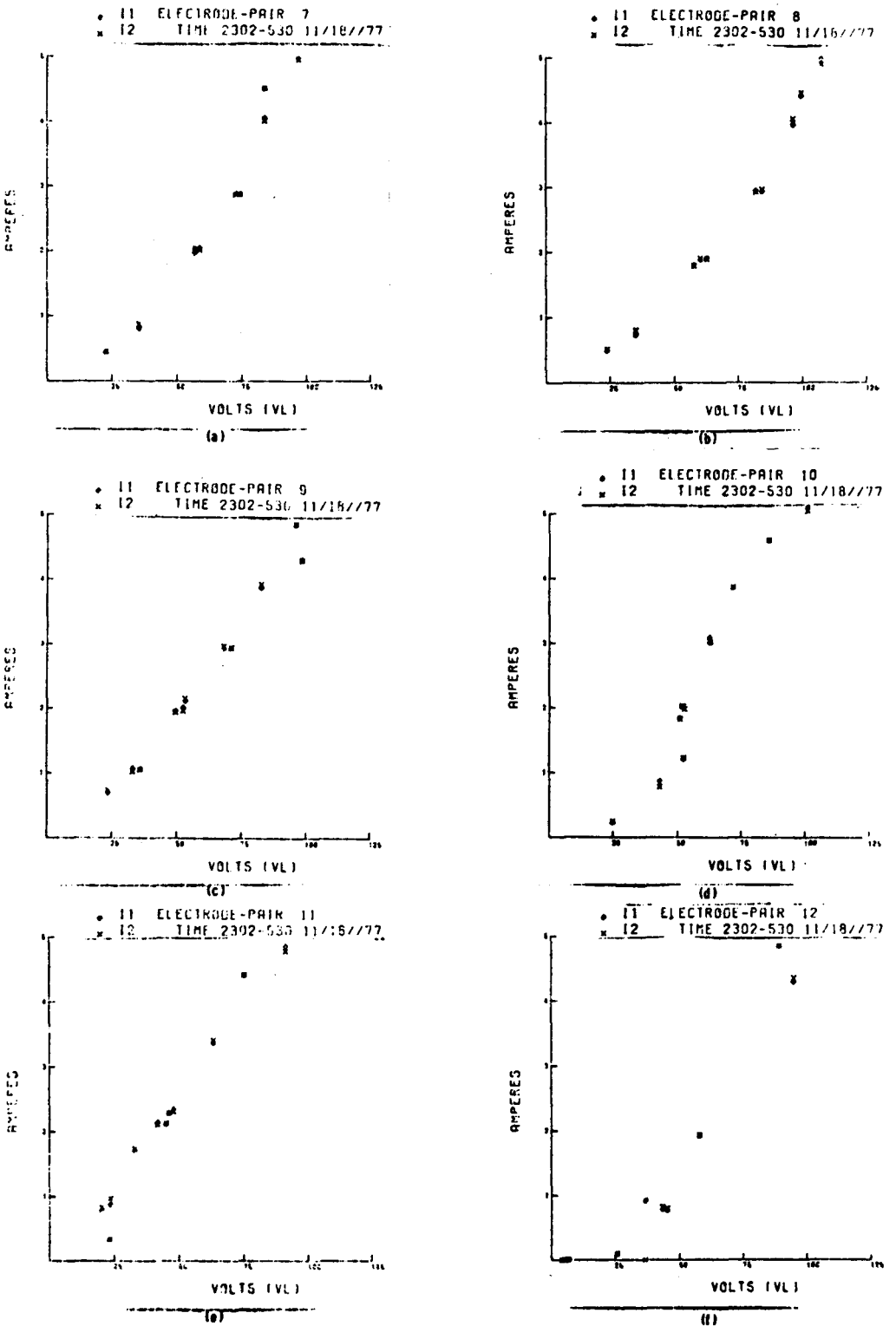

Figure 79. Load Current versus Applied Voltage V_L taken during Test 38

TABLE 25. DENSITIES AND POROSITIES OF MgO CENTER INSULATING BLOCKS

MATERIAL	PROCESSOR	PURITY (%MgO)	DENSITY	% TOTAL	POROSITY %CL	%OP
HW-0610	Harbison-Walker	99.9	3.18	11.02	0.1	10.92
HW-0701	Harbison-Walker	98	2.97	17.03	1.84	15.19
HW-0401	Harbison-Walker	98	3.04	15.01	0.49	14.52
NT-0102	Norton	99.9	3.01	16.0	3.8	12.2
KA-0101	Kaiser	98	2.93	18.5	1.93	16.57
HW-0801	Harbison-Walker	98	2.90	18.8	1.61	17.19

HW-401 12X

HW-0601 12X

HW-0710 12X

Figure 80. Microstructure of Different MgO Center Wall Insulation in Proof Test No. 2

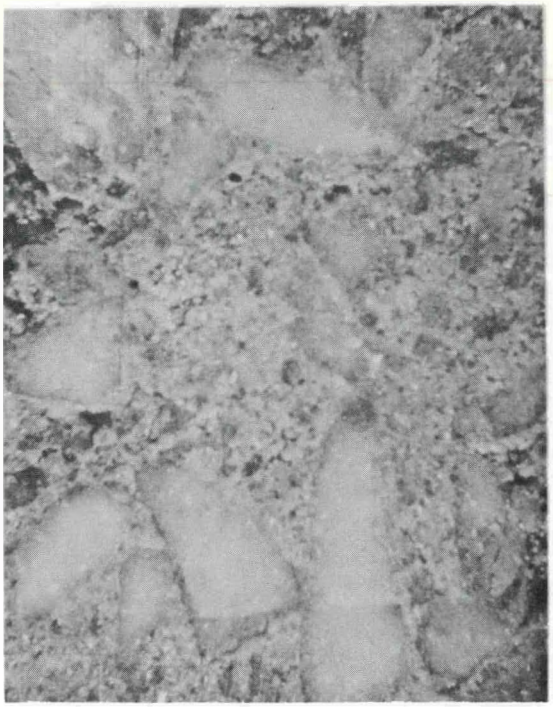

KA-0101 12X

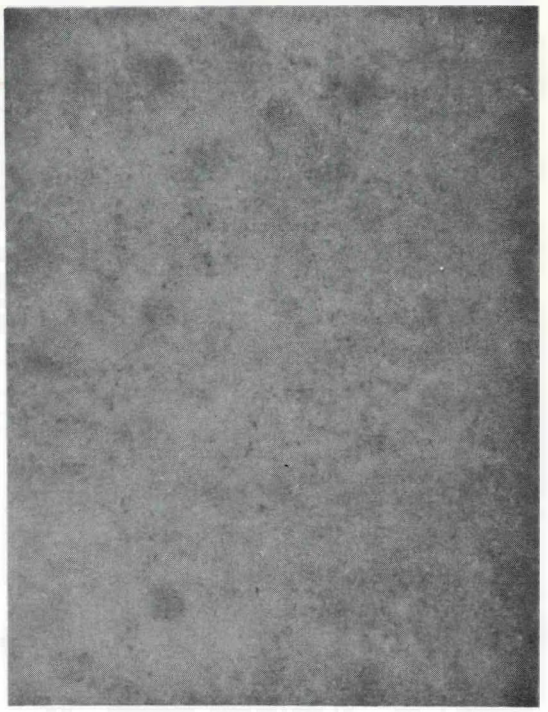

(Fused Grain) 12X
NT-0102

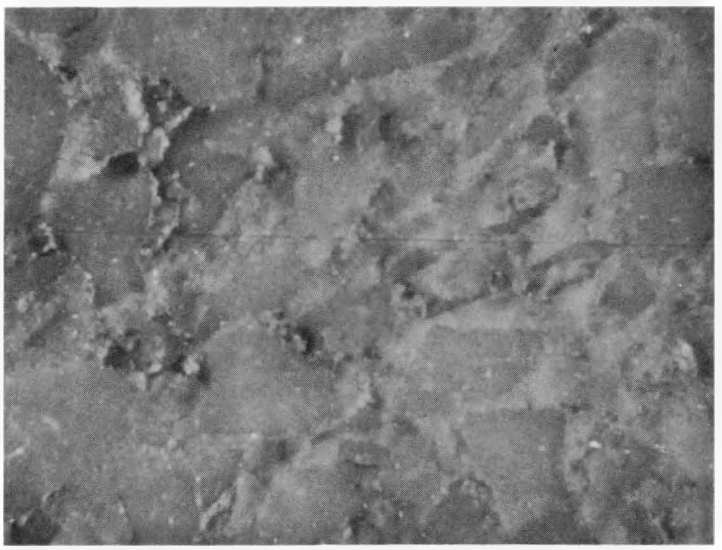

HW-0801

Figure 81. Microstructure of Different MgO Center Wall Insulation in Proof Test No. 2

6.0 WBS 1.6 - PROJECT MANAGEMENT AND DOCUMENTATION

The following project required documentation was issued during the reporting period.

- Work Plan - Proof Test 1
- Work Plan - Proof Test 2
- Work Plan - Proof Test 3
- Express Report - Proof Test 1
- Express Report - Proof Test 2
- Project Management Summary Baseline Report (Revised) dated 10/1/77
- Monthly Project Management Summary Report - September
- Monthly Project Management Summary Report - October
- Monthly Project Management Summary Report - November

7.0 REFERENCES

1. R. H. Eustis and J. K. Koester, "Coal Slag Phenomena in MHD Generators," First Int'l Conf., on Materials for Coal Conversion and Utilization, National Bureau of Standards, October, 1977.

2. S. Petty et al, "Electrode Phenomena in Slagging MHD Channels, Proc. of 16th Sym. on Eng. Aspects of MHD, Pittsburgh, Pa., March , 1977.

3. L. H. Cadoff et al, "The Evaluation of Electrode Materials for Slag Coated MHD Channels, Proc. of 16th Sym. on Eng. Aspects of MHD, Pittsburgh, Pa., March, 1977.

4. J. B. Heywood and G. J. Womack, "Open Cycle MHD Power Generation, Pergamon Press, 1969.

5. R. A. Perkins, "Evaluation of Electrode Materials for Slagging MHD Generators," 1st Int'l. Conf. on Materials for Coal Conversion and Utilization, National Bureau of Standards, October, 1977.

6. FE-2248, "Development, Testing and Evaluation of MHD Materials and Component Designs, Quarterly Report, January - March 1977," DOE Contract EX-76-C-01-2248, Westinghouse Electric Corporation, April 1977.

7. W. R. Dickson and E. B. Dismukes, "Electrolysis of FeO-CaO-SiO_2 Melts," TAIME, 224, 1962, p. 505.

8. H. P. Frederikse and W. R. Hosler, High Temperature MHD Materials, NBS Interim Report to OCR, Department of Interior, August, 1974.

9. J. L. Bates, "Electrical Conductivity of Molten Coal Slags Containing Potassium Seed," Proc. of 16th Symp. on Eng. Aspects of MHD, Pittsburgh, Pa., March, 1977.

10. J. K. Koester and R. M. Nelson, :Electrical Behavior of Slag Coatings in Coal-Fired MHD Generators," Proc. of 16th Sym. on Eng. Aspects of MHD, Pittsburgh, Pa., March, 1977.

11. FE-2248-17, "Development, Testing and Evaluation of MHD Materials and Component Designs, Quarterly Report for the Period July - September 1977," Contract EX-76-C-01-2248, Westinghouse Electric Corporation, February 1978.

12. WANL-TME-1872, "TAP-A, A Program for Computing Transient or Steady-State Temperature Distributions," Westinghouse Electric Corporation, December, 1969.

13. WECAN-Westinghouse Electric Computer Analysis," Westinghouse Electric Corporation, May 1974.

V. CONCLUSIONS

The understanding of the electrochemical corrision reactions has been shown to be critically important to the selection of electrode materials for MHD channels operating under semi-hot wall slagging conditions. The chemistry, mechanisms and kinetics of electrode/slag reactions have been evaluated. Important electrochemical reactions include slag electrolysis, preferential transfer of aggressive ion species in the slag to the cathodes and anodes, chemical reactions of electrodes with slag and with the products of the electrolysis of the slag, and cavitation/erosion of the anodes.

Completion of WESTF Tests 37 and 38 (U-02 Phase III Proof Tests 1 and 2) further demonstrated facility reliability. As a result of this testing experience a number of procedural and hardware changes were implemented including:

- Use of HOLDS at: a plasma temperature of 1850°C, 100°C below the electrode surface design point and at the design point
- Addition of sacrificial mixer and transition section gas stream thermocouples
- Use of unsheathed hot face electrode thermocouples
- Detailed comparison of test data for the three HOLD points with pre-test predictions.

Post-test visual observation of the electrode walls of Proof Test 2 (WESTF Test 38) showed all $LaCrO_3$ based electrode materials to be very resistant to the plasma conditions. This observation is supported by material characterization efforts currently in process. The plasma sprayed electrodes are subject to increased degradation from hydration when compared with hot pressed materials.

☆U.S. GOVERNMENT PRINTING OFFICE: 1978-740-306/ 4324 REGION NO. 4